

Development of Adsorbents from Brewer's Spent Grain for Uranyl  
Ion Removal from Wastewater

DISSERTATION

zur Erlangung des akademische Grades

Doctor rerum naturalium

(Dr.rer.nat)

vorgelegt

der Fakultät Mathematik und Naturwissenschaften

der Technischen Universität Dresden

von

M.Sc. Yi Su

Geboren am 11.06.1992 in Shandong, China

Eingereicht am \_\_\_\_\_

Die Dissertation wurde in der Zeit von 09/2018 bis 09/2022 in der Professur für  
Anorganische Molekülchemie der Technischen Universität Dresden angefertigt.

Gutachter:

Prof. Dr. Jan J. Weigand

*I am very much indebted to Prof. Dr. Jan. J. Weigand for his generous support, help and advice.*



# Content

1. Introduction .....	1
1.1. Uranium contamination in the aquatic environment .....	2
1.1.1. Physicochemical properties of uranium .....	2
1.1.2. Uranium toxicity and its contamination in aquatic environment .....	3
1.2. Uranium adsorption from the aquatic environment.....	6
1.2.1. Adsorbents for uranium removal.....	6
1.2.2. Biomass as adsorbents for uranium removal.....	8
1.2.3. Modification approach for lignocellulosic biomass as adsorbents.....	10
1.3. Production and composition of brewer's spent grain .....	13
1.3.1. Production of brewer's spent grain .....	13
1.3.2. Composition of brewer's spent grain .....	14
1.4. Use of brewer's spent grain .....	17
1.4.1. Current use of brewer's spent grain .....	17
1.4.2. Use of brewer's spent grain for adsorption .....	18
2. Objectives.....	21
3. Thermal conversion of brewer's spent grain for uranyl and rare earth metal ions adsorption.....	25
3.1. Hydrothermal treatment of brewer's spent grain.....	26
3.1.1. Effects of reaction temperature and time on adsorption capacity and chemical composition .....	26
3.1.2. Effects of reaction temperature and time on the surface functional groups.....	28
3.1.3. Effects of reaction temperature and time on Maillard reaction.....	30
3.2. Characterization of the adsorbents .....	33
3.2.1. <sup>13</sup> C CP/MAS solid state NMR spectra .....	33
3.2.2. Oxygen functional groups (OFG) .....	33
3.2.3. STA-GC-MS analysis .....	34
3.3. Batch adsorption experiments .....	37
3.3.1. Effect of pH value .....	37
3.3.2. Adsorption kinetics .....	39
3.3.3. Adsorption isotherm.....	40
3.3.4. Effect of temperature.....	42
3.4. Investigation of adsorption mechanism.....	46
4. Oxidation of brewer's spent grain for uranyl ion adsorption .....	49

4.1.	Oxidation of brewer's spent grain .....	50
4.2.	Characterization of the adsorbents .....	52
4.2.1.	FT-IR and solid-state NMR spectra .....	52
4.2.2.	Chemical composition and functional groups .....	54
4.2.3.	Thermogravimetric analysis .....	55
4.3.	Batch adsorption experiments .....	57
4.3.1.	Effect of pH value .....	57
4.3.2.	Adsorption kinetics .....	59
4.3.3.	Adsorption isotherm .....	62
4.3.4.	Effect of temperature .....	65
4.4.	Investigation of adsorption mechanism .....	66
4.5.	Desorption and reusability .....	68
4.6.	Performance at high salinity and under alkaline condition .....	69
5.	Brewer's spent grain-supported superabsorbent polymer for uranyl ion adsorption .....	71
5.1.	Synthesis of brewer's spent grain supported superabsorbent polymer (BSG-SAP) .....	72
5.2.	Characterization of the adsorbents .....	74
5.3.	Comparing properties of BSG-SAP with the reference polymer .....	78
5.4.	Batch adsorption experiments .....	80
5.4.1.	Adsorption kinetics .....	80
5.4.2.	Effect of pH value .....	83
5.4.3.	Effect of anions species and ionic strength .....	85
5.4.4.	Adsorption isotherm .....	86
5.4.5.	Performance at high salinity and under alkaline condition .....	88
5.4.6.	Adsorption selectivity .....	91
5.5.	Fixed bed column experiments .....	93
5.5.1.	Breakthrough curves and dynamic modeling study .....	93
5.5.2.	Performance at low concentration, high salinity and under alkaline conditions .....	96
5.5.3.	Desorption and reusability .....	97
5.6.	Investigation of adsorption mechanism .....	100
5.7.	Degradability test .....	104
6.	Surface ion-imprinted brewer's spent grain for selective uranyl ion adsorption .....	107
6.1.	Synthesis of surface ion-imprinted brewer's spent grain (IIP-BSG) .....	109
6.2.	Characterization of the adsorbents .....	113
6.3.	Batch adsorption experiments .....	116

6.3.1	Adsorption kinetics and mass transfer mechanisms.....	116
6.3.2	Adsorption isotherm.....	120
6.3.3	Site energy distribution of IIP-BSG in single and binary solution .....	123
6.3.4	Effect of pH on adsorption capacity and selectivity .....	125
6.3.5	Effect of ionic strength and Eu(III)/U(VI) molar ratio.....	126
6.3.6	Desorption and reusability .....	128
6.4.	Investigation of adsorption mechanisms .....	129
7.	Application of the BSG-derived adsorbents under real-world conditions .....	131
7.1.	Adsorbent aging test .....	131
7.2.	Adsorption test in simulated nuclear wastewater .....	133
7.3.	Adsorption test in simulated mine and tailings water.....	136
8.	Summary .....	143
9.	Perspectives.....	149
10.	Experimental section .....	153
10.1.	General information .....	153
10.1.1	Materials.....	153
10.1.2	Preparation of standardized BSG .....	154
10.1.3	Chemical composition of BSG.....	154
10.1.4	General characterization methods .....	155
10.1.5	General analytical methods .....	156
10.1.6	Thermal stability and differential scanning calorimetry analysis .....	157
10.1.7	Adsorbent aging test in ultrapure water .....	158
10.1.8	Analysis of Maillard reaction products of BSG and ABSG.....	158
10.1.9	Cross-linking and swelling test for BSG-SAP .....	158
10.2.	Synthetic methods.....	161
10.2.1	Hydrothermal treatment of brewer's spent grain .....	161
10.2.2	Oxidation of brewer's spent grain .....	161
10.2.3	Synthesis of brewer's spent grain-supported superabsorbent polymer .....	162
10.2.4	Synthesis of surface ion-imprinted brewer's spent grain .....	163
10.3.	Batch adsorption experiments.....	166
10.3.1	General batch adsorption experiments .....	166
10.3.2	Adsorption experiments using <sup>169</sup> Yb radiotracer .....	167
10.3.3	Effect of temperature on the adsorption capacity.....	167
10.3.4	Desorption and reusability test.....	168

10.3.5	Adsorption selectivity and ion-imprinting factor .....	168
10.3.6	Adsorption performance in simulated wastewater .....	169
10.4.	Fixed bed column adsorption experiments of BSG-SAP .....	172
10.5.	Models and data processing .....	173
10.5.1	Batch adsorption kinetic models .....	173
10.5.2	Mass transfer resistance models .....	174
10.5.3	Batch adsorption isotherm models .....	174
10.5.4	Site energy distribution function .....	176
10.5.5	Dynamic model for fixed bed column experiments .....	177
10.5.6	Comparison of the performance of different models .....	177
10.6.	Degradability test of BSG-SAP .....	179
11.	References .....	181
12.	Acknowledgement.....	189
13.	Publications and conference contributions.....	191
	Versicherung .....	193
	Erklärung.....	193



# 1. Introduction

Global energy demand has risen sharply due to the rapid industrialization and population growth. To mitigate global climate change caused by carbon emission, nuclear energy has been considered as a possible low-carbon alternative.<sup>[1]</sup> According to the *World Nuclear Performance Report 2021* by the World Nuclear Association,<sup>[2]</sup> about 10% of the world's electricity is provided from about 440 operating nuclear power plants, making nuclear energy the world's second largest source of low-carbon power. In addition, about 50 more nuclear power plants are under construction. According to the International Atomic Energy Agency (IAEA), the annual global demand for uranium on January 1, 2019, amounted to 59,200 tons.<sup>[3]</sup> However, safety concerns about contamination from radioactive waste from nuclear power plant, related industry, and uranium mining have grown as nuclear energy has flourished. The unintentional release of uranium into the aquatic environment poses a serious threat to ecosystem and human health due to its radiological and chemical toxicity.<sup>[4]</sup> In 1998, the World Health Organization (WHO) drinking water guideline value for U was introduced as 2 µg/L and has increased to 30 µg/L as a current standard since 2011.<sup>[5,6]</sup> To tackle this challenge, numerous adsorbents including organic materials, inorganic materials, nanomaterials, and framework materials have been developed to remove uranium from wastewaters owing to their simplicity, fast kinetics, extensive applicability, cost-effectiveness, and non-secondary contamination.<sup>[1,7]</sup>

For several years biosorbents have been hailed as a promising choice among all adsorbents because of their apparent efficiency, similarity to conventional ion exchangers, and availability.<sup>[8]</sup> Brewer's spent grain (BSG) is the main by-product from beer brewery industry, with an annual global production of 39 million tons. BSG is a lignocellulose material rich in protein, which is a cheap, widely available and a continuously accessible raw material for biosorbents,<sup>[9]</sup> and despite the large produced amount, it has received little attention as a valuable commodity, and its disposal is often problematic to the environment.<sup>[10]</sup> Therefore, it is of great interest to develop effective, low-cost adsorbents from BSG for uranium decontamination of the aquatic environment, which would fulfill the purpose of 'dealing pollution with waste'.

## 1.1. Uranium contamination in the aquatic environment

### 1.1.1. Physicochemical properties of uranium

Uranium (U) is widely considered the last naturally occurring element with an atomic number of 92 and an atomic mass of 238 that is present in comparatively large quantities. Uranium is radioactive and belongs to the group of actinides existing in nature as several isotopes, namely  $^{238}\text{U}$  (99.27 wt%),  $^{235}\text{U}$  (0.72 wt%), and  $^{234}\text{U}$  (0.006 wt%) with a very long half-life of  $4.5 \times 10^9$ ,  $7.0 \times 10^8$ , and  $2.4 \times 10^5$  years and a specific activity concentration of  $1.2 \times 10^4$  Bq/g,  $8.0 \times 10^4$  Bq/g, and  $2.3 \times 10^8$  Bq/g, respectively.<sup>[4,11]</sup> This means that the radioactivity of natural U is very low. In addition, uranium is multivalent and can occur in the oxidation states +2, +3, +4, +5, or +6, whereas only the +4 and +6 oxidation states are found in nature. The tetravalent uranium U(IV) is found in reducing environments, relatively insoluble, and known to accumulate in anoxic sediments such as ore deposits and contaminated aquifers.<sup>[12]</sup> Whereas, the hexavalent uranium U(VI) mostly in form of  $\text{UO}_2^{2+}$  ion is highly soluble and mobile in aquatic environment, which rises more threats to environment and human health. Therefore, the current research focuses on the removal of U(VI), predominantly as the uranyl ions,  $\text{UO}_2^{2+}$ , in water.

The predominate species of U(VI) in aqueous environment is strongly affected by the pH value of the solution and shows strong impacts on the electrostatic effect between the adsorbents and the metal ions. The species distribution of U(VI) in aqueous solution as a function of pH could either obtained from literature<sup>[1,13]</sup> or calculated using Visual MINTEQ 3.1 software.<sup>[14]</sup> Fig 1.1 shows the species distribution of U(VI) as a function of pH in a 0.5 mM  $\text{UO}_2(\text{CH}_3\text{COOH})_2$  solution, which represents a model solution commonly used in the adsorption experiments. Generally,  $\text{UO}_2^{2+}$  is dominant in solution when  $\text{pH} < 3$ , and hydrolysed species like  $(\text{UO}_2)_2(\text{OH})_2^{2+}$  and  $(\text{UO}_2)_3(\text{OH})_5^+$  occur with reduced concentration of  $\text{UO}_2^{2+}$  as the pH value increases. As shown in Fig. 1.1, when the pH value further increases over 5, the saturation index of *Schoepite* ( $[(\text{UO}_2)_4\text{O}(\text{OH})_6]6\text{H}_2\text{O}$ ) becomes positive, indicating that the solution is supersaturated, and *Schoepite* could probably precipitate from the solution.<sup>[15]</sup> Thus, the pH range of possible precipitation should be carefully avoided (e.g.  $\text{pH} = 5\text{--}11$  when  $c_0(\text{U}) = 0.5$  mM) to accurately determine the adsorption capacity. Furthermore, it is important to consider the surface charge when select proper adsorbents in order to obtain maximum adsorption capacity of U(VI).

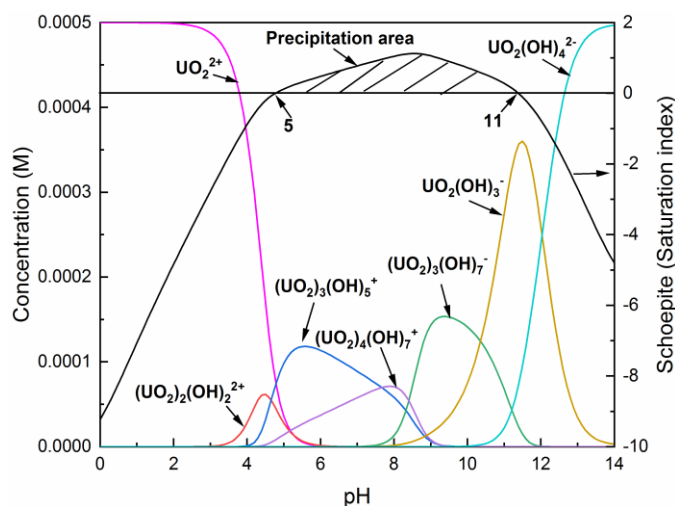


**Fig. 1.1.** Species distribution of U(VI) as a function of pH in a 0.5 mM  $\text{UO}_2(\text{CH}_3\text{COOH})_2$  solution.<sup>[14]</sup>

### 1.1.2. Uranium toxicity and its contamination in aquatic environment

Uranium has no known metabolic function in animals and therefore is regarded as a nonessential element. It is known for radiologic and chemical toxicity and has become a worldwide threat to the ecosystem and human health.<sup>[11]</sup> Although uranium may be considered carcinogenic due to its radioactivity, the chemical toxicity of uranium is a primary environmental health hazard posed by the hexavalent uranyl ions ( $\text{UO}_2^{2+}$ ).<sup>[16,17]</sup>  $\text{UO}_2^{2+}$  is a bioavailable species that can be efficiently complexed with bicarbonate, citrate and proteins and is stored and incorporated in bones, kidneys, and liver.<sup>[4]</sup> From experimental animal studies and human epidemiology, uranium presents renal, developmental and reproductive toxicity and causes diminished bone growth and DNA damage.<sup>[16]</sup> A review study including epidemiological and laboratory studies during 2000–2019 shows that uranium primarily poisons kidney (36.22%), bone (19.48%), liver (17.58%), the reproductive system (13.90%), lung (7.24%), and the nervous system (5.58%), causing health problems.<sup>[4]</sup> Among all the health effects, the nephrotoxicity may be considered as one of the most sensitive indicators of U toxicity.<sup>[17]</sup> For example, the epidemiological study of 325 people from southern Finland who are chronically exposed to uranium through drinking water for at least 1 year shows an association between increased uranium exposure and excretion of calcium in urine, which is consistent with the alterations of proximal tubular function.<sup>[18]</sup> Apart from health issues to human beings, uranium contamination has many ecological consequences. For example, it can affect the growth of plants, inhibit the photosynthesis, and damage the cell respiration of microorganisms.<sup>[19]</sup> Therefore, the widely uranium contamination and the health hazards of

uranium highlight the significance of uranium removal from the aquatic environment, especially uranyl ions.

In generally, the majority of uranium exposure in the environment is due to ingesting of water or food in uranium-contaminated areas.<sup>[20]</sup> Uranium naturally occurs at low concentrations in nearly all soils, sediments, rocks, natural waters, air, plants and animals. It is found with concentrations of 2.3 µg/g in the earth's crust,<sup>[4]</sup> 12 ng/L to 4.8 µg/L in stream water worldwide, and approximately 3.4 µg/L in seawater.<sup>[12]</sup> High concentrations of uranium in surface water, groundwater, and wastewater that exceed the standard value of WHO (30 µg/L) have been reported all around the world. The sources of elevated uranium concentration in the aquatic environment can be either natural or anthropogenic. Uranium may occur in natural waters because of weathering U-rich sediments and rocks, or the existence of *Autunite* [Ca(UO<sub>2</sub>)<sub>2</sub>(PO<sub>4</sub>)<sub>2</sub>], which shows high solubility.<sup>[21]</sup> Human activities also contribute to uranium contamination in the aquatic environment, and the effects of uranium mining and processing of U-bearing polymetallic ores have been widely reported.<sup>[22]</sup> In addition, uranium, as the most commonly used radioactive element, accounts for 94% of the spent nuclear fuel,<sup>[23]</sup> and nuclear accidents, waste disposal, and military activities are also responsible for uranium contamination. Moreover, the use of phosphate fertilizers may also lead to groundwater contamination, as natural occurring phosphate deposits can contain U in concentrations as high as 150 mg/kg.<sup>[11]</sup> Table 1.1 shows the uranium concentration detected in aquatic environment worldwide. For example, uranium concentrations as high as 11.7 g/L were reported at various United States Department of Energy (DOE) sites in 1992.<sup>[24]</sup> More recently in 2015, an uranium concentration of 5.4 mg/L was detected in the groundwater from the Central Valley aquifer in U.S..<sup>[25]</sup> In addition, a 2018 survey found large-scale uranium contamination in groundwater wells, with 75 of the 226 wells tested in Rajasthan and five of the 98 wells tested in Gujarat, India, having uranium concentrations that exceed WHO guideline of 30 µg/L.<sup>[26]</sup> Higher concentration of uranium has also been detected in the mining related waters (5–17 mg/L) in Germany<sup>[22]</sup> and bedrock water in the uraniferous granite areas of southern Finland (up to 12.4 mg/L).<sup>[27]</sup> Additionally, industrial effluent from Brazilian Nuclear Industry (BNI) was reported to contain uranium up to 43 mg/L.<sup>[28]</sup> Recently, researchers have indicated that the possibility of detecting U contamination in the coastal waters near the Fukushima Daiichi nuclear power plant will increase over time, and long-term contamination monitoring and treatment will be important for the environment and human health.<sup>[29]</sup> Therefore, the elevated level of uranium concentration in global aquatic environment and industrial effluent has risen more and more concerns, pointing at a great demand for new approaches for uranium removal.

**Table 1.1.** Global uranium contamination in waters.

Country	Water type	Area	U concentration ( $\mu\text{g/L}$ )		Reference
			Range	Median	
China	Groundwater	Datong basin, Shanxi	<0.02–288	10	[30]
U.S.		The High Plains aquifer	$\leq 2,674$	5.1	[25]
		The Central Valley aquifer	$\leq 5,400$	45	
		Northwestern Connecticut	<1–1,200		[31]
		Various United States Department of Energy (DOE) sites	0.001–11,700,000		[24]
India		Gujarat	<0.001–85.8		[26]
		Jaipur and Ajmer, Rajasthan	0.3–88.5		
Germany		Bamberg, Bavaria	0.006–42.33		[32]
Spain		Ridaura basin	0.258–152		[21]
Mongolia		Ulaanbaatar	<0.01–57		[33]
Burundi		Kirundo	0.238–734		[34]
Germany	Mine water	Schlema, Saxony		5,000	[22]
		Königstein, Saxony		17,000	
	Tailings water	Helmsdorf, Saxony		6,000	
Finland	Bedrock water	Uraniferous granite areas of southern Finland	Up to 12,400		[27]
Brazil	Industrial effluent			43,000	[28]

## 1.2. Uranium adsorption from the aquatic environment

### 1.2.1. Adsorbents for uranium removal

To deal with the uranium contamination, various technologies have been applied for its removal from the aqueous phase, including solid phase extraction,<sup>[35]</sup> solvent extraction,<sup>[23,36,37]</sup> electrochemical treatment,<sup>[38]</sup> biological treatment,<sup>[39]</sup> ion-floatation, reverse osmosis, ultra-filtration, chemical precipitation, etc.<sup>[40]</sup> However, these conventional methods are limited by disadvantages such as high cost, non-reusability, lower efficiency at low concentration and difficulty of sludge management.<sup>[40]</sup> Recently, adsorption process has risen more and more interests in both academic and industry fields to remove uranyl ions from contaminated waters. This is because adsorption demonstrates obvious advantages including (1) fast kinetics, high adsorption capacity, remarkable stability and regeneration potential;<sup>[41]</sup> (2) simplicity, low cost and wide-range availability;<sup>[23]</sup> and (3) avoidance of organic solvent and non-secondary contamination.<sup>[42]</sup> Numerous adsorbents have been developed and tested for uranium removal and are summarized in Table 1.2, sorted as five categories: inorganic materials, carbon materials, porous framework materials, synthetic polymer materials, and natural polymer/biomass materials. From the perspective of adsorption performance, the nanostructured carbon materials, porous framework materials and the synthetic polymers present high adsorption capacity, fast kinetics and high selectivity, which are promising for uranium removal.<sup>[7,43–46]</sup> Nevertheless, the application and commercialization of these adsorbents still face great challenges. For example, nanostructured carbon materials are very small in size and difficult to separate from the aqueous phase, and the safety of nanomaterials has not yet been proven.<sup>[7]</sup> In addition, the stability of porous framework materials is generally poor under real-world conditions, and the lack of reusability of the abovementioned adsorbents is also a common drawback.<sup>[43,44]</sup> Considering the chemical reagents and the steps involved to prepared these adsorbents, they are unlikely to be cheap enough for large-scale application. On the base of cost-to-performance ratio, biosorbents are most preferable and economically viable among all the adsorbents, as they are convenient, readily available and cheap.<sup>[47]</sup> They also present great potential as an eco-friendly alternative to synthetic adsorbents.<sup>[48]</sup> Although the adsorption capacity and selectivity may range from very low to excellent for different kinds of biomass, it has abundant functional groups that are suitable for functionalization to increase and stabilize the performance.<sup>[49,50]</sup> Thus, biomass is an interesting source with high potential to develop new kinds of biosorbents through various modification and functionalization methods.

**Table 1.2.** Comparison of different adsorbents for uranium adsorption.

Category		Advantages	Disadvantages	Reference
Inorganic materials	Layered double hydroxides	High mechanical strength; Easy to prepare; Good availability	Slow kinetics; Limited selectivity; Poor reusability	[7,45]
	Mesoporous silica	Fast kinetics; Excellent selectivity; Good reusability	Instability under very acidic/basic medium	[7]
	Titanium dioxide based sorbents	Good radiochemical stability; Negligible solubility; Photoreduction of uranium on titania surface	Difficulty of separation; Toxicity of nanoparticles	[51]
	Nanoscale zero-valent iron	Fast kinetics; Excellent selectivity; High loading; Good reusability	Difficulty of separation; Toxicity of nanoparticles	[52]
Carbon materials	Activated carbon	Low cost; Good availability	Low adsorption capacity	[43]
	Nanostructured carbon materials	High adsorption capacity; Fast kinetics; Excellent selectivity; Good reusability	Difficulty of separation; Toxicity of nanoparticles	[7]
Porous framework materials	Porous organic frameworks	High adsorption capacity; Excellent selectivity	Low mechanical properties; Poor reusability	[43,44]
	Metal organic frameworks	High adsorption capacity; Excellent selectivity	Poor chemical stability; Poor reusability	[7,46]
Synthetic polymers	Fibrous polymer materials	High adsorption capacity; Fast kinetics; Excellent selectivity; High mechanical strength	Poor reusability; Non-renewable raw materials	[43]
	Resins	High adsorption capacity; Fast kinetics; Excellent selectivity	Aging and poisoning; Low stability and poor reusability	[7,45]
Natural polymer/biomass materials		Low cost; Biocompatibility; Easy to functionalize; Good availability	Selectivity and adsorption capacity varies from cases to cases	[1,49]

### 1.2.2. Biomass as adsorbents for uranium removal

Biosorption is generally used to describe the removal of adsorbates by their passive binding to active or dead biomass materials in aqueous solutions.<sup>[53]</sup> The extra benefits of using biosorbents with adequate adsorption performance (removal efficiency, selectivity, etc.) include minimization of chemical or biological sludge, no additional nutrient requirement, possibility of metal recovery,<sup>[54]</sup> easy to functionalize, non-toxicity, and the possibility of further volume decrease by pyrolysis.<sup>[7]</sup> It should be noted that a biosorbent may be considered cost-efficient if it requires little processing, is abundant in nature, or is a by-product or waste material from another industry.<sup>[8]</sup> Therefore, direct use of the biomass without or with simple modification would be the first choice to find a suitable and cheap biosorbent. Table 1.3 summarizes biomass from different origins used for uranium adsorption, the functional groups that are involved in adsorption, and modification methods. Algae, bacteria, fungi, plant materials, materials of animal origin, and biomolecules have been explored for uranium adsorption.<sup>[49,50]</sup> The abundant functional groups of the biomass, such as carboxyl-, hydroxyl-, phenolic-, and phosphonate groups as well as ketone, aldehyde and amide functions provide the affinity towards the uranyl ions. For example, the bacteria *Brachybacterium* sp. G1,<sup>[55]</sup> the green alga *C. glomerata*,<sup>[56]</sup> and the fungus *Trichoderma harzianum*<sup>[57]</sup> are reported to have U(VI) adsorption capacities of 971 mg/g, 287.7 mg/g, and 612 mg/g, respectively. To improve mechanical stability and efficiency, immobilization is often used to modify algae, bacteria or fungi based adsorbents.<sup>[58]</sup> A large variety of plant materials, especially agro-industrial waste like rice and coffee husks, crops residues, straws, leaves, sugar beet pulp, and pomelo peels have also been investigated for uranium adsorption.<sup>[40,49,50]</sup> The plant materials are mainly composed of lignin and cellulose, whose modification methods are well explored and established and will be detailed discussed in the following Section 1.2.3. Biosorbents from animal origin generally include scales, eggshell membranes, bones and chitosan, among which chitosan/chitin is the most widely investigated.<sup>[50]</sup> For instance, chitin extracted from marine sponge *Aplysina aerophoba* shows an adsorption capacity for U(VI) of 288 mg/g.<sup>[59]</sup> Further manipulating the structure of chitosan/chitin could improve its performance, e.g. crosslinking could enhance its microbiological and mechanical resistance, production in the form of nanoparticles and nanocrystals could increase specific surface area, and association with other compounds could improve its porosity. In addition, chitosan can also be grafted onto artificial polymers to obtain superabsorbent polymers whose molecular weight and degree of acetylation can be adjusted as desired.<sup>[60]</sup>



Aside from the biomass that is frequently investigated, a few studies have explored the use of some biomolecules like dopamine and tannic acid to modify other biomass. Dopamine is an important biomolecule secreted by mussels and can easily polymerize to yield polydopamine, which shows great attraction in adsorption because of its strong adhesion, good biocompatibility, and their functional groups.<sup>[49]</sup> Immobilizing dopamine on the *Aspergillus niger* microspheres results in an adsorption capacity of the composite of 250.7 mg/g.<sup>[61]</sup> Tannic acid is widely distributed in the bark of many trees and fruits, which is rich in phenolic and carboxyl groups.<sup>[49]</sup> The tannic acid-chitosan hydrothermal carbon is reported to have an adsorption capacity of 97 mg/g of U(VI).<sup>[62]</sup> Moreover, the coordination and binding of U(VI) by different kinds of proteins such as phosvitin<sup>[63]</sup> and bovine milk proteins<sup>[64]</sup> are investigated, and engineered proteins designed by a computational screening process have shown a very high affinity and selectivity for U(VI) with a distribution coefficient ( $K_d$ ) of 7.4 femtomolar and >10,000-fold selectivity over other metal ions such as Cu(II), Ni(II), Zn(II), etc.<sup>[65]</sup> Water-soluble commercial proteins like bovine serum albumin (BSA), lysozyme and ovalbumin could be converted into adsorbents with high adsorption capacities of over 1000 mg/g within 2 h.<sup>[66]</sup> In addition, a hydrogel-like spidroin-based protein fiber shows an adsorption capacity of 12.3 mg/g and an ultrashort equilibration time of 3.5 days in natural seawater compared with other adsorbents (10-70 days) reported in literature.<sup>[67]</sup> Aside from this, little research has employed protein-rich biomass for uranium removal or investigated the function of proteins for uranium adsorption.

**Table 1.3.** Summary of functional groups and modification methods of certain biomass used for uranium adsorption.<sup>[49,50]</sup>

Biomass	Functional groups	Modification
Algae	Carboxyl, hydroxyl, amide, and thiol groups	Pretreatment, entrapment, surface modification, composites
Bacteria	Carboxyl, hydroxyl, amide, and phosphonate groups	
Fungi	Amine, imidazole, phosphate, sulphate, thiol and hydroxyl groups	NaOH pretreatment, magnetic modification, functionalization, immobilization, acetylation
Plant materials	Ketones, aldehydes, aromatic amines, carboxyl group, ethers, and phenolic groups	Acid/base treatment, chemical treatment, magnetic, surface functionalization, polymer grafting.
Biomass of animal origin	Amino/acetamido and hydroxyl groups	Cross-linking, magnetic functionalization, composites, gelation
Biomolecules	Carboxyl, amide, phenolic, catechol, and imine groups	Immobilization, modification of other adsorbents

### 1.2.3. Modification approach for lignocellulosic biomass as adsorbents

Lignocellulose, which consists of cellulose, hemicellulose, and lignin, is a major component of the plant-based biomass that is widely used for biosorbent production.<sup>[68]</sup> Cellulose makes up the majority of total biomass (30–50%) and is considered as the most abundant polymer in nature.<sup>[7]</sup> Therefore, modification approaches of cellulosic material to increase its adsorption performance have been widely investigated and applied to various lignocellulose materials. The modification approaches are summarized as follows including thermal treatment, direct chemical modification, and polymer grafting.

**(1) Thermal treatment:** Comparing with the chemical modification or polymer grafting methods for the biomass, thermal treatment presents some unique benefits as a greener and economical approach. However, it is less investigated in the application of uranium adsorption. One thermal treatment method is to produce activated carbon (AC) from the biomass source by pyrolysis followed by chemical or physical activation. Activated carbon is one of the most extensively used adsorbents for wastewater treatment due to its low cost and ease to modification. For example, Zhu et al. have reported a  $\text{KMnO}_4$ -modified hazelnut shell AC with an adsorption capacity for U(VI) of 22.27 mg/g.<sup>[69]</sup> Nevertheless, ACs generally have a hydrophobic surface and thus need to be functionalized with appropriate functional groups to improve their adsorption capacity and selectivity.<sup>[70]</sup> It is reported that amidoxime-grafted AC<sup>[71]</sup> and 2-aminobenzoic acid functionalized AC<sup>[70]</sup> has a high adsorption capacity for U(VI) of 191.6 mg/g and 194.2 mg/g, respectively. Hydrothermal treatment is another thermal approach to modify the biomass which is highly flexible on the choice of feedstock and there is no need of pre-drying of the biomass feeds and no toxic chemicals are required.<sup>[72]</sup> In this context, hydrothermal carbonization (HTC) is the most commonly used hydrothermal process for biosorbent production, and is typically performed at temperatures of up to 250 °C during which the biomass is submerged in water and heated under pressure.<sup>[73]</sup> The resulting solid product, named hydrochar, possesses abundant surface functional groups and has a high affinity towards uranyl ions.<sup>[74]</sup> For example, hydrochar prepared from pine needles<sup>[75]</sup> and carbonaceous spheres from glucose with  $\text{AlCl}_3$  as catalyst,<sup>[76]</sup> present adsorption capacity for U(VI) of 62.7 mg/g and 163 mg/g, respectively.

**(2) Direct chemical modification:** The direct chemical modification of cellulose includes esterification, halogenation, oxidation, etherification, alkaline treatment, amidoxime modification, and silylation.<sup>[37,77]</sup> Introduction of a amidoxime group ( $-\text{C}(\text{NH}_2)\text{NOH}$ ) is one of the most popular ways in the adsorbent construction due to its high affinity and selectivity toward the uranyl ions.<sup>[37]</sup> For example, amidoximated cellulose fiber membrane<sup>[78]</sup> and

amidoximated hydroxypropyl methylcellulose<sup>[79]</sup> show promising adsorption capacity for U(VI) of 52.9 mg/g and 765 mg/g, respectively. However, the modification of biomass using amidoxime groups is generally complex and tedious, including the grafting of acrylonitrile and the converting of cyano groups (–CN) into the desired amidoxime groups with hydroxylamine under basic conditions.<sup>[80]</sup> This makes it less attractive when considering the cost-effectiveness and the sustainability. Moreover, oxidation of cellulosic materials is also a promising choice due to the obtained high content of carboxyl groups that have a high affinity towards metal ions.<sup>[81]</sup> According to the literature,<sup>[82]</sup> nitrogen oxides, permanganates, peroxides and stable and non-persistent nitroxyl radicals (TEMPO and PINO) have been applied for the oxidation of cellulose. For example, Ma et al.<sup>[83]</sup> have obtained ultrafine cellulose nanofibers from wood pulp by TEMPO oxidation with a carboxyl group content of 1.4 mmol/g and a U(VI) adsorption capacity of 167 mg/g. Nevertheless, the widely applied nitroxyl radicals present some obvious drawbacks like high cost and the use of toxic reagents, and are only effective on cellulose components with little impurities.<sup>[82]</sup> Early work by Kumar and Yang<sup>[84]</sup> report the combination of H<sub>3</sub>PO<sub>4</sub>/HNO<sub>3</sub>-NaNO<sub>2</sub> as oxidants to produce carboxycellulose from untreated biomass, which is termed as ‘nitro-oxidation’. This provides a simple and selective oxidation without the use transition metals as catalysts. Carboxycellulose nanofiber obtained from jute fiber employing this method shows a high affinity towards U(VI) with clear precipitation (pH = 7, c<sub>0</sub>(U) = 2120 mg/L).<sup>[85]</sup> The reported adsorption capacity is higher than expected considering the available carboxyl groups of the nanofibers. This is mainly due to the aggregation of the nanofibers and the mineralization of uranyl ions forming uranyl hydroxide crystals rather than the interactions with carboxyl groups.<sup>[85]</sup> This makes it a rare example employing nitro-oxidation cellulose nanofibers for uranyl ions adsorption.

**(3) Polymer grafting:** Polymer grafting creates branches of synthetic polymers that impart specific functional groups onto the cellulose substrate for adsorption.<sup>[86]</sup> This is achieved commonly either by the ‘grafting-to’ approach or the ‘grafting-from’ approach. In the ‘grafting-to’ approach, a pre-formed polymer with a reactive end-group is coupled with the functional groups that are located on the cellulose backbone. Whereas in the ‘grafting-from’ approach, the growth of polymer chains occurs from the initiated sites on the cellulose backbone.<sup>[87]</sup> To increase the adsorption capacity and improve the mass transfer, the biomass-supported adsorbent is commonly fabricated as a superabsorbent polymer (SAP) through graft polymerization. This is because that the SAP shows strong affinity, abundant adsorption sites,<sup>[88]</sup> three-dimensional (3D) network, and good hydrophilicity.<sup>[89]</sup> Previous studies have reported several SAP (hydrogel) for the U(VI) adsorption with high adsorption capacities, such

as the poly(acrylic acid-co-acrylamide) hydrogel (713.2 mg/g),<sup>[90]</sup> the cellulose hydrogel (148 mg/g),<sup>[91]</sup> and the composite hydrogel of glutamic acid, gum tragacanth, and anionic polyacrylamide (384.6 mg/g).<sup>[92]</sup> Moreover, the cellulose and other biomass could be considered as a high potential, economically viable choice of the support materials when preparing polymer or composite adsorbents. The commonly used support materials, for instance, porous carbon, silica materials, and polyolefin fibers, are lack of abundant functionalities to bind U(VI) efficiently and are difficult to functionalize.<sup>[1]</sup> On the contrary, the biomass shows abundant functional groups and good hydrophilicity, which becomes a promising alternative. In summary, the currently available studies indicate a great potential of developing uranium adsorbents from biomass. However, commercially applied biosorption techniques are rare, facing the challenges of increasing its adsorption capacity, selectivity and stability.<sup>[50]</sup> At the same time, the modification method should be carefully chosen to lower the cost of the material and waste production.<sup>[7]</sup> Moreover, the performance of biosorbents in real wastewater, the regeneration and reuse of the biosorbents, and the fate of biosorbents after uranium removal still need further investigation.

### 1.3. Production and composition of brewer's spent grain

#### 1.3.1. Production of brewer's spent grain

Beer is one of the most popular beverage around the world with a global production over  $2.3 \times 10^{11}$  L annually.<sup>[93]</sup> Brewer's spent grain (BSG) is the most abundant by-product from the beer brewery process, accounting for 85% of the total generated solid waste. About 20 kg of BSG is generated when producing 100 L of beer, and the annual production of BSG is estimated to be  $4.6 \times 10^{10}$  kg by 2020.<sup>[9]</sup> According to the *Barth Haas Report* (Hops 2020/2021), the five leading beer-producing countries in the world are China, the USA, Brazil, Mexico, and Germany.<sup>[94]</sup> More than half of the beer produced worldwide was brewed in these five countries. Table 1.4 lists the beer production in the five countries and the estimated production of BSG. BSG is considered as a low commercial value by-product, and is largely produced, easily available from not only large factories but also small breweries.

**Table 1.4.** Beer and BSG production of the top five beer production countries worldwide.

Country	Beer production in 2020 (L) <sup>[94]</sup>	Estimated BSG production (kg)
China	$3.4 \times 10^{10}$	$6.8 \times 10^9$
the USA	$2.1 \times 10^{10}$	$4.2 \times 10^9$
Brazil	$1.5 \times 10^{10}$	$3.0 \times 10^9$
Mexico	$1.3 \times 10^{10}$	$2.6 \times 10^9$
Germany	$8.7 \times 10^9$	$1.7 \times 10^9$

BSG is produced mainly from barley, which is the main raw material for beer production. The brewing process is divided into six key stages of malting, milling, mashing, brewing, cooling, and fermentation.<sup>[95,96]</sup> Fig. 1.2 shows the generation of BSG during the beer brewing process. After harvest, the barely is cleaned, grounded and sorted. Then it goes through a malting process including steeping, germination, and drying or kilning to increase the enzymatic content of the grains.<sup>[9]</sup> Then the malted barley is milled, mixed with water with steady increased temperatures to promote the enzymatic hydrolysis of malt component. During this process, starch is converted to fermentable sugars (mainly maltose, and maltotriose) and non-fermentable sugars (dextrins), and proteins are partially degraded to polypeptides and amino acids. This enzymatic conversion stage (mashing) produces a sweet liquid known as wort, which is separated from the solid through a filtration (lautering) step. After this, the wort is used for the following beer production, and the insoluble, undegraded part of the malted barley grain is known as the

BSG.<sup>[9,95]</sup> The amount of water, the time and temperature during the mashing process influence the chemical composition of BSG.

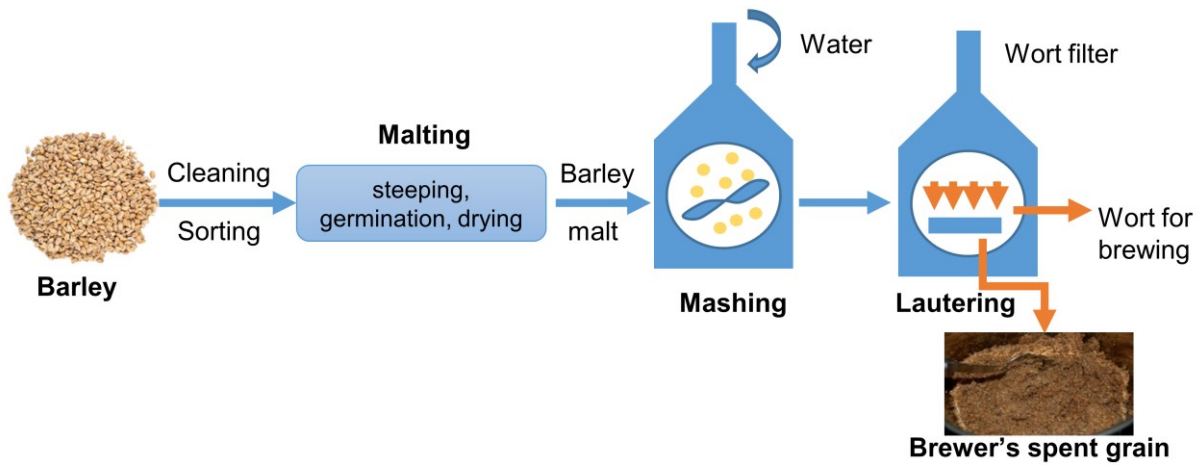


Fig. 1.2. Generation of BSG during the beer brewing process.

### 1.3.2. Composition of brewer's spent grain

BSG basically consists of the husk–pericarp–seed coat layers that cover the original barley grain.<sup>[9]</sup> Depending on the efficiency of mashing, more or less starchy endosperm and walls of empty aleurone cells may remain.<sup>[97]</sup> Fresh BSG has 70–80 wt% of moisture, sweet taste, malt smell, and is considered to be a lignocellulose material rich in protein and fiber.<sup>[98]</sup> BSG is a heterogeneous substance, and the chemical composition of BSG may vary from case to case depending on the barley variety, harvest time, malting and mashing conditions, and the quality and type of adjuncts added in the brewing process.<sup>[93,95]</sup> Table 1.5 summarizes the range of reported value of various compositions of BSG. The most abundant ingredients of BSG are hemicellulose (19.2–43 wt%), lignin, (5.8–28 wt%), protein (10–35.4 wt%) and cellulose (0.3–33 wt%). In addition, BSG also contains several mineral and vitamins, of which silicon, phosphorus, calcium and magnesium are the most abundant.<sup>[97,98]</sup> Compared with other agro-industrial by-products such as rice straw, wheat straw and rice husks, BSG presents elevated hemicellulose and protein amount, similar lignin content and a lower cellulose content.<sup>[10]</sup>

**Table 1.5.** Variability in composition of brewer's spent grain. All values are expressed in g per 100 g dry matter (wt%).<sup>[9,93,97-99]</sup>

Component	Component in wt%	
	Lowest Value	Highest Value
Protein	10	35.4
Lipids	3	13
Starch	1	13
Ash	1.1	6
Non-starch glucans (incl. cellulose)	0.3	33
Hemicellulose (arabinoxylan)	19.2	43
Lignin	5.8	28
Phenolics	0.7	2

Fig. 1.3 shows the chemical structure of cellulose,<sup>[86]</sup> BSG arabinoxylan (AX),<sup>[100]</sup> precursors of lignin,<sup>[101]</sup> and L-lysine. Cellulose is composed of repeating  $\beta$ -D-anhydro-glucopyranose units linked by  $\beta$ -1,4-glycosidic bonds (Fig. 1.3, a), being a linear polymer with free hydroxyl groups.<sup>[86]</sup> Hemicellulose primarily consists of arabinoxylan (AX) and its general structure is shown in Fig. 1.3, b. BSG AX are reported to be composed by a backbone of ( $\beta$ 1 $\rightarrow$ 4)-linked xylose residues containing only single units of L-arabinofuranose as side chains, with some of them substituted with ferulic acid residues.<sup>[100]</sup> In addition, Coelho et al. found that additional substituted groups such as hexose, uronic acid, methylated uronic acid, and acetyl groups might be present in BSG AX, substituting the terminally linked arabinose residues.<sup>[102]</sup> Therefore, BSG AX contains many functional groups such as hydroxyl, carboxyl, phenolic and acetyl groups. Lignin is a poly-phenolic macromolecule of complex structure, which is important to maintain the structural rigidity and integrity of plant cell walls. It is formed by in situ radical polymerization of three kinds of precursors, namely *p*-coumaryl alcohol, coniferyl alcohol, and sinapyl alcohol (see Fig. 1.3, c), generating inter-unit linkages. The lignin structure is characterized by various functional groups including methoxyl, phenolic hydroxyl, aliphatic hydroxyl, and other carbonyl groups.<sup>[101]</sup> Moreover, the most abundant proteins in BSG are hordeins, glutelins, globulins, and albumins. 30% of the protein content are essential amino acids, with L-lysine being the most abundant.<sup>[97]</sup> The proteins in BSG provide amide and carboxyl groups for this biomass. Overall, the major components of BSG (cellulose, hemicellulose, lignin, and protein) could contribute to the potential adsorption capacity of BSG due to their abundant functional groups.

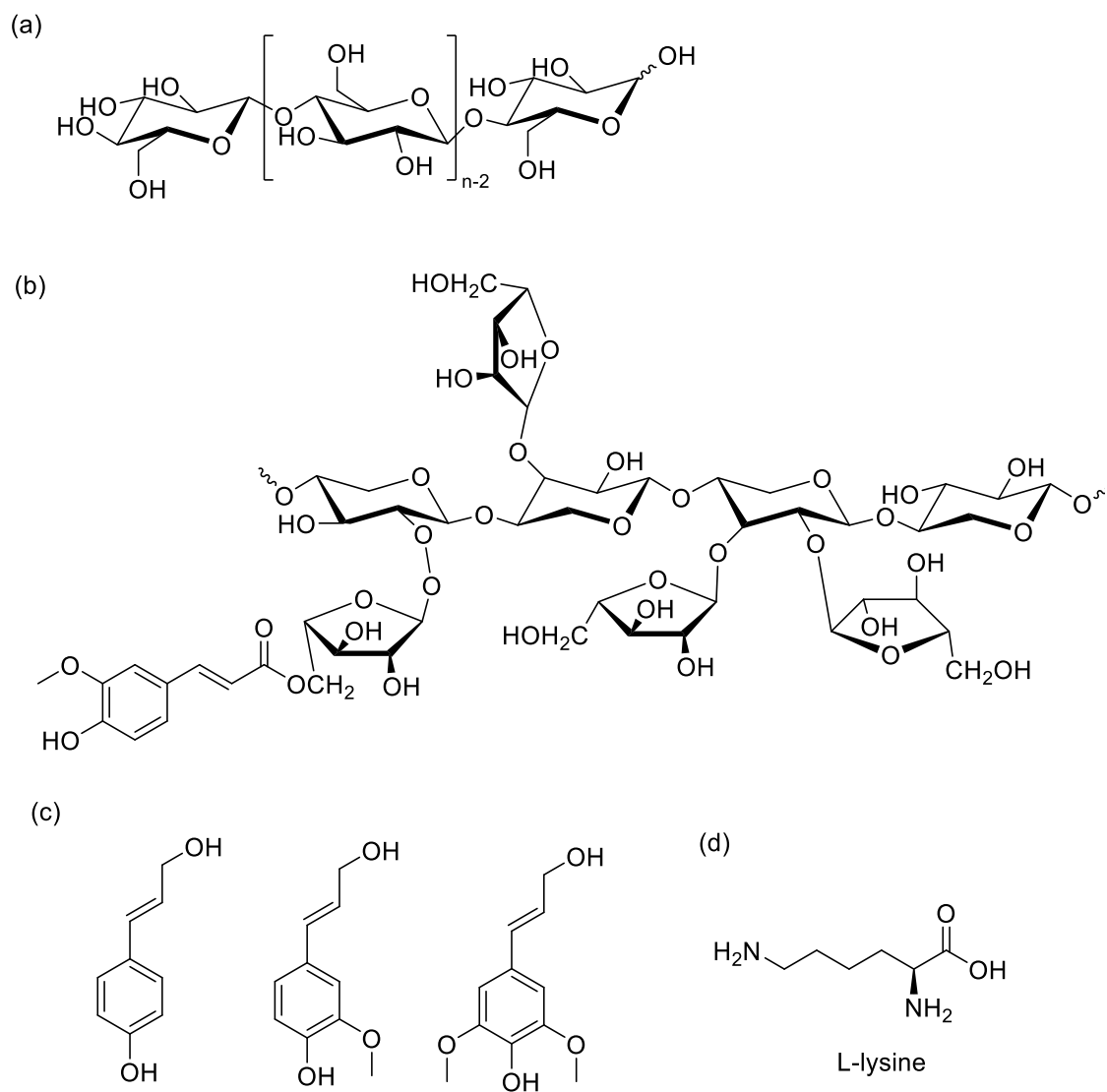


**Fig. 1.3.** The molecular structure of (a) cellulose ( $n = DP$ , degree of polymerisation),<sup>[86]</sup> (b) BSG arabinoxylan (AX),<sup>[100]</sup> (c) precursors of lignin,<sup>[101]</sup> and (d) L-lysine.



## 1.4. Use of brewer's spent grain

BSG is produced in large quantity all year around, and its disposal and application have become a major concern for the brewing industry. The wet BSG is difficult to store with a short shelf life of only 7–10 days due to high moisture content (70–80 wt%),<sup>[98]</sup> and drying is energy intensive, and thus, very costly.<sup>[93]</sup> In addition, transporting of wet BSG is also expensive: Mussatto<sup>[10]</sup> estimated in a paper in 2014 that it costed ~\$16 to transport one ton of BSG a distance of 8 km away from the brewery. Currently, the BSG is only used for the animal feed for the nearby farms, but the production may surpass the demand. Currently, BSG is only used as supplement for animal feed in in nearby farms, but the production surpasses the demand. In addition, the high content of moisture, proteins and fibers in BSG favors the growth of microorganisms, which causes environmental problems when disposed of in a landfill.<sup>[97]</sup> Therefore, finding new applications would create a new market for BSG and utilize the bio-waste instead of disposing it landfills.

### 1.4.1. Current use of brewer's spent grain

The current investigated use of BSG can be summarized in several fields, including (1) supplement in animal feeding and human diet;<sup>[97]</sup> (2) reuse in brewing process as antifoaming agent or carrier for immobilizing brewers' yeast;<sup>[9]</sup> (3) energy application through direct combustion or conversion to fuels, biogas and ethanol;<sup>[10]</sup> (4) as a source of value added products such as polysaccharides, phenolic compounds, and proteins;<sup>[103]</sup> (5) biotechnology application, as a substrate for microorganism cultivation or enzyme production, carrier for cell mobilization, and raw materials for fertilizer;<sup>[95]</sup> and (6) material production such as building materials, adsorbents, pulp and paper production, and polymer production (Fig. 1.4).<sup>[98,104]</sup> It should be noted that none of these applications are used on an industrial scale, and the supply of BSG to farms near the brewery as supplement in animal feeding has been the only applicable solution for BSG disposal until the recent past. In addition, some breweries have made attempts to use BSG as their own energy source and have successfully recovered over 50% of energy costs in this way.<sup>[10]</sup> A bibliometric analysis regarding the literature from 1900–2020 indicates the main research interests of BSG application focus on the production of ethanol and the utilization of BSG for food formulation and functionalization.<sup>[96]</sup> In contrast, BSG has little application for material production, especially as a biosorbent, and few studies have been conducted in this research area.

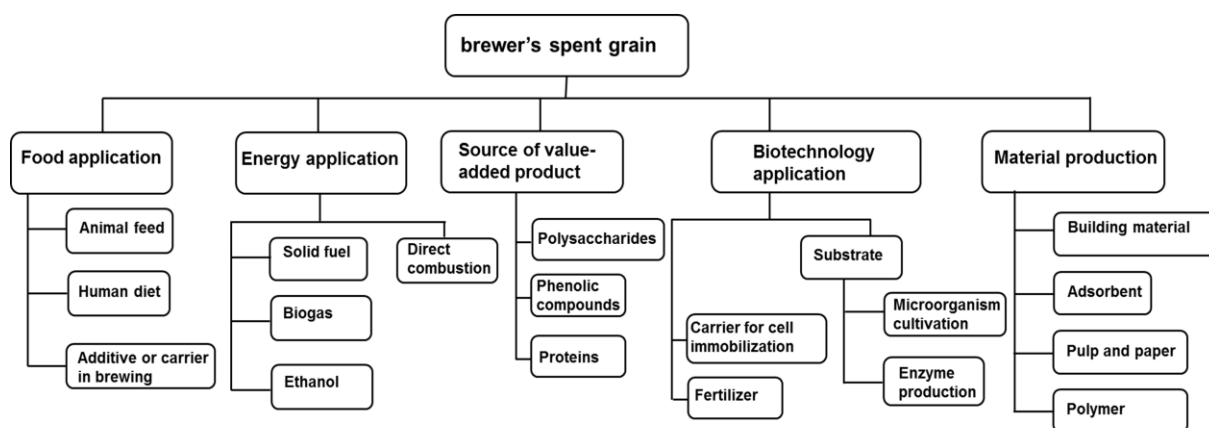


Fig. 1.4. Summary of the application of BSG.<sup>[9,10,95,97,98,103,104]</sup>

### 1.4.2. Use of brewer's spent grain for adsorption

BSG has numerous functional groups such as hydroxyl, carboxyl, and amide groups, which makes it a promising candidate for adsorption of metal ions, dyes and organic compounds from aqueous solution.<sup>[105]</sup> The use of raw BSG as biosorbents is reported and summarized in Table 1.6, and for modified BSG in Table 1.7. The adsorption of several dyes from wastewater was tested on the raw BSG,<sup>[106–108]</sup> and the adsorption of pharmaceuticals like acetaminophen<sup>[109]</sup> and carbamazepine<sup>[110]</sup> were tested on the activated biochar and hydrochar from BSG. Mostly, however, the research focuses on the adsorption of heavy metal ions, including Pb(II), Cd(II), Cr(VI), Cr(III), Zn(II), As(III), As(V), Mn(II), Ni(II), Cu(II), Hg(II), Fe(III) and Ag(I) that show chemical toxicity and considered as risks to human health. Moreover, BSG has also been modified by epichlorohydrin-triethylamine to remove NO<sub>3</sub><sup>-</sup> from wastewater.<sup>[111]</sup> The latest study by Carrasco et al. has employed BSG originating from *Hefeweißbier* (WB-BSG) and *Original Helles* (H-BSG) for Fe(III)/Fe(II) removal from real water samples in German mining region and the national guidelines ( $\leq 1.8$  mg/L) were satisfied after adsorption.<sup>[112]</sup> Nevertheless, there is no literature that reports the adsorption performance of BSG or modified BSG for the adsorption of *f*-elements (uranium and the rare earth metal ions) before the reported studies here. The unmodified BSG and pretreated BSG (alkaline, acid, and NaCl pretreatment) generally show low adsorption capacity toward metal ions. For example, the HCl pretreated BSG shows adsorption capacity lower than 10 mg/g for Mn(II), Ni(II), Cu(II), Zn(II), and Cd(II), and only 19.1 mg/g for Pb(II).<sup>[113]</sup> Modification methods of BSG to increase its adsorption performance including thermal conversion,<sup>[114]</sup> esterification,<sup>[115]</sup> thiol-

functionalization,<sup>[116]</sup> yeast immobilization,<sup>[117]</sup> graft polymerization,<sup>[118]</sup> and chemically modified by epichlorohydrin-triethylamine<sup>[111]</sup> and polyacrylamide.<sup>[119]</sup> However, the exploration of modifying BSG for metal ions adsorption is still insufficient compared to biomass treatment methods discussed in Section 1.2.3. In addition, only a few cases show significant increases in the adsorption capacity, and little attention has been paid to modify the selectivity of the biosorbents. Therefore, investigating the modification of BSG as an adsorbent for uranyl ions removal could further fill the research gaps in this field and provide inspirations for dealing with uranium contamination and BSG disposal.

**Table 1.6.** Summary of studies using raw BSG as adsorbents.

Adsorbent	Adsorbate	$q_e$ (mg/g)	Reference
BSG	Methylene blue	285	[120]
	Tartrazine yellow	26	
BSG	Methylene blue	12.8	[106]
	Congo red	13.2	
BSG	Acid orange 7	29	[107]
BSG	Congo red	36.5	[108]
	Malachite green	2.5	
NTSG	Cr(III)	18	[121]
BSG	Cr(III)	16.7	[122]
BSG	Zn(II)	126	[116]
BSG	Cu(II)	10.5	[123]
H-BSG	Fe(III)/Fe(II)	7.1	[112]
	Mn(II)	3.7	
	Ni(II)	2.8	
	Cd(II)	6.7	
WB-BSG	Fe(III)/Fe(II)	11.7	
	Mn(II)	5.7	
	Ni(II)	6.1	
	Cd(II)	11.4	
BSG	Fe(III)	8	[124]
BSG	Ag(I)	30	[125]

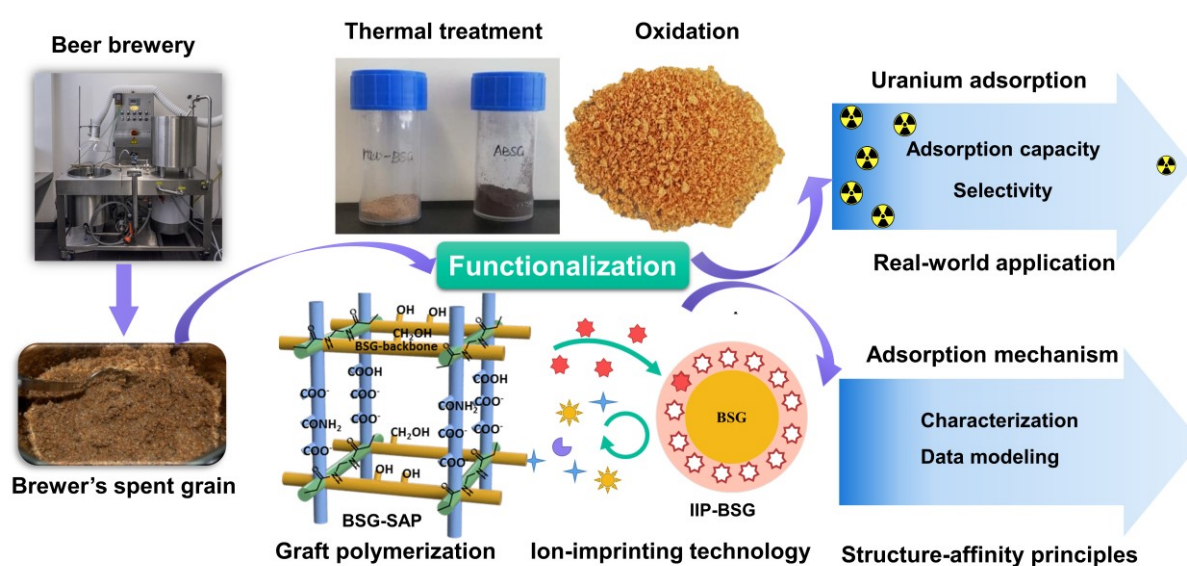
**Table 1.7.** Summary of studies using modified BSG as adsorbents.

Adsorbent	Modification method	Adsorbate	$q_e$ (mg/g)	Reference
Activated hydrochar from BSG	Hydrothermal treatment; chemical activation	Acetaminophen	318	[109]
Activated carbon	Carbonization, chemical activation	Carbamazepine	190	[110]
BAC-K	Activated carbon from BSG	Pb(II)	77% <sup>a</sup>	[114]
Esterified BSG	Esterification	Cd(II)	474	[115]
Esterified BSG	Esterification	Pb(II)	293	[126]
Modified BSG	Epichlorohydrin-triethylamine	NO <sub>3</sub> <sup>-</sup>	23	[111]
BSG-g-Ac-co-Am	Graft polymerization	Cr(VI)	16	[118]
TSG	NaOH treatment	Cr(III)	14	[121]
BSG+yeast	Yeast immobilization	Pb(II)	15.5	[117]
BSG	NaOH treatment	Cd(II)	17	[127]
		Pb(II)	35.5	
PSGs	Modified with polyacrylamide	As(III)	0.03	[119]
TFSG	Thiol-functionalization	Zn(II)	227	[116]
MSG	NaCl treatment	Pb(II)	31	[128]
BSG	HCl treatment	Cr(VI)	19	[129]
Conditioned BSG	HCl treatment	Mn(II)	2.4	[113]
		Ni(II)	2.9	
		Cu(II)	5.1	
		Zn(II)	3.3	
		Cd(II)	7.3	
		Pb(II)	19.1	
BSG	Treated with Ca(OH) <sub>2</sub> saturated solution	As(V)	13.4	[130]
		As(III)	5	
MSG	NaCl treatment	Ag(I)	158	[125]
TFSG	Thiol-functionalization	Hg(II)	222	[131]

a). Removal ratio,%.

## 2. Objectives

The objective of this work is to develop low-cost and efficient adsorbents from brewer's spent grain (BSG) for uranium removal with high adsorption capacity, fast kinetics, selectivity and reusability. Functionalization methods including thermal treatment, chemical modification (oxidation) and polymer grafting are explored, and surface ion-imprinting technology is employed to tune the selectivity. The adsorption properties of the BSG-derived adsorbents are tested under various conditions for real-world application, and structure-affinity principles are derived based on the characterization, data modeling and experimental results (Scheme 2.1).



**Scheme 2.1.** Preparation of adsorbents for uranium adsorption from BSG by thermal treatment, oxidation, graft polymerization and ion-imprinting technology; testing of adsorption performance and developing structure affinity principles.

The uranium contamination in the aquatic environment has become a public health threat worldwide due to increased human activities regarding to mining and nuclear power plants. Biosorbents derived from waste biomass are the most economically viable choice to tackle this challenge. Current research of biosorbents focus mainly on lignocellulose materials, whereas few studies have employed biomass rich in both protein and fibers such as BSG. BSG is produced in large amount annually, and its disposal is often problematic to the environment due to its high moisture content and easy perishability. Therefore, novel approaches for the use of BSG are of great interests. Currently, the research regarding biosorbents derived from BSG is insufficient, and the adsorption of *f*-elements (uranium and rare earth metal ions) by BSG has not been explored yet. In addition, the modification of BSG for enhanced adsorption capacity

and selectivity is hardly investigated. Thus, the first part of this work explores the adsorption of uranyl and rare earth metal ions onto the unmodified BSG. Meanwhile, a mild hydrothermal treatment is expected to improve the adsorption capacity of BSG with the aid of the Maillard reaction between carbohydrates and proteins forming melanoidins. The employed treatment aim to minimize energy consumption at a low temperature and make it possible to dispense additional activation processes, so that current disadvantages of the hydrothermal carbonization (HTC) process are overcome. This part of work focuses on studying the effects of reaction temperature and time on the adsorption capacity, the properties of products and the Maillard reaction to shed light on the involved reaction mechanisms.

BSG is speculated to be an ideal raw material for the nitro-oxidation method to oxidize its hydroxyl groups to carboxyl groups and thus increasing its adsorption capacity. This is because that BSG is rich in proteins and could produce and maintain foams during the oxidation process, which is crucial for a successful nitro-oxidation. Therefore, the second part of this work explores the feasibility of oxidizing BSG to improve its adsorption capacity and provides an efficient and simple approach for surface modification of BSG. The oxidized BSG (OBSG) is tested for adsorption capacity under various conditions, as well as its reusability.

Although thermal conversion and oxidation could increase the adsorption capacity of BSG, the increase is limited by the transformation of surface functional groups (e.g. from hydroxyl groups to carboxyl groups) without significantly increase of their total amount. The third part of this work would synthesize BSG-supported superabsorbent polymers (SAP) with different cross-linking densities for the first time via one-pot swelling and graft polymerization. The BSG-SAP is expected to graft with abundant carboxyl and amide groups and have a strongly hydrophilic polymer network, which improves the adsorption capacity and mass transfer. The obtained BSG-SAP will be tested for high salinity and alkaline conditions, selectivity in the presence of competing ions, suitability and reusability in continuous flow systems, and degradability in natural soil, which would provide more information regarding practical application.

The fourth part of this study aims to adjust the selectivity of BSG-derived adsorbents by ion-imprinting technology to solve the adsorbent poisoning and increase the removal efficiency in real wastewater. Herein, a surface ion-imprinted brewer's spent grain (IIP-BSG) is going to be prepared for the first time using 2-hydroxyethyl methacrylate (HEMA) and diethyl vinylphosphonate (DEVP) as monomers with an extremely high M:T ratio of 500:1. The selective adsorption sites of IIP-BSG are expected to be formed through the multi-point interactions between the uranyl ions and the monomers. The adsorption capacity, selectivity

and reusability of IIP-BSG toward U(VI) in the presence of model competing ions (Eu(III)) will be studied in various conditions. Moreover, this part of work investigates the mass transfer mechanisms and the heterogeneity of the adsorption sites of IIP-BSG by models and theoretical calculation, respectively.

Based on the batch and fixed bed column experiments, the application of BSG and its derived adsorbents are tested in real-world conditions, including adsorbent aging test and adsorption in simulated wastewaters.





### **3. Thermal conversion of brewer's spent grain for uranyl and rare earth metal ions adsorption**

In a first approach, a simple thermal conversion is explored to improve the adsorption capacity of brewer's spent grain (BSG). As BSG shows high content of moisture, hydrothermal treatment that is feasible to use the wet biomass feeds and requires no toxic chemicals would be a greener and economical choice for modification.<sup>[72]</sup> However, conventional hydrothermal carbonization (HTC) processes usually employ high temperatures of up to 250 °C<sup>[73]</sup> in combined with a physical or chemical activation to achieve satisfactory adsorption capacity of hydrochar,<sup>[132]</sup> which inevitably undermines its ecological advantages.

There are several types of lignocellulosic biomass available for HTC processes worldwide, of which BSG is of great importance due to its availability and particular composition containing both lignocellulose and protein.<sup>[9]</sup> Therefore, it can be assumed that the Maillard reaction proceeds under the mild hydrothermal conditions studied in this work (temperature of 150 °C) and generates products that could increase the adsorption capacity of BSG.<sup>[133]</sup> The results show the important role of Maillard reaction between carbohydrates and proteins with the formation of melanoidins in the enrichment of functional groups suitable for metal coordination, thus resulting in high adsorption capacity of the altered biosorbent (ABSG) towards U(VI) without further treatment. This has overcome the current disadvantages of the HTC process by minimizing energy consumption and making it possible to dispense additional activation processes, making it a simpler and eco-friendly alternative for biosorbent production. The reaction mechanisms involved were elucidated by studying the effects of reaction temperature and time on adsorption capacity, the product properties, and the Maillard reaction process. Furthermore, the biosorbents were fully characterized by spectroscopic and thermogravimetric methods. The adsorption properties and mechanisms of U(VI) and lanthanides onto BSG-based biosorbents were examined, using La(III), Eu(III) and Yb(III) as representatives of the early, middle and late lanthanides.

### 3.1. Hydrothermal treatment of brewer's spent grain

#### 3.1.1. Effects of reaction temperature and time on adsorption capacity and chemical composition

The hydrothermal process and the properties of the reaction product ABSG are strongly influenced by the reaction temperature and time. The effects of temperature and time on the adsorption capacity of La(III) are recorded (Fig. 3.1, a and b), and the obtained chemical composition of ABSG are given in Table 3.1. For a detailed description of the employed treatment, the respective reaction temperature and time are added to the samples name, e.g. ABSG-150 °C, 16 h for a hydrothermal treatment at 150 °C for 16 h. Fig. 3.1 shows that the adsorption capacity for La(III) increases as the reaction temperature and time increase, from 16 mg/g for BSG to a maximum of 34.1 mg/g for a treatment at 150 °C for 16 h. Further increasing the reaction temperature and time of the hydrothermal treatment beyond the optimum conditions results in an obvious decrease in adsorption capacity to 6.5 mg/g (175 °C for 16 h). Therefore, the sample produced at 150 °C for 16 h with the highest adsorption capacity (designated as ABSG) was chosen for the adsorption study and the general characterization (<sup>13</sup>C solid state NMR, oxygen functional groups and STA-MS-CS analysis).

Table 3.1 shows the different elemental compositions of ABSG obtained from different reaction temperature and time. With increasing reaction temperature and prolonging reaction time, the carbon content of ABSG increases, while the hydrogen and oxygen content decreases. One possible reason is that the BSG undergoes condensation polymerization, which causes a loss of O-containing functional groups and low polarity of ABSG.<sup>[134]</sup> This results in the decreased adsorption capacity when the temperature and time exceed the optimum values (Fig. 3.1). The change in nitrogen content of ABSG remains small, indicating a higher persistence of N-containing groups than O-containing functional groups. In this case, the N-containing groups may be incorporated into ABSG via Maillard reaction as discussed in Section 3.1.3.<sup>[135]</sup>

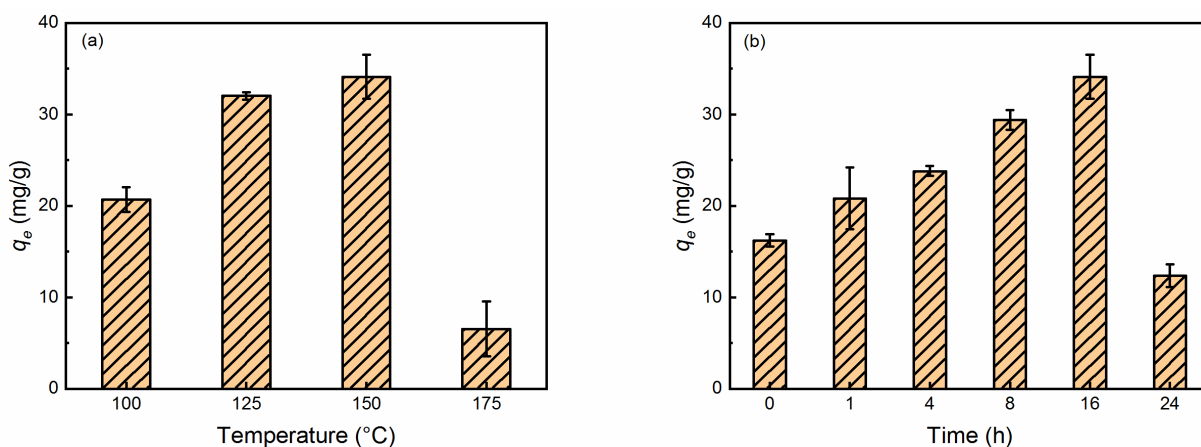


**Fig. 3.1.** Effects of (a) reaction temperature (for 16 h) and (b) time (at 150 °C) on the adsorption capacity of ABSG. For adsorption experiments: 2 mg ABSG/ 2 mL solution, pH = 5.7,  $c_0(L_a) = 100$  mg/L,  $t = 2$  h, room temperature.

**Table 3.1.** Effects of reaction temperature (for 16 h) and time (at 150 °C) on the elemental composition of ABSG.

	N (wt%)	C (wt%)	H (wt%)	S (wt%)	Mineral (wt%)	O (wt%) <sup>a</sup>
BSG	5.1 ± 0.1	49.1 ± 0.1	6.1 ± 0.2	0.3 ± 0.1	1.4 ± 0.1	38.0 ± 0.6
ABSG-1 h, 150 °C	4.9 ± 0.1	47.4 ± 1.5	6.5 ± 0.2	0.4 ± 0.1	1.3 ± 0.02	39.4 ± 1.9
ABSG-4 h, 150 °C	4.5 ± 0.1	48.5 ± 0.1	7.6 ± 1.0	0.2 ± 0.1	1.3 ± 0.01	38.0 ± 1.3
ABSG-8 h, 150 °C	4.2 ± 0.5	49.4 ± 0.7	7.8 ± 0.2	0.03 ± 0.02	1.3 ± 0.03	37.3 ± 1.4
ABSG-16 h, 150 °C	5.0 ± 0.1	53.4 ± 0.1	6.8 ± 0.2	0.3 ± 0.01	1.6 ± 0.01	32.8 ± 0.4
ABSG-24 h, 150 °C	4.6 ± 0.1	60.8 ± 0.2	6.8 ± 0.15	0.4 ± 0.02	0.4 ± 0.01	27.0 ± 0.5
ABSG-16 h, 100 °C	4.4 ± 0.2	48.2 ± 0.7	7.3 ± 0.2	0.2 ± 0.1	1.2 ± 0.01	38.7 ± 1.2
ABSG-16 h, 125 °C	4.2 ± 0.1	48.2 ± 0.2	7.1 ± 0.1	0.3 ± 0.01	1.3 ± 0.02	38.9 ± 0.4
ABSG-16 h, 175 °C	4.1 ± 0.05	63.0 ± 0.01	6.2 ± 0.05	0.3 ± 0.01	0.3 ± 0.01	26.0 ± 0.1

a). Calculated by mass balance considering the content of carbon, nitrogen, hydrogen, sulfur and the mineral elements.

Fig. 3.2 shows a Van Krevelen diagram<sup>[136]</sup> plotting the H/C atomic ratios against the O/C atomic ratios of various samples and reference materials to further investigate the reaction type during hydrothermal treatment. Here, BSG found to be a type of lignocellulosic material with elemental composition more similar to that of cellulose than that of pure lignin. The direct vector points at a dehydration pathway when increasing the temperature, while both the dehydration and decarboxylation reaction occur when prolonging the reaction time. Both

reaction pathways could lead to the lower H/C and O/C ratios of ABSG.<sup>[136]</sup> In addition, the decrease in the H/C ratio also indicates potential aromatization during the hydrothermal conversion.<sup>[137]</sup> It is suggested that all the reaction mechanisms leading to the properties of ABSG, including dehydration, decarboxylation, aromatization, and Maillard reaction, may occur in parallel network of different pathways rather than in consecutive steps.

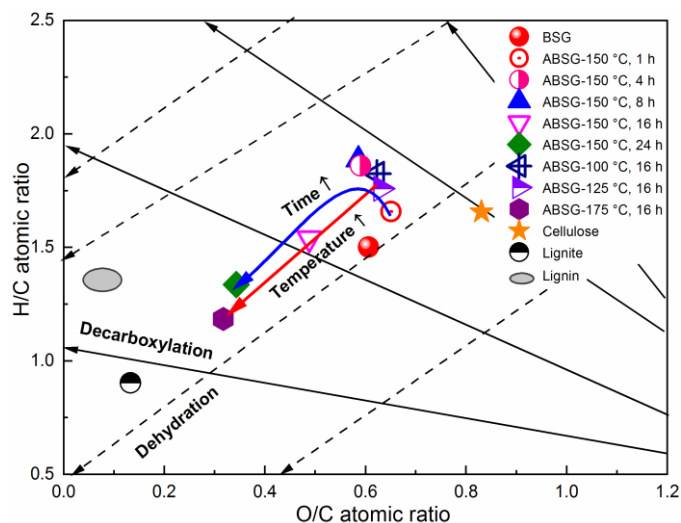


**Fig. 3.2.** Van Krevelen diagram of BSG-based biosorbents, typical biomass and coal.<sup>[136]</sup>

### 3.1.2. Effects of reaction temperature and time on the surface functional groups

To gain information of the surface functional groups on ABSG during the treatment, FT-IR spectra during the variation of temperature (Fig. 3.3, a) and the spectra upon variation time (Fig. 3.3, b) were recorded. For detailed comparison, the FT-IR spectra of BSG and ABSG treated a 150 °C for 16 hours (ABSG-150 °C, 16 h) are displayed in Fig. 3.4. Basically, the chemical structure and functional groups of BSG remain unaffected during hydrothermal treatment, and the ABSG samples still retain a large number of functional groups. This is confirmed by the absorption bands assigned to hydroxyl and amine groups vibration ( $3285\text{ cm}^{-1}$ ),  $-\text{CH}_2-$  antisymmetric and symmetric stretching vibration ( $2924\text{ cm}^{-1}$ ,  $2853\text{ cm}^{-1}$ ), amide I ( $1650\text{ cm}^{-1}$ ) and amide II ( $1518\text{ cm}^{-1}$ ) vibration,  $-\text{COO}^-$  symmetric stretching vibration ( $1453\text{ cm}^{-1}$ ), C–N stretching vibration ( $1245\text{ cm}^{-1}$ ) and C–O stretching vibration ( $1159\text{ cm}^{-1}$ ) in ester groups,<sup>[126,138]</sup> which are observed for both BSG and the ABSG samples (see Fig. 3.4). However, the intensity of  $-\text{COOH}$  groups stretching vibration ( $1742\text{ cm}^{-1}$ ) gradually decreases as the temperature increases and time prolongs, which is probably because of the dehydration and condensation polymerization as discussed in the

Section 3.1.1. In addition, the intensity of the C=O stretching vibration ( $1650\text{ cm}^{-1}$ ) increases when the temperature increases over  $150\text{ }^{\circ}\text{C}$  and the reaction time is longer than 8 h. In addition, the intensity of C–O stretching vibration ( $1021\text{ cm}^{-1}$ ) decreases continuously with increasing temperature and time. These changes show that the C–O bonds in the glucose units of cellulose and hemicellulose are transformed to C=O bonds during the hydrothermal reaction,<sup>[137]</sup> which results in the increased adsorption capacity when the temperature and time increase. All above mentioned absorption bands decrease in intensity when the temperature increases over  $175\text{ }^{\circ}\text{C}$ , indicating the loss of functional groups and thus decreasing adsorption capacity (Fig. 3.1).

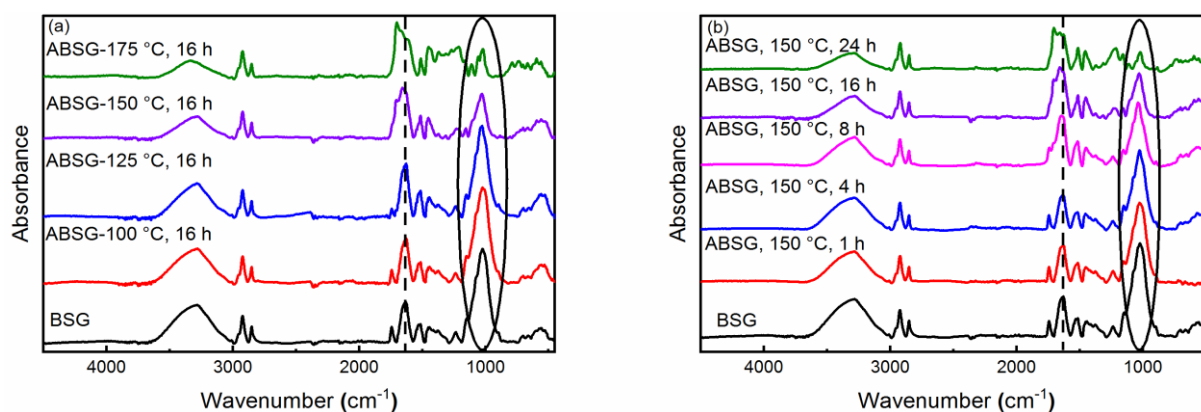


**Fig. 3.3.** FT-IR spectra of BSG and ABSG samples with different (a) reaction temperature (for 16 h) and (b) time (at  $150\text{ }^{\circ}\text{C}$ ).

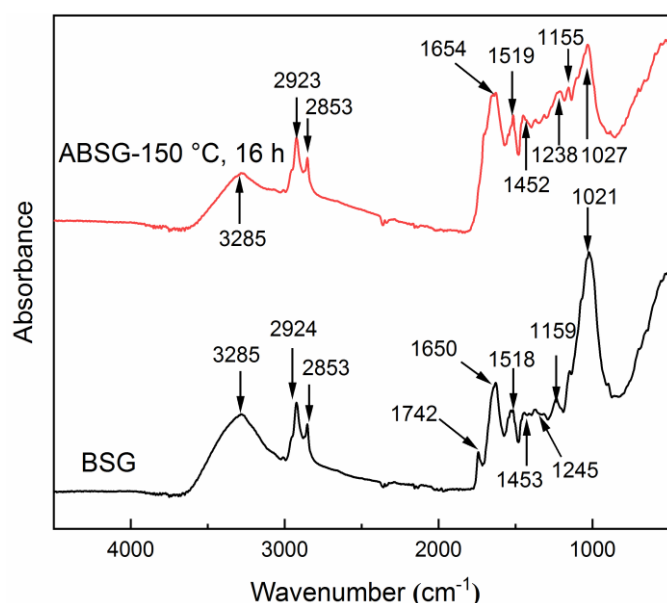


**Fig. 3.4.** Raw FT-IR spectra of BSG and ABSG- $150\text{ }^{\circ}\text{C}$ , 16 h with bands position.

### 3.1.3. Effects of reaction temperature and time on Maillard reaction

Maillard reaction is well-known process that would occur when amino acids are mixed with reducing sugars at elevated temperature.<sup>[133]</sup> Because BSG is characterized as the biomass rich in both protein and lignocellulose, investigating the Maillard reaction is important for further understanding the hydrothermal treatment. As the major starting materials involved in the Maillard reaction,<sup>[139]</sup> the contents of two amino acids (lysine and arginine) depending on the treatment temperature are recorded (Fig. 3.5, a). And the effect of reaction temperature on the total content of Maillard reaction products (total MRPs) and the content of five typical MRPs, namely N- $\epsilon$ -(carboxymethyl)lysine (CML), N- $\epsilon$ -(carboxyethyl)lysine (CEL), pyrrolidine, methylglyoxal-derived hydroimidazolone-1 (MG-H1) and maltosine, is studied (Fig. 3.5, b). The chemical structures of investigated MRPs are shown in Fig. 3.6. MG-H1 shows the highest content of all studied MRPs with 22 mg/100 g dry sample in the ABSG treated at 125 °C for 16 h (Fig. 3.5, b), dominating their overall amount and dependency on the reaction temperature. The formation of MG-H1 is probably through the reaction between 1,2-dicarbonyl compounds from the reducing sugar of BSG and the guanidino group of arginine.<sup>[140]</sup> The remaining MRPs are present in lower concentration (<5 mg/ 100 g dry sample) and follow in general the observed trend of MG-H1 (Fig. 3.5, b). Nevertheless, the total MRPs content is considered in the following discussion and analysis because all MRPs may be involved in the metal adsorption. The content of total MRPs increases when the reaction temperature increases from 100 °C to 125 °C. Meanwhile, the content of lysine and arginine decreases, indicating a promotion of the Maillard reaction by elevating the temperature. When the temperature increases to 150 °C, the content of MRPs begins to decrease, while lysine and arginine are continuously consumed, indicating the MRPs and amino acids react further to form large, brown-black color polymeric compounds, such as melanoidins.<sup>[141]</sup> The formation of melanoidins is also the reason for the dark-brown color of ABSG (Fig. 3.7) because carbonization of the BSG at the employed temperature is less possible. Owing to their abundant functional groups and anionic charge, the detected MRPs and melanoidins show high affinity for metal ion complexation.<sup>[141]</sup> The reaction time shows a similar effect on the Maillard reaction (Fig. 3.5, c and d). Prolonging the reaction time promotes the Maillard reaction as amino acids are consumed and MRPs are generated. Consequently, the adsorption capacity of ABSG increases. However, the content of lysine and arginine decreases to a constant value after 16 h of hydrothermal treatment, and further extension of the reaction time leads to a lower adsorption capacity due to the loss of functional groups.

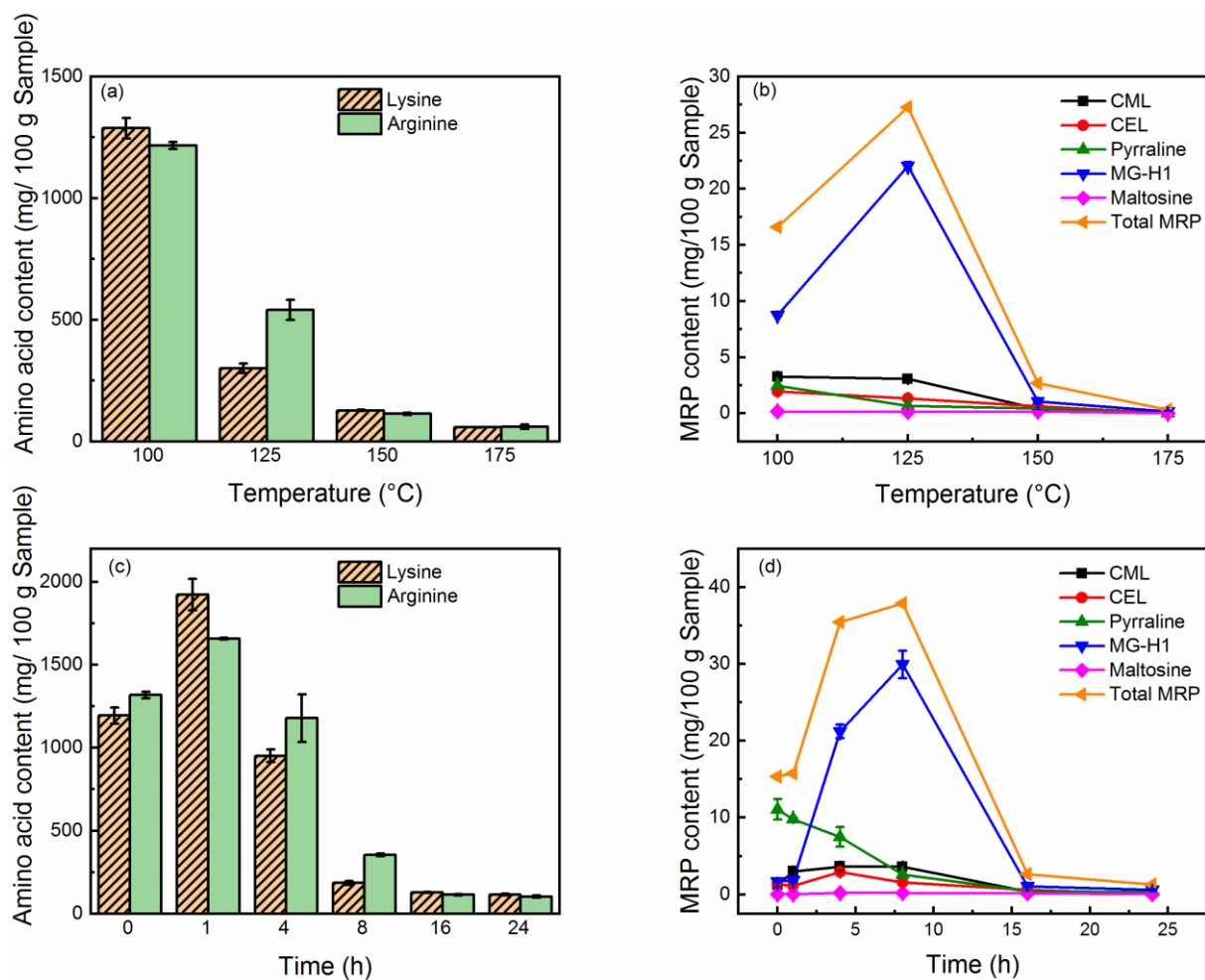


**Fig. 3.5.** Effects of reaction temperature (for 16 h) on (a) the content of amino acids and (b) the content of MRPs, and effects of reaction time (at 150 °C) on (c) the content of amino acids and (d) the content of MRPs.

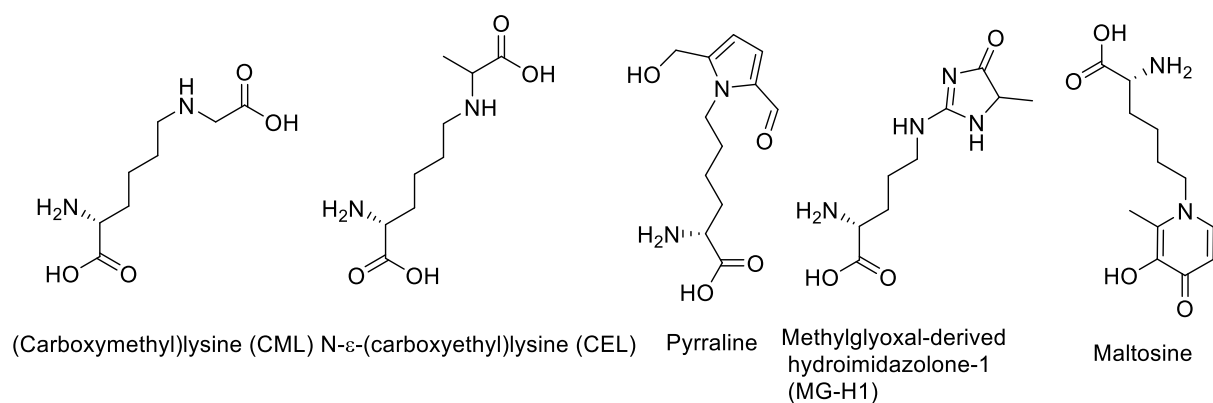


**Fig. 3.6.** Chemical structure of investigated MRPs.



**Fig. 3.7.** Pictures of BSG (left) and ABSG-150 °C, 16 h (right).



## 3.2. Characterization of the adsorbents

### 3.2.1. $^{13}\text{C}$ CP/MAS solid state NMR spectra

To gain information about structure changes of BSG after hydrothermal treatment,  $^{13}\text{C}$  CP/MAS solid state NMR spectra (Fig. 3.8, a) were recorded using a 3.2 mm MAS NMR probe and operating at a resonance frequency of 201.2 MHz with the MAS frequency of 15 kHz. The main chemical structure of BSG is conserved after hydrothermal treatment as shown in the spectra. The resonances in both spectra can be divided into four groups: aliphatic carbons (10–40 ppm), typical cellulose carbons C1 (105 ppm), C4 (80–90 ppm), C2,3,5 (72–75 ppm), C6 (62–65 ppm), lignin aromatic carbons (130 ppm) and carboxyl carbons (174 ppm).<sup>[142,143]</sup> Emerging resonance between 110–160 ppm after hydrothermal treatment suggests an increased unsaturated or aromatic carbon content in ABSG. This is consistent with the increased intensity of the stretching vibration of the C=O bond ( $1650\text{ cm}^{-1}$ ) in the FT-IR spectra (Fig. 3.4) and the increase in the H/C ratio obtained in the elemental analysis (Table 3.1). Compared to BSG, the  $^{13}\text{C}$  NMR spectrum of ABSG shows a more intense signal at  $\delta = 56$  ppm, which corresponds to the methoxyl carbons that presumably bound to an aromatic ring due to the aromatization during hydrothermal treatment.<sup>[143]</sup> Nevertheless, it must be noted that the quantitative analysis of CP spectra is limited by the different polarization transfer efficiencies of the various signals and depends on the water content of the sample. Probably, the extremely restricted mobility of the protons in BSG and/or their chemical inhomogeneity result in broad and hence practically invisible signals. In contrast, the slightly higher water content of ABSG may lead to better-resolved signals in the spectrum. Note that a higher mobility of the protons can also cause a weakening or even suppression of the CP signals.

### 3.2.2. Oxygen functional groups (OFG)

To quantify the content of the oxygen functional groups (OFG) of BSG and ABSG, the Boehm titration was carried out (Fig. 3.8, b). The results show a decrease in the content of the hydroxyl groups for ABSG (0.48 mmol/g) compared to BSG (0.8 mmol/g). At the same time, the content of the lactonic groups increases from 0.15 mmol/g for BSG to 0.47 mmol/g for ABSG. The content of the carboxyl groups rises even more from 0.15 mmol/g for BSG to 1.46 mmol/g for ABSG, which is comparable to the promoted oxidization of cellulosic materials (1.4 mmol/g).<sup>[83]</sup> However, because the decarboxylation and dehydration during the hydrothermal treatment of BSG would cause a loss of O-containing functional groups, this

increase is rather unexpected. Three reasons can be given as possible causes for this behavior: First, the carboxyl groups could be originated from small fraction acids that are formed during the degradation of cellulose and hemicellulose, which are incorporated within the matrix as terminal groups.<sup>[144]</sup> Second, the Maillard reaction produces various products with abundant functional groups, especially carboxyl groups (Fig. 3.6). And third, it is possible that wet oxidation occurs producing carboxyl groups at the employed temperature (150 °C).<sup>[145]</sup> The latter is supported by experiments employing an argon atmosphere during the hydrothermal treatment (150 °C, 16 h) yielding in an adsorbent (ABSG-Ar) with a reduced adsorption capacity for uranyl ion as well as La(III), Eu(III) and Yb(III) (Fig. 3.8, c).

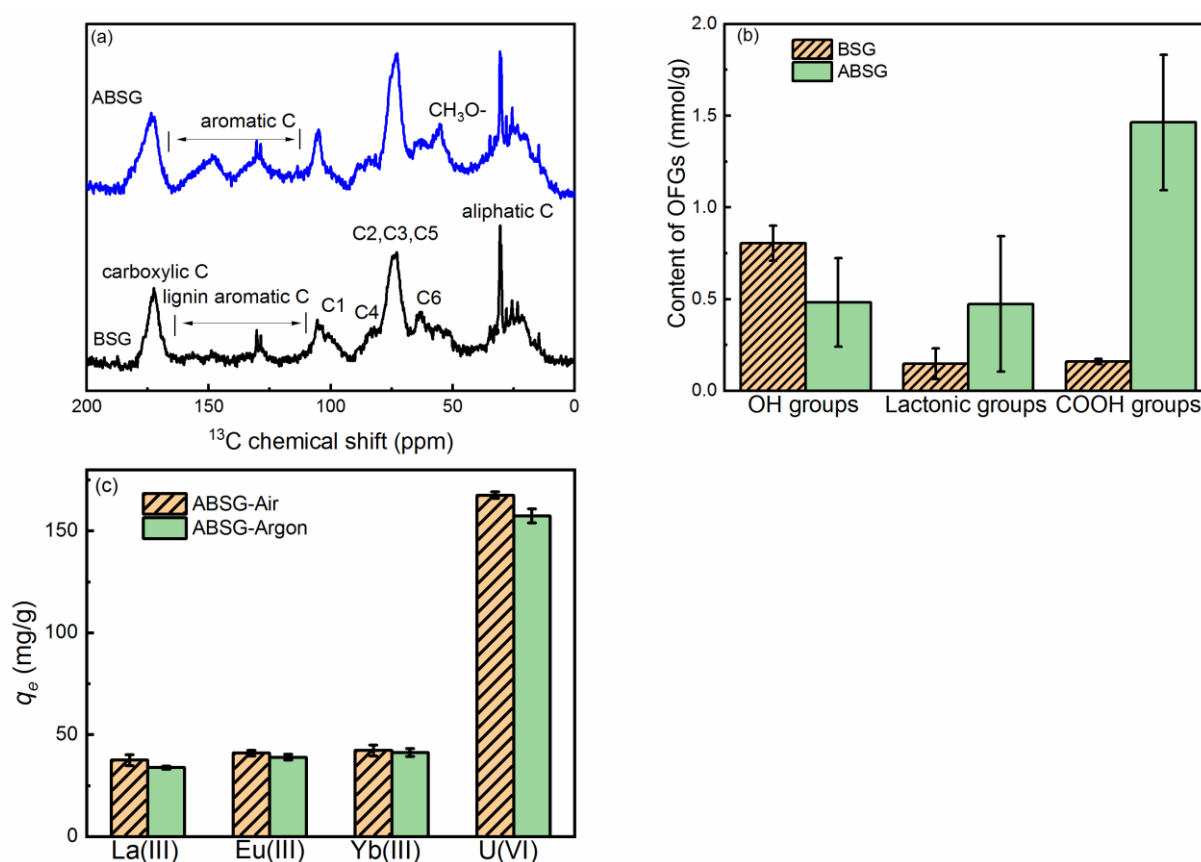


**Fig. 3.8.** (a) <sup>13</sup>C CP/MAS solid-state NMR spectra of BSG and ABSG, (b) oxygen functional groups (OFGs) of BSG and ABSG, (c) adsorption capacity of La(III), Eu(III), Yb(III) and U(VI) onto ABSG obtained employing air (ABSG-Air) and argon (ABSG-Ar) atmosphere. For hydrothermal treatment: 150 °C, 16 h. For adsorption: 2 mg adsorbent/ 2 mL solution, c<sub>0</sub>(La, Eu, Yb) = 100 mg/L, c<sub>0</sub>(U) = 300 mg/L, pH(La, Eu, Yb) = 5.7, pH<sub>0</sub>(U) = 4.7, 1 h, room temperature.

### 3.2.3. STA-GC-MS analysis

To obtain information on the thermal stability and structural changes during the hydrothermal treatment and adsorption, the thermal decomposition of BSG, ABSG and Yb(III)-loaded ABSG

(Yb-ABSG) was explored by STA-GC-MS analysis. Both BSG and ABSG show three derived thermogravimetric (DTG) peaks (maximum decomposition temperature) while Yb-ABSG shows only two peaks (Fig. 3.9, a). The first DTG peak at around 100 °C could be attributed to the evaporation of water with a mass loss of 3.0 wt% (BSG), 4.3 wt% (ABSG) and 4.6 wt% (Yb-ABSG) in thermogravimetric curves (TG, Fig. 3.9, b). The extrapolated onset temperatures in the TG of BSG, ABSG and Yb-ABSG are 276 °C, 226 °C and 361 °C, respectively. The earlier start of mass loss (lower onset temperature) after hydrothermal treatment suggests a lower thermal stability of ABSG due to the increased content of negatively charged carboxyl groups.<sup>[146]</sup> Whereas, the onset temperature for Yb-ABSG increases to 361 °C after adsorption, because the coordination of the functional groups towards the metal ions results in an increase in the thermal stability.<sup>[147]</sup> The DTG-2 and DTG-3 peaks could be assigned to the decomposition of hemicellulose and cellulose, and the continuous decomposition of cellulose materials and lignin, respectively.<sup>[114]</sup> The larger DTG-3 peak area of ABSG than that of BSG is a result of the degradation of intermediate hydrothermal products, e.g. advanced Maillard reaction products and polymerized melanoidins.<sup>[148]</sup> For Yb-ABSG, DTG-2 and DTG-3 peaks overlap and form one large decomposition peak at higher temperature (405 °C). All samples undergo a moderate decomposition and carbonization stage at even higher temperature with a small change of sample mass. In this stage, some molecules in the hydrothermal samples (ABSG and Yb-ABSG) crosslink within the matrix,<sup>[149]</sup> resulting in increased thermal stability and residue mass from 21.7 wt% (BSG) to 29.0 wt% (ABSG) and 27.8 wt% (Yb-ABSG).

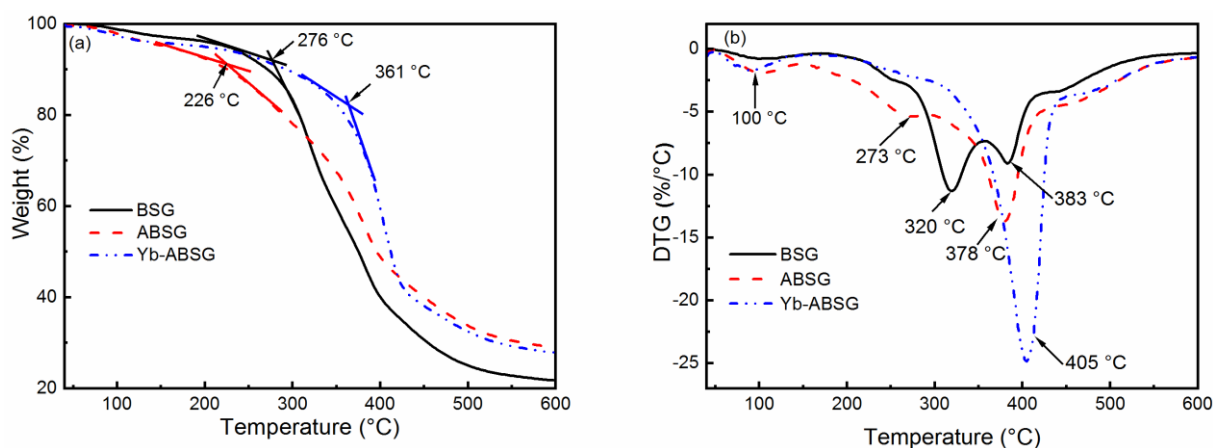


**Fig. 3.9.** (a) TG and (b) DTG of BSG, ABSG and Yb-ABSG (20 °C/min, He atmosphere).

The volatile products at 375–385 °C (BSG, ABSG) and at 340–360 °C (Yb-ABSG) are analyzed by GC-MS (Table 3.2). The most abundant products are CO<sub>2</sub> and water, of which CO<sub>2</sub> counting for 67.7% (BSG), 48.6% (ABSG) and 42.1% (Yb-ABSG) and water for 25.4% (BSG),

43.8% (ABSG) and 39.7% (Yb-ABSG) of the total analyzed products. The decomposition of O-functional groups results in the release of CO<sub>2</sub>, while the dehydration and fragmentation of the hydroxyl substituents in lignin, hemicellulose and cellulose are the sources of water.<sup>[150]</sup> A group of furan-derivatives e.g. 3-methylfuran and 2,5-dimethylfuran are detected with over 0.9% among the products, and small molecules such as acetic anhydride and 1-hydroxypropan-2-one are also noticed. These products are evolved from cellulose degradation under helium atmosphere.<sup>[138]</sup> Acetic acid is not detected during the decomposition of BSG, but approximately 1–3% among the decomposition products of ABSG (1.3%) and Yb-ABSG (2.7%) are detected as acetic acid. This increase indicates an enhanced presence of carboxyl groups on the surface of ABSG, which is consistent with the previous discussion in Section 3.2.2.

**Table 3.2.** STA-GC-MS results of BSG (375–385 °C), ABSG (375–385 °C) and Yb-ABSG (340–360 °C). For STA, 20 °C/min, helium atmosphere. For GC, 35 °C for 3 min, increased with 5 °C/min until 220 °C, and hold at 220 °C for 3 min.

Name	Retention time (GC, min)	Formula	BSG, Area %	ABSG, Area %	Yb-ABSG, Area %
Carbondioxide	9.51	CO <sub>2</sub>	67.7	48.6	41.2
Water	9.78	H <sub>2</sub> O	25.4	43.8	39.7
Acetaldehyde	10.14	C <sub>2</sub> H <sub>4</sub> O	0.2	0.2	0.3
Acetic anhydride	11.25	C <sub>4</sub> H <sub>6</sub> O <sub>5</sub>	0.7	0.5	2.7
Hydroxyacetaldehyde	12.43	C <sub>2</sub> H <sub>4</sub> O <sub>2</sub>	0.3	0.1	4.9
Acetic acid	13.04	C <sub>2</sub> H <sub>4</sub> O <sub>2</sub>	0	1.3	2.7
2-Butanone	13.49	C <sub>4</sub> H <sub>8</sub> O	0.4	0.3	0.8
3-Methylfuran	13.93	C <sub>5</sub> H <sub>6</sub> O	1.5	1.8	1.3
2-methylfuran	14.01	C <sub>5</sub> H <sub>6</sub> O	0.3	0.4	0.3
1-Hydroxypropan-2-one	15.14	C <sub>3</sub> H <sub>6</sub> O <sub>2</sub>	1.2	0.2	1.9
3-Penten-2-one	15.92	C <sub>5</sub> H <sub>8</sub> O	0.5	0.6	0.6
2,5-Dimethylfuran	17.38	C <sub>6</sub> H <sub>8</sub> O	0.9	1.0	0.9
Pyridin	18.62	C <sub>5</sub> H <sub>5</sub> N	0	0.6	1.1
Furfural	21.79	C <sub>5</sub> H <sub>4</sub> O <sub>2</sub>	0.2	0.2	0.6
1,2-Cyclopentanedione	25.48	C <sub>5</sub> H <sub>6</sub> O <sub>2</sub>	0.7	0.5	0.9

### 3.3. Batch adsorption experiments

The ABSG treated at 150 °C and 16 h shows the highest adsorption of 34.1 mg/g for La(III) in the preliminary adsorption experiments for optimizing the reaction conditions (Fig. 3.1) and thus used for the batch adsorption experiments using U(VI), La(III), Eu(III) and Yb(III). The adsorption capacity was determined by measuring the concentration of the metal ions before and after the adsorption by inductively coupled plasma-optical emission spectrometry (ICP-OES). In addition, the radiotracer technique employing the radiation from  $^{169}\text{Yb}$  was also employed. Comparable results are depicted in Fig. 3.10 regarding adsorption capacities for BSG (21 mg/g for ICP method and 22 mg/g for radiotracer method) and ABSG (42 mg/g for ICP method and 49 mg/g for radiotracer method), indicating that both methods can be used.

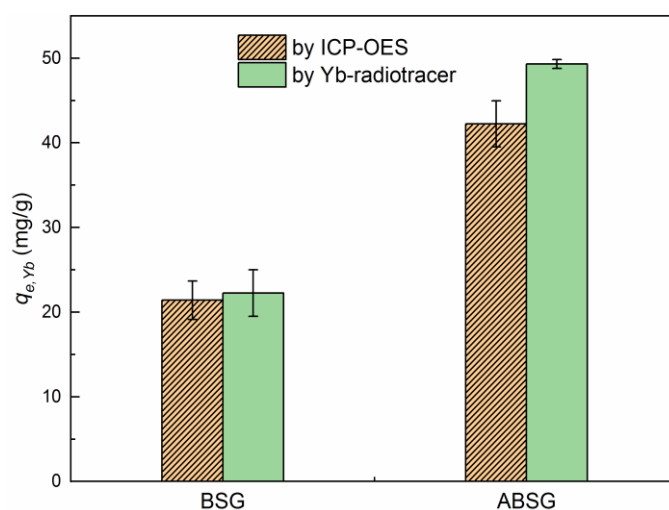


**Fig. 3.10.** Comparison of Yb(III) adsorption capacity onto BSG and ABSG determined by ICP method and radiotracer method (1 mg adsorbent/ 1 mL solution,  $c_0(\text{Yb}) = 100$  mg/L, pH= 5.5, 2 h, room temperature).

#### 3.3.1. Effect of pH value

Both, the surface properties of adsorbents and the species of adsorbates, are influenced by the initial pH of the target aqueous phase, which is crucial for the adsorption process. Fig 3.11 shows the effects of initial pH on the adsorption capacity of BSG and ABSG. The determined point of zero charge ( $\text{pH}_{\text{pzc}}$ ) of ABSG (4.1) is lower than that of BSG ( $\text{pH}_{\text{pzc}} = 5.7$ , Fig. 3.12). This is due to the increased number of carboxyl groups, which cause a more negative charged surface of ABSG. The surface charge of adsorbent would be positive when the initial pH of adsorption is lower than the  $\text{pH}_{\text{pzc}}$  of the adsorbent. In this case the functional groups are protonated, and the electrostatic repulsive effect is unfavorable for the metal ion adsorption.<sup>[151]</sup>

Furthermore, large amount of  $H^+$  in low pH solution would compete with the metal ions for the adsorption sites, which hinders the adsorption process.<sup>[113]</sup> Therefore, a low adsorption capacity is obtained for all studied metal ions for a pH ranging from 1 to 3 (Fig. 3.11). The only exception is the U(VI) adsorption onto BSG with adsorption capacity higher than 20 mg/g, which may be due to the coordination effect of amide groups in the low pH region.<sup>[35,152]</sup> When the initial pH  $> pH_{pzc}$ , the functional groups are deprotonated, thus the adsorbent surface becomes negative, and electrostatic attraction towards the adsorbates increases. As a consequence, the adsorption of La(III), Eu(III) and Yb(III) increases as the pH increases, and gradually reaches saturated adsorption capacity at the pH between 5 and 6. However, the adsorption capacity of U(VI) increases without plateau owing to the change of uranyl species from  $UO_2^{2+}$  to the co-occurrence of  $(UO_2)_2(OH)_2^{2+}$ ,  $UO_2OH^+$  and  $(UO_2)_3(OH)_5^+$ ,<sup>[153]</sup> which are more easily adsorbed due to their high affinity to solid surfaces.<sup>[154]</sup>

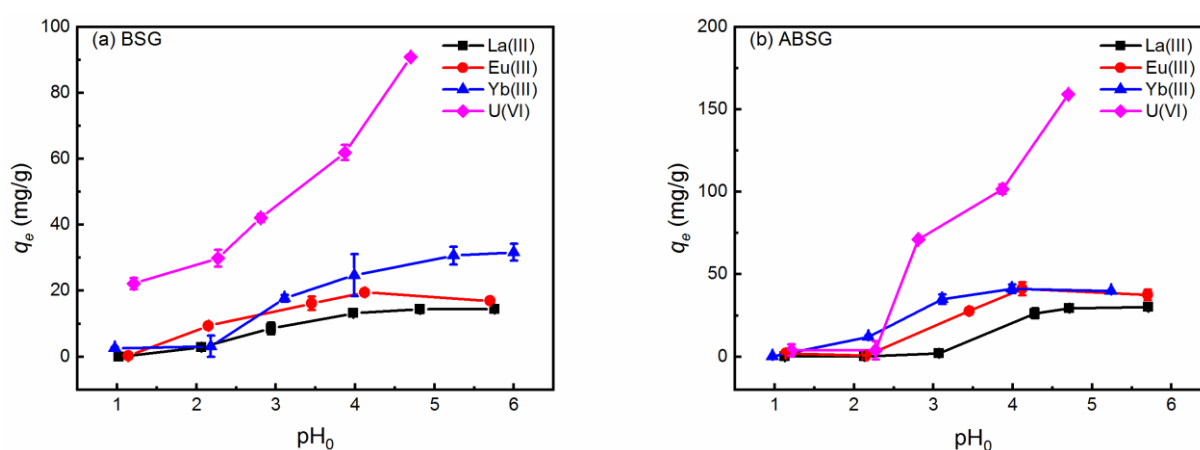


**Fig. 3.11.** Effect of initial pH on the adsorption capacity of (a) BSG and (b) ABSG. For adsorption: 2 mg adsorbent/ 2 mL solution,  $c_0(\text{La, Eu, Yb}) = 100 \text{ mg/L}$ ,  $c_0(\text{U}) = 300 \text{ mg/L}$ , 2 h, room temperature.

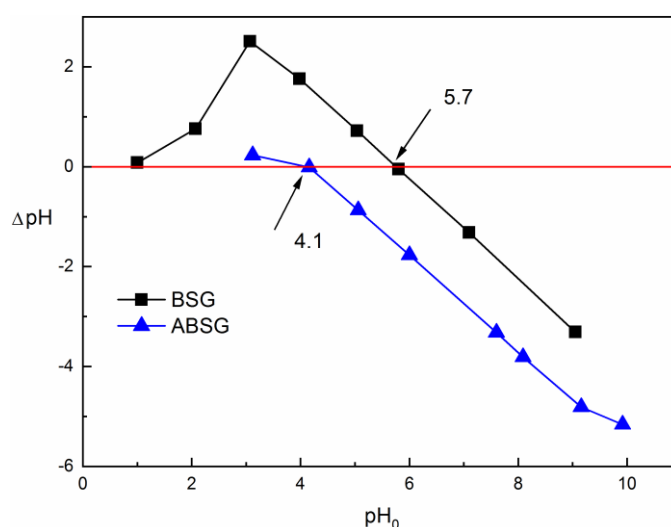


**Fig. 3.12.** Determination the point of zero charge ( $pH_{pzc}$ ) of BSG and ABSG.

### 3.3.2. Adsorption kinetics

Fig. 3.13 shows the amount of adsorbed metal ions as a function of the contact time for BSG and ABSG. The obtained results are fitted using linear form of pseudo-first order kinetic (PFO) model (equation (23), see Section 10.5.1) and pseudo-second order kinetic (PSO) model (equation (25), see Section 10.5.1) as shown in Table 3.3.<sup>[155]</sup> The adsorption process on BSG is generally slow, especially in the case of U(VI), and 2 h are required to complete the adsorption process. In contrast, rapid kinetics of ABSG is observed for all four ions in the first 30 minutes, and equilibrium is reached after 1 h. The fast adsorption at the initial stage indicates that adsorption mainly takes place on the outer surface of ABSG where large amounts of adsorption sites are available.<sup>[155]</sup> For both adsorbents, the PSO model shows a higher coefficient of determination ( $R^2$ ) and a better prediction of the experimental equilibrium adsorption capacity ( $q_{e,exp}$ , mg/g) by the calculated equilibrium adsorption capacity ( $q_{e,cal}$ , mg/g) than the PFO model. Taking the U(VI)-ABSG adsorption data as an example, the  $R^2$  of PSO model (0.9996) is higher than the  $R^2$  of the PFO model (0.9955), and the  $q_{e,cal}$  of the PSO model (175.1 mg/g) is in good agreement with the experimental  $q_{e,exp} = 177.0$  mg/g compared to a  $q_{e,cal} = 75.2$  mg/g for the PFO model (see Table 3.3). Thus, the PSO model could better describe and predict the adsorption behavior of ABSG, indicating the rate control step of the adsorption process is the adsorption onto active sites.<sup>[123]</sup>

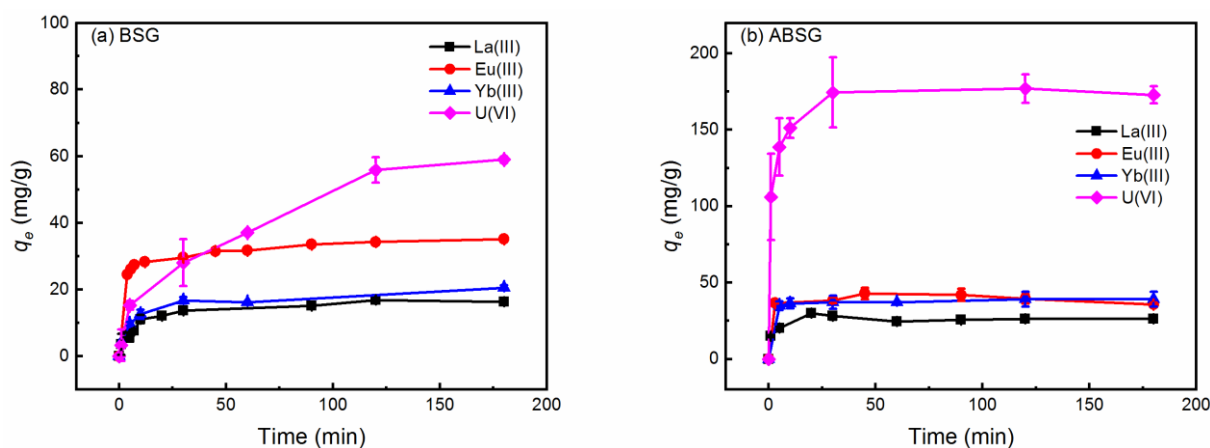


**Fig. 3.13.** Effect of contact time on the adsorption capacity of (a) BSG and (b) ABSG. For adsorption, 2 mg adsorbent/ 2 mL solution,  $c_0(\text{La, Eu, Yb}) = 100$  mg/L,  $c_0(\text{U}) = 300$  mg/L,  $\text{pH}_0(\text{La, Eu, Yb}) = 5.7$ ,  $\text{pH}_0(\text{U}) = 4.7$ , room temperature.

**Table 3.3.** Kinetic fitting results and parameters of BSG and ABSG. For adsorption, 2 mg adsorbent/ 2 mL solution,  $c_0(\text{La, Eu, Yb}) = 100 \text{ mg/L}$ ,  $c_0(\text{U}) = 300 \text{ mg/L}$ ,  $\text{pH}_0(\text{La, Eu, Yb}) = 5.7$ ,  $\text{pH}_0(\text{U}) = 4.7$ , room temperature.

Model	Adsorbent	Adsorbate	$R^2$	$k_1 (\text{min}^{-1})$	$q_{e, \text{cal}} (\text{mg/g})$	$q_{e, \text{exp}} (\text{mg/g})$
Pseudo-first order kinetic model	BSG	La(III)	0.3078	0.0011	4.1	16.9
		Eu(III)	0.9835	0.0203	9.8	35.1
		Yb(III)	0.5726	0.0206	11.6	20.6
		U(VI)	0.9439	0.0230	59.2	59.0
	ABSG	La(III)	0.9510	0.0267	9.0	30.0
		Eu(III)	0.8576	0.0158	4.1	40.2
		Yb(III)	0.6214	0.0074	2.8	39.2
		U(VI)	0.9955	0.1126	75.2	177.0
Model	Adsorbent	Adsorbate	$R^2$	$k_2 (\text{g}\cdot\text{mg}^{-1}\cdot\text{min}^{-1})$	$q_{e, \text{cal}} (\text{mg/g})$	$q_{e, \text{exp}} (\text{mg/g})$
Pseudo-second order kinetic model	BSG	La(III)	0.9982	0.0055	16.5	16.9
		Eu(III)	0.9987	0.0032	35.4	35.1
		Yb(III)	0.9988	0.0140	20.9	20.6
		U(VI)	0.9604	0.0140	67.0	59.0
	ABSG	La(III)	0.9968	0.7062	26.0	30.0
		Eu(III)	0.9986	0.0213	36.9	40.2
		Yb(III)	0.9983	0.0181	39.2	39.2
		U(VI)	0.9996	0.0077	175.1	177.0

### 3.3.3. Adsorption isotherm

To understand the adsorption process and quantitatively compare the adsorption capacity in different adsorption systems, the equilibrium relationships of the adsorption process, namely the isotherms, are essential for the adsorption studies.<sup>[156]</sup> The adsorption isotherms of La(III), Eu(III), Yb(III) and U(VI) onto BSG and ABSG are given in Fig. 3.14, and the fitting results of linear Langmuir (equation (32), see Section 10.5.3) and Freundlich (equation (35), see Section 10.5.3) models are summarized in Table 3.4. Typical graphical features of the Langmuir type adsorption are observed in the adsorption isotherms, which the adsorption capacity increases along with the increase of equilibrium concentration and then followed by a plateau.<sup>[157]</sup> In addition, higher coefficients of determination of the Langmuir model ( $R^2 > 0.98$ ) for all studied adsorption processes are obtained compared with the Freundlich model, giving better prediction of the adsorption. The Langmuir isotherm model assumes a monolayer adsorption with identical and equivalent adsorption sites on the surface of adsorbents,<sup>[156]</sup> and has been widely applied to evaluate the performance of different biosorbents.<sup>[50]</sup> Furthermore,



the separation factor ( $R_L$ , equation (33), see Section 10.5.3) defined by Webber and Chakravorti<sup>[158]</sup> was calculated, which reflects the adsorption nature of the studied ions. In all cases, the  $R_L$  is in the range of 0 to 1 (Table 3.4), which indicates a favorable adsorption process. The maximum adsorption capacities of La(III) (37.5 mg/g), Eu(III) (68.3 mg/g), Yb(III) (46.0 mg/g) and U(VI) (220.6 mg/g) on ABSG have increased by 27%, 172%, 65% and 130% compared with those on BSG (La(III) 29.4 mg/g, Eu(III) 25.1 mg/g, Yb(III) 27.8 mg/g, and U(VI) 96.0 mg/g). The higher adsorption capacity of Eu(III) over Yb(III) and La(III) may indicate differences in the binding mode of metal ions in the adsorption process (see Section 3.4), and was observed previously in studies using immobilized *Pseudomonas aeruginosa* as biosorbent.<sup>[159]</sup> The adsorption capacity of ABSG is higher for U(VI) than the ultrafine cellulose nanofibers (167 mg/g)<sup>[83]</sup> and is comparable to typical biosorbents for the rare earth metal ions, such as pectin (41.2 mg/g for La(III))<sup>[160]</sup> and yeast embedded cellulose (25.9 mg/g for Eu(III)).<sup>[161]</sup> The performance of ABSG for the selected rare earth metal ions is also better than some graphene oxide (GO) composites reported in the literature, for example, GO-melamine composites (25.04 mg/g for La(III), 26.68 mg/g for Eu(III) and 20.88 mg/g for Yb(III))<sup>[162]</sup> and GO-tris(4-aminophenyl) amine composites (10.52 mg/g for La(III), 30.88 mg/g for Yb(III)).<sup>[163]</sup> Higher adsorption capacities for synthetic adsorbents, for example, elastic diglycolamic-acid modified chitosan sponges (CSs-DGAA)<sup>[164]</sup> for Eu(III) of 79 mg/g and GO-activated carbon felt composite for U(VI) of 298 mg/g<sup>[165]</sup> are also reported in literature. However, the production of synthetic adsorbents is often costly, complicated and environmentally unsustainable. On the contrary, the preparation of ABSG is simple and environmentally friendly, which does not require harmful chemicals and complicated processes and minimizes the energy consumption by applying a temperature that is 70 °C lower than HTC. Neither BSG nor ABSG exhibited significant selectivity among rare earth metal ions, except for the adsorption preference towards uranyl ions with a high adsorption capacity. However, it does not underline the benefit of ABSG for environment remediation, because ABSG could simultaneously remove the hazardous uranyl and rare earth metal ions from the wastewater, thereby simplifying treatment procedures and reducing costs.

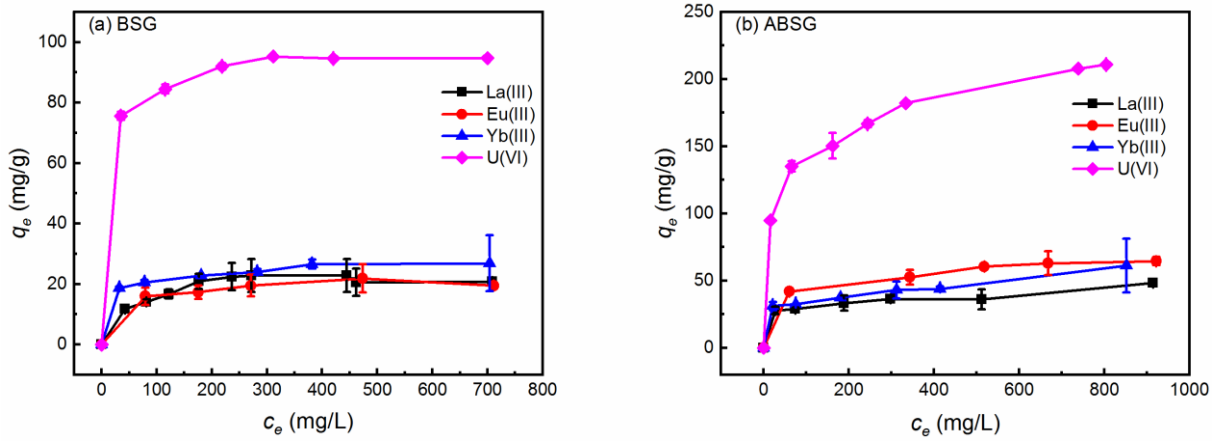


**Fig. 3.14.** Effect of equilibrium concentration on the adsorption capacity of (a) BSG and (b) ABSG. For adsorption, 2 mg adsorbent/ 2 mL solution,  $t_{(BSG)} = 2$  h,  $t_{(ABSG)} = 1$  h,  $pH_0(\text{La, Eu, Yb}) = 5.7$ ,  $pH_0(\text{U}) = 4.7$ , room temperature.

**Table 3.4.** Isotherms fitting results and parameters of BSG and ABSG. For adsorption, 2 mg adsorbent/ 2 mL solution,  $t_{(BSG)} = 2$  h,  $t_{(ABSG)} = 1$  h,  $pH_0(\text{La, Eu, Yb}) = 5.7$ ,  $pH_0(\text{U}) = 4.7$ , room temperature.

Adsorbate	Adsorbent	Langmuir model			Freundlich model	
		$R^2$	$q_m$ (mg/g)	$R_L$	$R^2$	$n$
La(III)	BSG	0.9823	29.4	0.2073–0.6108	0.9775	2.60
	ABSG	0.9981	37.4	0.0837–0.4773	0.8975	9.74
Eu(III)	BSG	0.9981	25.1	0.0630–0.4022	0.9738	6.03
	ABSG	0.9926	68.3	0.0596–0.3880	0.9809	6.12
Yb(III)	BSG	0.9972	27.8	0.0286–0.5706	0.9631	8.00
	ABSG	0.9930	46.0	0.0258–0.3164	0.8654	8.03
U(VI)	BSG	0.9997	96.0	0.0092–0.0915	0.9907	9.42
	ABSG	0.9914	220.6	0.0541–0.5411	0.9872	4.97

### 3.3.4. Effect of temperature

The thermodynamic analysis was performed by recording adsorption isotherms of uranyl and rare earth metal ions for BSG and ABSG (Fig. 3.15). A linear fitting of the isotherms using Langmuir model (Fig. 3.16) was used to obtain the isotherm equilibrium constants ( $K_L$ , L/mg) to calculate the dimensionless thermodynamic equilibrium constant ( $K_e^0$ ) (equation (13), see Section 10.3.3). Then a linearized plot of  $\ln K_e^0$  versus  $1/T$  was used for thermodynamic parameter calculations (Fig. 3.17, equation (11) and equation (12), see Section 10.3.3), and the thermodynamic parameters of different adsorption process are given in Table 3.5. A spontaneous adsorption process is indicated by the negative values of  $\Delta G^0$  in all cases studied. Moreover, an increase in randomness at the solid-liquid interface during the adsorption is shown by the positive values of  $\Delta S^0$  in all cases.<sup>[166]</sup> Comparing the  $\Delta H^0$  values with  $-T\Delta S^0$  values shows that the thermodynamic driving force of the uranyl and rare earth metal ions onto the

biosorbents is the change of entropy.<sup>[167]</sup> The positive  $\Delta H^0$  values in the adsorption of the studied rare earth metal ions on ABSG and BSG indicate an endothermic process, as it is also described in most publications.<sup>[168]</sup> The adsorption of U(VI) onto BSG is also endothermic ( $\Delta H^0 = 55.8$  kJ/mol), which is generally observed when the uranyl ions are complexed by anionic organic ligands, leading to endothermic enthalpies and large positive entropies of complexation.<sup>[165]</sup> On the contrary, the adsorption of U(VI) on ABSG is exothermic ( $\Delta H^0 = -12.6$  kJ/mol). The various thermodynamic mechanisms of uranyl adsorption resulting from the different surface properties of biochar have been described in the literature.<sup>[167]</sup> Therefore, variations of the surface characters of BSG and ABSG such as the content of carboxyl groups (0.15 mmol/g for BSG and 1.46 mmol/g for ABSG) and  $\text{pH}_{\text{PZC}}$  (5.7 for BSG and 4.1 for ABSG) may result in the observed difference in  $\Delta H^0$ .

**Table 3.5.** Thermodynamic parameters of uranyl and rare earth metal ions adsorption onto BSG and ABSG. For adsorption, 2 mg adsorbent/ 2 mL metal solution,  $c_0 = 100\text{--}600$  mg/L,  $t_{\text{BSG}} = 2$  h,  $t_{\text{ABSG}} = 1$  h,  $\text{pH}_0(\text{U}) = 4.7$ ,  $\text{pH}_0(\text{La, Eu, Yb}) = 5.7$ ,  $T = 25$  °C, 45 °C, 65 °C, stirrer speed = 180 rpm.

Adsorbent	Adsorbate	$\Delta H^0$ (kJ/mol)	$\Delta S^0$ (J/(mol·K))	$\Delta G^0$ (kJ/mol)			$-\text{T}\Delta S^0$ (kJ/mol)		
				298 K	318 K	338 K	298 K	318 K	338 K
ABSG	U(VI)	-12.6	39.6	-24.4	-25.2	-25.9	-11.8	-12.6	-13.4
	Yb(III)	14.4	113.1	-19.3	-21.5	-23.8	-33.7	-36.0	-38.2
	Eu(III)	18.0	124.3	-19.1	-21.6	-24.0	-37.0	-39.5	-42.0
	La(III)	12.2	109.5	-20.4	-22.6	-24.8	-32.6	-34.8	-37.0
BSG	U(VI)	55.8	261.1	-22.0	-27.2	-32.5	-77.8	-83.0	-88.3
	Yb(III)	27.0	146.3	-16.6	-19.5	-22.4	-43.6	-46.5	-49.4
	Eu(III)	12.6	108.1	-19.6	-21.8	-24.0	-32.2	-34.4	-36.5
	La(III)	7.5	89.8	-19.3	-21.1	-22.9	-26.8	-28.6	-30.4

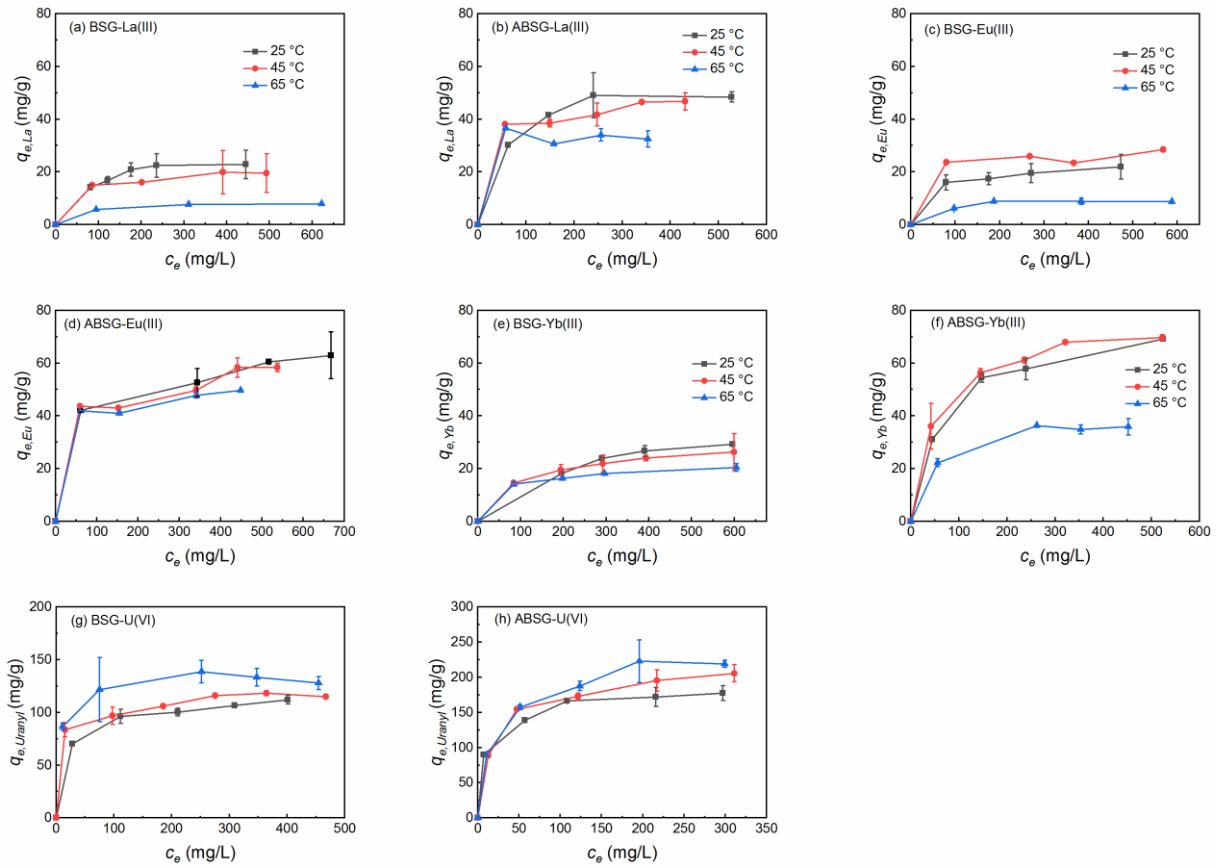


**Fig. 3.15.** Adsorption isotherms of (a) La(III) onto BSG, (b) La(III) onto ABSG, (c) Eu(III) onto BSG, (d) Eu(III) onto ABSG, (e) Yb(III) onto BSG, (f) Yb(III) onto ABSG, (g) U(VI) onto BSG and (h) (VI) onto ABSG. For adsorption, 2 mg adsorbent/ 2 mL metal solution,  $c_0 = 100\text{--}600$  mg/L,  $t_{BSG} = 2$  h,  $t_{ABSG} = 1$  h,  $pH_0(U) = 4.7$ ,  $pH_0(La, Eu, Yb) = 5.7$ ,  $T = 25$  °C, 45 °C, 65 °C, stirrer speed = 180 rpm.

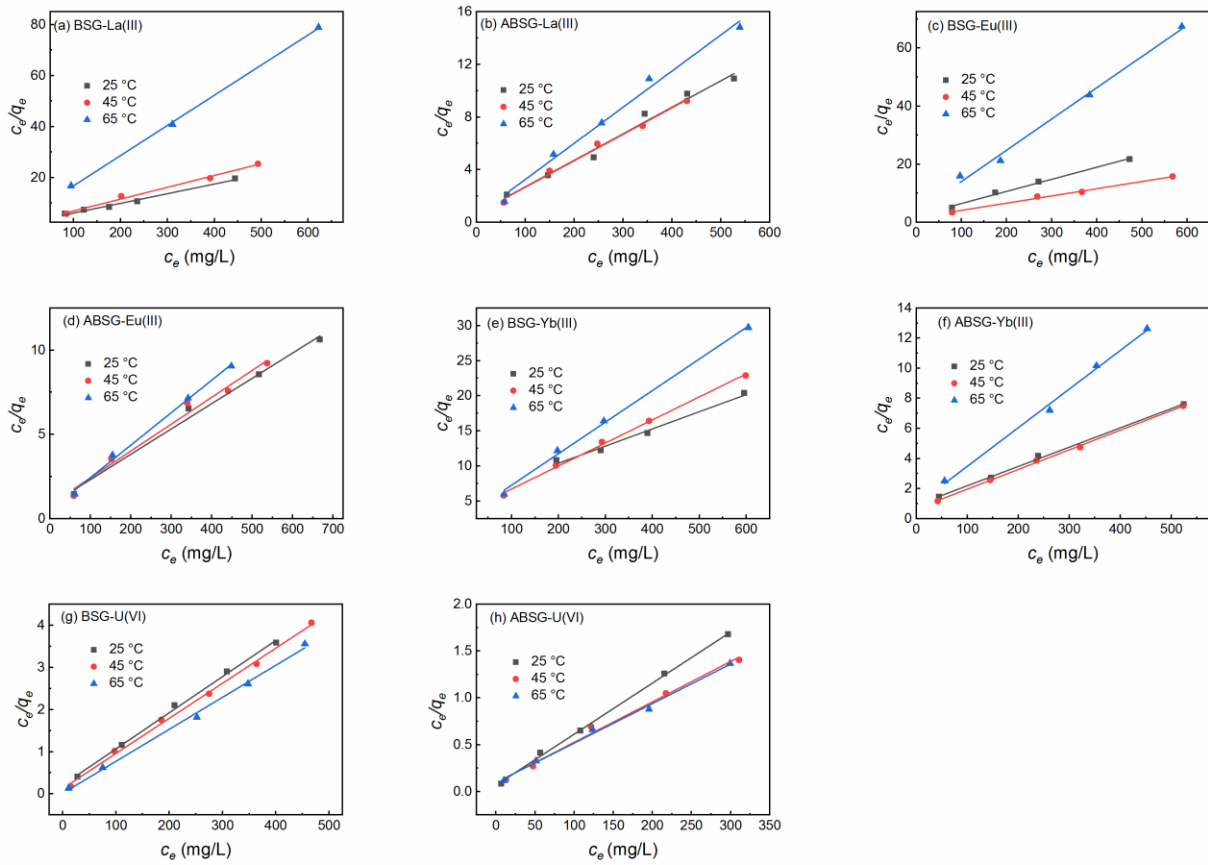


**Fig. 3.16.** Langmuir model fitting of isotherms (a) La(III) onto BSG, (b) La(III) onto ABSG, (c) Eu(III) onto BSG, (d) Eu(III) onto ABSG, (e) Yb(III) onto BSG, (f) Yb(III) onto ABSG, (g) U(VI) onto BSG and (h) U(VI) onto ABSG.

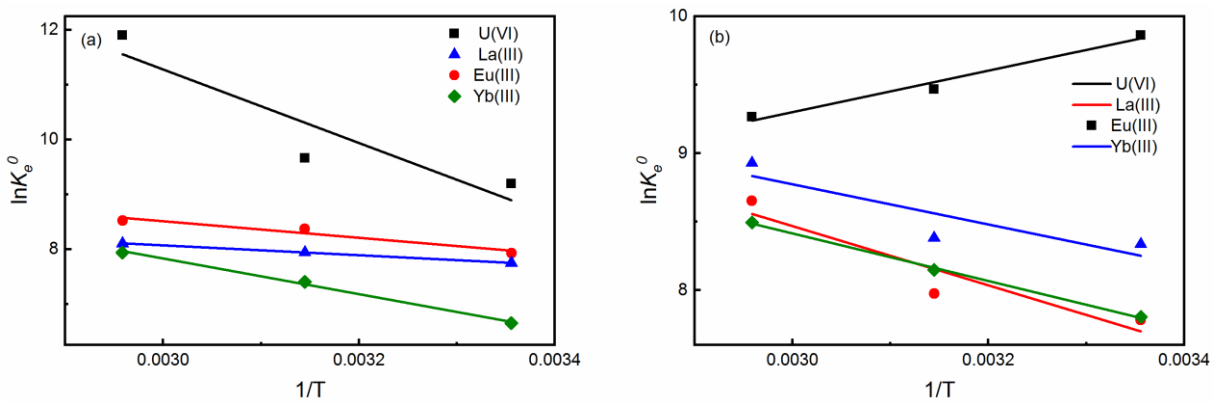


**Fig. 3.17.**  $\ln K_e^0$  versus  $1/T$  plots for thermodynamic parameter calculations for (a) BSG and (b) ABSG.

### 3.4. Investigation of adsorption mechanism

The BET surface area of BSG and ABSG is determined to be  $< 2 \text{ m}^2/\text{g}$ , which is consistent with the reported BET surface area of  $0.48 \text{ m}^2/\text{g}$  for BSG.<sup>[169]</sup> Thus, no obvious pore structure of the studied biosorbents could contribute significantly to the adsorption process.

SEM/EDX analysis demonstrates the adsorption of metal ions to the ABSG surface, as shown in the SEM image, EDX elemental mapping, and uranium distribution of uranyl ion-loaded ABSG from Fig. 3.18. Similar results are obtained for the examined rare earth metal ions (Fig. 3.19), whereas the following discussion focuses on the uranyl ion-loaded ABSG as a representative. An irregular and rough surface of ABSG with no apparent pore structure is shown in the SEM image (Fig. 3.18, a) as indicated by the low BET surface area. Therefore, the adsorption of the metal ions by ABSG is predominantly driven by interactions of the functional groups on the surface, supported by the EDX element mapping (Fig. 3.18, b) and the distribution of uranium (Fig. 3.18, c). The irregular shape of the particles results in distinct shadows, so no uniform recording of the X-ray signal can be expected. However, the uranyl ions appear to be more or less uniformly distributed on the surface of the ABSG, except for some small areas with uranium aggregation.

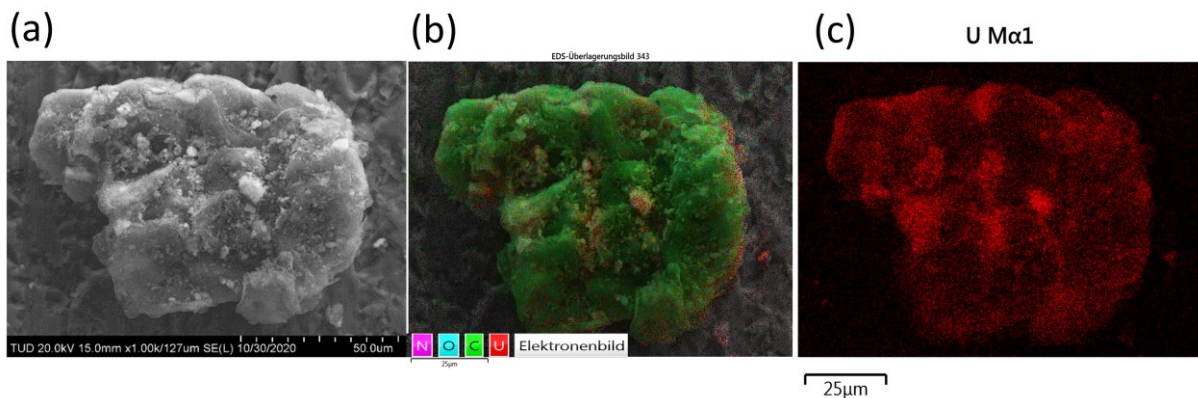


**Fig. 3.18.** (a) SEM image (magnification of 1000 times) of uranyl ions loaded-ABSG, (b) EDX element mapping of uranyl ions loaded-ABSG (20 kV/10  $\mu\text{A}$ , magnification of 1000 times, 25 frames) and (c) distribution of uranium on uranyl ions loaded-ABSG. For ion-loading: 50 mg ABSG/ 50 mL solution,  $\text{pH}_0 = 4.7$ ,  $c_0(\text{U}) = 300 \text{ mg/L}$ ,  $t = 1 \text{ h}$ , room temperature.

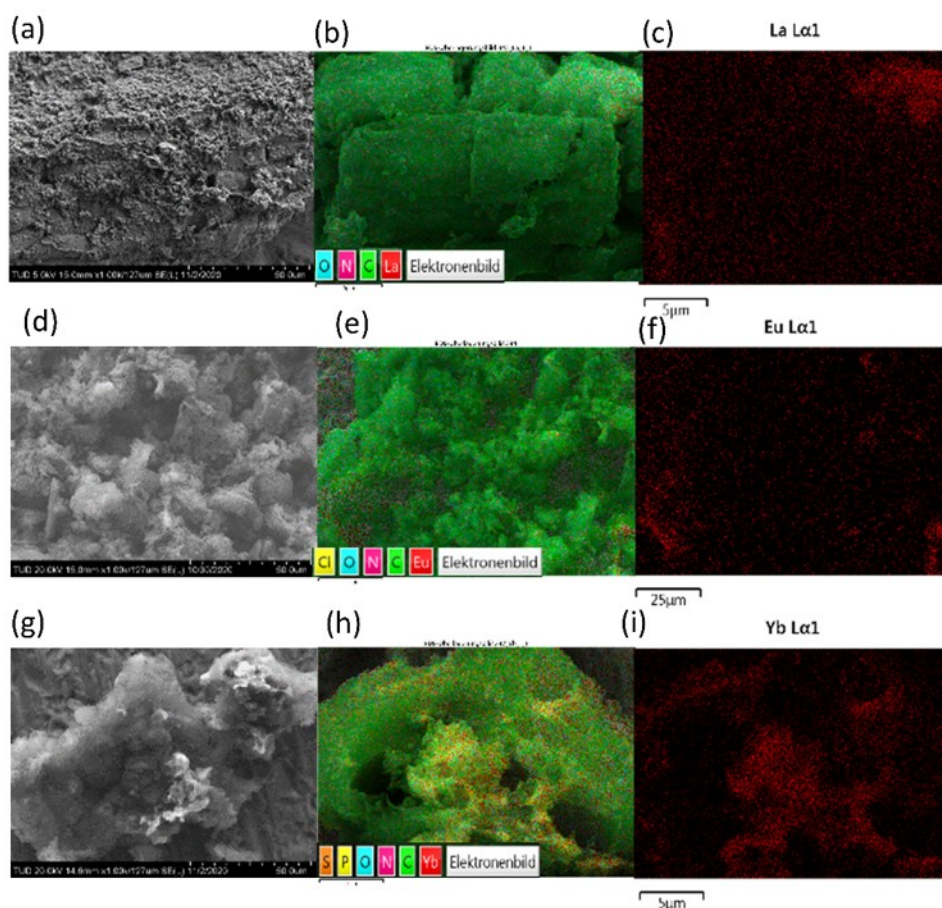


**Fig. 3.19.** (a-c) SEM image (1000x), EDX element mapping (20 kV/10  $\mu$ A, 5000x, 25 frames) and distribution of La on La loaded-ABSG, (d-f) SEM image (1000x), EDX mapping (20 kV/10  $\mu$ A, 1000x, 25 frames) and distribution of Eu on Eu loaded-ABSG and (g-i) SEM image (1000x), EDX mapping (20 kV/10  $\mu$ A, 5000x, 25 frames) and distribution of Yb on Yb loaded-ABSG. For ion-loading: 50 mg ABSG/ 50 mL solution, pH= 5.7,  $c_0$ = 100 mg/L,  $t$  = 1 h, room temperature.

FT-IR spectra of ABSG before and after adsorption are displayed in Fig. 3.20. The intensity of the antisymmetric stretching vibration of  $-\text{COO}^-$  groups (at  $1654\text{ cm}^{-1}$ ) reduces for all ion-loaded samples, indicating the involvement of carboxyl groups in the adsorption process. The differences between the antisymmetric and symmetric stretching bands of the  $-\text{COO}^-$  groups ( $\Delta_{\text{vas-vs}}$ ) are used to calculate the chelate model. As shown in Table 3.6,  $\Delta_{\text{vas-vs}}$  values of  $197\text{ cm}^{-1}$  and  $201\text{ cm}^{-1}$  are obtained for La(III) and Yb(III) loaded samples, respectively. Considering the resolution of the recorded spectra ( $4\text{ cm}^{-1}$ ), this small difference is negligible. The obtained value of  $\Delta_{\text{vas-vs}} \approx 200\text{ cm}^{-1}$  indicates a monodentate binding of La(III) and Yb(III) with the carboxyl groups, which involves electrostatic effect and ion exchange.<sup>[170]</sup> In contrast,  $\Delta_{\text{vas-vs}}$  of  $179\text{ cm}^{-1}$  and  $187\text{ cm}^{-1}$  are obtained for the Eu(III) and U(VI) loaded samples, pointing at a different binding mode. In the case of U(VI), the presence of hydrated uranyl species may result in a more complex coordination, which is indicated by a new absorption band occurring at

922  $\text{cm}^{-1}$  assigned to the antisymmetric stretching vibration of  $\text{U}=\text{O}$  in  $(\text{UO}_2)_3(\text{OH})_5^+$ .<sup>[171]</sup> In addition, all studied metal ions after adsorption result in new absorption bands at 530 to 540  $\text{cm}^{-1}$  and 440 to 450  $\text{cm}^{-1}$ , which could be ascribed to metal–N vibration and metal–O vibration, respectively.<sup>[172]</sup> This is cited in the literature as evidence for the involvement of O- and N-containing functional groups in the adsorption of uranyl<sup>[173]</sup> and rare earth metal ions.<sup>[163]</sup> Therefore, the major adsorption mechanism of La(III), Eu(III), Yb(III) and U(VI) onto ABSG is concluded as the electrostatic effect between negatively charged functional groups and cations. However, in the case of Eu(III) and U(VI), the coordination of cations with O- and N-containing functional groups is also of great importance, resulting in higher adsorption capacity than La(III) and Yb(III), as observed in the isothermal study (Section 3.3.3).

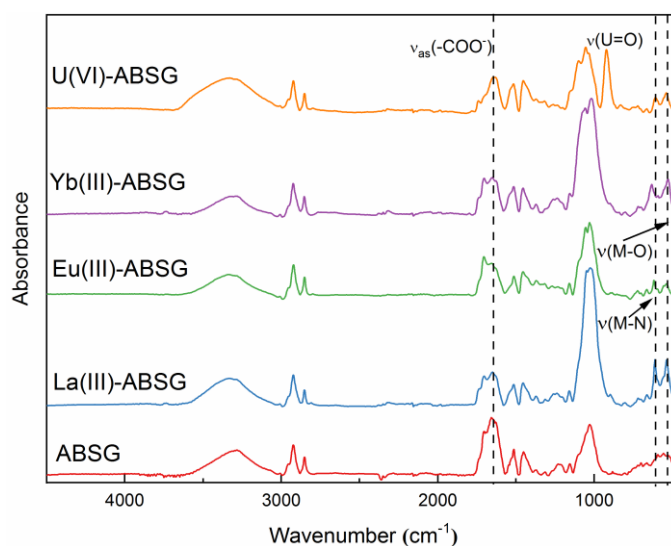


**Fig. 3.20.** FT-IR spectra of ABSG and ion-loaded ABSG. For ion-loading: 50 mg ABSG/ 50 mL solution, pH(La, Eu, Yb) = 5.7, pH<sub>0</sub>(U) = 4.7, c<sub>0</sub>(La, Eu, Yb) = 100 mg/L, c<sub>0</sub>(U) = 300 mg/L, t = 1 h, room temperature.

**Table 3.6.** Calculation results of the FT-IR data.

	ABSG	La-ABSG	Eu-ABSG	Yb-ABSG	U(VI)-ABSG
Antisymmetric stretching of $-\text{COO}^-$ ( $\nu_{\text{as}}$ ), $\text{cm}^{-1}$	1654	1650	1631	1655	1639
Symmetric stretching of $-\text{COO}^-$ ( $\nu_{\text{s}}$ ), $\text{cm}^{-1}$	1452	1453	1453	1454	1452
$\Delta\nu_{\text{as-vs}}$ , $\text{cm}^{-1}$	202	197	179	201	187



## 4. Oxidation of brewer's spent grain for uranyl ion adsorption

This part of work aims to convert brewer's spent grain (BSG) to an effective and reusable biosorbent by direct chemical modification, namely nitro-oxidation, which is a simple and selective oxidation method without transition metals as catalysts.<sup>[84]</sup> Contrary to the fact that most studies on biomass oxidation have only focused on pure cellulose or commercial fibers, large quantities of cheap and readily available biomass from agricultural or industrial waste streams, such as BSG, are still waiting for exploration. Furthermore, only a few studies have discussed desorption and reusability of oxidized cellulose materials. This raises the problem that non-renewable biosorbents would increase the operation cost and waste production of the adsorption process, thereby undermining the economic and ecologic benefits of the biosorbents.<sup>[174]</sup>

As reported in the literature,<sup>[175]</sup> the success of nitro-oxidation is highly depended on the occurrence and maintenance of a long-time stable foam which generated by liberated nitrogen oxides in highly viscous  $H_3PO_4$ . Therefore, BSG is proposed as an ideal raw material for the nitro-oxidation of cellulose, which is rich in proteins and could produce and maintain foams during the oxidation process. To the best of our knowledge, no attempt has been made in the literature to oxidize BSG and use it as a biosorbent. A preliminary experiment employing nitro-oxidation,<sup>[84]</sup>  $H_2O_2$  and  $KMnO_4$  as oxidants shows that only nitro-oxidation could successfully oxidize BSG, which thereby has been intensively studied. The effect of BSG particle size on the nitro-oxidation was studied, and the chemical structure, functional groups and thermal stability of oxidized BSG (OBSG) were characterized. Adsorption properties, adsorption mechanisms and the reusability of OBSG were also investigated to gain a comprehensive understanding of its potential as a biosorbent for U(VI) removal.

#### 4.1. Oxidation of brewer's spent grain

To explore an appropriate oxidation method for BSG,  $\text{H}_2\text{O}_2$ <sup>[176,177]</sup> and  $\text{KMnO}_4$ <sup>[178]</sup> were tested as oxidizing agents in the present study aside from nitro-oxidation. The FT-IR spectra of the oxidation products are provided in Fig. 4.1, a, and their adsorption capacity for U(VI) ( $c_0(\text{U}) = 300 \text{ mg/L}$ ) is shown in Fig. 4.1, b. Only the product obtained from the nitro-oxidation method ( $\text{H}_3\text{PO}_4/\text{NaNO}_2$  as oxidants) shows a significant increased adsorption capacity for U(VI) from 79.6 mg/g for BSG to 201.6 mg/g for OBSG, indicating the successful modification of BSG and a significant enhancement of the U(VI) adsorption. Compared to BSG, the oxidation products from other studied oxidants show lower adsorption capacity owing to the loss of surface functional groups during the non-selective oxidation. The analysis of the FT-IR spectra (Fig. 4.1, a) further confirms this. Only OBSG derived from nitro-oxidation shows an increased intensity of the C=O stretching vibration band from  $-\text{COOH}$  groups ( $1732 \text{ cm}^{-1}$ ), while applying other oxidation methods results in a decrease in band intensity. The results prove that nitro-oxidation is an effective oxidation method for BSG. The nitroxonium ions ( $\text{NO}^+$ ) are released when  $\text{H}_3\text{PO}_4$  and  $\text{NaNO}_2$  are in excess acid and selectively oxidize the primary hydroxyl group ( $-\text{CH}_2\text{OH}$ ) of cellulose at the C6 position to carboxyl groups.<sup>[84,85]</sup> The  $\text{H}_3\text{PO}_4$  is a good swelling agent for cellulose, which helps to remove impurities (lignin, protein and hemicellulose) from untreated BSG, and thus, benefits the selective oxidation of cellulose.

The adsorption capacity of BSG with different particle sizes and the adsorption capacity of OBSG prepared from BSG with different size are shown in Fig. 4.2 ( $c_0(\text{U}) = 300 \text{ mg/L}$ ). The adsorption capacity of BSG increases with decreasing particle size, from 21.3 mg/g ( $>710 \mu\text{m}$ ) to 79.6 mg/g ( $<315 \mu\text{m}$ ), since smaller particle fraction of BSG contains more protein and starch-rich components with larger amounts of functional groups such as hydroxyl groups and carboxyl groups,<sup>[179]</sup> leading to the observed increased adsorption capacity. The specific surface area of raw materials (BSG) also increases with decreasing particle size, making BSG easier to swell and increasing the availability of active sites for effective oxidation.<sup>[108]</sup> Therefore, the adsorption capacity after oxidation (OBSG) increases as the particle sizes of the raw material (BSG) decreases, from  $> 710 \mu\text{m}$  (89.1 mg/g) to 315–710  $\mu\text{m}$  (138.8 mg/g) and  $<315 \mu\text{m}$  (201.6 mg/g). Since the OBSG obtained from the smallest fraction ( $<315 \mu\text{m}$ ) shows the highest adsorption capacity of 201.6 mg/g, this fraction ( $<315 \mu\text{m}$ ) of BSG and OBSG was used for the detailed adsorption studies and further characterizations.

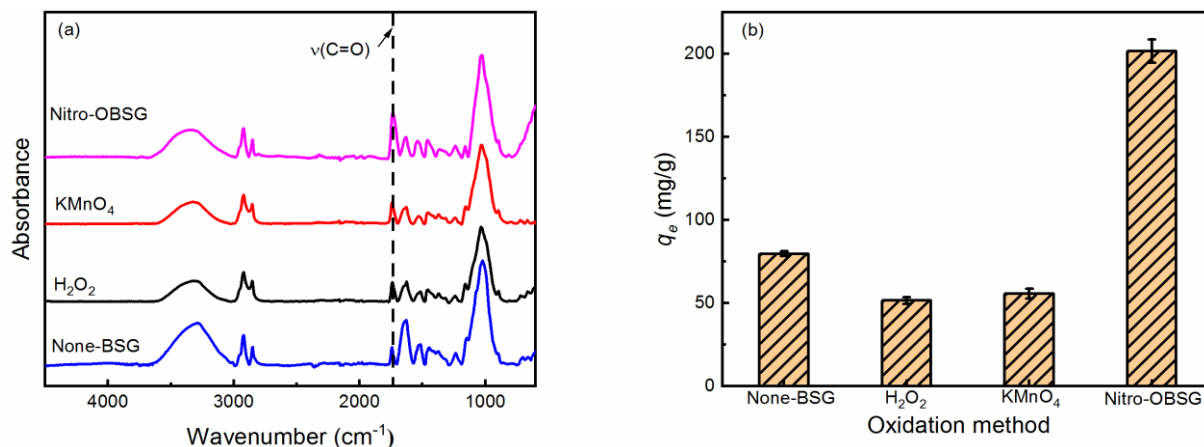


**Fig. 4.1.** (a) FT-IR spectra of oxidized products by different oxidation methods. H<sub>2</sub>O<sub>2</sub> method: 2 g BSG, 10 mL 35 wt % H<sub>2</sub>O<sub>2</sub>, 0.4 mL 1 M HCl, reflux at 100 °C for 2 h. KMnO<sub>4</sub> method: 1 g BSG, 0.18 g KMnO<sub>4</sub>, 20 mL 0.15 M H<sub>2</sub>SO<sub>4</sub> at 60 °C for 2 h. H<sub>3</sub>PO<sub>4</sub>/NaNO<sub>2</sub> method: 1 g BSG, 16 mL 85 wt % H<sub>3</sub>PO<sub>4</sub>, 0.8 g NaNO<sub>2</sub> at room temperature for 16 h and (b) adsorption capacity of the U(VI) onto oxidized products using different oxidation methods (BSG < 315 μm). For adsorption: 2 mg adsorbent/ 2 mL solution,  $c_0(\text{U}) = 300$  mg/L, pH = 4.7, 2 h, room temperature.

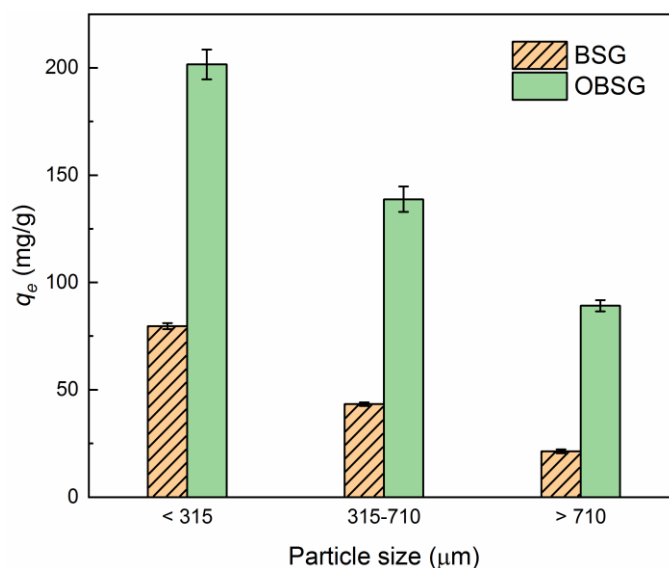


**Fig. 4.2.** Effect of particle size on the adsorption capacity before and after nitro-oxidation. For adsorption: 2 mg adsorbent/ 2 mL solution,  $c_0(\text{U}) = 300$  mg/L, pH = 4.7, 2 h, room temperature.

## 4.2. Characterization of the adsorbents

### 4.2.1. FT-IR and solid-state NMR spectra

The FT-IR spectra of BSG and OBSG provides important information about the structure and major functional groups (Fig. 4.3, a). The spectra show that the carbon chain of cellulose is not affected by oxidation and abundant hydroxyl groups are present on the surface of OBSG. The observed broad absorption bands at 3200–3400  $\text{cm}^{-1}$  for both BSG and OBSG correspond to the overlap of O–H and N–H stretching vibrations common in lignocellulose and proteins. The bands around 2900 and 2800  $\text{cm}^{-1}$  are assigned to the antisymmetric and symmetric stretching vibrations of  $-\text{CH}_2-$  groups of cellulose and hemicellulose, and the bands at 1240  $\text{cm}^{-1}$  and 1021  $\text{cm}^{-1}$  are attributed to the C–N and C–O–C stretching vibrations, respectively.<sup>[126]</sup> The attribution of bands at 1742  $\text{cm}^{-1}$  (BSG) and 1732  $\text{cm}^{-1}$  (OBSG) to the C=O vibration of  $-\text{COOH}$  groups is confirmed through shifting the absorption bands down by 3  $\text{cm}^{-1}$  upon  $\text{D}^+$  labelling (see Fig. 4.3, b and Table 4.1). The  $\text{D}^+$  labelling was performed by suspending 30 mg of adsorbents with 2 mL  $\text{D}_2\text{O}$  for 64 h using a magnetic stirrer (stirrer speed = 180 rpm). The obtained solids were dried at 60 °C for 12 h before FT-IR spectra were measured in the region of interest (2000–1200  $\text{cm}^{-1}$ ) with a resolution of 1  $\text{cm}^{-1}$  and averaged over 64 scans. A shift of the C=O vibration of the  $-\text{COOH}$  groups from 1742  $\text{cm}^{-1}$  to 1732  $\text{cm}^{-1}$  after oxidation with a significant increase in intensity shows that the number of carboxyl groups increases due to oxidation.<sup>[177]</sup> Furthermore, the absorption bands related to the overlapping of  $-\text{COO}^-$  antisymmetric stretching vibration with the protein-related bonds (amide I groups) and the amide II groups in proteins occur in BSG spectrum at 1635  $\text{cm}^{-1}$  and 1524  $\text{cm}^{-1}$ , respectively. The intensity of the band at 1635  $\text{cm}^{-1}$  decreases in OBSG spectrum, indicating the loss of protein during the oxidation process. However, the symmetric stretching vibration of  $-\text{COO}^-$  groups is still observed at 1451  $\text{cm}^{-1}$  (1453  $\text{cm}^{-1}$  for BSG).<sup>[180]</sup>

**Table 4.1.** Shifts of  $\nu(\text{COOH})$  vibration in BSG and OBSG FT-IR spectra upon  $\text{D}^+$  labelling.

	$\nu(\text{origin})$	$\nu(\text{D}_2\text{O})$	$\Delta\nu$
BSG	1742 $\text{cm}^{-1}$	1739 $\text{cm}^{-1}$	3 $\text{cm}^{-1}$
OBSG	1732 $\text{cm}^{-1}$	1729 $\text{cm}^{-1}$	3 $\text{cm}^{-1}$

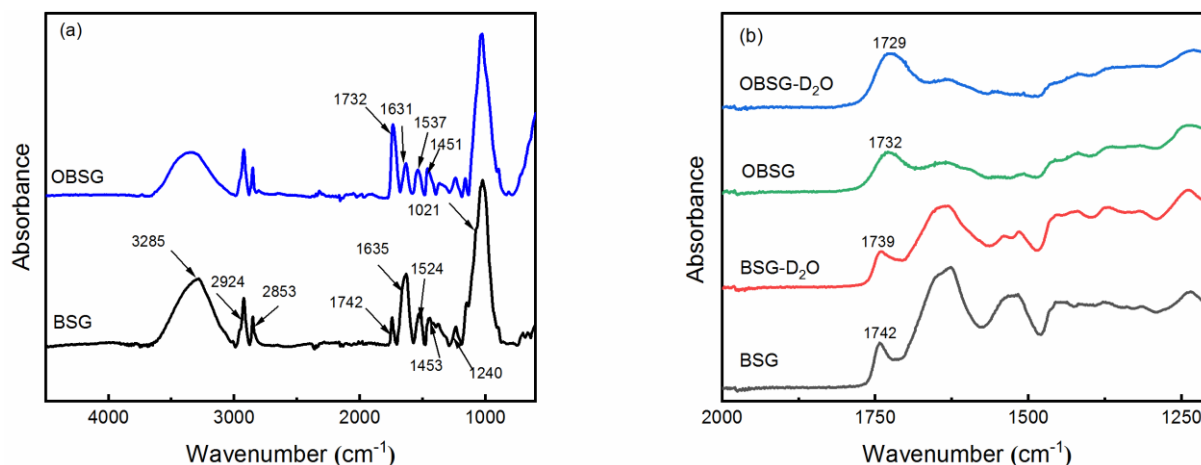


**Fig. 4.3.** (a) FT-IR spectra of BSG and OBSG, resolution = 4 cm<sup>-1</sup>, averaged over 32 scans, and (b) detailed FT-IR spectra of BSG and OBSG with or without D<sup>+</sup> labelling. For D<sup>+</sup> labelling: 30 mg adsorbents/ 2 mL D<sub>2</sub>O for 64 h; for IR measurement: resolution = 1 cm<sup>-1</sup>, averaged over 64 scans.

<sup>13</sup>C CP/MAS solid-state NMR spectra of BSG and OBSG provide further structural information about the biosorbents in addition to the FT-IR spectra (Fig. 4.4). The structure of OBSG is similar to oxidized cellulose described in literature.<sup>[181]</sup> Generally, resonances associated to the carbon backbone of cellulose are observed at 105 ppm (C1), 84 ppm (C4), 73 ppm (C2, C3, C5) and 64 ppm (C6), and the resonance at 173 ppm is attributed to carboxyl groups.<sup>[182]</sup> Moreover, the resonances in the OBSG spectrum assigned to the lignin aromatic C (120–160 ppm) and aliphatic C (30 ppm) from sugar chains<sup>[142]</sup> are less pronounced than those in the BSG spectrum, which is probably due to the removal of impurities during oxidation.

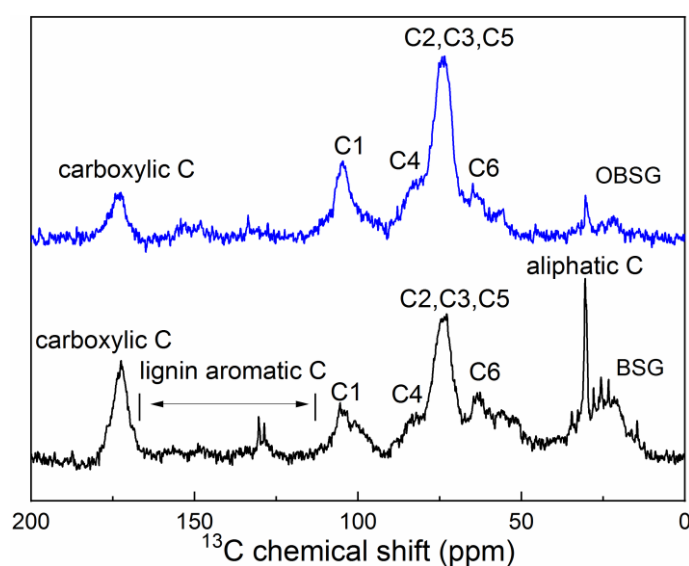


**Fig. 4.4.** <sup>13</sup>C CP/MAS solid-state NMR spectra of BSG and OBSG.

#### 4.2.2. Chemical composition and functional groups

Table 4.2 shows the contents of C, H, N and O of BSG and OBSG in weight percent. After oxidation, the content of N decreases from 5.1 wt% to 1.1 wt%, thus the protein content is estimated to drop from 29.5 wt% to 6.4 wt%. This shows that most of the protein is removed during the oxidation, which is supported by the decrease of the absorption band intensity of the amide I groups ( $1635\text{ cm}^{-1}$ ) in the FT-IR spectra (see Fig. 4.3). However, the presence of protein during oxidation is important. When  $\text{H}_3\text{PO}_4$  reacts with  $\text{NaNO}_2$  to release  $\text{N}_2\text{O}_3$ , it acts as a surfactant to form a large amount of foam. In the literature it is stated that,<sup>[175]</sup> the high specific surface area of the foam and positive pressure inside are crucial for a successful oxidation. The content of C decreases from 49.1 wt% (BSG) to 42.6 wt% (OBSG), and the content of H decreases from 6.1 wt% (BSG) to 5.4 wt% (OBSG). In addition, the O content calculated by difference increases from 38.0 wt% (BSG) to 49.8 wt% (OBSG). Furthermore, the phosphorous content of OBSG ( $760 \pm 30\text{ mg/kg}$ ) is significantly lower than that of BSG ( $5284 \pm 3\text{ mg/kg}$ ) (see Table 4.3) despite the usage of phosphoric acid during the oxidation. This suggests that the increased adsorption capacity of OBSG is not due to the presence of residual phosphoric acid in the OBSG sample that would have favored the precipitation of uranyl phosphate, but is due to the increase in the available carboxyl groups.

**Table 4.2.** Elemental analysis of BSG and OBSG.

	N (%)	C (%)	H (%)	S (%)	Mineral (%)	O (%)
BSG	$5.1 \pm 0.1$	$49.1 \pm 0.1$	$6.1 \pm 0.2$	$0.3 \pm 0.1$	$1.4 \pm 0.1$	$38.0 \pm 0.6$
OBSG	$1.1 \pm 0.1$	$42.6 \pm 0.8$	$5.4 \pm 0.1$	$0.1 \pm 0.1$	$1.0 \pm 0.1$	$49.8 \pm 1.2$

**Table 4.3.** Mineral elements content (mg/kg) of BSG and OBSG.

	K	Na	P	Ca	Fe	Mg	Mn	Zn	Si	Mineral (%)
BSG	$808 \pm 0.2$	$9 \pm 1$	$5284 \pm 3$	$1096 \pm 2$	0	$1487 \pm 0.2$	0	0	$5184 \pm 0.4$	$1.4 \pm 0.1$
OBSG	0	0	$760 \pm 30$	$1.1 \pm 0.1$	0	0	0	0	$9400 \pm 270$	$1.0 \pm 0.1$

Errors are those obtained from the ICP measurements.

Fig. 4.5 shows the determined content of the functional groups involved in adsorption in both BSG and OBSG. Apparently, the successful oxidation of BSG is confirmed by a significant increase in carboxyl groups from 0.15 mmol/g to 1.3 mmol/g, which is comparable to the carboxyl group content of oxidized cellulose (0.4–1.4 mmol/g) as described in literature.<sup>[83,183]</sup> Meanwhile, the content of free amine groups drops from 0.4 mmol/g to not detectable, which is also consistent with the removal of protein under the applied oxidation condition. Furthermore, despite the conversion of primary hydroxyl groups to carboxyl groups, the content

of hydroxyl groups (0.8 mmol/g BSG, 1.2 mmol/g OBSG) and lactone groups (0.2 mmol/g BSG, 0.7 mmol/g OBSG) increase after oxidation. It is speculated that the overall changes in material composition, such as the removal of proteins, lead to an increase in oxygen-containing functional groups. In particular, the increase in the number of carboxyl groups has a great benefit on the adsorption of uranium.

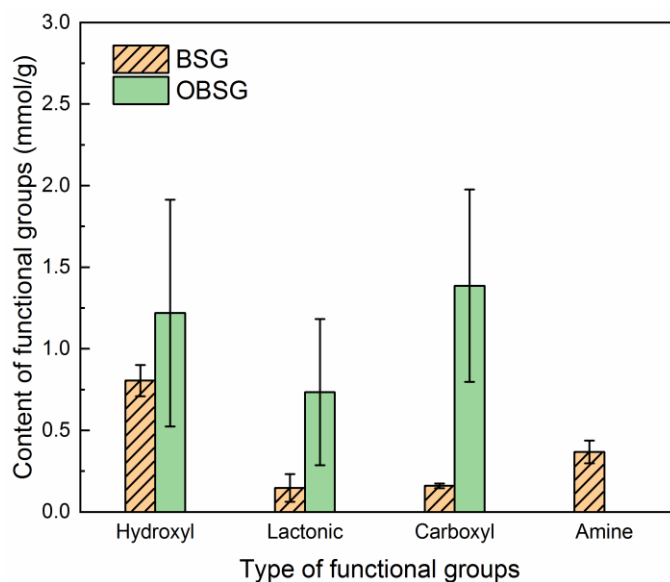


**Fig. 4.5.** Content of functional groups of BSG and OBSG.

#### 4.2.3. Thermogravimetric analysis

To explore the thermal degradation properties of the adsorbents, thermogravimetric (TG) analysis was employed for BSG and OBSG (Fig. 4.6), and a four-step decomposition of both BSG and OBSG is observed. Both samples display a maximum decomposition temperature (DTG peak) at 106 °C, and the mass loss between 40 and 162 °C of 3.0 wt% (BSG) and 3.6 wt% (OBSG) stems from the evaporation of water. The onset temperature is 276 °C for BSG following a second step from 162 to 358 °C with a DTG peak at 320 °C. A mass loss of 40.4 wt% of BSG is due to the decomposition of protein, degradation of hemicellulose (from 220 °C) and cellulose (from 310 °C).<sup>[184]</sup> In addition, lignin is also gradually decomposed over a wide temperature range from 180 to 550 °C.<sup>[185]</sup> Further decomposition of hemicellulose, cellulose and lignin results in a DTG peak at 383 °C for the third step. The fourth step occurs when the temperature exceeds 439 °C associated with the decomposition of lignin and the carbonation process,<sup>[186]</sup> yielding a residue of 21.7 wt%. In contrast, OBSG has a somewhat lower onset temperature of 223 °C, which probably results from the increase in

anhydroglucuronic acid units on its surface with lower thermal stability.<sup>[187]</sup> The earlier degradation of oxidized cellulose also shifts the second step of OBSG to a lower temperature range (162–321 °C) with a DTG peak at 278 °C. In addition, the third step is shifted to a slightly lower temperature (DTG peak at 336 °C) because of the acid hydrolysis and mass loss of lignin and hemicellulose.<sup>[135]</sup> Although the thermal stability of OBSG at the early heating stage is lower than that of BSG, its residual mass after decomposition is higher (30.1 wt%) owing to the formation of carbonaceous layers on the surface of OBSG that delays its thermal decomposition.<sup>[188]</sup>

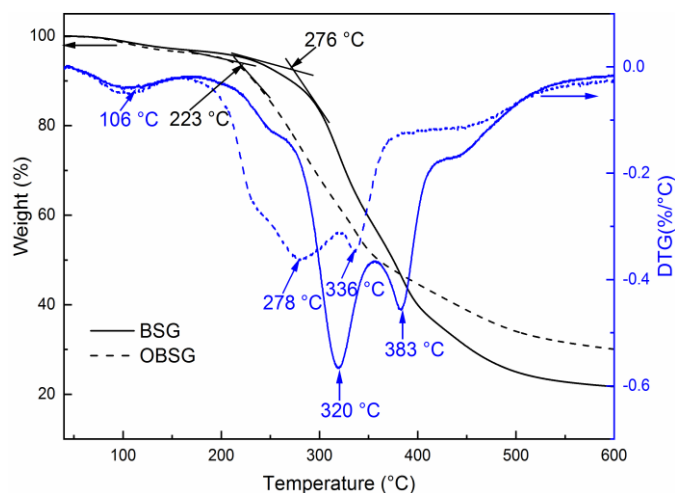


**Fig. 4.6.** TG and DTG of BSG and OBSG (20°C/min, He atmosphere).



### 4.3. Batch adsorption experiments

#### 4.3.1. Effect of pH value

The pH of the metal solution is a crucial factor for adsorption, as it determines the surface properties of the adsorbent and the speciation of the metal ions. The effect of initial pH on the U(VI) adsorption capacity of OBSG is depicted in Fig. 4.7, a, and the determination of the point of zero charge ( $\text{pH}_{\text{PZC}}$ ) is shown in Fig. 4.7, b. Visual MINTEQ 3.1 software<sup>[14]</sup> was used to calculate the species distribution of uranyl acetate solution that contains 300 mg/L U(VI) (=1.26 mM) as a function of pH. As shown in Fig. 4.8, when the pH value rises above 5, the saturation index of  $\text{UO}_2(\text{OH})_2$  is  $> 0$ , indicating a supersaturated solution and possible precipitation of  $\text{UO}_2(\text{OH})_2$ . Therefore, the pH range of 1–5 was employed for pH dependency experiments to prevent the precipitation. In addition, the equilibrium pH is not equal to the initial pH of the uranium solution when there is no pH-buffer in the current adsorption system. This is because of the  $\text{H}^+$  release from the carboxyl groups of OBSG upon the coordination of U(VI).<sup>[189]</sup> Both initial and equilibrium pH are given in Table 4.4. The adsorption capacity of OBSG for U(VI) increases from 3 mg/g to 163 mg/g as the pH values of the metal solution increase from 1 to 5 (Fig. 4.7, a). The electrostatic repulsion between the positively charged adsorbent surfaces and  $\text{UO}_2^{2+}$  species leads to a low adsorption capacity when the pH of metal solution  $< \text{pH}_{\text{PZC}}$  of OBSG ( $\text{pH} < 2.1$ ).<sup>[190]</sup> When the equilibrium pH rises over the  $\text{pH}_{\text{PZC}}$ , the surface charge of OBSG becomes negative due to the deprotonation of carboxyl groups, causing strong electrostatic attraction towards  $\text{UO}_2^{2+}$ . In addition, the strongly negative-charged surface of OBSG prevents the aggregation of OBSG particles, providing more opportunities for the interaction between  $\text{UO}_2^{2+}$  and the surface functional groups. Meanwhile, the species of uranyl ions in solution have changed from predominant  $\text{UO}_2^{2+}$  ( $\text{pH} < 3$ ) to hydrolyzed species such as  $(\text{UO}_2)_2(\text{OH})_2^{2+}$ ,  $\text{UO}_2\text{OH}^+$  and  $(\text{UO}_2)_3(\text{OH})_5^+$  coexisting with  $\text{UO}_2^{2+}$  ( $\text{pH} = 3\text{--}5$ ) as shown in Fig. 4.8.<sup>[153]</sup> In general, the solid surface has a higher affinity towards the hydrolyzed species  $(\text{UO}_2)_2(\text{OH})_2^{2+}$  than  $\text{UO}_2^{2+}$  despite the same charge.<sup>[190,191]</sup> Although the monocationic species  $\text{UO}_2\text{OH}^+$  and  $(\text{UO}_2)_3(\text{OH})_5^+$  have a reduced electrostatic effect due to their low charge, the ion-exchange ratio between the carboxyl groups and the uranyl species decreases from 2:1 to 1:1. Thus, more functional groups are available for interactions towards uranyl ions in the adsorption process. As a result, a considerable adsorption capacity ( $>30$  mg/g) of U(VI) is achieved for an initial pH higher than 2.

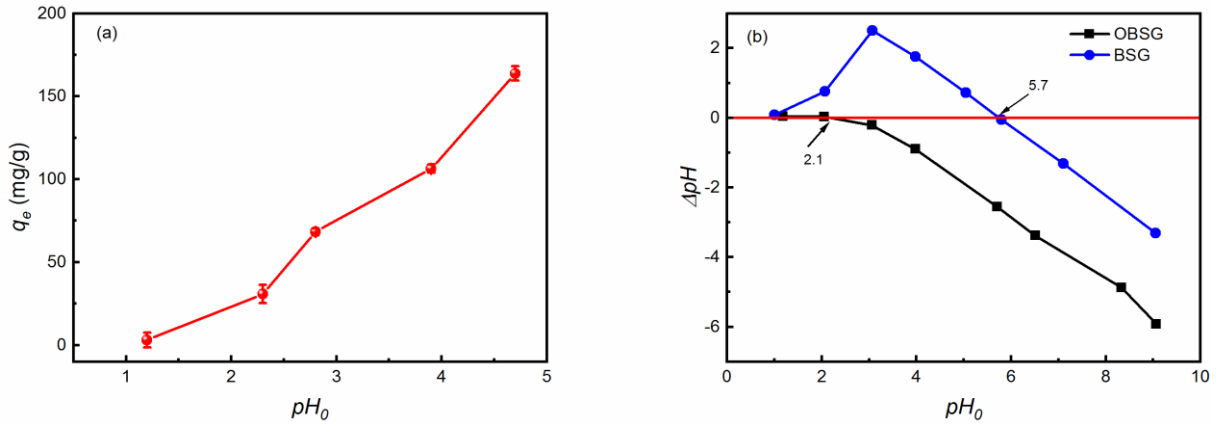


**Fig. 4.7.** (a) Effect of initial pH on the adsorption capacity. For adsorption, 2 mg adsorbent/ 2 mL solution,  $c_0(\text{U}) = 300 \text{ mg/L}$ , 1 h, room temperature, (b) determination of  $\text{pH}_{\text{pzc}}$  of BSG and OBSG.

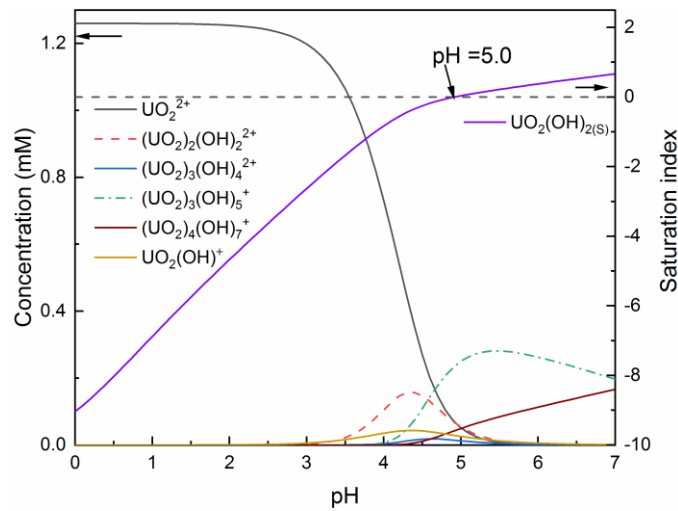


**Fig. 4.8.** Distribution diagram of uranyl acetate solution. For input data,  $c_0(\text{U}) = 300 \text{ mg/L} = 1.26 \text{ mM}$ ,  $c(\text{CH}_3\text{COO}^-) = 2.52 \text{ mM}$ , alkalinity: no specification,  $\text{pH} = 0-7.0$ , increment = 0.1, calculated by Visual MINTEQ 3.1.<sup>[14]</sup>

**Table 4.4.** Comparison of pH value of uranyl ions solution before and after adsorption.

Experiment Number	pH (before)	pH (after)
1	4.7	4.2
2	3.9	3.2
3	2.8	2.7
4	2.3	2.3
5	1.2	1.3

### 4.3.2. Adsorption kinetics

Adsorption dynamics generally consists of three steps, namely external diffusion, internal diffusion and adsorption of adsorbates on the active sites of the adsorbent.<sup>[192]</sup> Herein, the effect of contact time on the adsorption of U(VI) onto OBSG is recorded to study the adsorption kinetics (Fig. 4.9, a). At the early stage (0–30 min), the amount of U(VI) adsorbed onto OBSG increases rapidly due to the large concentration gradient between liquid and solid phase and the large number of vacant adsorption sites on the adsorbent surface.<sup>[193]</sup> After 30 minutes, the concentration gradient decreases as the adsorption sites are occupied, and the adsorption rate slows down and reaches equilibrium at 60 min with an adsorption amount of 159.5 mg/g. In addition, non-linear fits of pseudo-first order (equation (22), see Section 10.5.1) and pseudo-second order (equation (24), see Section 10.5.1) kinetic models were used to describe the diffusion step and the adsorption at active sites, respectively.<sup>[194]</sup> Several statistical parameters ( $R^2$  (coefficient of determination), RSS (Residual Sum of Squares) and  $\chi^2$  (Reduce Chi-square))<sup>[194]</sup> and well-known statistical methods (F test, Akaike's Information Criterion (AIC) and Bayesian Information Criteria (BIC) test)<sup>[195]</sup> were applied to evaluate the performance of the kinetic models. The fitting results and kinetic parameters are summarized in Table 4.5, and the detailed statistical evaluations are given in Table 4.6. Better results in terms of statistical parameters (smaller  $R^2$ ,  $RSS$ ,  $\chi^2$ ) and the estimation of equilibrium adsorption capacity ( $q_{e,cal1}$  of 160.0 mg/g compared with  $q_{e,cal2}$  of 184.6 mg/g) are obtained for the pseudo-first order kinetic than pseudo-second order kinetic model. All three statistical methods (AIC, BIC and F test) favor the pseudo-first order kinetic model as the best result (Table 4.6). All the results indicate that the adsorption dynamics is controlled by the diffusion step.<sup>[196]</sup> To figure out exactly which diffusion step controls the adsorption process, intraparticle diffusion model (equation (26), see Section 10.5.1) was also applied using piecewise linear regression (Fig. 4.9, b).<sup>[195]</sup> If the adsorption process is governed by the intraparticle diffusion, the plot of  $q_t$  versus  $t^{0.5}$  would be linear and pass through the origin.<sup>[195]</sup> However, the plot is not linear and does not pass through the origin, but could be divided into two linear regions with a breakpoint of  $t^{0.5} = 4.8 \text{ min}^{0.5}$  (Fig. 4.9, b). This shows that adsorption rate is probably controlled by the film diffusion in the early stage and then gradually governed by the intraparticle diffusion.<sup>[197]</sup> However, because OBSG is a non-porous material, intraparticle diffusion is expected to have little effect on the adsorption rate. The smaller  $k_{i2}$  value (2.6586) compared to the first linear region ( $k_{i1} = 33.6488$ ) and the slow increase in adsorption after the breakpoint confirm this finding.

**Table 4.5.** Parameters of kinetic models. For adsorption, 2 mg OBSG/ 2 mL solution,  $c_0(U) = 300$  mg/L, pH = 4.7, rotation speed = 60 rpm, room temperature.

Pseudo-first order kinetic model	$k_1$ ( $\text{min}^{-1}$ )	$q_{e,exp}$ (mg/g)	$q_{e,calc1}$ (mg/g)	$R^2$	RSS	$\chi^2$
	0.0962	159.5	160.0	0.9994	3.07	0.51
Pseudo-second order kinetic model	$k_2$ ( $\text{g} \cdot \text{mg}^{-1} \cdot \text{min}^{-1}$ )	$q_{e,exp}$ (mg/g)	$q_{e,calc2}$ (mg/g)	$R^2$	RSS	$\chi^2$
	0.0006	159.5	184.6	0.9941	29.92	4.99

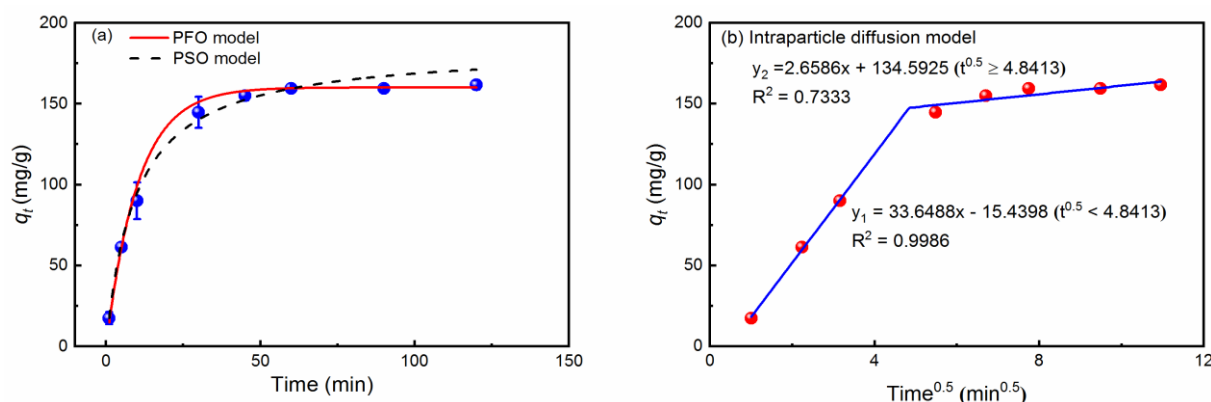


**Fig. 4.9.** (a) Adsorption kinetics of U(VI) onto OBSG and non-linear fitting of pseudo-first order (PFO) and pseudo-second order (PSO) kinetic model. For adsorption, 2 mg OBSG/ 2 mL solution,  $c_0(U) = 300$  mg/L, pH = 4.7, rotation speed = 60 rpm, room temperature, (b) piecewise linear regression of the intraparticle diffusion model.

**Table 4.6.** Results of statistical methods using for comparing pseudo-first order and pseudo-second order kinetic model (rotation speed = 60 rpm).

Preferred model	Model Name				
AIC	Pseudo-first order kinetic model				
BIC	Pseudo-first order kinetic model				
F-Test	Pseudo-first order kinetic model				
Akaike Information Criterion (AIC)	RSS	$N^a$	$p^b$	AIC	Akaike's weights
Pseudo-first order kinetic model	3.0747	8	2	4.3501	0.9999
Pseudo-second order kinetic model	29.9194	8	2	22.5525	0.0001
Bayesian Information Criteria (BIC) test	RSS	$N$	$p$	BIC	$\Delta BIC$
Pseudo-first order kinetic model	3.0747	8	2	-1.4116	0
Pseudo-second order kinetic model	29.9194	8	2	16.7909	18.2025
F-Test	RSS	$DF^c$	$F$	Prob > F	
Pseudo-first order kinetic model	3.0747	6	0.1028	0.9930	
Pseudo-second order kinetic model	29.9194	6			

a). Number of data points, b) number of parameters, and c) degree of freedom.

Since the film diffusion is considered the main rate-controlling step of the adsorption process, additional kinetic studies were performed to reduce this effect and increase the adsorption rate by increasing the rotational speed. When the rotation speed increases from 60 rpm to 80 rpm,

the adsorption of U(VI) on OBSG slightly increases in the first 10 min (Fig. 4.10, a). Furthermore, the kinetics data at 80 rpm are fitted with the kinetic models (Fig. 4.10, b), and the fitting results and statistical parameters are provided in Table 4.7 and Table 4.8, respectively. The analysis shows that the pseudo-second-order kinetic model can better represent the data at 80 rpm. This may suggest that as the rotational speed increases, the rate-controlling step of adsorption may change from film diffusion to adsorption on active sites.<sup>[196]</sup> However, for both rotation speeds, the adsorption process requires 60 min to reach the adsorption equilibrium, and the obtained difference in the adsorption capacity (159.5 mg/g for 60 rpm and 167 mg/g for 80 rpm) is within 5%. Since the overall adsorption kinetics did not improve significantly after increasing the rotational speed, 60 rpm was chosen for the following experiments.

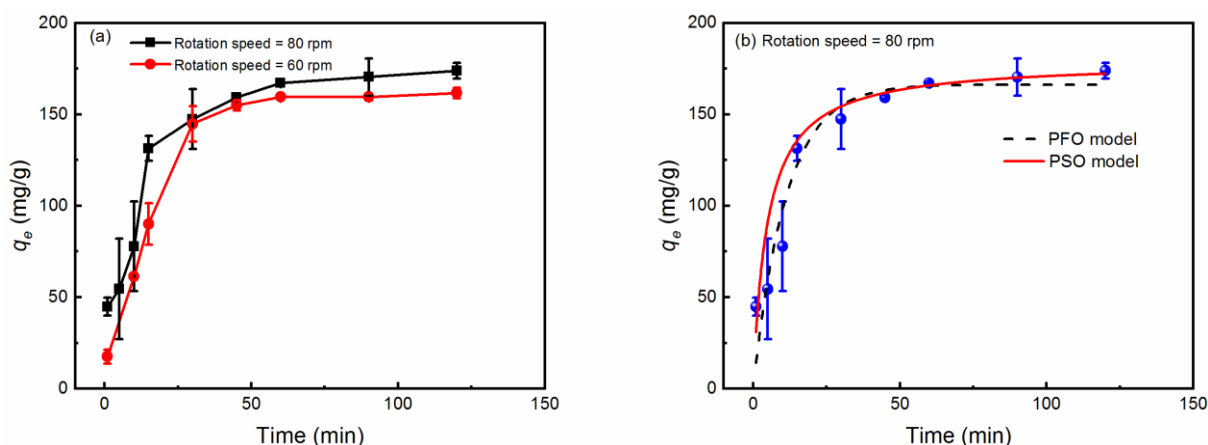


**Fig. 4.10.** (a) Effect of rotation speed on the adsorption kinetics. For adsorption, 2 mg OBSG/ 2 mL solution,  $c_0(\text{U}) = 300 \text{ mg/L}$ ,  $\text{pH} = 4.7$ , room temperature, and (b) non-linear fitting of pseudo-first order (PFO) and pseudo-second order (PSO) kinetic model of the kinetic data for rotation speed = 80 rpm.

**Table 4.7.** Parameters of kinetic models at higher rotation speed. For adsorption, 2 mg OBSG/ 2 mL solution,  $c_0(\text{U}) = 300 \text{ mg/L}$ ,  $\text{pH} = 4.7$ , rotation speed = 80 rpm, room temperature.

Pseudo-first order kinetic model	$k_1 \text{ (min}^{-1}\text{)}$	$q_{e,exp}$ (mg/g)	$q_{e,cal1}$ (mg/g)	$R^2$	RSS	$\chi^2$
	0.0888	167.0	166.2	0.9107	60.0	8.6
Pseudo-second order kinetic model	$k_2 \text{ (g} \cdot \text{mg}^{-1} \cdot \text{min}^{-1}\text{)}$	$q_{e,exp}$ (mg/g)	$q_{e,cal2}$ (mg/g)	$R^2$	RSS	$\chi^2$
	0.0012	167.0	179.0	0.9692	20.7	3.0

**Table 4.8.** Results of statistical methods using for comparing pseudo-first order and pseudo-second order kinetic model (rotation speed = 80 rpm).

Preferred model	Model Name				
AIC	Pseudo-second order kinetic model				
BIC	Pseudo-second order kinetic model				
F-Test	Pseudo-second order kinetic model				
Akaike Information Criterion (AIC)	<i>RSS</i>	<i>N<sup>a</sup></i>	<i>p<sup>b</sup></i>	<i>AIC</i>	<i>Akaike's weight</i>
Pseudo-first order kinetic model	60.0214	9	2	27.8759	0.0082
Pseudo-second order kinetic model	20.6690	9	2	18.2827	0.9918
Bayesian Information Criteria (BIC) test	<i>RSS</i>	<i>N</i>	<i>p</i>	<i>BIC</i>	$\Delta BIC$
Pseudo-first order kinetic model	60.0214	9	2	23.6676	9.5932
Pseudo-second order kinetic model	20.6690	9	2	14.0744	0
F-Test	<i>RSS</i>	<i>DF<sup>c</sup></i>		<i>F</i>	Prob > F
Pseudo-first order kinetic model	60.0214	7		2.9039	0.0915
Pseudo-second order kinetic model	20.6690	7			

a). Number of data points, b) number of parameters, and c) degree of freedom.

### 4.3.3. Adsorption isotherm

The effect of initial metal concentration on the adsorption capacity of OBSG is depicted in Fig. 4.11, a. The Langmuir model (equation (31), see Section 10.5.3), Freundlich model (equation (34), see Section 10.5.3) and Redlich-Peterson (R-P) model (equation (36), see Section 10.5.3) are used to fit the data considering standard deviations.<sup>[156]</sup> The fit results and isotherm parameters in Table 4.9 show that the Langmuir model with the lowest  $R^2$  (0.9739) and the highest error functions ( $RSS = 249$  and  $\chi^2 = 27.7$ ) provides the worst fit. In contrast, both Freundlich model and the R-P model show good fitting results ( $R^2 > 0.99$ ) with very similar the statistical parameters (Table 4.9) and overlapping simulated curves (see Fig. 4.11, a). This is explained by the fact that the R-P model can be approximated as Freundlich model when  $a_{RC}e^{\beta} \gg 1$  ( $a_{RC}e^{\beta} = 8-54$  in current case) as described in the literature.<sup>[198]</sup> Thus, F test, AIC and BIC test were performed to compare the complex (R-P model) and the simple model (Freundlich model) to avoid over parameterization. The results presented in Table 4.10 suggest that the R-P model is not inherently better than the Freundlich model, and therefore the simpler Freundlich model should be used to describe the adsorption isotherm, which indicates that the adsorption of U(VI) onto OBSG is a multi-layer adsorption on a heterogeneous surface.<sup>[199]</sup>

**Table 4.9.** Parameters and nonlinear fitting results of isotherm models. For adsorption: 2 mg OBSG/ 2 mL solution,  $c_0(\text{U}) = 50\text{--}900 \text{ mg/L}$   $t = 1 \text{ h}$ ,  $\text{pH} = 4.6\text{--}4.7$ , room temperature.

Langmuir model	$q_{max} \text{ (mg/g)}$	$k_L \text{ (L/mg)}$	$R^2$	$RSS$	$\chi^2$	
	308.7	0.0154	0.9739	249	27.7	
Freundlich model	$k_F \text{ ((mg/g) (L/mg)}^{1/n})$	$n$	$R^2$	$RSS$	$\chi^2$	
	25.0	2.6	0.9955	42	4.73	
R-P model	$k_R \text{ (L/g)}$	$a_R \text{ (L}^\beta/\text{mg}^\beta)$	$\beta$	$R^2$	$RSS$	$\chi^2$
	21.9	0.6	0.67	0.9960	38	4.74

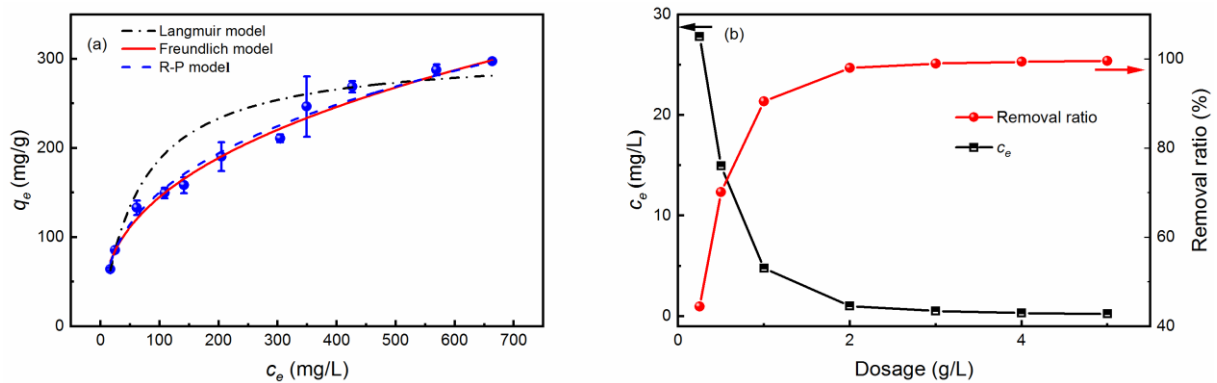


**Fig. 4.11.** (a) Adsorption isotherm of U(VI) onto OBSG and nonlinear fitting curves of Langmuir model, Freundlich model and R-P model. For adsorption: 2 mg OBSG/ 2 mL solution,  $t = 1 \text{ h}$ ,  $\text{pH} = 4.6\text{--}4.7$ , room temperature, and (b) a calculation of the equilibrium concentration ( $c_e$ ,  $\mu\text{g/L}$ ) and removal ratio (%) using a given initial U(VI) concentration of  $50 \mu\text{g/L}$  according to the Freundlich model determined in Fig. 4.11, a.

**Table 4.10.** Results of statistical methods using for comparing R-P model and Freundlich model.

Preferred model	Model Name				
AIC	Freundlich model				
BIC	Inconclusive				
F-Test	Freundlich model				
Akaike Information Criterion (AIC)	$RSS$	$N^a$	$p^b$	$AIC$	$Akaike's \text{ weight}$
Freundlich model	42.5480	11	2	24.3087	0.8790
R-P model	37.9033	11	3	28.2752	0.1210
Bayesian Information Criteria (BIC) test	$RSS$	$N$	$p$	$BIC$	$\Delta BIC$
Freundlich model	42.5480	11	2	22.0738	0
R-P model	37.9033	11	3	23.2001	1.1264
F-Test	$F$	$df_1\text{--}df_2^c$	$df_2$	Prob > F	
	0.9803	1	8	0.3511	

a). Number of data points, b) number of parameters, and c) degree of freedom.

The OBSG shows a highest adsorption capacity for U(VI) of  $297.3 \text{ mg/g}$  ( $c_0(\text{U}) = 900 \text{ mg/L}$ ) from the current isotherm, which is 210% higher compared to the unmodified BSG

(96 mg/g).<sup>[200]</sup> This is also higher compared to the biosorbents and synthetic adsorbents reported in literature (see Table 4.11), e.g. hydrochar (67 mg/g),<sup>[75]</sup> ion-imprinted resin based on carboxymethyl cellulose (U-CMC-SAL, 180 mg/g),<sup>[201]</sup> and cellulose nanofibers (167 mg/g).<sup>[83]</sup> Although some adsorbents like chitosan derived adsorbent (CTPP)<sup>[202]</sup> and graphene oxide derived adsorbent (CoFe<sub>2</sub>O<sub>4</sub>-rGO)<sup>[166]</sup> show a close adsorption capacity (> 220 mg/g) compared to OBSG, they usually take longer time to reach adsorption equilibrium (72 h for CTPP and 3 h CoFe<sub>2</sub>O<sub>4</sub>-rGO). In contrast, OBSG shows fast adsorption kinetics of only 1 h. In practical application, the U(VI)-trace concentration is usually in the µg/L range rather than the mg/L range when decontaminating uranium from wastewater and natural waters.<sup>[11]</sup> Therefore, a calculation of the equilibrium concentration ( $c_e$ , µg/L) and removal ratio (%) was performed according to the Freundlich isotherm (determined in Fig. 4.11, a), where the initial U(VI) concentration is 50 µg/L and the adsorbent dosage ranges from 0.25 g/L to 5 g/L. An equilibrium U(VI) concentration of lower than 1 µg/L with a removal ratio of 98% is obtained by an adsorbent dosage of 2 g/L (Fig. 4.11, b). Further increasing the adsorbent dosage to more than 2 g/L would result in removal rates above 99%, indicating the great potential of OBSG as a cost-effective and sustainable alternative to synthetic adsorbents for uranium removal in the real aqueous environment.

**Table 4.11.** Summary of the adsorption capacity of U(VI) onto different adsorbents.

Adsorbent	$q_{max}$ (mg/g)	Conditions	Reference
BSG	96	$m = 2$ mg, $V = 2$ mL, $t = 2$ h, pH = 4.7, $c_0(\text{U}) =$ 100–1000 mg/L, room temperature	[200]
ABSG	220	$m = 2$ mg, $V = 2$ mL, $t = 1$ h, pH = 4.7, $c_0(\text{U}) =$ 100–1000 mg/L, room temperature	[200]
OBSG	297.3	$m = 2$ mg, $V = 2$ mL, $t = 1$ h, pH = 4.6–4.7, $c_0(\text{U}) = 50$ –900 mg/L, room temperature	This study
Cellulose nanofibers	167	0.05 wt%, $t = 2$ h, pH = 6.5 ± 0.5, $c_0(\text{U}) = 80$ – 1530 ppm	[83]
U-CMC-SAL	180	$m = 0.03$ g, $V = 30$ mL, $t = 3$ h, pH = 5.0, $c_0(\text{U}) = 10$ –400 mg/L, $T = 30$ °C	[201]
CoFe <sub>2</sub> O <sub>4</sub> -rGO	227	$m = 0.02$ g, $V = 50$ mL, $t = 3$ h, pH = 6.0, $T =$ 25 °C	[166]
CTPP	237	$m = 50$ mg, $V = 50$ mL, $t = 72$ h, pH = 5.0, $c_0(\text{U}) = 100$ –2000 mg/L, $T = 25 ± 0.5$ °C	[202]
hydrochar	67	$m = 0.01$ g, $V = 50$ mL, $t = 50$ min, pH = 6.0, $c_0(\text{U}) = 10$ –120 mg/L, $T = 25$ °C	[75]



#### 4.3.4. Effect of temperature

Adsorption isotherms at 25, 35, 45 and 65 °C were recorded (Fig. 4.12, a) in order to study the effect of the temperature on U(VI) adsorption. The results show that the elevated temperature favors the adsorption of U(VI) on OBSG. For example, at an initial concentration of 500 mg/L, increasing the temperature from 25 °C to 65 °C results in an increase in adsorption capacity from 195.3 mg/g to 280.9 mg/g, which is due to an increase in available active sites on the swollen OBSG as the temperature increases.<sup>[203]</sup> However, the adsorption isotherms show obvious decrease in the amount of U(VI) adsorbed on OBSG in the presence of 0.1 M NaClO<sub>4</sub> as the supporting electrolyte (Fig. 4.12, b). This is probably because the supporting electrolyte would reduce the swelling of OBSG, which has already reported for lignocellulose materials (kraft-liner pulps).<sup>[204]</sup> Therefore, elevated temperature no longer promotes the increase in available active sites originated from the enhanced OBSG swelling, and temperature dependence of the adsorption capacity is no longer observed.

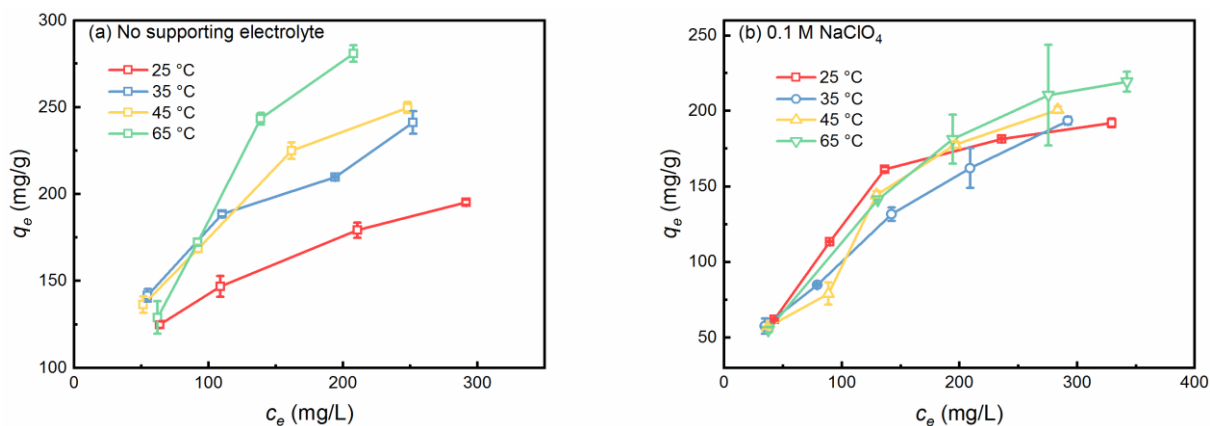


**Fig. 4.12.** Adsorption isotherms of U(VI) onto OBSG at different temperature (a) without supporting electrolyte and (b) with 0.1 M NaClO<sub>4</sub>. For adsorption: 2 mg OBSG/ 2 mL solution,  $c_0(\text{U}) = 100\text{--}500$  mg/L,  $t = 1$  h,  $\text{pH} = 4.7$ , temperature = 25–65 °C, stirrer speed = 180 rpm.

#### 4.4. Investigation of adsorption mechanism

Oxidation does not affect the specific surface area of the biosorbents, as the determined BET surface area of BSG and OBSG are less than  $2 \text{ m}^2/\text{g}$ , which is consistent with the BET surface area of BSG reported in the literature ( $0.48 \text{ m}^2/\text{g}$ ).<sup>[169]</sup> Fig. 4.13 shows the surface morphology of OBSG and the distribution of uranium on OBSG obtained from the SEM-EDX analysis. The rough surface and irregular shape of OBSG with no obvious pore structure are observed (Fig. 4.13, a). Thus, the adsorption of U(VI) should mainly occur on the surface of OBSG since it is non-porous. In addition, the even distribution of uranium on the OBSG surface (Fig. 4.13, b and c) points at numerous carboxyl groups that are equally distributed on the surface of OBSG and strongly interact with the uranyl ions.

FT-TR spectra of OBSG before and after U(VI) adsorption were recorded (Fig. 4.14) to get further information about the interactions between functional groups and the adsorbates and to explore the structure of metal-adsorbent complex. The involvement of carboxyl groups in the adsorption is confirmed by shifts of the antisymmetric and symmetric stretching vibration of  $\text{COO}^-$  from  $1631$  and  $1451 \text{ cm}^{-1}$  (OBSG) to  $1568$  and  $1410 \text{ cm}^{-1}$  (U(VI)-loaded OBSG). According to reports in the literature,<sup>[205]</sup> the complexation model between carboxyl groups and metal ions, namely whether one or both oxygen atoms of the carboxyl groups interact with the metal ions, could be defined by the differences between the antisymmetric and symmetric stretching bands ( $\Delta\nu_{\text{as-vs}}$ ). Typically, a value of  $\Delta\nu_{\text{as-vs}} > 200 \text{ cm}^{-1}$  suggests a monodentate structure, whereas  $\Delta\nu_{\text{as-vs}} < 150 \text{ cm}^{-1}$  indicates a bidentate binding of metal ions by the carboxyl groups. Thus, the calculated  $\Delta\nu_{\text{as-vs}}$  of  $158 \text{ cm}^{-1}$  upon the adsorption of U(VI) suggests a bidentate binding mode. In addition, a new absorption band at  $925 \text{ cm}^{-1}$  associated with the presence of  $\text{U=O}$  vibration appears in the spectrum of U(VI)-loaded OBSG. One possible assignment for this band is the antisymmetric stretching vibration of  $(\text{UO}_2)_3(\text{OH})_5^+$ , because this hydrolyzed species occurs in the current  $\text{pH} = 4.7$  and could be adsorbed onto OBSG.<sup>[171]</sup> Whereas, as reported by Müller et al., this band could also be attributed to  $\text{UO}_2(\text{CH}_3\text{COO})_3^-$ .<sup>[206]</sup> In the present study, interactions with several carboxyl groups to  $\text{UO}_2^{2+}$  or other hydrolyzed species are more likely the reason of the observed absorption band at  $925 \text{ cm}^{-1}$ . On the basis of above studies, the ion-exchange between  $\text{UO}_2^{2+}$  and  $\text{H}^+$  released from carboxyl groups of OBSG via electrostatic effect and bidentate binding of  $\text{UO}_2^{2+}$  with two oxygen atoms of the carboxyl groups are proposed to be the adsorption mechanisms of  $\text{UO}_2^{2+}$  on OBSG.

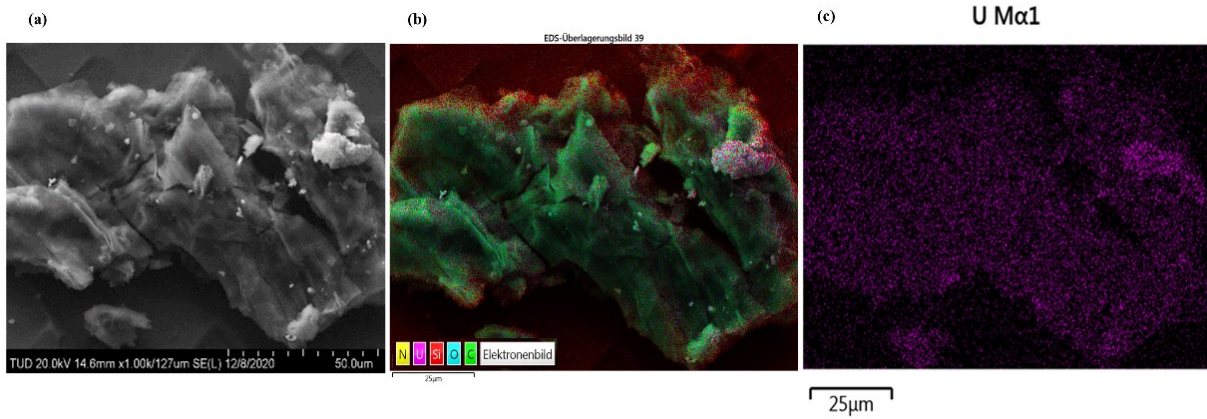


**Fig. 4.13.** (a) SEM image (magnification of 1000 times) of uranyl ions loaded-OB SG, (b) EDX element mapping of uranyl ions loaded-OB SG (20 kV/10  $\mu$ A, magnification of 1000 times, 25 frames) and (c) distribution of uranium on uranyl ions loaded-OB SG. For ion-loading: 50 mg OB SG/ 50 mL solution, pH = 4.7,  $c_0(\text{U}) = 500 \text{ mg/L}$ , 1 h, room temperature.

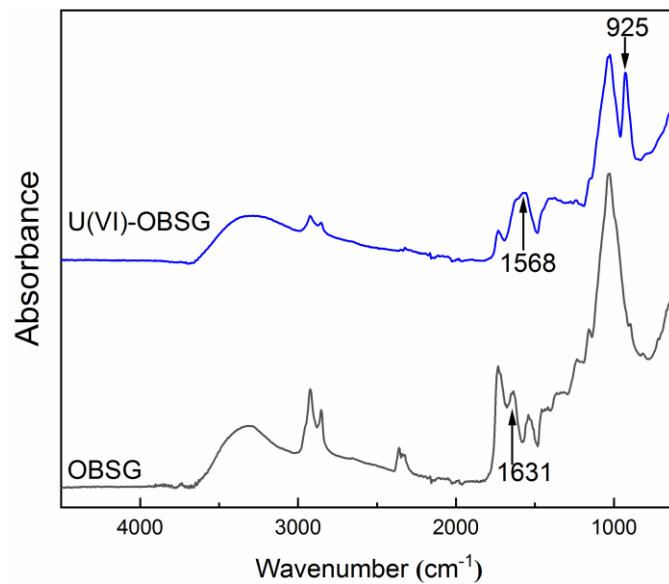


**Fig. 4.14.** FT-IR spectra of OB SG and U(VI) loaded OB SG. For metal loaded: 50 mg OB SG/ 50 mL solution,  $c_0(\text{U}) = 500 \text{ mg/L}$ , pH = 4.7, 1 h, room temperature.

## 4.5. Desorption and reusability

To minimize waste generation and achieve economic benefits for the adsorption process, the adsorbents must have excellent desorption properties and can be reused. In the present study, 0.5 M HCl is used as desorption and regeneration agent for U(VI)-loaded OBSG, and the adsorption capacity ( $q_e$ , mg/g) and desorption ratio ( $D_e$ , %) for 5 cycles are shown in Fig. 4.15. During the reuse cycles, the adsorption capacity of OBSG towards U(VI) decreases gradually from 167.4 mg/g of new-prepared OBSG to 100.3 mg/g after 5 times of regeneration. Possible reasons for this include the hydrolysis of the biomass under strong acidic conditions and the loss of some surface functional groups.<sup>[207]</sup> Meanwhile, a good recovery of U(VI) could be realized, indicated by that the desorption ratio that increases after the first cycle and reaches nearly 90% after the third cycle. OBSG preserves a good adsorption capacity (60% of the original adsorption capacity) with a desorption ratio of 89% after 5 cycles despite the decreased adsorption capacity. Therefore, OBSG can be used for multiple cycles, further reducing cost and waste generation of the decontamination process.

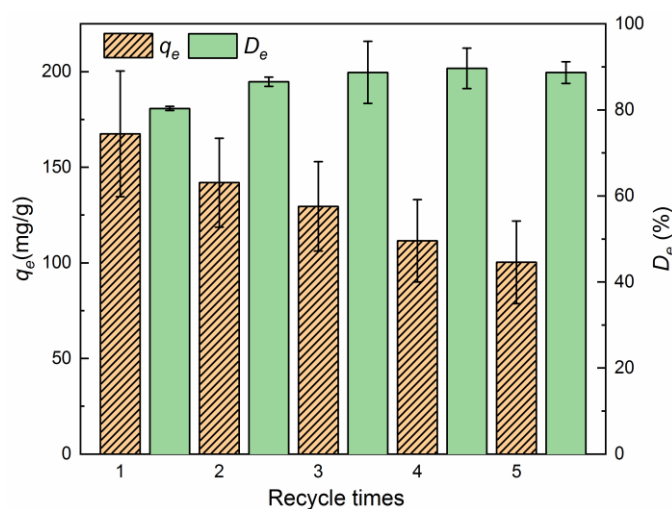


**Fig. 4.15.** Adsorption capacity and desorption ratio of U(VI) onto OBSG during adsorption-desorption cycles. For adsorption, 1 mg OBSG/ mL solution,  $c_0(\text{U}) = 300$  mg/L, pH = 4.7, 1 h, room temperature. For desorption, 5 mg U(VI)-OBSG/ mL 0.5 M HCl, 2 h, room temperature.

#### 4.6. Performance at high salinity and under alkaline condition

In order to explore the practical application of OBSG, we have chosen to use pH adjusted simulated seawater as a test-matrix due to its high ionic strength and alkaline condition. The high ionic strength of seawater also allows it to be used as a simulant for some biological fluids, such as extracellular fluid and blood plasma.<sup>[208,209]</sup> As shown in Table 4.12, OBSG presents an adsorption capacity of  $10.8 \pm 0.1$  mg/g ( $c_0(\text{U}) = 10$  mg/L,  $\text{pH}_0 = 7.7$ ) and  $23.8 \pm 0.7$  mg/g ( $c_0(\text{U}) = 30$  mg/L,  $\text{pH}_0 = 7.0$ ) in the simulated seawater, which performs better than some synthetic adsorbents such as pA@Poly(VBC-co-DVB) (14.8 mg/g)<sup>[210]</sup> and IIP polymer (15.3 mg/g)<sup>[211]</sup> at a higher concentration (30 mg/L). Nevertheless, the results are somewhat lower than those of some modified biosorbents reported in literature at a low concentration of 10 mg/L, e.g., functionalized natural cellulose fibers (16 mg/g)<sup>[212]</sup> and SSUP fiber (15.1 mg/g).<sup>[67]</sup> These results show an interesting potential of using OBSG for uranium adsorption at high salinity and under alkaline condition.

**Table 4.12.** Comparison of the U(VI) adsorption capacity in the high salinity and alkaline condition.

Adsorbent	$q_e$ (mg/g)	Conditions	Reference
OBSG	$10.8 \pm 0.1$	$m/V = 0.2$ g/L, $c_0(\text{U}) = 10$ mg/L, 193 mg/L $\text{NaHCO}_3$ , 25.6 g/L $\text{NaCl}$ , $\text{pH}_0 = 7.7$ , $t = 16$ h	This study
OBSG	$23.8 \pm 0.7$	$m/V = 0.2$ g/L, $c_0(\text{U}) = 30$ mg/L, 193 mg/L $\text{NaHCO}_3$ , 25.6 g/L $\text{NaCl}$ , $\text{pH}_0 = 7.0$ , $t = 16$ h	This study
Functionalized natural cellulose fibers	16	$m/V = 0.2$ g/20 mL, $c_0(\text{U}) = 10$ mg/L, $\text{pH}_0 = 8.2$ , $t = 48$ h	[212]
SSUP fiber	15.1	$c_0(\text{U}) = 8$ mg/L, simulated seawater	[67]
pA@Poly(VBC-co-DVB) (beads)	14.8	$c_0(\text{U}) = 50$ mg/L, $\text{pH}_0 = 8$ , in artificial seawater	[210]
IIP polymer	15.3	$c_0(\text{U}) = 200$ mg/L, $\text{pH}_0 = 9$ , with $\text{Na}_2\text{CO}_3$	[211]



## **5. Brewer's spent grain-supported superabsorbent polymer for uranyl ion adsorption**

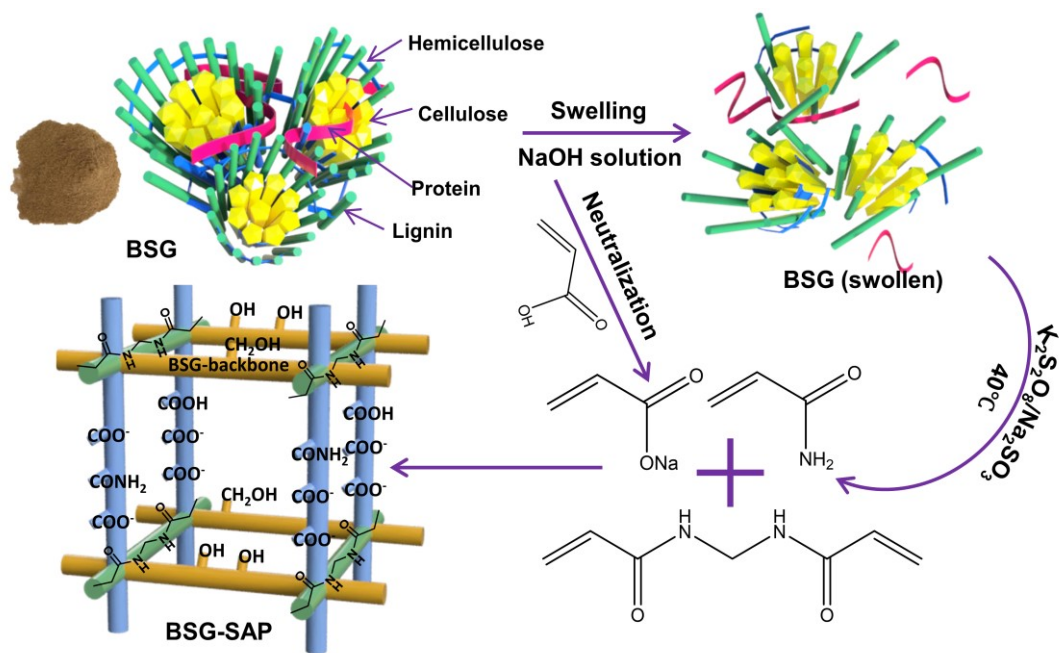
Synthetic polymer adsorbent as a promising solution for uranium removal from wastewater has been widely investigated and is the closest to practical application.<sup>[213]</sup> However, the adsorption capacity and mass transfer of the synthetic polymer adsorbents are limited by the grafting difficulty of functional groups onto its polyolefin-based support and the poor hydrophilicity.<sup>[214,215]</sup> In addition, the synthetic polymer adsorbents are expensive and unsustainable for wastewater decontamination because they require a complex synthetic process and chemicals. Therefore, natural biomass, such as brewer's spent grain (BSG), is considered as a promising alternative to replace the polyolefin-based fibers as the support for polymer adsorbents. However, the accessibility of the reagents to the functional groups on biomass is low because of the complex physical structure, the heterogeneous nature of the cellulose fibers, and the impurities of biomass.<sup>[86]</sup> An extraction process of cellulose to improve its accessibility is almost imperative for graft polymerization employing natural biomass such as wheat straw,<sup>[216]</sup> rice husk,<sup>[217]</sup> and bamboo powder.<sup>[218]</sup> This process is cumbersome, time-consuming, and inefficient due to impurities<sup>[219]</sup> and it produces additional wastewater. As a result, the economic and environmental benefits of using natural biomass are compromised. Therefore, omitting the cellulose extraction process and using untreated biomass directly in the graft polymerization may be a better option to exploit its advantages.

The present study aims to design a BSG-supported superabsorbent polymer (BSG-SAP) to meet the criteria of treating uranium-contaminated water, namely high adsorption capacity, fast kinetics, selectivity, reusability, and suitability to deploy in continuous adsorption systems. The accessibility of BSG is enhanced by swelling the raw material in 7 wt% NaOH solution rather than pre-extracting the cellulose fraction using strong acidic and alkaline condition, providing a scale-up feasible and mild synthetic approach.<sup>[86]</sup> The adsorption capacity and mass transfer are largely promoted by the grafted carboxyl and amide groups and the hydrophilic polymer network of BSG-SAP. Compared with the reference polymers (RP), incorporating BSG leads to the higher adsorption capacity and better reusability of BSG-SAP. Furthermore, adsorption capacity in various conditions and the selectivity of BSG-SAP were investigated in batch experiments, and the reusability was tested in a fixed bed column. In addition, various characterization technologies were used to study the adsorption mechanisms.

## 5.1. Synthesis of brewer's spent grain supported superabsorbent polymer (BSG-SAP)

As illustrated by Scheme 5.1, BSG-SAP is prepared by a one-pot free radical graft polymerization of acrylic acid (AA) and acrylamide (AM) onto the BSG backbone in the presence of cross-linker N,N-methylenebisacrylamide (MBA). Sulfate anion-radicals are generated by the redox initiator system  $K_2S_2O_8$ - $Na_2SO_3$  upon heating at 40 °C, forming radicals on the BSG backbone.<sup>[220]</sup> Then, the active radical sites on BSG would initiate the vinyl groups of AA and AM to develop chains propagation. After adding different amount of MBA, the polymeric chains react synchronously with both end vinyl groups of the cross-linkers (MBA) to develop three-dimensional (3D) polymeric networks with different cross-linking densities.<sup>[221]</sup> Finally, when the chain termination occurs due to the combination of two growing chains, disproportionation and transfer of the propagating radicals, the polymerization stops.<sup>[86]</sup> Traditional graft polymerization process often uses NaOH to neutralize the AA to a desired degree to control the reaction rate and generate polymer chains with a sufficient number of carboxyl groups.<sup>[222]</sup> In the present study, a 7 wt% NaOH solution could swell the BSG to increase its accessibility at first and then neutralize the AA to 75 mol%. Because the cellulose extraction step is omitted, no additional chemicals are required, and the alkaline wastewater is avoided, the synthetic procedure is much simpler. The swelling agent (NaOH solution) improves the accessibility of BSG by removing impurities, penetrating the highly ordered regions of cellulose, and splitting the bonds between chains and fibrils, thereby increasing the degree of disorder in natural fibers.<sup>[86]</sup> The swelling of BSG is expected to also improve the utilization of raw materials and the grafting density of functional groups. Thus, a hydrophilic and cross-linked 3D network with carboxyl and amide groups is obtained, which is beneficial to the adsorption capacity and rate of BSG-SAP.





Scheme 5.1. Proposed mechanism for the synthesis of BSG-SAP.

## 5.2. Characterization of the adsorbents

To investigate the structure changes during the graft polymerization, FT-IR spectra of BSG, monomers (AA and AM), the cross-linker (MBA), BSG-SAP, and the reference polymer (RP) were recorded. Different amounts of cross-linker show no obvious differences in the obtained spectra for both RP (Fig. 5.1, b) and BSG-SAP (Fig. 5.1, c), but the presence of BSG in the polymer results in significant changes (Fig. 5.1, d). Due to the graft polymerization, three absorption bands related to the C=O vibration ( $1664\text{ cm}^{-1}$ ), asymmetric ( $1552\text{ cm}^{-1}$ ) and symmetric ( $1404\text{ cm}^{-1}$ ) vibrations of the  $-\text{COO}^-$  groups occur in the BSG-SAP-L spectrum (Fig. 5.1, d).<sup>[221]</sup> Corresponding absorption bands are observed in the FT-IR spectrum of AA at  $1699\text{ cm}^{-1}$ ,  $1635\text{ cm}^{-1}$ , and  $1411\text{ cm}^{-1}$  (Fig. 5.1, a), showing good consistency. In the BSG-SAP-L spectrum, the stretching vibration of C–O–C moiety from the sugar rings of BSG caused by  $\beta$ -1,4-glycosidic bond disappears at  $1021\text{ cm}^{-1}$ .<sup>[216]</sup> One possible reason is the low BSG/monomer mass ratio (1/16) in the BSG-SAP-L. Another possibility is the oxidative cleavage of C2–C3 bond of the cellulose due to the radical initiated graft polymerization.<sup>[223]</sup> Furthermore, the cleavage of sugar rings may generate a new absorption band at  $1134\text{ cm}^{-1}$  (BSG-SAP-L), which is ascribed to the alkyl ether bonds (C–O–C stretching vibration) of the linear BSG backbone.<sup>[224]</sup> The C–N vibration caused by grafting the amide groups and the presence of cross-linker ( $1120\text{ cm}^{-1}$  for RP-L) may also occur at this position, causing overlap of the two bands.<sup>[225]</sup> In the RP-L spectrum, a new absorption band attributed to the C–OH and O–H coupling interactions of the  $-\text{COOH}$  groups occurs at  $1454\text{ cm}^{-1}$ ,<sup>[226]</sup> which is observed at  $1450\text{ cm}^{-1}$  for BSG-SAP-L and probably overlaps with the aromatic methyl vibration of lignin from BSG.<sup>[227]</sup> All the above results indicate the successful grafting of AA and AM onto the BSG backbone.

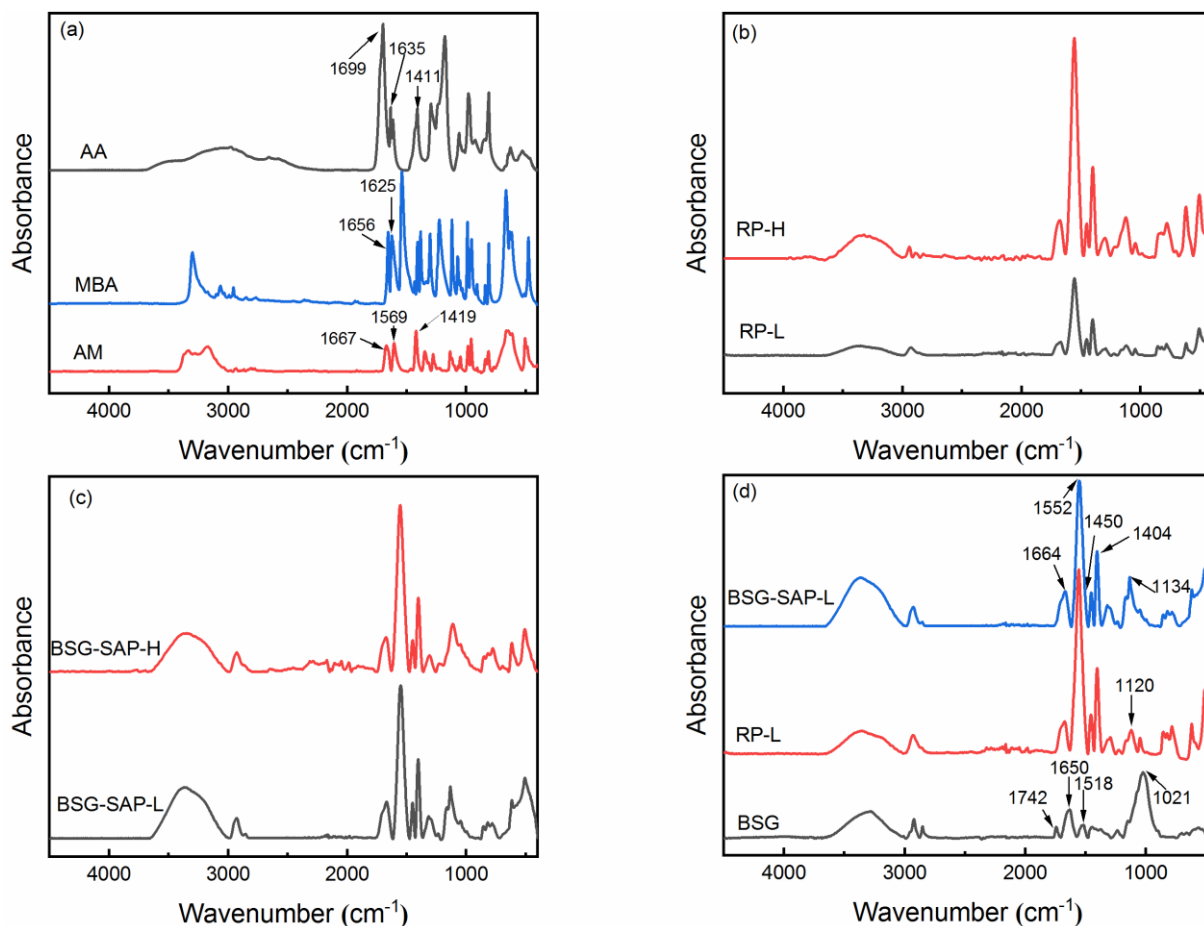


**Fig. 5.1.** FT-IR spectra of (a) acrylic acid (AA), acrylamide (AM) and N,N-methylenebisacrylamide (MBA), (b) reference polymer (RP) with different amount of cross-linker, (c) BSG-SAP with different amount of crosslinker, and (d) BSG, RH-L, and BSG-SAP-L.

To provide further structural information, <sup>13</sup>C solid-state NMR spectra of BSG and BSG-SAP-L are depicted in Fig. 5.2. In the BSG-SAP-L spectrum, no typical resonance of cellulose is observed, namely those at 105 ppm (C1), 84 ppm (C4), 73 ppm (C2, C3, and C5), and 64 ppm (C6) in as compared to a typical BSG spectrum.<sup>[228]</sup> The disruption of the sugar rings during the graft polymerization and the low BSG/monomer mass ratio of the polymer are probably responsible for this change. The aliphatic C at 30 ppm in BSG spectrum also shifts to 45 ppm in BSG-SAP-L spectrum due to graft polymerization. In addition, the resonance associated with carboxyl and carbonyl C shifts from 173 ppm of BSG to 185 ppm with increased intensity,<sup>[228]</sup> which confirms the successful grafting of carboxyl groups. Presumably, the grafting of functional groups and the cross-linked 3D structure of the BSG-SAP contributes to its excellent adsorption capacity and rapid mass transfer.

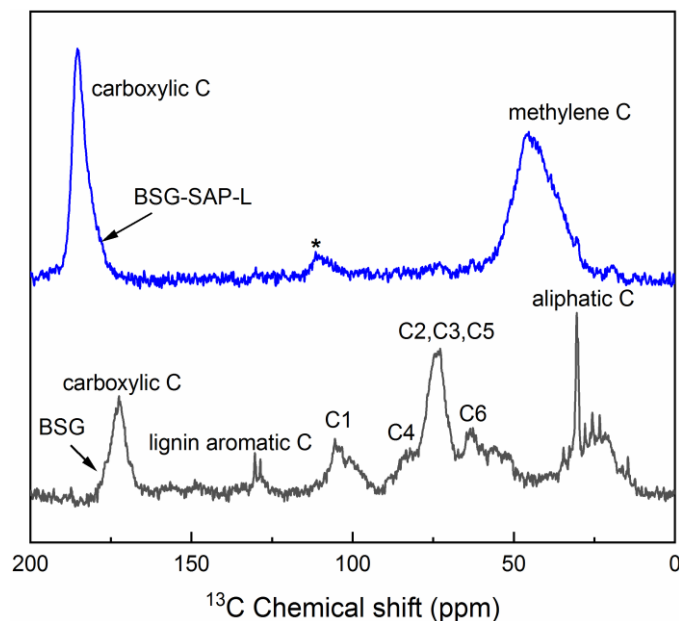


**Fig. 5.2.**  $^{13}\text{C}$  solid-state NMR spectra of BSG and BSG-SAP-L (the spinning sideband is marked with an asterisk).

To investigate the thermal stability of BSG-SAP and reveal the influence of cross-linker amount, thermogravimetric (TG)-differential scanning calorimetry (DSC) analysis of BSG-SAP was performed using a heating rate of  $20\text{ }^{\circ}\text{C}/\text{min}$  under Helium atmosphere. Fig. 5.3 shows three derivative thermogravimetric peaks (DTG peaks, maximum decomposition temperature) for both samples, which is consistent with the SAP reported in the literature.<sup>[216,229]</sup> The extrapolated onset temperature is determined for BSG-SAP-L to be  $287.4\text{ }^{\circ}\text{C}$  and for BSG-SAP-H to be  $324.0\text{ }^{\circ}\text{C}$  according to the standard ISO 11358-1,<sup>[230]</sup> indicating that the highly cross-linked BSG-SAP-H has a better thermal stability at the starting period. Both BSG-SAP show a slow decrease in sample weight before the extrapolated onset temperature, which is attributed to the loss of remaining moisture and volatiles.<sup>[231]</sup> The following DTG peak corresponding to the decomposition of carbohydrates from the BSG backbone occurs at  $365.5\text{ }^{\circ}\text{C}$  for BSG-SAP-L and  $389.5\text{ }^{\circ}\text{C}$  for BSG-SAP-H.<sup>[232]</sup> The second DTG peak at  $447.9\text{ }^{\circ}\text{C}$  (BSG-SAP-L) and  $454.0\text{ }^{\circ}\text{C}$  (BSG-SAP-H) is assigned to the decomposition of amide<sup>[233]</sup> and carboxyl groups.<sup>[231]</sup> Furthermore, the decomposition and carbonation of the polymer chains contribute to the third DTG peak at  $486.0\text{ }^{\circ}\text{C}$  (BSG-SAP-L) and  $488.7\text{ }^{\circ}\text{C}$  (BSG-SAP-H).<sup>[232]</sup> Finally, the residue mass of BSG-SAP-H ( $44.2\text{ wt}\%$ ) is comparable to that of the BSG-SAP-L ( $44.0\text{ wt}\%$ ) with a similar thermal stability at high temperature. In addition, the glass transition temperature ( $T_g$ ) was calculated using the data of TG and DSC curves between  $90\text{--}160\text{ }^{\circ}\text{C}$  according to the ASTM standard (ASTM E 1356-08).<sup>[234]</sup> As shown in Fig. 5.4, a  $T_g$  value of  $114\text{ }^{\circ}\text{C}$  for both BSG-SAP-L and BSG-SAP-H is observed, which is comparable to the values of similar polymers reported in the literature ( $106\text{--}131\text{ }^{\circ}\text{C}$ ).<sup>[235,236]</sup> The value is also higher than the  $T_g$  ( $108\text{ }^{\circ}\text{C}$ )

reported in the literature for the AA and AM copolymers, indicating an effective cross-linking.<sup>[237]</sup> Previous studies have shown that slightly cross-linked polymers (cross-linker ratio < 1 mol%) can give widely varying  $T_g$  values in parallel samples, so no significant correlation between  $T_g$  and cross-linker ratio can be obtained.<sup>[236]</sup> This might explain that BSG-SAP samples with different cross-linker ratios (0.5 and 2 mol%) result in the same  $T_g$  value during the measurement.

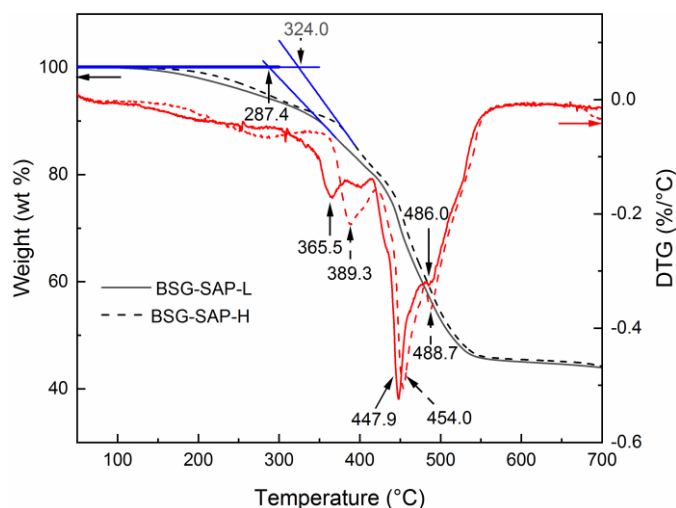


**Fig. 5.3.** TG-DTG curves of BSG-SAP-L and BSG-SAP-H (20 °C/min, He).

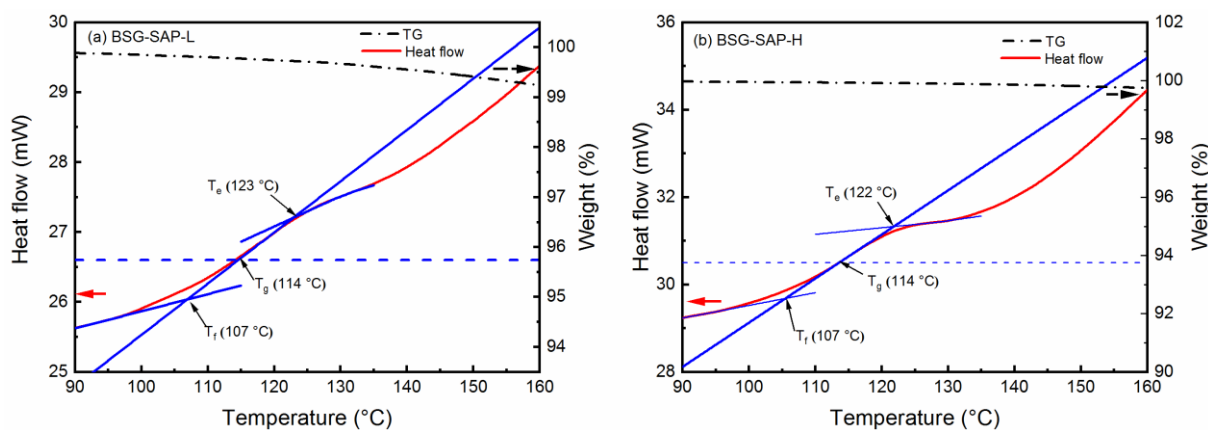


**Fig. 5.4.** DSC and TG curves of (a) BSG-SAP-L and (b) BSG-SAP-H to determine the glass transition temperature ( $T_g$ ). The  $T_e$  is the extrapolated end temperature,  $T_f$  is the extrapolated onset temperature, and the midpoint temperature is reported as the  $T_g$  according to ASTM E1356-08(2014).<sup>[234]</sup>

### 5.3. Comparing properties of BSG-SAP with the reference polymer

Preliminary tests of the graft polymer (BSG-SAP) and the reference polymer without BSG (RP) regarding the adsorption capacity ( $c_0(\text{U}) = 1000 \text{ mg/L}$ ) and reswelling ratio after regeneration are performed to demonstrate the benefits of BSG in the adsorbents as shown in Fig. 5.5. Table 5.1 lists the swelling ratio and the average molecular weight between cross-links ( $\bar{M}_C$ ) of the polymers, whose value is inversely proportional to the cross-linking density.<sup>[238]</sup> BSG-SAP presents a cross-linked polymer network that could hold the water within its structure, which is indicated by high swelling ratios of 104 (BSG-SAP-L) and 64 (BSG-SAP-H) in the ultrapure water (Table 5.1). The high swelling ratio also suggests that the polymer network is strongly hydrophilic due to the presence of functional groups such as hydroxyl, carboxyl, and amide groups,<sup>[239]</sup> which would facilitate mass transfer inside the adsorbent. Compared with the reference polymer, the graft polymer is characterized by the grafting of one or more homopolymer blocks to the backbone as branches, which could form 3D polymer networks with the cross-linkers.<sup>[240]</sup> Therefore, the value of  $\bar{M}_C \times 10^5$  for BSG-SAP-L ( $11 \pm 0.5$ ) is lower than the RP-L ( $54 \pm 0.1$ ), indicating a higher cross-linking density under the same amount of cross-linker. A comparable value of  $\bar{M}_C \times 10^5$  ( $3.2 \pm 0.3$ ) for BSG-SAP-H to RP-H ( $3.8 \pm 0.1$ ) is obtained due to the high cross-linker amount that weakens the influence of BSG. This higher cross-linking density of BSG-SAP-L allows for better reusability of the adsorbent. The reswelling ratios of BSG-SAP-L (53.4 wt%) and BSG-SAP-H (94.4 wt%) are higher than their corresponding reference polymers (31.6 wt% for RP-L and 81.9 wt% for RP-H) after one cycle of adsorption, acid desorption, base regeneration, and reswelling in ultrapure water (Fig. 5.5), which is critical for the reuse of adsorbents in practical application. Furthermore, the adsorption capacity of U(VI) increases from 907 mg/g for RP-L to 960 mg/g for BSG-SAP-L and from 863 mg/g for RP-H to 970 mg/g for BSG-SAP-H (Fig. 5.5). These results provide great motivations to use BSG as a sustainable raw material and to investigate the uranium adsorption behavior of BSG-SAP in detail.

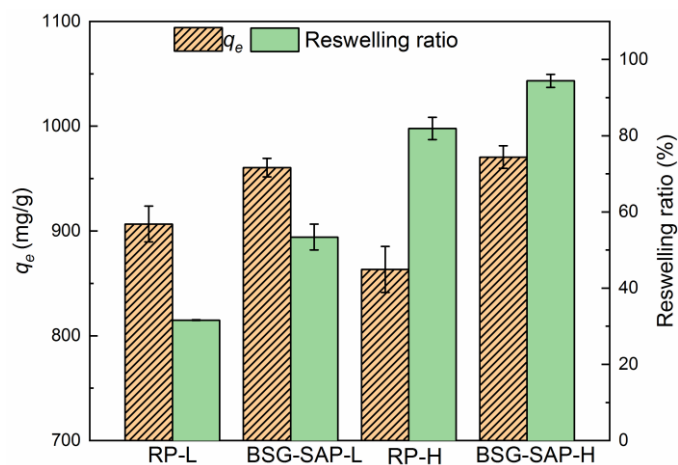


**Fig. 5.5.** Adsorption capacity and reswelling ratio of BSG-SAP and RP. For adsorption, 50 mg adsorbent/50 mL solution,  $c_0(U) = 1000$  mg/L, 45 min,  $pH_0 = 4.6$ , room temperature, for desorption, 50 mL of 0.5 M HCl, 30 min; and for regeneration, 20 mL of 0.1 M NaOH, 10 min.

**Table 5.1.** The average molecular weight between cross-links ( $\bar{M}_c$ ), swelling ratio ( $S$ ) and the polymer density ( $\rho$ ) of BSG-SAP and reference polymer.

	$\bar{M}_c \times 10^5$	Swelling ratio, in ultrapure water ( $S$ )	Swelling ratio, in simulated seawater ( $S$ ) <sup>a</sup>	Polymer density ( $\rho$ , g/cm <sup>3</sup> )
BSG-SAP-L	$11 \pm 0.5$	$104 \pm 2.3$	$19.3 \pm 0.3$	1.3
RP-L	$54 \pm 0.1$	$334 \pm 0.3$		1.1
BSG-SAP-H	$3.2 \pm 0.3$	$64 \pm 3.1$	$15.2 \pm 0.1$	1.3
RP-H	$3.8 \pm 0.1$	$55 \pm 0.9$		1.1

a). Simulated seawater: 25.6 g/L NaCl, 193 mg/L NaHCO<sub>3</sub>,  $pH_0 = 7.0$ , no U(VI).

## 5.4. Batch adsorption experiments

### 5.4.1. Adsorption kinetics

It is essential to study adsorption kinetics before designing the adsorption system, because it provides information on the adsorption rate and the mass transfer mechanism. For the U(VI) adsorption kinetics study of BSG-SAP, pseudo-first order kinetic (equation (22), see Section 10.5.1) and pseudo-second order kinetic (equation (24), see Section 10.5.1) models are employed to describe the diffusion step and the step of adsorption on active sites, respectively.<sup>[192]</sup> Various statistical parameters,  $R^2$  (coefficient of determination), RSS (residual sum of squares), and  $\chi^2$  (reduced Chi-square) were used to evaluate the performance of the kinetic models.<sup>[194]</sup> A preliminary kinetic test shows that the adsorption equilibrium could be achieved at 45 min at a low initial concentration of 200 mg/L (Fig. 5.6). However, the equilibrium adsorption capacity of BSG-SAP-L (26.3 mg/g) is significantly smaller than that of BSG-SAP-H (148 mg/g), which is unusual compared with previous results obtained at  $c_0(\text{U}) = 1000$  mg/L (Fig. 5.5). In addition, the fitting results of the pseudo-first order and pseudo-second order kinetic models are poor ( $R^2 < 0.9$ , Table 5.2). A possible explanation is that at the current sorbent dosage (1 g/L), the low initial concentration of uranium ions cannot provide a sufficient driving force of concentration gradient to overcome the mass transfer resistance of uranium from the aqueous to the inside of the swollen SAP under the current adsorbent dosage (1 g/L).<sup>[75,241]</sup> Furthermore, the maximum adsorption capacity of BSG-SAP is expected to be very high due to the abundant functional groups and cross-linked polymer network ( $> 900$  mg/g, as shown in Fig. 5.5). Whereas, at a low initial concentration, the adsorption sites may not be fully saturated, resulting in results that do not reflect the actual properties of the adsorbents. Therefore, the kinetic study of BSG-SAP was performed using the data collected at a high initial concentration ( $c_0(\text{U}) = 1000$  mg/L) with sufficient driving force of concentration gradient as shown in Fig. 5.7. The results shows that in the first 15 min, BSG-SAP-L and BSG-SAP-H reaches 85% (786 mg/g) and 81% (778 mg/g) of its equilibrium adsorption capacity, respectively, indicating a fast adsorption kinetics. The adsorption reaches equilibrium at 45 min with an adsorption capacity of 929 mg/g (BSG-SAP-L) and 964 mg/g (BSG-SAP-H), which could be considered as a potential advantage to shorten the operation time and save the costs in practical usage. Compared with the pseudo-first order kinetic model, the pseudo-second order kinetic model shows better fitting results for both BSG-SAP-L and BSG-SAP-H with higher  $R^2$  and lower function errors (Table 5.3), indicating that the adsorption process is controlled by the U(VI) adsorption on the active sites of adsorbents.<sup>[194]</sup> However, the pseudo-first order and



pseudo-second order kinetic models are empirical models and have recently been criticized for their lack of concrete physical meaning.<sup>[194]</sup> Therefore, Ritchie's equation (equation (27), see Section 10.5.1)<sup>[242]</sup> was also employed to confirm this conclusion. The physical meaning of the Ritchie's equation is that the adsorption is dominated by the adsorption on the active sites, and one adsorbate ion/molecule could occupy  $n$  active sites.<sup>[194]</sup> Statistical analysis (Table 5.4) shows that the pseudo-second order kinetic model gives the best results for BSG-SAP-L and that the Ritchie equation could best represent the data for BSG-SAP-H. Thus, the rate-controlling step is the adsorption on the active sites, and the diffusion step is very fast due to the strong hydrophilicity of the adsorbent.<sup>[243]</sup>

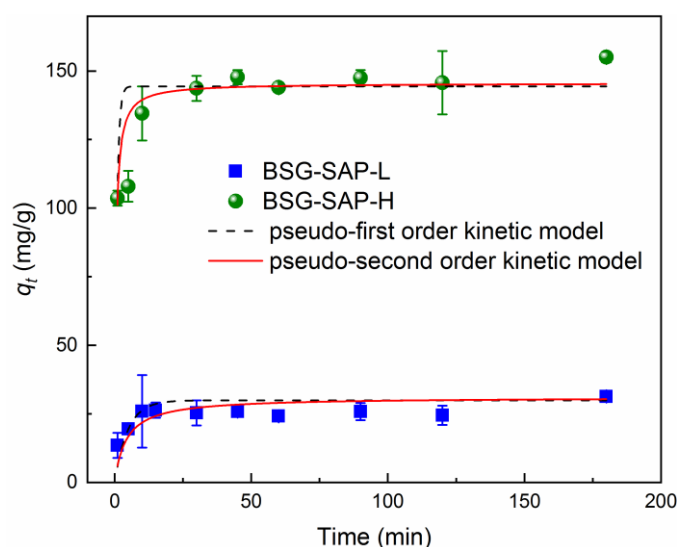


**Fig. 5.6.** Adsorption kinetics of U(VI) onto BSG-SAP and the nonlinear fitting of kinetic models. For adsorption, 2 mg adsorbent/ 2 mL solution,  $c_0(\text{U}) = 200$  mg/L,  $\text{pH}_0 = 4.7$ , room temperature.

**Table 5.2.** Kinetic and statistical parameters of different models. For adsorption, 2 mg adsorbent/ 2 mL solution,  $c_0(\text{U}) = 200$  mg/L,  $\text{pH}_0 = 4.7$ , room temperature.

PFO model <sup>a</sup>	$k_1$ ( $\text{min}^{-1}$ )	$q_{e,cal1}$ (mg/g)	$q_{e,exp}$ (mg/g)	$R^2$	RSS	$\chi^2$
BSG-SAP-L	0.2095	29.9	26.3	0.4520	1469	184
BSG-SAP-H	1.2576	144	148	0.7420	76	11
PSO model <sup>b</sup>	$k_2$ ( $\text{g} \cdot \text{mg}^{-1} \cdot \text{min}^{-1}$ )	$q_{e,cal2}$ (mg/g)	$q_{e,exp}$ (mg/g)	$R^2$	RSS	$\chi^2$
BSG-SAP-L	0.0076	31.0	26.3	0.6263	1002	125
BSG-SAP-H	0.0157	146	148	0.8231	52	7

a) PFO model: pseudo-first order kinetic model, b) PSO model: pseudo-second order kinetic model.

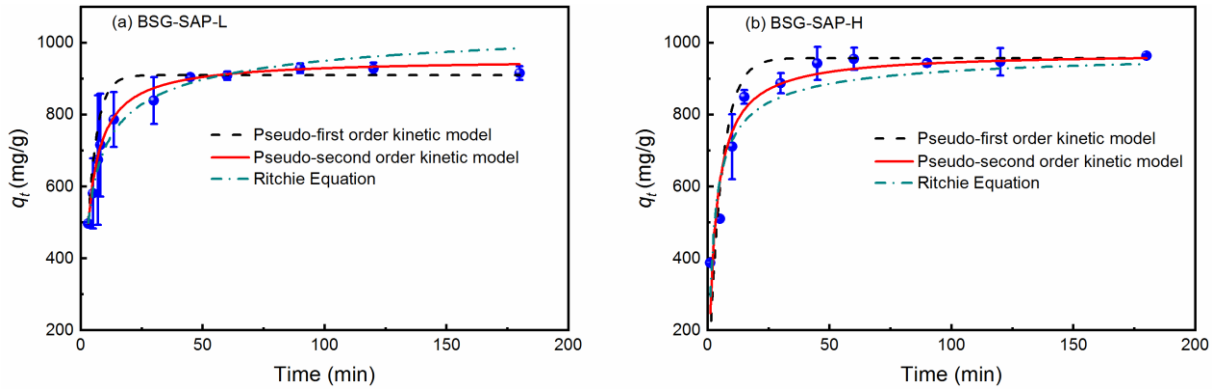


**Fig. 5.7.** Adsorption kinetics of U(VI) onto (a) BSG-SAP-L and (b) BSG-SAP-H and the nonlinear fitting of kinetic models. For adsorption, 2 mg adsorbent/ 2 mL solution,  $c_0(\text{U}) = 1000 \text{ mg/L}$ ,  $\text{pH}_0 = 4.6$ , room temperature.

**Table 5.3.** Kinetic and statistical parameters of different models. For adsorption, 2 mg adsorbent/ 2 mL solution,  $c_0(\text{U}) = 1000 \text{ mg/L}$ ,  $\text{pH}_0 = 4.6$ , room temperature.

PFO model <sup>a</sup>	$k_1 (\text{min}^{-1})$	$q_{e,cal1} (\text{mg/g})$	$q_{e,exp} (\text{mg/g})$	$R^2$	RSS	$\chi^2$
BSG-SAP-L	0.2631	910	929	0.9975	8	0.9
BSG-SAP-H	0.1918	960	964	0.8600	1747	218
PSO model <sup>b</sup>	$k_2 (\text{g} \cdot \text{mg}^{-1} \cdot \text{min}^{-1})$	$q_{e,cal2} (\text{mg/g})$	$q_{e,exp} (\text{mg/g})$	$R^2$	RSS	$\chi^2$
BSG-SAP-L	$3.8 \times 10^{-6}$	954	929	0.9992	3	0.3
BSG-SAP-H	$3.5 \times 10^{-6}$	970	964	0.9206	991	124
Ritchie's equation	$\alpha (\text{min}^{-1})$	$n$	$q_\infty (\text{mg/g})$	$R^2$	RSS	$\chi^2$
BSG-SAP-L	0.45	3.4	1113	0.9935	26	3
BSG-SAP-H	0.48	2.6	988	0.9384	767	96

a)PFO model: pseudo first-order kinetic model; b)PSO model: pseudo-second order kinetic model.

**Table 5.4.** Comparison of kinetic models ( $c_0(\text{U}) = 1000 \text{ mg/L}$ ).

Sample	Model	RSS	AIC	Akaïke Weight	Preferred model	BIC	BIC difference	Preferred model
BSG-SAP-L	PFO model <sup>a</sup>	8.4	6.4	0.004	No	4.2	11.14	No
	PSO model <sup>b</sup>	3.0	-4.7	0.996	Yes	-6.9	0	Yes
BSG-SAP-L	Ritchie's equation	26.0	18.9	$7.6 \times 10^{-6}$	No	16.7	23.6	No
	PSO model	3.0	-4.7	0.996	Yes	-6.9	0	Yes
BSG-SAP-H	Ritchie's equation	1747.0	53.4	0.984	Yes	50.3	0	Yes
	PFO model	990.9	61.6	0.016	No	58.5	8.2	No
BSG-SAP-H	Ritchie's equation	768.9	53.4	0.780	Yes	50.3	0	Yes
	PSO model	990.9	56.0	0.220	No	52.9	2.5	No

a) PFO model: pseudo-first order kinetic model, b) PSO model: pseudo-second order kinetic model.

### 5.4.2. Effect of pH value

The pH of the metal solution shows significant influence on surface properties of adsorbents, the speciation of the uranyl ions, and the swelling ability of BSG-SAP, which determines adsorption properties. A distribution diagram of uranyl ions ( $c_0(\text{U}) = 1000 \text{ mg/L}$ , Fig. 5.9, b) calculated using Visual MINTEQ 3.1 software<sup>[14]</sup> suggests a range from 1 to 4.6 of the initial pH ( $\text{pH}_0$ ) to avoid the presence of  $\text{UO}_2(\text{OH})_2$  in the solution. Fig. 5.8 shows that the adsorption capacity of U(VI) onto BSG-SAP increases as the  $\text{pH}_0$  rises, yielding adsorption capacities for BSG-SAP-L and BSG-SAP-H of 919 mg/g and 930 mg/g, respectively, when  $\text{pH}_0 = 4.6$ . The carboxyl groups of BSG-SAP are gradually deprotonated when the  $\text{pH}_0$  increases, which favors the electrostatic interaction between uranyl ions and the functional groups.<sup>[92]</sup> However, as the point of zero charge ( $\text{pH}_{\text{PZC}}$ ) of the BSG-SAP-L and BSG-SAP-H is 6.1 and 6.2 (Fig. 5.9, a), respectively, the surface of the adsorbents is positively charged throughout the process ( $\text{pH} < \text{pH}_{\text{PZC}}$ ). This suggests that despite the electrostatic repulsion effect on the BSG-SAP surface, other mechanisms also contribute to the increased adsorption capacity.<sup>[244]</sup> One of the reason is the deprotonation of carboxyl groups reduces the hydrogen bond interactions between the  $-\text{COOH}$  groups in BSG-SAP and increases the electrostatic repulsion effect between the negatively charged  $-\text{COO}^-$  groups. Consequently, the swelling ratio of the polymer increases, thereby increasing the availability of the active adsorption sites toward uranyl ions.<sup>[225]</sup> Furthermore,  $\text{UO}_2^{2+}$  dominates the solution when  $\text{pH} < 2.5$  (Fig. 5.9, b). Hydrolyzed species like  $(\text{UO}_2)_2(\text{OH})_2^{2+}$ ,  $(\text{UO}_2)_3(\text{OH})_5^+$ , and  $(\text{UO}_2)_4(\text{OH})_7^+$  appears with  $\text{UO}_2^{2+}$  when the pH increases from 2.5 to 4.6. The hydrolyzed  $(\text{UO}_2)_2(\text{OH})_2^{2+}$  cation is easier adsorbed on the polymer due to its higher affinity toward solid surface compared with the unhydrolyzed  $\text{UO}_2^{2+}$ .<sup>[190]</sup> Moreover, the pH value of the solution increases after U(VI) adsorption (Table 5.5). One possible reason is that the hydrolyzed U(VI) species release  $\text{OH}^-$  groups when interacting with carboxyl groups.<sup>[245]</sup> When  $\text{pH}_0 < \text{pH}_{\text{PZC}}$ , the pH value of the aqueous solution without uranyl ions also increases after adding the polymers (Fig. 5.9, a). This indicates that the increased pH value after adsorption may be also due to the protonation of carboxyl groups and the release of  $\text{Na}^+$  from the BSG-SAP. Further evidence of  $\text{Na}^+$  release during the adsorption is discussed in the Section 5.4.6.

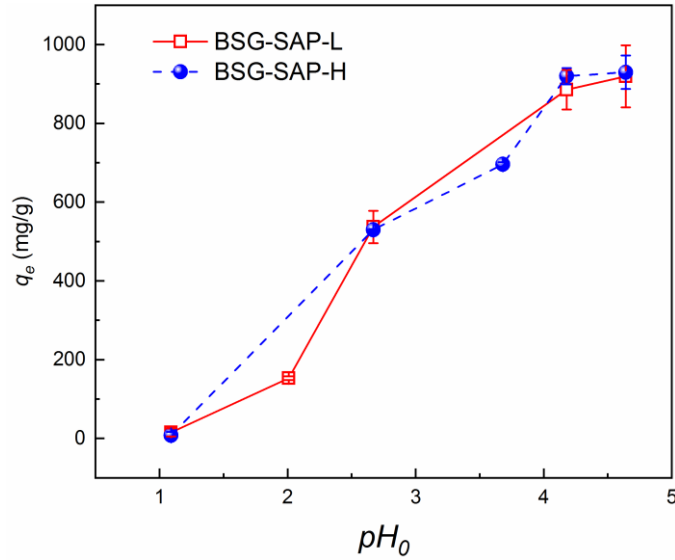


**Fig. 5.8.** Adsorption capacity of U(VI) in dependence of the initial pH. For adsorption: 2 mg adsorbent/ 2 mL solution,  $c_0(\text{U}) = 1000 \text{ mg/L}$ ,  $t = 45 \text{ min}$ , room temperature.

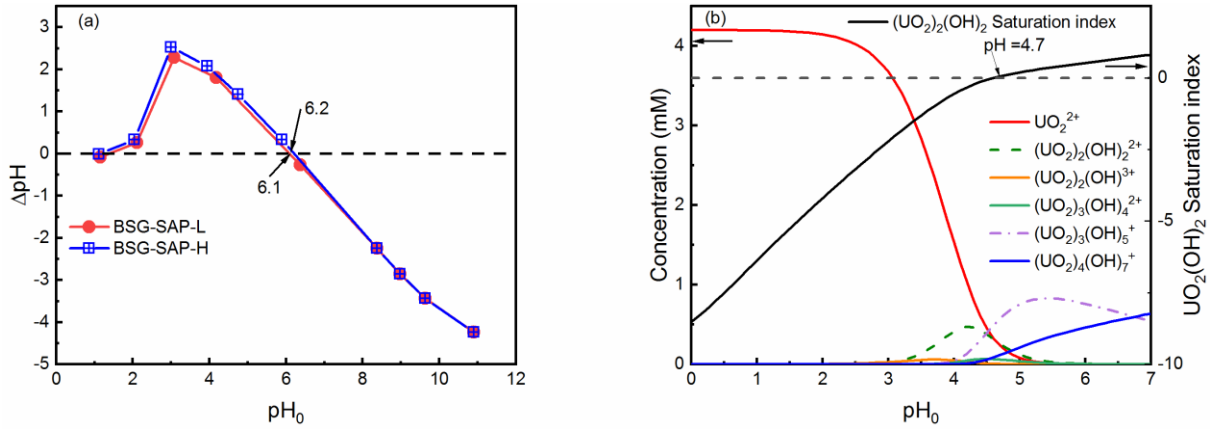


**Fig. 5.9.** (a) Determination of point of zero charge ( $\text{pH}_{\text{PZC}}$ ) of BSG-SAP-L and BSG-SAP-H, and (b) distribution diagram of uranium acetate solution calculated by Visual MINTEQ 3.1 software ( $c_0(\text{U}) = 1000 \text{ mg/L} = 4.2 \text{ mM}$ ).<sup>[14]</sup>

**Table 5.5.** The change of pH during adsorption experiments. For adsorption: 2 mg adsorbent/ 2 mL solution,  $c_0(\text{U}) = 1000 \text{ mg/L}$ ,  $t = 45 \text{ min}$ , room temperature.

BSG-SAP-L			BSG-SAP-H		
$\text{pH}_0$	$\text{pH}_e$	$\Delta\text{pH}$	$\text{pH}_0$	$\text{pH}_e$	$\Delta\text{pH}$
1.1	1.1	0	1.1	1.1	0
2.0	2.1	0.1	2.7	2.9	0.2
2.7	2.9	0.2	3.7	3.8	0.1
4.2	4.5	0.3	4.2	4.6	0.4
4.6	5.1	0.5	4.6	5.1	0.5

### 5.4.3. Effect of anions species and ionic strength

The presence of anions such as  $\text{Cl}^-$ ,  $\text{SO}_4^{2-}$ , and  $\text{NO}_3^-$  in the aquatic environment can significantly affect the adsorption capacity of U(VI), since they can form complexes with uranyl ions.<sup>[246]</sup> Herein, the effect of different anions on the adsorption capacity of the BSG-SAP at the same ionic strength ( $I = 0.1 \text{ mol/L}$ ) is studied. The adsorption capacity of U(VI) decreases in the presence of anions (Fig. 5.10, a). Both adsorbents present the least decrease in the adsorption capacity with  $\text{ClO}_4^-$  (836 mg/g of BSG-SAP-L and 818 mg/g of BSG-SAP-H), while the adsorption capacity in the presence of  $\text{SO}_4^{2-}$  decreases the most (744 mg/g of BSG-SAP-L and 720 mg/g of BSG-SAP-H). This is in good agreement with the speciation results calculated by Visual MINTEQ 3.1 software (Table 5.6),<sup>[14]</sup> which shows that under the studied condition,  $\text{NO}_3^-$ ,  $\text{Cl}^-$ , and  $\text{SO}_4^{2-}$  form stable complexes ( $\text{UO}_2\text{Cl}^+$ ,  $\text{UO}_2\text{NO}_3^+$ ,  $\text{UO}_2\text{SO}_4(\text{aq})$ , and  $\text{UO}_2(\text{SO}_4)_2^{2-}$ ) with  $\text{UO}_2^{2+}$ , whereas  $\text{ClO}_4^-$  seem not to form stable complexes. Furthermore, using  $\text{NaClO}_4$  as the supporting electrolyte, the effect of ionic strength on the adsorption capacity is investigated. The adsorption capacity of U(VI) decreases from very low ionic strength without  $\text{NaClO}_4$  (919 mg/g for BSG-SAP-L and 930 mg/g for BSG-SAP-H) to the high ionic strength with 1 M  $\text{NaClO}_4$  (739 mg/g for BSG-SAP-L and 593 mg/g for BSG-SAP-H, see Fig. 5.10, b). This is may be due to the high concentration of  $\text{Na}^+$  that shields the electrostatic attraction between  $\text{UO}_2^{2+}$  and the carboxyl groups, competes with  $\text{UO}_2^{2+}$  for the adsorption sites, and affects the activity coefficient of  $\text{UO}_2^{2+}$ .<sup>[75]</sup> Furthermore, the anion-anion electrostatic repulsion within the polymer is inhibited when additional cations are added in the solution, and the osmotic pressure between the polymer network and the external solution decreases. This leads to a decrease in the swelling ratio of adsorbents as shown in Fig. 5.11.<sup>[220]</sup> Because the swelling and shrinking control the transport of the adsorbate into or out of a polymeric adsorbent,<sup>[239]</sup> the decrease in swelling ratio could also result in the decrease in adsorption capacity. Despite being affected by high ionic strength and complexing anions, BSG-SAP shows high adsorption capacities ( $>500 \text{ mg/g}$ ) and a great potential to remove U(VI) from real wastewater.

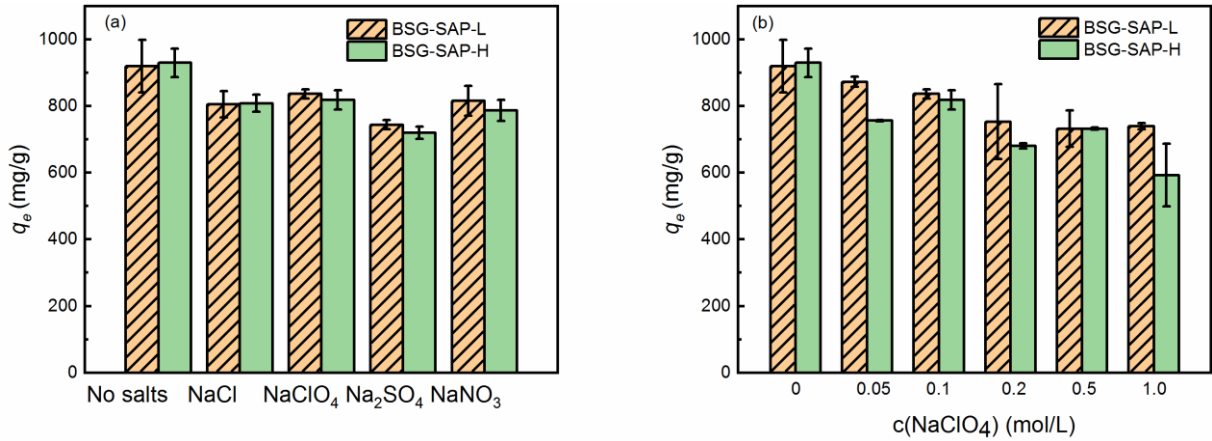


**Fig. 5.10.** Adsorption capacity of U(VI) in dependence of (a) the anion at constant ionic strength and (b) the ionic strength. For adsorption: 2 mg adsorbent/ 2 mL solution,  $c_0(\text{U}) = 1000$  mg/L,  $t = 45$  min, room temperature,  $\text{pH}_0 = 4.6$ , for (a):  $I = 0.1$  mol/L, and for (b):  $c(\text{NaClO}_4) = 0\text{--}1.0$  mol/L.

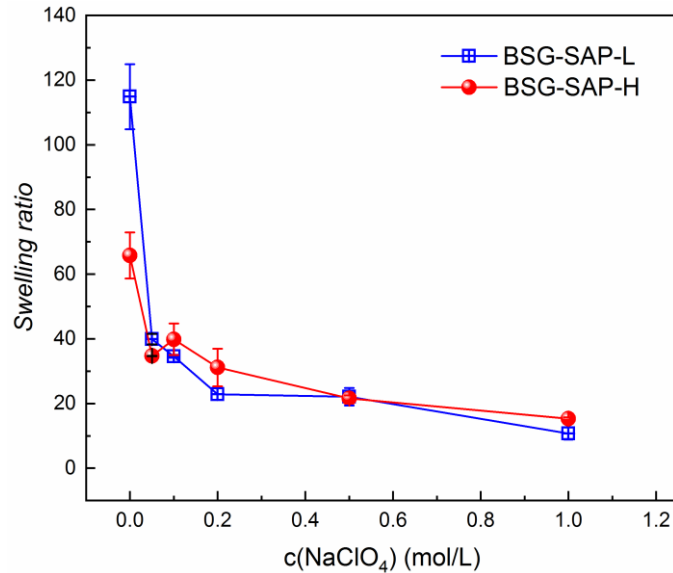


**Fig. 5.11.** Effect of ionic strength on the swelling ratio of BSG-SAP-L and BSG-SAP-H ( $\text{pH}_0 = 4.6$ ).

**Table 5.6.** Species calculation in the presence of anions using Visual MINTEQ 3.1<sup>[14]</sup> ( $c_0(\text{U}) = 1000$  mg/L,  $\text{pH} = 4.6$ ,  $I = 1.0$  mol/L).

Anions	Species name	% of total concentration
$\text{Cl}^-$	$\text{UO}_2\text{Cl}^+$	0.7
$\text{NO}_3^-$	$\text{UO}_2\text{NO}_3^+$	0.9
$\text{SO}_4^{2-}$	$\text{UO}_2\text{SO}_{4(\text{aq})}$	27.6
	$\text{UO}_2(\text{SO}_4)_2^{2-}$	7.7
$\text{ClO}_4^-$	None	0

#### 5.4.4. Adsorption isotherm

To obtain information about the adsorption mechanism, maximum adsorption capacity, and properties of the adsorbents, adsorption isotherms of U(VI) onto BSG-SAP are depicted in

Fig. 5.12. The isotherm data are fitted by Langmuir (equation (31), see Section 10.5.3), Freundlich (equation (34), see Section 10.5.3),<sup>[156]</sup> and Toth (equation (37), see Section 10.5.3) models,<sup>[247]</sup> and the fitting results and statistical parameters are summarized in Table 5.7. The results show that Langmuir and Freundlich isotherm models produce poor results of the BSG-SAP-L data with low correlation coefficients ( $R^2 < 0.9$ ) and high function errors. Therefore, it is difficult and inaccurate to estimate the maximum adsorption capacity of BSG-SAP-L using the Langmuir model. On the other hand, the Toth model fits both BSG-SAP samples best, as confirmed by the statistical parameters depicted Table 5.7 and the F-test<sup>[248]</sup> results at the 0.05 significant level (Table 5.8). In both cases, large deviations of the  $z$  values from one ( $z = 7.7$  for BSG-SAP-L and  $z = 0.5$  for BSG-SAP-H) indicate the heterogeneous property of the BSG-SAP adsorbents.<sup>[199]</sup> Therefore, the adsorption mechanism could be described as a monolayer adsorption of U(VI) onto a heterogeneous surface of BSG-SAP. Compared with the U(VI) adsorbents reported in the literature (Table 5.9), BSG-SAP-L and BSG-SAP-H present a significantly higher maximum adsorption capacity of U(VI) estimated by the Toth model ( $q_{max,T}$ ) of 1149 mg/g and 1465 mg/g, respectively. In particular, BSG-SAP presents a much higher adsorption capacity and a faster adsorption kinetics compared with the cellulose-based adsorbent (HPMC-g-AO, 765 mg/g and 12 days)<sup>[79]</sup> and the surface modified polypropylene fiber (SII-PNF, 133 mg/g and 15 h).<sup>[215]</sup> This is attributed to the improved grafting density and biomass utilization after swelling BSG, indicating a great potential of BSG-SAP in uranium removal from wastewater.

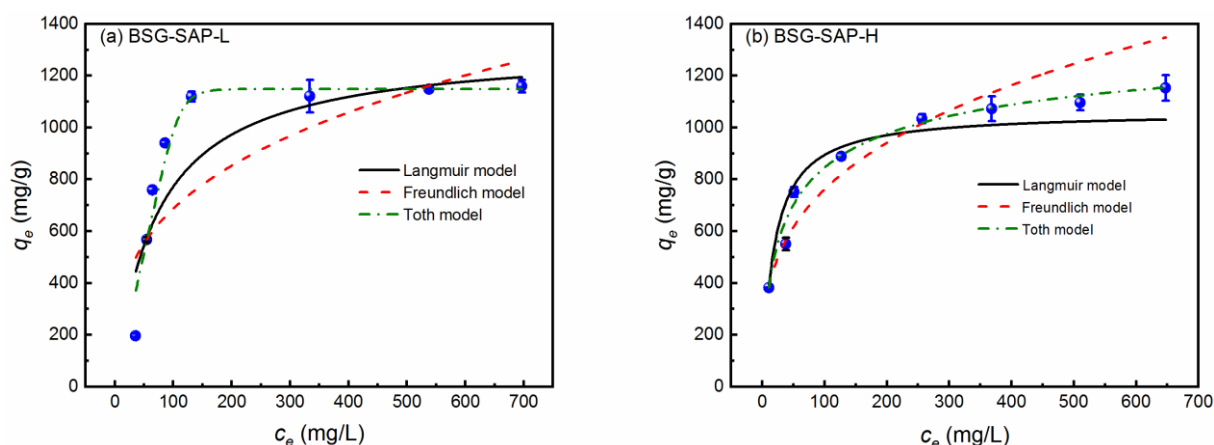


**Fig. 5.12.** Adsorption isotherm of U(VI) onto BSG-SAP and the nonlinear fitting of Langmuir, Freundlich, and Toth models. For adsorption, 2 mg adsorbent/ 2 mL solution,  $\text{pH}_0 = 4.6$ ,  $t = 45$  min, room temperature.

**Table 5.7.** Isotherm parameters of Langmuir, Freundlich, and Toth models. For adsorption, 2 mg adsorbent/ 2 mL solution, pH<sub>0</sub> = 4.6, t = 45 min, room temperature.

Isotherm model	Adsorbent	Parameters				
		$R^2$	$k_L$ (L/mg)	$q_{max,L}$ (mg/g)	RSS	$\chi^2$
Langmuir	BSG-SAP-L	0.8671	0.014	1315	1611	268
	BSG-SAP-H	0.9833	0.054	1060	74	12
Freundlich		$R^2$	$n$		RSS	$\chi^2$
	BSG-SAP-L	0.7843	3.2		2616	436
	BSG-SAP-H	0.9720	3.3		125	21
Toth		$R^2$	$z$	$q_{max,T}$ (mg/g)	RSS	$\chi^2$
	BSG-SAP-L	0.9578	7.7	1149	512	102
	BSG-SAP-H	0.9952	0.5	1465	21	4

**Table 5.8.** Results of the F-test to compare the Toth model with the Langmuir model.

		RSS	$N^a$	$p^b$	F	Prob>F
BSG-SAP-L	Toth model	512	8	3	10.7	0.022 < 0.05
	Langmuir model	1611	8	2		
BSG-SAP-H	Toth model	21	8	3	12.5	0.017 < 0.05
	Langmuir model	74	8	2		

a). Number of data points and b) number of parameters.

**Table 5.9.** Comparison of the U(VI) adsorption capacity in U(VI) spiked water.

Adsorbent	Equilibrium time	$q_{max}$ (mg/g)	Reference
BSG-SAP-L	45 min	1149	This study
BSG-SAP-H	45 min	1465	This study
PAO-CFs membrane	60 min	53	[78]
PAAM hydrogel	5 h	713	[90]
HPMC-g-AO	12 days	765	[79]
LDO-C	2 h	354	[249]
FeOOH-APAN	4 h	980	[196]
SII-PNF	15 h	133	[215]

#### 5.4.5. Performance at high salinity and under alkaline condition

To test the adsorbent performance at high salinity and under alkaline conditions, the adsorption experiments are carried out in U(VI) spiked simulated seawater (193 mg/L NaHCO<sub>3</sub> and 25.6 g/L NaCl) at various U(VI) concentration and initial pH of 7–8.<sup>[250,251]</sup> As shown in Fig. 5.13, the adsorption capacity of BSG-SAP-L decreases as the adsorbent dosage increases due to the inefficiency of excess amount of adsorbents.<sup>[160]</sup> In case of BSG-SAP-H, increasing



the dosage from 0.04 g/L to 0.07 g/L slightly increases the adsorption capacity at higher initial concentrations ( $c_0(\text{U}) = 10$  and  $30$  mg/L) due to the increase in available adsorption sites,<sup>[207]</sup> which is not observed at  $c_0(\text{U}) = 8$  mg/L. In order to be comparable to other studies, the results at a lower initial concentration ( $c_0(\text{U}) = 8$  mg/L) and a  $\text{pH}_0$  value more close to natural seawater (8.0) are further discussed. Maximum adsorption capacities of BSG-SAP-L and BSG-SAP-H at  $c_0(\text{U}) = 8$  mg/L are 13.8 mg/g at 0.07 g/L and 17.6 mg/g at 0.04 g/L, respectively. Furthermore, removal efficiency increases sharply as the adsorbent dosage increases, and BSG-SAP-H reaches 46% of uranium removal at the dosage of 1g/L (Fig. 5.13, d). As shown in Table 5.10, the synthesized BSG-SAP displaces higher adsorption capacity under similar conditions comparing with the current reported natural polymer-derived adsorbents, e.g. functionalized natural cellulose fibers (16 mg/g),<sup>[212]</sup> SSUP fiber (15.1 mg/g),<sup>[67]</sup> and modified collagen fibrils (NCFs-HTO-BT, 14.9 mg/g).<sup>[252]</sup> The adsorption capacity is also higher than the synthetic polymer derived from chemically-initiated polymerization (pA@Poly(VBC-co-DVB), 14.8 mg/g).<sup>[210]</sup> Synthetic polymers obtained from radiation-induced graft polymerization (RIGP) (160 mg/g, PE-graft-poly(AO-co-MA))<sup>[253]</sup> and atom-transfer radical polymerization (ATRP) (179 mg/g, PE-graft-poly(VBC)-graft-poly(AO-co-tBA))<sup>[250]</sup> show better performance of up to 4 times higher than BSG-SAP but with longer equilibrium time of 24 h. Moreover, synthetic polymers are unlikely to be cheap enough for practical application considering the cost of precursors and the number of synthetic steps.<sup>[212]</sup> In contrast, the production of BSG-SAP is likely to be cost-effective because it is a one-pot synthetic approach using very cheap raw materials, and BSG-SAP-H has high adsorption capacity and fast kinetics at high salinity and under alkaline conditions, which is promising for practical application.

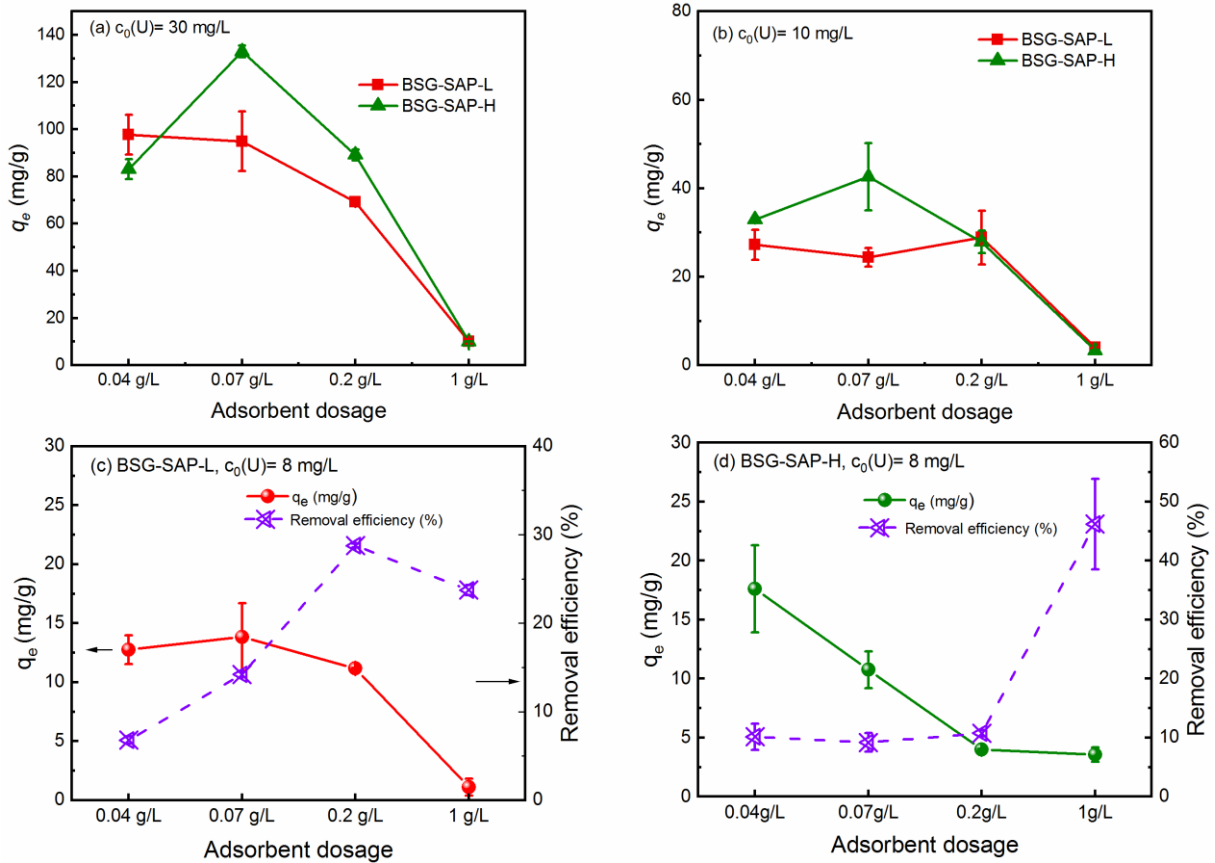


**Fig. 5.13.** Adsorption capacity and removal efficiency of U(VI) on BSG-SAP-L and BSG-SAP-H in U(VI) spiked simulated seawater with various U(VI) condition and  $pH_0$ . For adsorption,  $c(\text{NaCl}) = 25.6$  g/L,  $c(\text{NaHCO}_3) = 193$  mg/L,  $t = 2$  h, room temperature, for (a)  $pH_0 = 7$ , for (b)  $pH_0 = 7.7$ , and for (c) and (d)  $pH_0 = 8$ .

**Table 5.10.** Comparison of the U(VI) adsorption capacity at high salinity and under alkaline conditions.

Adsorbent	$q_e$ (mg/g)	Conditions	Time	Reference
BSG-SAP-H	17.6	$c_0(U) = 8$ mg/L, 193 mg/L $\text{NaHCO}_3$ , 25.6 g/L NaCl, $pH = 8$	2 h	This study
Functionalized natural cellulose fibers	16	$c_0(U) = 10$ mg/L, $pH = 8.2$	1 h	[212]
SSUP fiber	15.1	$c_0(U) = 8$ mg/L, simulated seawater	30 min	[67]
NCFs-HTO-BT	14.9	$c_0(U) = 8$ mg/L, $pH = 8$	24 h	[252]
pA@Poly(VBC-co-DVB) (beads)	14.8	$c_0(U) = 50$ mg/L, $pH = 8$ , in artificial seawater	72 h	[210]
PE-graft-poly(AO-co-MA)	160	$c_0(U) = 7.9$ mg/L, 193 mg/L $\text{Na}_2\text{CO}_3$ , 25.6 g/L NaCl, $pH = 8.3$	24 h	[253]
(PE-graft-poly(VBC)-graft-poly(AO-co-tBA)	179	$c_0(U) = 6$ mg/L with NaCl and $\text{NaHCO}_3$ , $pH = 8$	24 h	[250]

#### 5.4.6. Adsorption selectivity

To improve the removal efficiency of uranium from the aquatic environment, high adsorption selectivity of BSG-SAP for U(VI) is an important characteristic. In alkaline conditions, the selectivity of U(VI) in the presence of V(V) was tested as a representative.<sup>[254,255]</sup> Moreover, a series of competing metal ions that occur in many cases in the uranium contaminated water (K(I), Na(I), Mg(II), Zn(II), Co(II), Ni(II), Cu(II), Pb(II), and Fe(III)) are selected to investigate the adsorption selectivity.<sup>[214,256]</sup> The selectivity coefficient ( $S_U$ , %) was calculated according to equation (15) (see Section 10.3.5) to describe the selectivity toward U(VI). As shown in Fig. 5.14, the adsorption capacity of BSG-SAP for U(VI) is always the highest among all the competing ions, presenting an excellent selectivity in the presence of V(V), Na(I), Mg(II), Zn(II), Co(II) and Ni(II) and a good selectivity in the presence of K(I) and Cu(II) ( $S_U > 60\%$ ). As a hard Lewis acid, uranyl ion could form more stable complex with the hard Lewis bases such as carboxyl and amide groups in the BSG-SAP compared with the metal ions that are classified as borderline Lewis acids (Zn(II), Co(II), Ni(II), Cu(II) etc.), resulting in a higher adsorption capacity of uranium.<sup>[257]</sup> Moreover, the higher affinity of U(VI) to the functional groups may be related to its higher charge (+2) compared with K(I) and Na(I) and its higher electronegativity (1.38).<sup>[190,258,259]</sup> The poor selectivity toward U(VI) in the presence of Fe(III) (Fig. 5.14, c) is probably because of the lower first hydrolysis constant of  $\text{Fe}^{3+}$  ( $\text{pK}_{\text{h1}} = 3.1$ )<sup>[260]</sup> than  $\text{UO}_2^{2+}$  ( $\text{pK}_{\text{h1}} = 5.6$ ),<sup>[261]</sup> leading to a higher affinity to the functional groups.<sup>[190,258]</sup> It is also found that the  $\text{Na}^+$  concentration increases from 50 mg/L to 53.6 mg/L (BSG-SAP-L) and 59.3 mg/L (BSG-SAP-H) after adsorption, indicating a cation exchange between  $\text{Na}^+$  and the uranyl ions.<sup>[262]</sup>

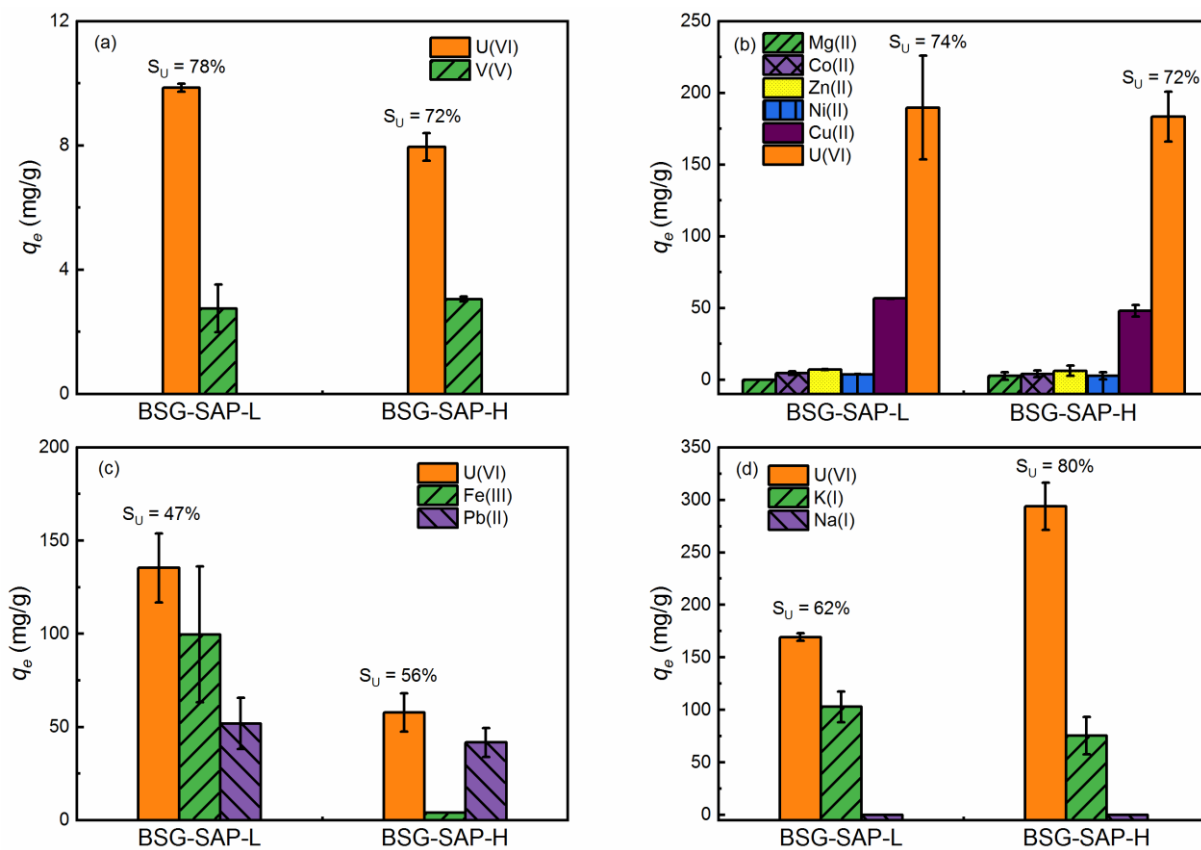


**Fig. 5.14.** Selectivity of BSG-SAP toward U(VI) in the presence of (a) V(V), (b) Mg(II), Zn(II), Co(II), Ni(II) and Cu(II), (c) Pb(II), and Fe(III), and (d) K(I), Na(I). For (a): 2 mg adsorbent/50 mL solution,  $c_0 = 5$  mg/L,  $pH_0 = 8.0$ , 2 h; for (b) and (c): 2 mg adsorbent/16 mL solution,  $c_0 = 30$  mg/L,  $pH_0 = 3.2$ , 2 h; and for (d): 2 mg adsorbent/16 mL solution,  $c_0 = 50$  mg/L,  $pH_0 = 4.7$ , 2 h.

## 5.5. Fixed bed column experiments

### 5.5.1 Breakthrough curves and dynamic modeling study

When large scale adsorption techniques are applied, continuous systems are often used to treat the large-volume influent in a short operation time and fully utilize the adsorption capacity of the adsorbents at low concentrations.<sup>[263]</sup> However, little research has reported the adsorption behavior of superabsorbent polymer in continuous flow systems. A fixed bed column packed with adsorbents in laboratory can be easily scaled up for industrial use and provides important information on the practical application parameters.<sup>[264]</sup> Moreover, previous batch adsorption experiments in Section 5.4.1 (adsorption kinetics) and 5.4.5 (performance at high salinity and under alkaline condition) show a significant decrease in adsorption capacity of BSG-SAP when the initial concentration of U(VI) is low. On the contrary, it is reported in literature that the adsorption efficiency of fixed bed column is much higher than that of the batch adsorption for low concentrations that are in the steep part of the adsorption isotherm.<sup>[265]</sup> Therefore, BSG-SAP was tested in the fixed bed column units to evaluate its full potential for uranium removal. In this section, BSG-SAP-L was tested on the fixed bed column using La(III) and U(VI) model solution to get some basic information about the adsorption properties.

The breakthrough curves of BSG-SAP-L toward La(III) with different bed depths show a typical S shape (Fig. 5.15, a). The breakthrough point ( $t_B$ ) is designated at the time when  $c_t/c_0$  reaches to 0.05, and the exhaustion point ( $t_E$ ) is designated at the time when  $c_t/c_0$  reaches to 0.9. BSG-SAP-L shows early  $t_{B1} = 4$  min and  $t_{E1} = 40$  min when the bed depth is 7 cm, which dramatically increase to  $t_{B2} = 40$  min and  $t_{E2} = 96$  min as the bed depth increases to 13.5 cm. In addition, the adsorption capacity of La(III) increases from 127 mg/g to 175 mg/g (Table 5.11). This is because as the bed depth increases, more adsorption sites are available (larger adsorbent mass) and the bed efficiency is improved because the metal ions have sufficient time to diffuse into the entire mass of the SAP.<sup>[266]</sup> Similar trend has been observed using U(VI) model solution as the bed depth increases (Fig. 5.15, b), and the breakthrough point changes from  $t_{B1} = 40$  min to  $t_{B2} = 100$  min. The exhaustion point for U(VI) has not reached within working period in the preliminary trials, indicating a much higher adsorption capacity for U(VI). The adsorption capacity of U(VI) decreases slightly from 565 mg/g to 552 mg/g when the bed depth increases from 7 cm to 13 cm (Table 5.11), which is probably due to the inefficiency of excess amount of adsorbents.<sup>[160]</sup> Compared with the batch adsorption experiments at the same initial concentration (91 mg/g,  $c_0 = 100$  mg/L), the adsorption capacity of BSG-SAP-L for U(VI) is 4

times higher, indicating a high efficiency of the fixed bed column. The competitive adsorption of U(VI) and La(III) on BSG-SAP-L is depicted in Fig. 5.15, c. Both U(VI) and La(III) show the breakthrough at 30 min, while the exhaustion time of La(III) ( $t_E(\text{La}) = 80$  min) is much earlier than that of U(VI) ( $t_E(\text{U}) = 220$  min), indicating a higher adsorption affinity of U(VI) (224 mg/g) than La(III) (130 mg/g) with a  $S_U = 63.3\%$  (Table 5.11).

To predict the breakthrough curves of the biosorbent and provide information about the dynamic adsorption mechanisms, Thomas<sup>[267]</sup> and Bohart-Adams<sup>[268]</sup> models are commonly used in the fixed bed column studies. The Bohart-Adams model assumes that the rate of adsorption depends on the concentration of adsorbates and the remaining adsorption capacity,<sup>[269]</sup> while the Thomas model assumes a Langmuir isotherm with a pseudo-second order rate expression.<sup>[270]</sup> According to the isotherm studies in batch experiments, the isotherms of BSG-SAP for U(VI) adsorption follow the description of the Toth model rather than the Langmuir model. In addition, the accurate form of the Thomas model is computationally cumbersome and difficult to use in practice. Furthermore, the simplified equation of the Thomas model is mathematically equivalent to the Bohart-Adams model, making the Langmuir isotherm assumption irrelevant.<sup>[271]</sup> Therefore, the Bohart-Adams model (equation (45), see Section 10.5.5) is more suitable for predicting the behavior of the breakthrough curves and the maximum adsorption capacity in the current study. As shown in Table 5.11, the Bohart-Adams model shows good fitting results of the breakthrough curves with high coefficient of determination ( $R^2 > 0.98$ ) and low function errors except for the U(VI) breakthrough curve in the U(VI)/La(III) binary solution ( $R^2 = 0.9392$ ). It should be noticed that the swollen adsorbents would shrink during the adsorption, resulting in a decrease in bed depth as the working duration prolongs (Fig. 5.15, a and b). This the shrinkage of hydrogel beads upon adsorption has also been reported in literature.<sup>[263]</sup> In the present study, the shrinkage of BSG-SAP does not make the shape of the breakthrough curves significantly different from the typical S shape. However, it could explain the deviation between the breakthrough curves and the model prediction, because the Bohart-Adams model assumes the bed depth to be a constant value. The shrinkage of the BSG-SAP-L at the early stage leaving voids between the hydrogel particles, leading to a higher U(VI) concentration in the effluent than the model prediction. As the shrinkage continues, the bed are more efficiently packed with the help of water pressure, reducing channeling along the walls of the column and resulting in better contact with the bulk solution. This would result in a lower U(VI) concentration than the model prediction.<sup>[263]</sup> However, The maximum adsorption capacity ( $q_M$ ) of the column test derived from Bohart-Adams model is close to the experimental results when the exhaustion points of the breakthrough curves have been reached

(Table 5.11, except for U(VI) with a bed depth 13.5 cm, which the adsorbent is far from exhaustion), indicating a reliable prediction.

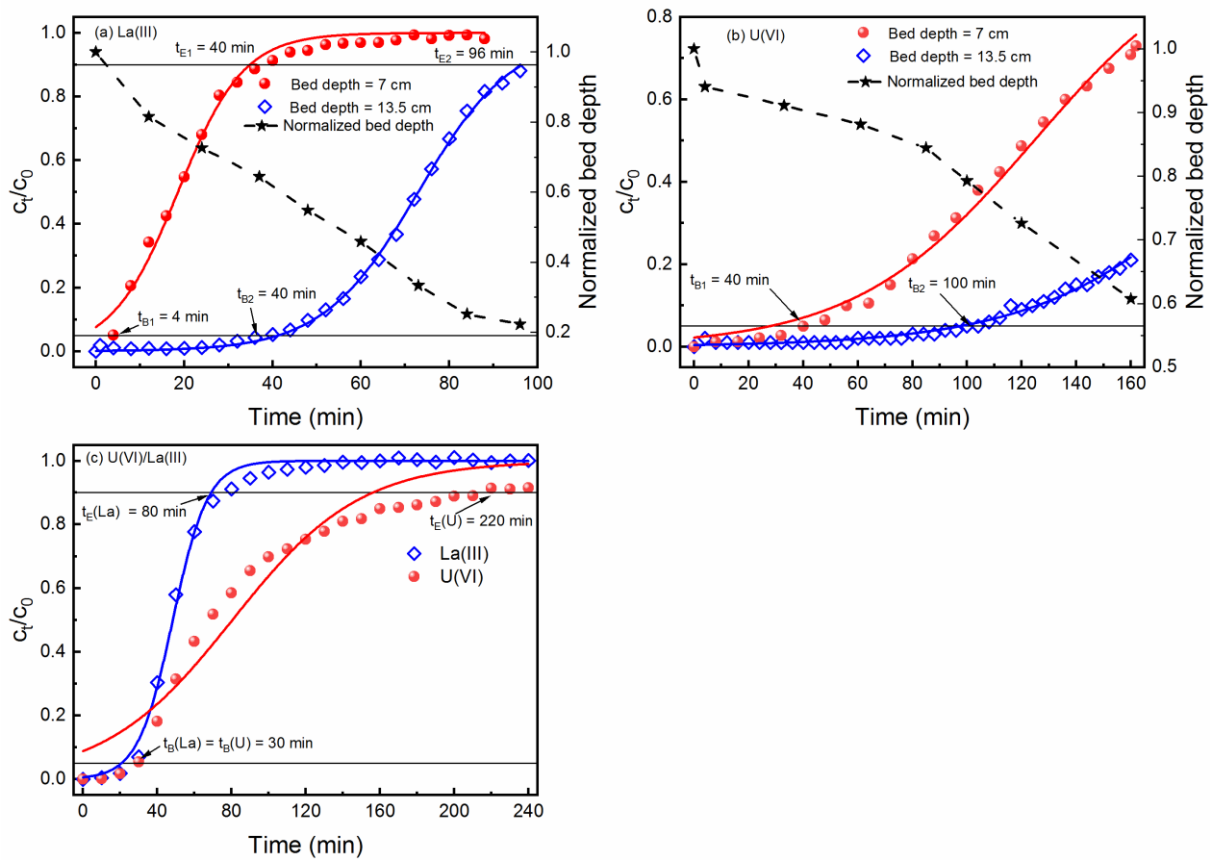


**Fig. 5.15.** Effect of bed depth on the breakthrough curves of BSG-SAP-L for (a) La(III) and (b) U(VI) model solution and the change of normalized bed depth during the adsorption process (initial bed depth = 13.5 cm), and (c) break through curves of BSG-SAP-L using U(VI)/La(III) binary solution. For (a)  $c_0(\text{La}) = 100 \text{ mg/L}$ ,  $Q = 3 \text{ mL/min}$ ,  $\text{pH}_0 = 5.7$ ; For (b)  $c_0(\text{U}) = 100 \text{ mg/L}$ ,  $Q = 3 \text{ mL/min}$ ,  $\text{pH}_0 = 4.7$ ; and for (C)  $c_0(\text{La}) = c_0(\text{U}) = 100 \text{ mg/L}$ ,  $Q = 3 \text{ mL/min}$ ,  $\text{pH}_0 = 4.6$ , bed depth = 11.5 cm.

**Table 5.11.** Adsorption capacity and fitting results of Bohart-Adams model using BSG-SAP-L.

Breakthrough curve	$q_e$ (mg/g)	$k_{BA}$ (L/(mg·min))	$N_0$ (mg/L)	$q_M$ (mg/g)	$R^2$	RSS	$\chi^2$
La(III)-bed depth 7 cm	127	0.0014	912	123	0.9902	0.02	0.001
La(III)-bed depth 13.5 cm	175	0.0009	1582	176	0.9989	0.003	0.0001
U(VI)-bed depth 7 cm	529	0.0004	5014	565	0.9922	0.01	0.0006
U(VI)-bed depth 13.5 cm	401	0.0003	4409	552	0.9879	0.001	0.00005
La(III) in the binary solution	137	0.0011	1173	130	0.9958	0.014	0.0006
U(VI) in the binary solution	246	0.0003	2026	224	0.9392	0.155	0.0067

### 5.5.2 Performance at low concentration, high salinity and under alkaline conditions

Since uranium is always present in wastewater at even lower concentrations, further studies of BSG-SAP-L and BSG-SAP-H will be conducted using fixed bed column with an U(VI) initial concentration of 30 mg/L. BSG-SAP-L and BSG-SAP-H exhibit similar breakthrough curves and reach  $c_t/c_0 \approx 0.4$  after running for 7 h (Fig. 5.16, a). Compared with the breakthrough curves at the higher initial concentrations (Fig. 5.15), the exhaustion time has been largely increased due to poor driving force caused by lower concentration gradient, resulting in slow mass transfer between the adsorbate and adsorbent.<sup>[268]</sup> The column is not fully saturated to reduce the uranium wastewater generate during the experiments, and it is expected that the adsorption capacity will be higher if the working time is extended. BSG-SAP-L shows a higher adsorption capacity (349.5 mg/g) than BSG-SAP-H (254.4 mg/g) (Table 5.12) because it has lower cross-linking density and higher swelling ratio (see Table 5.1). This results in a lower dry adsorbent dosage (0.067 g/ 840 mL for BSG-SAP-L and 0.105 g/ 840 mL for BSG-SAP-H) at the same bed depth and packing density, favoring the diffusion of  $UO_2^{2+}$  inside the polymer network.<sup>[272]</sup> However, BSG-SAP-L suffers from a significant mass loss and poor stability during the regeneration process, with only 11.4 wt% remaining after reswelling in the ultrapure water. This makes the BSG-SAP-L sample almost impossible to reuse. In contrast, the mass loss of BSG-SAP-H is minor thanks to its high cross-linking density with a reswelling ratio of 89.2 wt%.<sup>[273]</sup> Considering the practical application and operation cost, the highly cross-linked BSG-SAP-H would be a better choice for further testing of its performance and reusability at high salinity and under alkaline condition. After running in the simulated seawater ( $c_0(U) = 30$  mg/L) for 7 h, the obtained adsorption capacity (34.1 mg/g) of BSG-SAP-H is much lower than that for U(VI) spiked water, which is probably because of the low swelling ratio (15.2, see Table 5.1) and the high ionic strength under this condition. In addition, Table 5.12 shows good fit results using the Bohart-Adams model for all the breakthrough curves at low concentration and in simulated seawater with  $R^2 > 0.94$  and low error functions. Therefore, reasonable estimations of the  $q_M$  at  $c_0(U) = 30$  mg/L are obtained as 770 mg/g for BSG-SAP-L and 334 mg/g for BSG-SAP-H in the U(VI) spiked water, and the  $q_M$  for BSG-SAP-H in the simulated seawater is 77 mg/g. The results show that BSG-SAP-H is possible to be integrated in continuous flow systems for uranium removal.



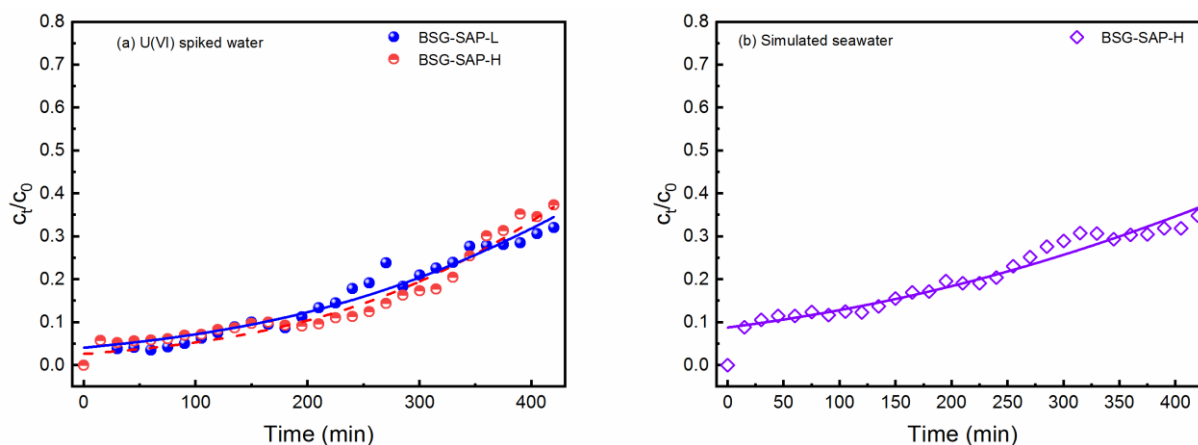


**Fig. 5.16.** Breakthrough curves and non-linear fitting of Bohart-Adams model of (a) BSG-SAP-H, BSG-SAP-L in U(VI) spiked water ( $c_0(\text{U}) = 30 \text{ mg/L}$ ,  $\text{pH}_0 = 4.9$ ), and (b) BSG-SAP-H in simulated seawater ( $c_0(\text{U}) = 30 \text{ mg/L}$ ,  $c(\text{NaCl}) = 25.6 \text{ g/L}$ ,  $c(\text{NaHCO}_3) = 193 \text{ mg/L}$ ,  $\text{pH}_0 = 7.0$ ). For column experiment, bed depth = 6.5 cm,  $Q = 2 \text{ mL/min}$ .

**Table 5.12.** Adsorption experiments and fitting results of the Bohart-Adams model for column experiments.

Adsorbent	Condition	$q_e$ (mg/g)	$k_{BA}$ (L/(mg·min))	$N_0$ (mg/L)	$q_M$ (mg/g)	$R^2$	RSS	$\chi^2$
BSG-SAP-L	U(VI) spiked water ( $c_0(\text{U}) = 30 \text{ mg/L}$ )	349.5	0.00015	4800	770	0.9457	0.01	0.0003
BSG-SAP-H	U(VI) spiked water ( $c_0(\text{U}) = 30 \text{ mg/L}$ )	254.4	0.0002	3500	334	0.9670	0.01	0.0005
BSG-SAP-H	simulated seawater ( $c_0(\text{U}) = 30 \text{ mg/L}$ )	34.1	0.0001	3700	77	0.9505	0.001	0.00035

### 5.5.3 Desorption and reusability

In order to reduce costs and waste generation in practical application, the desorption and regeneration properties of the adsorbents are of great importance and need to be investigated comprehensively. Thus, the desorption and reusability of BSG-SAP-H are explored in the fixed bed column in both U(VI) spiked water and simulated seawater, and the breakthrough curves are given in Fig. 5.17. The adsorption capacity of BSG-SAP-H for U(VI) spiked water decreases from 254.4 mg/g to 201.9 mg/g during the four cycles because of increased mass loss (Fig. 5.18, a). Nevertheless, 80% of the adsorption capacity is retained, imposing good stability without massive loss of functional groups. In simulated seawater (Fig. 5.18, b), the adsorption capacity increases from 27.6 mg/g to 37.4 mg/g after the first regeneration process, probably because of the use of NaOH as regeneration agent deprotonating all the carboxyl groups. Afterwards, the adsorption capacity decreases slightly, reaching 33.4 mg/g (90%) in the fourth cycle with good stability and no obvious loss of adsorption capacity. In addition, the high

desorption ratio ( $> 90\%$ ) guarantees the utilization of adsorption sites and a high adsorption capacity in the next adsorption cycle. After desorption, the uranyl ions in the water spiked with U(VI) could be concentrated to 14.6 folders in the first cycle and to 8.3 folders in the fourth cycle (Table 5.13). In simulated seawater, the enrichment factor is 9.2 for the first cycle and well above 12 for following three cycles (Table 5.13). The concentrated uranium in the acidic elution could be precipitated in the form of uranyl peroxide by  $\text{H}_2\text{O}_2$  treatment, as has been reported for the recovery of uranium from eluted solution or the treatment of uranium-contaminated effluents.<sup>[274,275]</sup> Based on batch and fixed bed column studies, BSG-SAP-H is able to meet the requirements for a sustainable adsorbent for uranium removal, including low cost, high adsorption capacity, fast kinetics, and excellent reusability.

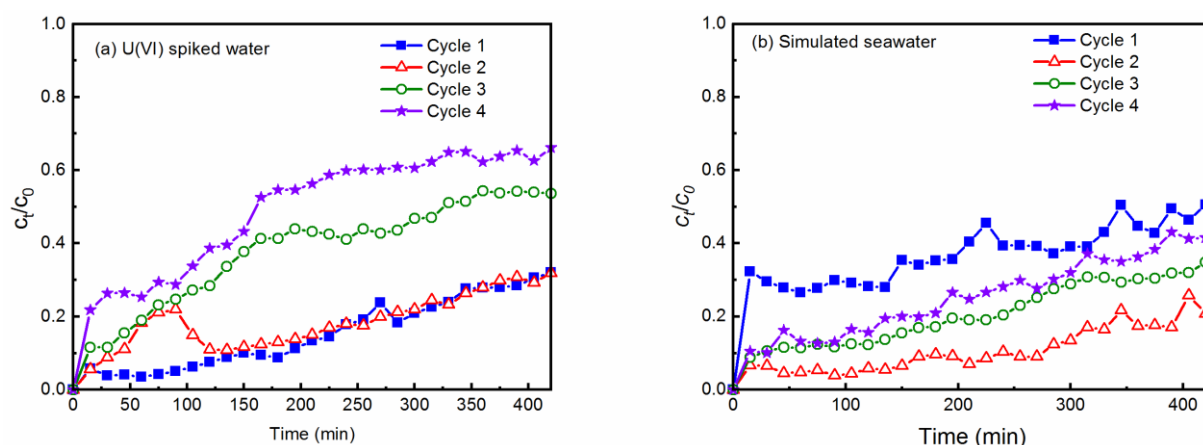


**Fig. 5.17.** Breakthrough curves of BSG-SAP-H in (a) U(VI) spiked water ( $c_0 = 30 \text{ mg/L}$ ,  $\text{pH}_0 = 4.9$ ), and (b) in simulated seawater ( $c_0 = 30 \text{ mg/L}$ ,  $c(\text{NaCl}) = 25.6 \text{ g/L}$ ,  $c(\text{NaHCO}_3) = 193 \text{ mg/L}$ ,  $\text{pH}_0 = 7.0$ ). For column experiment, bed depth = 6.5 cm,  $Q = 2 \text{ mL/min}$ . For desorption, 50 mL 0.5 M HCl,  $Q = 2 \text{ mL/min}$ . For regeneration, 25 mL 0.1 M NaOH, 500 mL ultrapure water,  $Q = 2 \text{ mL/min}$ .

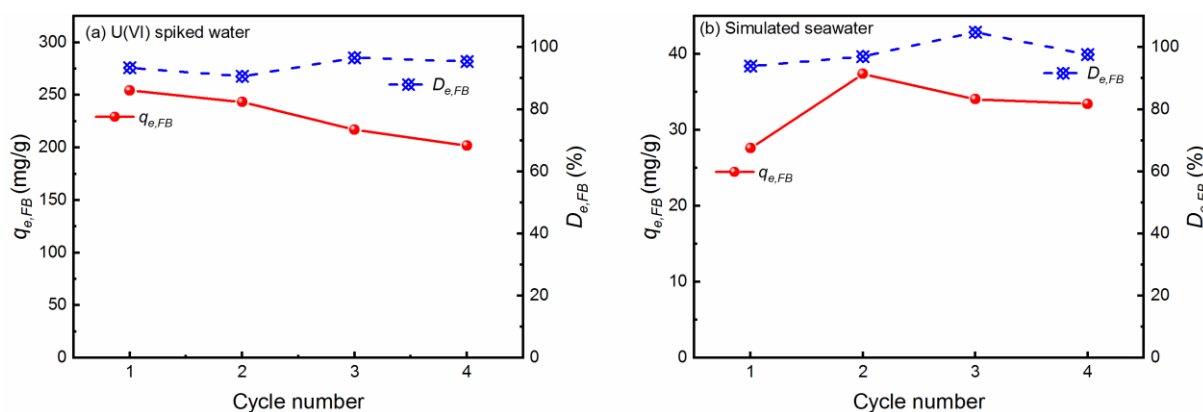


**Fig. 5.18.** Adsorption capacity ( $q_{e,FB}$ ) and desorption ratio ( $D_{e,FB}$ ) of BSG-SAP-H in (a) U(VI) spiked water ( $c_0(\text{U}) = 30 \text{ mg/L}$ ,  $\text{pH}_0 = 4.9$ ), and (b) simulated seawater ( $c_0(\text{U}) = 30 \text{ mg/L}$ ,  $c(\text{NaCl}) = 25.6 \text{ g/L}$ ,  $c(\text{NaHCO}_3) = 193 \text{ mg/L}$ ,  $\text{pH}_0 = 7.0$ ). For column experiment, bed depth = 6.5 cm,  $Q = 2 \text{ mL/min}$ . For desorption, 50 mL 0.5 M HCl,  $Q = 2 \text{ mL/min}$ . For regeneration, 25 mL 0.1 M NaOH, 500 mL ultrapure water,  $Q = 2 \text{ mL/min}$ .

**Table 5.13.** Elution concentration and enrichment factor of uranium during the four cycles of fixed bed column experiments.

Cycle number	U(VI) spiked water		Simulated seawater	
	Elution concentration (mg/L)	Enrichment factor	Elution concentration (mg/L)	Enrichment factor
1	438.4	14.6	276.7	9.2
2	462.2	15.4	387.3	12.9
3	338.4	11.3	381.2	12.7
4	248.7	8.3	348.8	11.6

## 5.6. Investigation of adsorption mechanism

SEM images of BSG-SAP-L and U(VI)-loaded BSG-SAP-L ( $\text{pH}_0 = 4.6$ ) were recorded (Fig. 5.19, a and b) to investigate the accumulation of uranium on the adsorbent surface. It can be noticed that the surface precipitation probably occurs at  $\text{pH}_e = 5.1$  when  $\text{pH}_0 = 4.6$  (Table 5.5), as indicated by the species calculation (Fig. 5.9, b). Thus, an additional U(VI)-loaded BSG-SAP-L sample was also prepared without the possibility of surface precipitation ( $\text{pH}_0 = 4.0$  with a  $\text{pH}_e = 4.2$ ), and the SEM image was recorded (Fig. 5.19, c) for comparison. No evidence of  $\text{UO}_2(\text{OH})_2$  precipitation on BSG-SAP after adsorption is observed in Fig. 5.19. The EDX mappings (Fig. 5.20) of the U(VI)-loaded BSG-SAP-L ( $\text{pH}_0 = 4.6$  and  $\text{pH}_0 = 4.0$ ) present uniform distributions of elemental uranium together with the carbon and oxygen from the adsorbents, indicating a strong interaction between the uranyl ions and the functional groups. In addition, research on uranium sorption has reported that no precipitation of  $\text{UO}_2(\text{OH})_2$  is observed in supersaturated uranium solution even at pH above 4.7 for several hours, which is consistent with the current observation.<sup>[276]</sup>

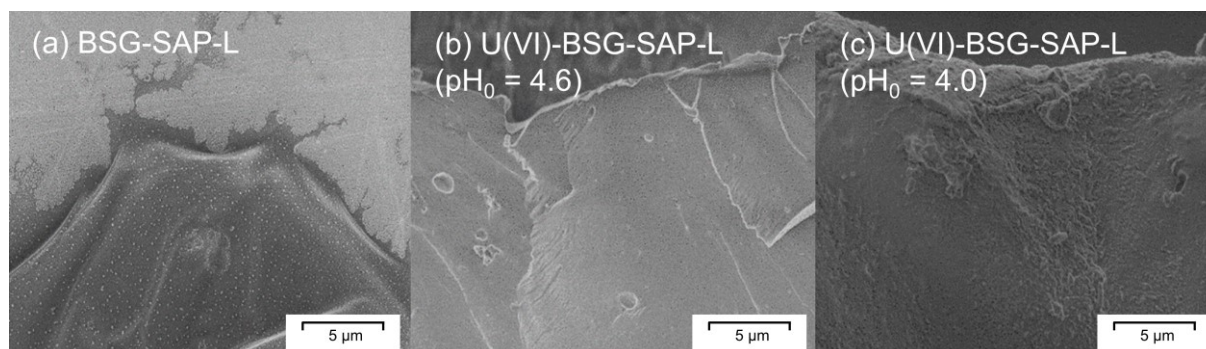


**Fig. 5.19.** SEM images of (a) BSG-SAP-L, (b) U(VI)-BSG-SAP-L ( $\text{pH}_0 = 4.6$ ) and (c) U(VI)-BSG-SAP-L ( $\text{pH}_0 = 4.0$ ) at 2.0 kV, magnification = 5000 times. For adsorption, 50 mg adsorbent/ 50 mL solution,  $c_0(\text{U}) = 1000$  mg/L,  $t = 45$  min, room temperature.

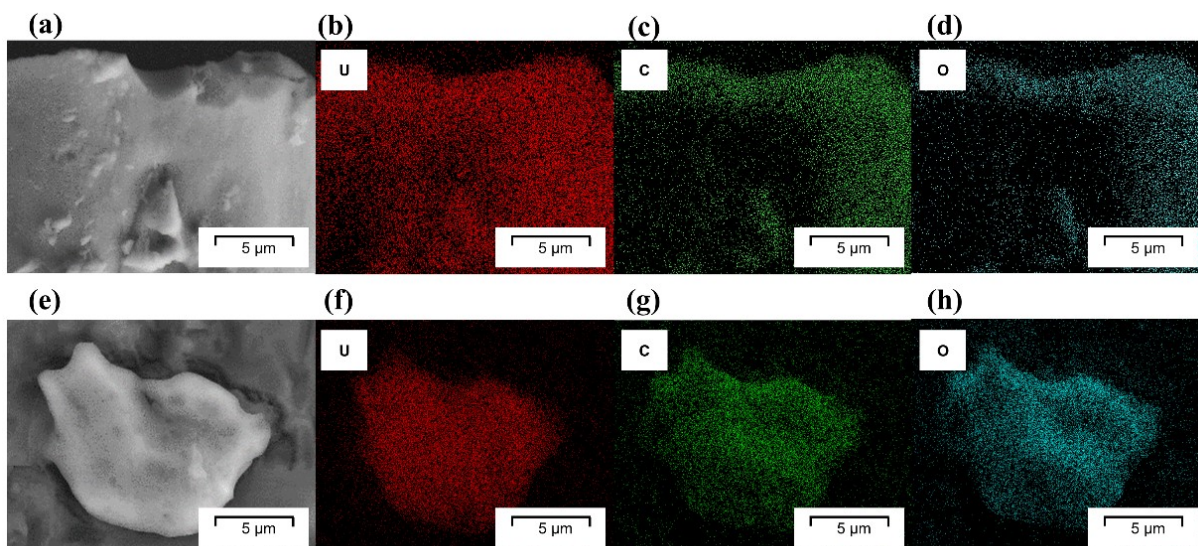


**Fig. 5.20.** SEM images and the distributions of elemental U, C, and O of U(VI)-BSG-SAP-L at  $\text{pH}_0 = 4.0$  (a-d) and U(VI)-BSG-SAP-L at  $\text{pH}_0 = 4.6$  (e-h). SEM images were taken at 20 kV, magnification = 5000 times, and EDX mappings were taken at 20 kV/10  $\mu\text{A}$ , magnification = 5000 times, 25 frames. For adsorption, 50 mg adsorbent/ 50 mL solution,  $c_0(\text{U}) = 1000 \text{ mg/L}$ ,  $t = 45 \text{ min}$ , room temperature.

To provide complementary information about the adsorption mechanisms, FT-IR (Fig. 5.21, a) and  $^{13}\text{C}$  solid-state NMR (Fig. 5.21, d) spectra of BSG-SAP-L before and after U(VI) adsorption as a representative of the BSG-supported adsorbents are compared. In the FT-IR spectra, the absorption bands attributed to the asymmetric ( $1552 \text{ cm}^{-1}$ ) and symmetric vibration ( $1404 \text{ cm}^{-1}$ ) of the  $-\text{COO}^-$  groups shift to  $1509 \text{ cm}^{-1}$  and  $1418 \text{ cm}^{-1}$ , respectively, after U(VI) loading. This observation clearly indicates that carboxyl groups are involved in the coordination of the uranyl ions. Subsequently, the differences between the antisymmetric and symmetric stretching bands of the  $-\text{COO}^-$  groups ( $\Delta\nu_{\text{as-vs}}$ ) decreases from  $148 \text{ cm}^{-1}$  to  $91 \text{ cm}^{-1}$ , which is characteristic for the formation of a bidentate binding structure involving  $\text{UO}_2^{2+}$  cations.<sup>[277]</sup> Furthermore, new absorption bands appear at  $531 \text{ cm}^{-1}$  and  $436 \text{ cm}^{-1}$  after  $\text{UO}_2^{2+}$  loading, which are assigned to the vibration of  $\nu(\text{U-N})$  and  $\nu(\text{U-O})$ , respectively, suggesting the coordination of  $\text{UO}_2^{2+}$  by the nitrogen atoms of amide groups and the oxygen atoms of carboxyl groups of BSG-SAP-L.<sup>[278]</sup> In addition, a strong absorption band corresponding to the asymmetric stretching mode of U(VI) ( $\nu_3(\text{UO}_2)$ )<sup>[171]</sup> occurs at  $916 \text{ cm}^{-1}$ . An absorption band at  $848 \text{ cm}^{-1}$  in the Raman spectra (Fig. 5.21, c) assigned to the symmetric stretching mode of U(VI) ( $\nu_1(\text{UO}_2)$ ) further confirms this. This band is assigned to either the  $(\text{UO}_2)_2(\text{OH})_2^{2+}$  species or a complex between  $\text{UO}_2^{2+}$  and carboxylate anions.<sup>[279]</sup> The later assignment of  $\text{UO}_2^{2+}$ -carboxylate anion complex is consistent with the release of  $\text{OH}^-$  anions from the hydrolyzed U(VI) species during the adsorption process, resulting in the observed increase in the pH value of the solution (Table 5.5). No differences

are observed in the FT-IR and Raman spectra for the two U(VI)-loaded samples prepared at different pH<sub>0</sub> (Fig. 5.21, b and c). Furthermore, no detected absorption band in the Raman spectra could be assigned to the possible precipitation of uranyl ions (UO<sub>2</sub>(OH)<sub>2</sub> at 837 cm<sup>-1</sup>),<sup>[279]</sup> which provides additional evidence that no surface precipitation occurs during the adsorption process.

The <sup>13</sup>C CP/MAS solid-state NMR spectra also confirm the interactions between UO<sub>2</sub><sup>2+</sup> and carboxyl groups (Fig. 5.21, d). The resonance of carboxyl C at 185 ppm in BSG-SAP-L splits into two resonances at 194 ppm and 182 ppm after UO<sub>2</sub><sup>2+</sup> adsorption, which has also been reported in the uranium adsorption onto glutamate glucan.<sup>[280]</sup> The downfield shift of carboxyl C to 194 ppm indicates an increase in the polarization of the C=O bond due to the electronic effect of UO<sub>2</sub><sup>2+</sup>.<sup>[281]</sup> In conclusion, the electrostatic interaction between UO<sub>2</sub><sup>2+</sup> and the carboxyl groups is the dominant adsorption mechanism for U(VI) adsorption on BSG-SAP, forming bidentate binding structures. In addition, the nitrogen atoms of amide groups of BSG-SAP also participate in the coordination of UO<sub>2</sub><sup>2+</sup>. The adsorption process is also accompanied by the cation exchange between Na<sup>+</sup> and UO<sub>2</sub><sup>2+</sup> and a possible release of OH<sup>-</sup> from the hydrolyzed U(VI) species, which no evidence of surface precipitation is observed.

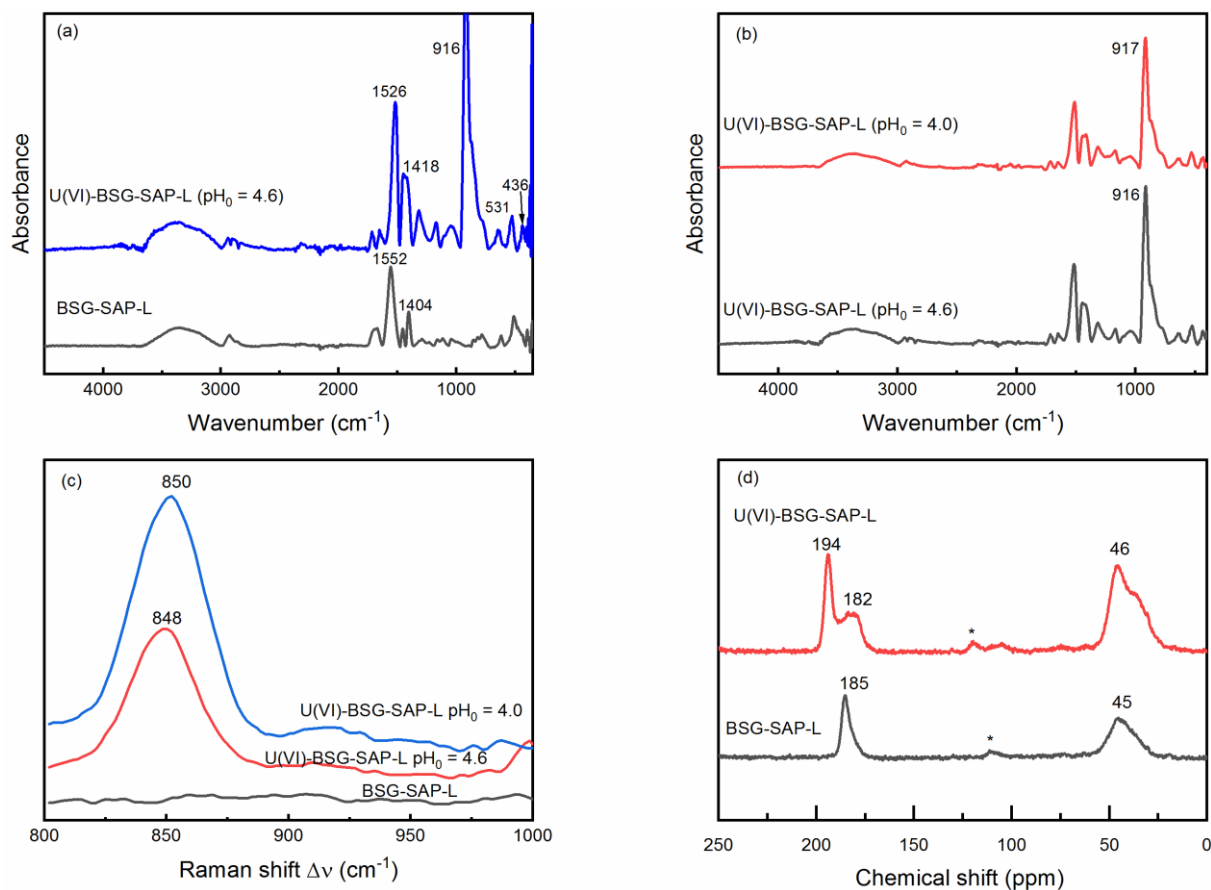


**Fig. 5.21.** (a) FT-IR spectra of BSG-SAP-L before and after U(VI) adsorption, (b) FT-IR spectra of U(VI)-loaded BSG-SAP-L prepared at different initial pH, (c) Raman spectra of U(VI)-loaded BSG-SAP-L prepared at different initial pH and (d)  $^{13}\text{C}$  CP/MAS solid-state NMR spectra of BSG-SAP-L before and after U(VI) adsorption (the spinning sidebands are marked with asterisks). For adsorption, 50 mg adsorbent/ 50 mL solution,  $c_0(\text{U}) = 1000$  mg/L,  $\text{pH}_0 = 4.6$  or 4.0,  $t = 45$  min, room temperature.

## 5.7. Degradability test

The degradability test of BSG-SAP and the reference polymer (RP) is designed to evaluate the extent to which the biodegradability of BSG backbone could contribute to the degradation of BSG-SAP in the soil. Subsequently, it could provide information about how to treat the retired adsorbents. The degradation behavior of BSG-SAP in terms of percentage weight remaining is studied by the soil burial method (Fig. 5.22, a). The residue mass of all four samples decreases continuously with an increased number of days. After 49 days, 50.1 wt% of BSG-SAP-L and 46 wt% of BSG-SAP-H remain in the soil, contrasting to 64.8 wt% of RP-L and 74.5 wt% of RP-H. Previous research has reported a mass loss of gum rosin alcohol/psyllium cross-linked poly(acrylic acid) hydrogel of 84.6 wt% after 63 days using soil buried method.<sup>[282]</sup> The lower residue mass of BSG-SAP compared with the reference polymers after 49 days is probably due to the biodegradable BSG. The polysaccharide units in BSG are first consumed by microorganisms, increasing the surface area of the synthetic polymer and weakening the polymeric matrix.<sup>[283]</sup> FT-IR spectrum of BSG-SAP-H after 49 days (Fig 5.22, b) also indicates a possible breakdown of the cross-links and BSG backbone since the absorption band at  $1112\text{ cm}^{-1}$  assigned to the overlap of C–N and C–O–C vibrations disappears. However, the mass loss discussed here is not equal to the mass of polymer that is biodegraded and mineralized. It is commonly reported that the superabsorbent polymer would degrade in soil at a rate of 0.12–0.24 wt% per six months.<sup>[284]</sup> The large mass loss of BSG-SAP and the reference polymers in the current study is probably because the water-soluble polymer segments detached from the BSG backbone are washed away during the cleaning process. Thus, it is proposed that the BSG-SAP would degrade into two fractions in the natural soil, i.e. the BSG segments and the polymer segments. The BSG segments could completely degrade in the natural environment with no hazardous impact, and the polymer segments are possible to be biodegraded by the synergetic effect of white-rot fungi and soil microbes, which shows little impact on the soil properties.<sup>[285,286]</sup> Moreover, the toxicity of acrylic monomers is derived from their active unsaturated double bonds.<sup>[287]</sup> The double bonds of the monomers are converted into saturated single bonds during the graft polymerization, leading to a decrease in toxicity of the polymer segments. Therefore, BSG could probably promote the degradation of retired BSG-SAP in the environment into low-hazard components.



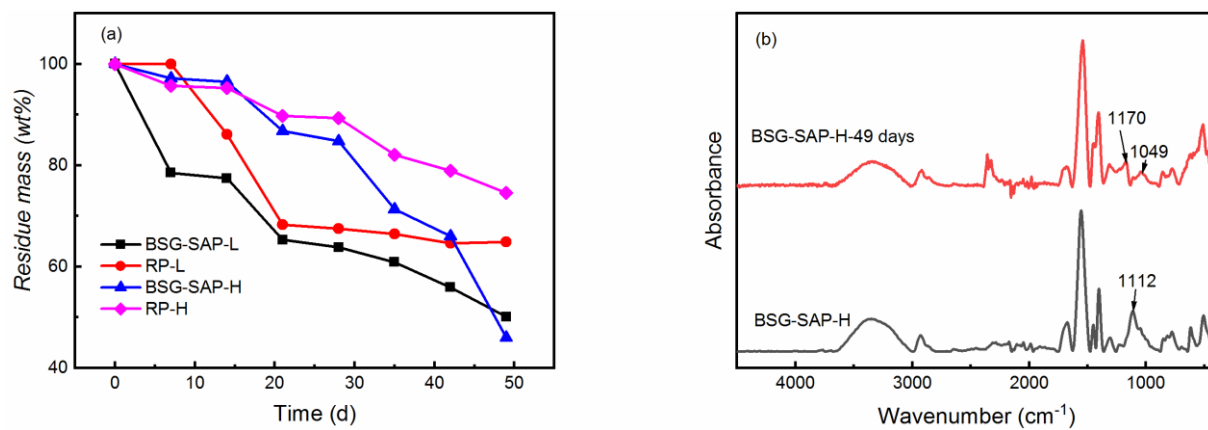


**Fig. 5.22.** (a) Residue mass of BSG-SAP and RP-P polymers buried in the soil for 49 days, and (b) FT-IR spectra of BSG-SAP-H before and after 49 days of degradability test.



## 6. Surface ion-imprinted brewer's spent grain for selective uranyl ion adsorption

In the actual wastewater, a large number of competing ions, often associated with the uranyl ions, would strongly compete for the limited number of adsorption sites, resulting in poisoning of adsorbent.<sup>[288]</sup> Therefore, it is technically imperative to develop new adsorbents with high selectivity to improve the efficiency of uranyl ion removal from wastewater.

Ion imprinting technique (IIT) is a promising option to improve adsorption selectivity, which has been widely explored in the removal of radionuclides.<sup>[289]</sup> Recently, the shortcomings of conventional IIT, including small adsorption capacity, high diffusion resistance, low mass transfer rate, and poor site accessibility, which are due to a lot of adsorption sites are embedded deeply inside the polymers, are overcome by surface IIT.<sup>[290]</sup> A surface ion-imprinted polymer (surface IIP) is prepared by grafting the pre-assembled monomers and templates onto the support surface and forming a thin polymer layer.<sup>[291]</sup> After the template removal, the tailor-made adsorption sites with complementary size and shape to target ions are established for selective adsorption.<sup>[292]</sup> The surface IIT not only ensures the complete removal of template ions and increases the accessibility of adsorption sites, but also facilitates the reuse of adsorbents.<sup>[292]</sup> So far, only a few studies have explored the adsorption of uranyl ions using adsorbents derived from surface IIT.<sup>[293,294]</sup>

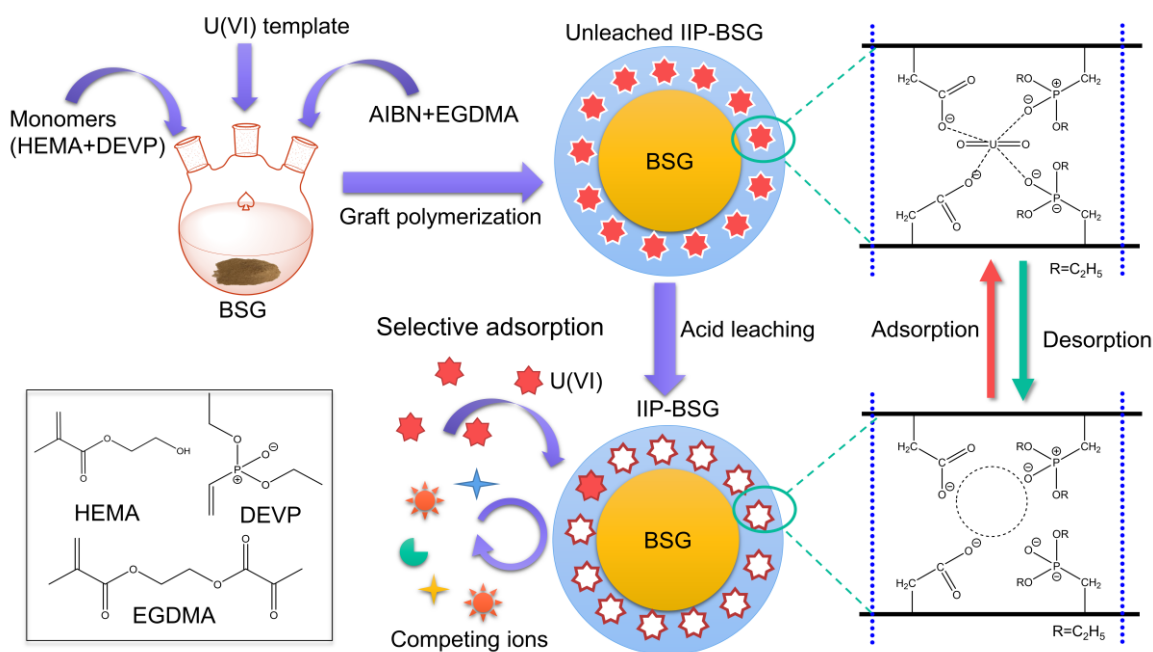
The functional monomers of surface IIP provide electrostatic interactions and coordination of the metal ions, and the molar ratio between monomer and template (M:T ratio) decides the affinity of adsorbents and the template removal, which are two crucial synthetic parameters for the performance of surface IIP.<sup>[295]</sup> The multi-point interactions from two or multiple functional monomers complementary to each other can improve the affinity and selectivity between the target ions and the adsorbent.<sup>[296]</sup> For example, IIP prepared from the ternary  $\text{UO}_2^{2+}$  complex of salicylaldehyde (SALO) and 4-vinylpyridine (4-VP) presents a better enrichment of uranyl ions compared with the IIP prepared from individual binary complex with SALO or 4-VP.<sup>[297]</sup> In addition, organophosphorus groups have also received increasing attention in recent years because of their strong coordination to uranyl ions with high selectivity.<sup>[298]</sup> Using vinyl phosphoric acid and N-isopropylacrylamide as functional monomers, imprinted microspheres have been prepared for uranium recovery from highly saline radioactive effluent with an adsorption capacity of 122.7 mg/g.<sup>[299]</sup> Nevertheless, related studies are rare, and it is tempting

to combine the P-containing monomer with traditional monomers such as 2-hydroxyethyl methacrylate (HEMA) in the surface IIP to improve its selectivity.<sup>[300]</sup> Furthermore, a successful ion-imprinting process generally requires to add an excess amount of monomers to the synthetic mixture.<sup>[295]</sup> Based on the stoichiometry studies, a M:T ratio of 4:1 is the most common choice for uranyl ion-imprinted polymers.<sup>[293,300]</sup> This means a relatively high amount of uranyl ions are consumed in the synthetic procedure, leading to various disadvantages, such as incomplete template removal, template bleeding during adsorption process, high cost, and the secondary pollution from toxic template leaching.<sup>[295,301]</sup> One possible solution is to aim for extremely high M:T ratios (e.g. 500:1), which can produce significant ion-imprinting effects when fewer template ions are used. This strategy has been tested in some studies using the molecular-imprinting technology<sup>[301]</sup> but has not been explored and used for surface IIP.

Natural polymers are considered ideal support materials for surface IIP and, due to their structural properties, could simultaneously provide functional groups for the modification and adsorption of metal ions.<sup>[302]</sup> Compared to the most commonly used natural polymers, chitosan and  $\beta$ -cyclodextrin,<sup>[302]</sup> brewer's spent grain (BSG) is a more affordable choice because it is a widely produced by-product from the beer brewery industry. In the current study, the surface ion-imprinted BSG (IIP-BSG) has been prepared for the first time using HEMA and diethyl vinylphosphonate (DEVP) as monomers using an extremely high M:T ratio of 500:1. The selective adsorption sites of IIP-BSG are formed through the multi-point interactions between the uranyl ions and the two monomers. Using Eu(III) as a model competing ion, the adsorption capacity, selectivity, and reusability of IIP-BSG toward U(VI) were investigated in various conditions. Moreover, the mass transfer mechanism of the U(VI) adsorption was studied using theoretical models, and the heterogeneity of the binding sites of IIP-BSG was described by the site energy distribution theory. The adsorption mechanism was proposed based on various characterization technologies and the experimental results.

## 6.1. Synthesis of surface ion-imprinted brewer's spent grain (IIP-BSG)

Using BSG as support, uranyl ions as the template, diethyl vinylphosphonate (DEVP) and 2-hydroxyethyl methacrylate (HEMA) as the functional monomers and ethylene glycol dimethacrylate (EGDMA) as the cross-linker, IIP-BSG was prepared by free radical polymerization as shown in Scheme 6.1. The DEVP and HEMA assemble around uranyl ions via multi-point coordination and electrostatic interactions and be grafted on the BSG surface in the presence of EGDMA to form a thin layer of cross-linked polymers. Then, the template is removed by 0.5 M HCl to obtain selective adsorption cavities (size, shape, and functionality).<sup>[303]</sup> The non-ion-imprinted BSG (NIP-BSG) and the ion-imprinted polymer without BSG (IIP-Polymer) were also prepared for reference study. As shown in Table 6.1, the template loading during the synthetic procedure is confirmed by the U contents of unleached IIP-BSG (4.1 mg/g) and IIP-Polymer (5.7 mg/g). After acid elution, almost all uranyl ions (98%) are eluted from the IIP-BSG, whereas only 87% of the template is removed for the NIP-Polymer. Thus, the surface imprinted sites of IIP-BSG are available for almost quantitative template removal, thus preventing the typical drawback of conventional IIPs of template leaking.<sup>[304]</sup> According to the microwave digestion results, the M:T ratio calculated from the mass balance of P element is 498:1 (Table 6.2), which is in a good agreement with the synthetic formula (500:1).



**Scheme 6.1.** Preparation of IIP-BSG with selective adsorption sites.

**Table 6.1.** Contents of P, U and the elution efficiency of studied adsorbents.

	P (unleached, mg/g)	P (leached, mg/g)	U (unleached, mg/g)	Elution efficiency (%)
IIP-BSG	9.1 ± 1.1	1.6 ± 0.5	4.1 ± 0.2	98 ± 1.4
NIP-BSG	8.2 ± 5.4			
IIP-Polymer	10.0 ± 4.1	4.1 ± 2.0	5.7 ± 0.2	87 ± 2.8
IIP-BSG-r <sup>a</sup>		2.2 ± 0.1		

Errors are those obtained from ICP-OES. a) IIP-BSG-r: IIP-BSG after the five adsorption-desorption cycles

**Table 6.2.** M:T ratios from the synthetic formula of IIP-BSG and the digestion results of IIP-BSG.

	HEMA (mmol)	DEVP (mmol)	U (mmol)	M:T
Synthetic formula of IIP-BSG	4.1	5.2	0.0186	500
Digestion results of IIP-BSG	4.1 <sup>a</sup>	0.8 <sup>b</sup>	0.01	498

a) Graft efficiency of HEMA is not considered, and b) calculated by mass balance of the element P.

The adsorption capacity and selectivity of IIP-BSG, NIP-BSG and IIP-Polymer were determined to demonstrate the ion-imprinting effect and the advantages of surface IIT (Fig. 6.1). Since Eu(III) is a strong Lewis acid, which has high affinity to strong Lewis basic sites such as hydroxyl, carboxyl and phosphoryl groups present in the adsorbents, Eu(III) and U(VI) were used as competing ions in this study.<sup>[305,306]</sup> In addition, when studying the U(VI)/Ln(III) separation for the treatment of nuclear wastewater and disposal of spent nuclear fuel, Eu(III) is commonly used to represent the group of lanthanides.<sup>[23,307]</sup> Although the IIP-Polymer presents a high selectivity coefficient ( $S_U$ ) of 89% in a U(VI)/Eu(III) binary solution ( $c_0(\text{U}, \text{Eu}) = 0.5 \text{ mM}$ ), its adsorption capacity is low (9 mg/g) due to the poor accessibility of the imprinted sites,<sup>[308]</sup> which has little chance for practical application. The  $S_U$  of IIP-BSG in the binary solution has increased from 77% to 91% compared with the NIP-BSG. A ion-imprinting factor  $\beta > 1$  (1.2) indicates that IIP-BSG has imprinted adsorption sites with higher affinity toward U(VI) than NIP-BSG.<sup>[309]</sup> Furthermore, Cu(II) and V(V) are also known for their significant effects on U(VI) adsorption.<sup>[255,310]</sup> Thus, IIP-BSG and NIP-BSG are tested in U(VI)/Cu(II) ( $c_0 = 0.5 \text{ mM}$ ,  $\text{pH}_0 = 4.7$ ) and U(VI)/V(V) ( $c_0 = 0.1 \text{ mM}$ ,  $\text{pH}_0 = 3$ ) binary solution. The lower initial concentration and pH value of the U(VI)/V(V) binary solution were employed to avoid co-precipitation of U(VI) and V(V). According to the calculation performed with the Visual MINTEQ 3.1 software, the dominate species are  $\text{UO}_2^{2+}$  and  $\text{VO}_2^+$  in the model solution (Table 6.3).<sup>[14]</sup> As shown in the Fig. 6.2, IIP-BSG shows higher selectivity of  $S_U = 97\%$  in the U(VI)/Cu(II) binary solution and  $S_U = 91\%$  in the U(VI)/V(V) binary solution compared with the NIP-BSG ( $S_U = 88\%$  for U(VI)/Cu(II) and  $S_U = 86\%$  for U(VI)/V(V)). This confirms the excellent selectivity of IIP-BSG against various competing ions. The adsorption capacity of IIP-BSG in U(VI) single solution (80 mg/g) is significantly higher than that of the IIP-Polymer

(9 mg/g) with comparable selectivity, indicating greater potential for practical application. However, the adsorption capacity of IIP-BSG is lower than the NIP-BSG (196 mg/g). One possible explanation is the loss of physically attached monomers during the leaching process, as shown by the decrease in P content from 9.1 mg/g to 1.6 mg/g after acid elution compared to the NIP-BSG (8.2 mg/g, Table 6.1). Additionally, it has been reported that the adsorption capacity of IIP is generally lower than that of NIP when the monomer/cross-linker ratio is higher than 1/6 (2/1 for IIP-BSG).<sup>[311]</sup>

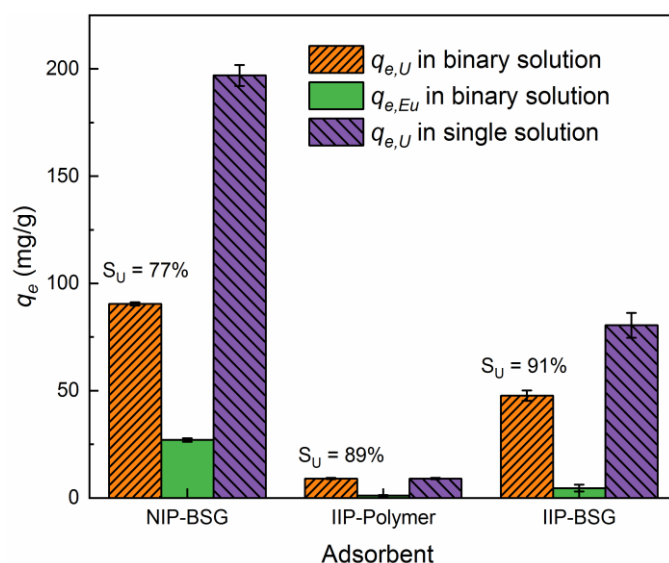


**Fig. 6.1.** Adsorption capacity and calculated selectivity coefficient ( $S_U$ ) of IIP-BSG, NIP-BSG, and IIP-Polymer in U(VI) single solution and U(VI)/Eu(III) binary solution. For adsorption: 2 mg adsorbent/ 2mL solution,  $pH_0 = 4.7$ ,  $t = 2$  h, for single solution  $c_0(U) = 1.2$  mM, and for binary solution  $c_0(U, Eu) = 0.5$  mM.

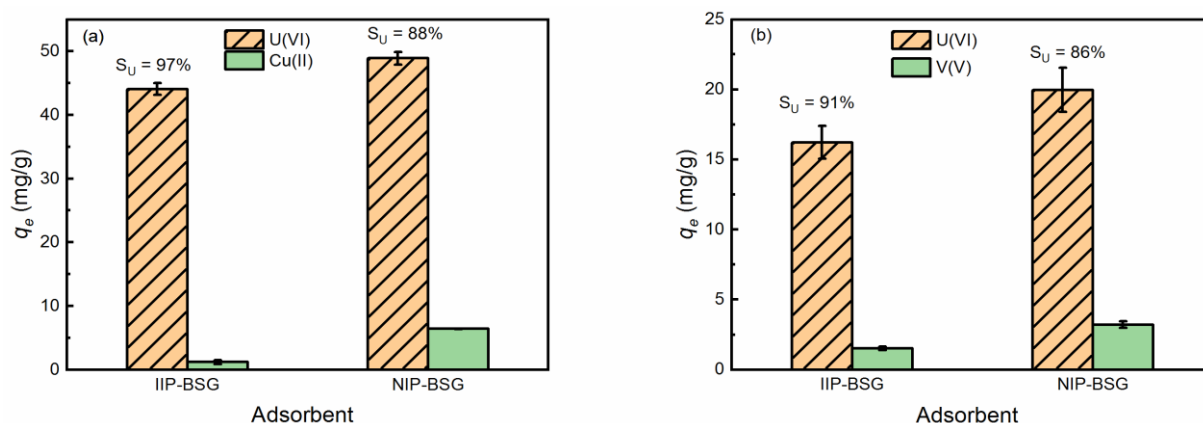


**Fig. 6.2.** Adsorption capacity and calculated selectivity coefficient ( $S_U$ ) of IIP-BSG and NIP-BSG in (a) U(VI)/Cu(II) ( $c_0 = 0.5$  mM,  $pH_0 = 4.7$ ) and (b) U(VI)/V(V) ( $c_0 = 0.1$  mM,  $pH_0 = 3$ ) binary solution. For adsorption: 2 mg adsorbent/ 2 mL solution,  $t = 2$  h.

**Table 6.3.** Species calculation of the U(VI)/V(V) binary solution with concentration of 0.1 mM each at pH = 3.0.<sup>[14]</sup>

Species name	% of total concentration
UO <sub>2</sub> <sup>2+</sup>	99.4
UO <sub>2</sub> OH <sup>+</sup>	0.5
(UO <sub>2</sub> ) <sub>2</sub> (OH) <sub>2</sub> <sup>2+</sup>	0.04
(UO <sub>2</sub> ) <sub>2</sub> OH <sup>3+</sup>	0.04
VO <sub>2</sub> <sup>+</sup>	93.2
H <sub>2</sub> VO <sub>4</sub> <sup>-</sup>	6.8
H <sub>2</sub> V <sub>2</sub> O <sub>7</sub> <sup>2-</sup>	0.02

Moreover, a reference adsorbent with a M:T ratio of 4:1 (IIP-BSG(4:1)) was synthesized, which is the most common choice for uranyl ion-imprinted polymers based on the stoichiometry studies.<sup>[293,300]</sup> The high template loading of unleached IIP-BSG(4:1) is confirmed by a strong absorption band of U=O stretching vibration at 923 cm<sup>-1</sup> in the FT-IR spectrum (Fig. 6.3, a). In contrast, this absorption band is not observed in the spectrum of unleached IIP-BSG, presumable due to a low template loading (M:T = 500:1). Adsorption experiments show that IIP-BSG with an adsorption capacity of 80 mg/g and a selectivity  $S_U = 91\%$  actually performs better than IIP-BSG(4:1) (adsorption capacity 74 mg/g and  $S_U = 84\%$ , Fig. 6.3, b). This shows that the M:T ratio can be increased to an extremely high value to reduce the amount of template required, but still maintain the imprinting effect and selectivity.<sup>[289]</sup> Therefore, the as-prepared IIP-BSG overcomes the poor accessibility of adsorption sites and the difficulty of template removal of conventional IIPs to a certain extent, and its adsorption performance for uranyl ions are studied in detail.

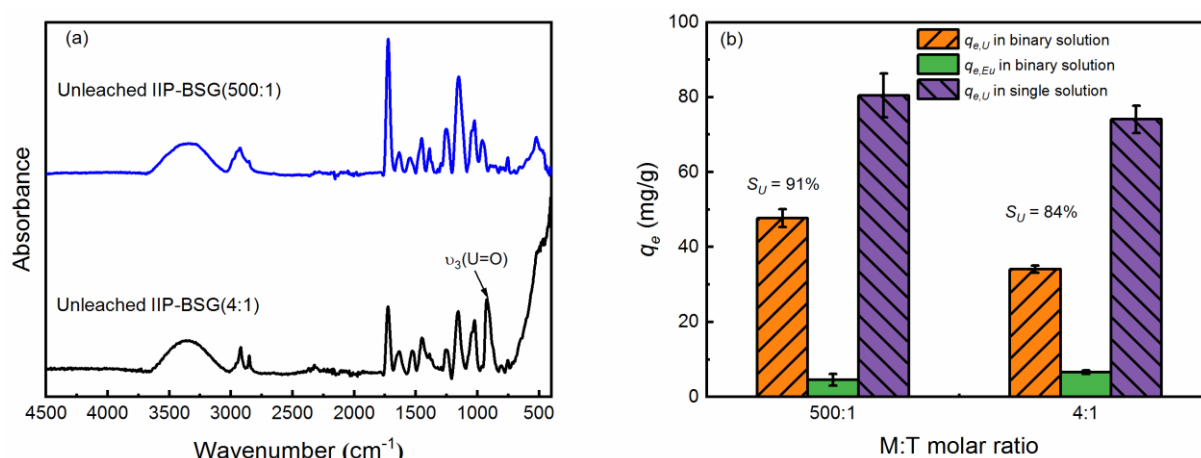


**Fig. 6.3.** (a) FT-IR spectra of unleached IIP-BSG with different M:T molar ratio, and (b) Effect of M:T molar ratio on the adsorption capacity and selectivity of IIP-BSG, for adsorption: 2 mg adsorbent/ 2 mL solution, pH<sub>0</sub> = 4.7, t = 2 h, for single solution c<sub>0</sub>(U) = 1.2 mM, for binary solution c<sub>0</sub>(U, Eu) = 0.5 mM.



## 6.2. Characterization of the adsorbents

To demonstrate the changes in chemical structure and functional groups after the surface ion imprinting, the FT-IR spectra of BSG, IIP-BSG and IIP-Polymer are shown in Fig. 6.4, a. The spectra of HEMA, DEVP and EGDMA are given in Fig. 6.4, b. The adsorption band with significantly increased intensity obtained at  $1722\text{ cm}^{-1}$  for IIP-BSG ( $1720\text{ cm}^{-1}$  of IIP-Polymer) is attributed to the C=O groups from the monomer HEMA ( $1707\text{ cm}^{-1}$ ) and the cross-linker EGDMA ( $1706\text{ cm}^{-1}$ ).<sup>[226]</sup> In the IIP-BSG spectrum, the asymmetric and symmetric stretching vibration of  $\text{-COO}^-$  groups are observed at  $1634$  and  $1454\text{ cm}^{-1}$ , respectively.<sup>[221]</sup> The occurrence of  $\text{-COO}^-$  groups is probably due to the partial hydrolysis of HEMA monomer in the alkaline solution used for BSG swelling.<sup>[312]</sup> The strong band at  $1144\text{ cm}^{-1}$  for IIP-BSG is ascribed to the C–O stretching vibration from HEMA ( $1168\text{ cm}^{-1}$ ) and EGDMA ( $1145\text{ cm}^{-1}$ ).<sup>[226]</sup> These results confirm the successful grafting of HEMA and the cross-linking through EGDMA. In addition, three characteristic bands of DEVP indicating the grafting of DEVP appear in the spectrum of IIP-BSG at  $1247$ ,  $1032$ , and  $960\text{ cm}^{-1}$ , which are assigned to the P=O stretching vibration, the asymmetric vibration ( $\nu_{\text{as}}$ ) of P–O–C coupled with the stretching vibration of C–O–C, and the second  $\nu_{\text{as}}(\text{P–O–C})$ , respectively.<sup>[313,314]</sup> Moreover, compared to the IIP-Polymer spectrum, a new absorption band at  $1541\text{ cm}^{-1}$  assigned to the vibration of aromatic rings present in lignin of BSG is observed in the IIP-BSG spectrum.<sup>[224]</sup> It is speculated that the grafted HEMA and DEVP would provide multi-point interactions with the uranyl ion-template to form the selective adsorption sites with increased affinity.

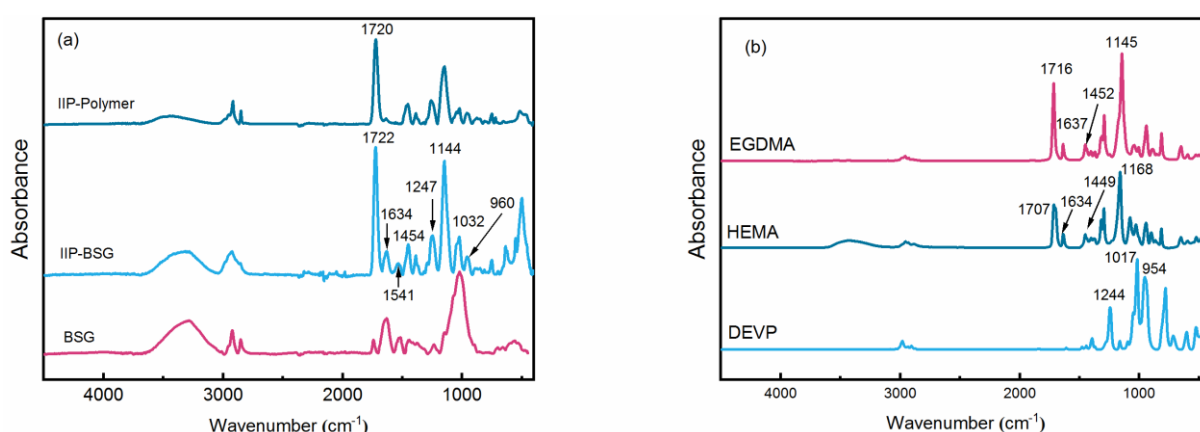
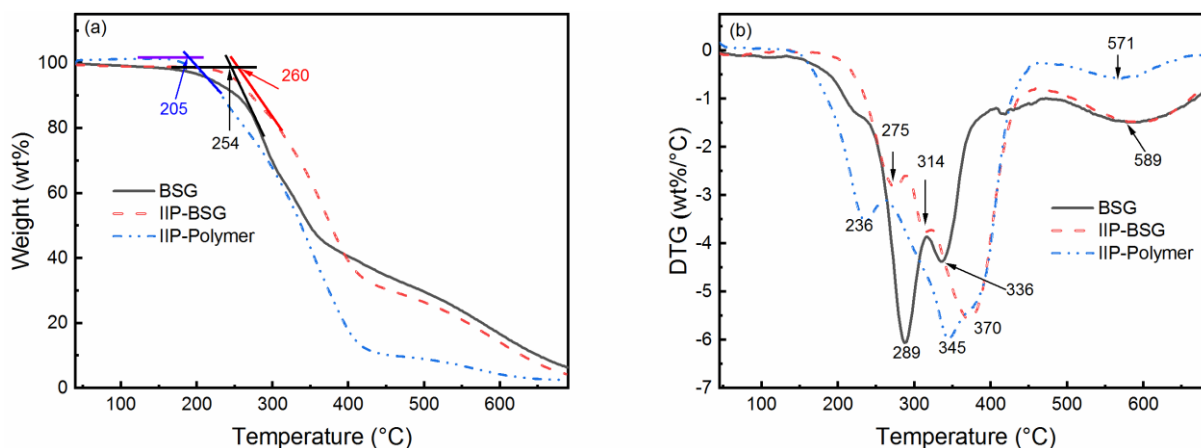


Fig. 6.4. FT-IR spectra of BSG, IIP-BSG, and IIP-Polymer.

In general, radioactive wastewater can have relatively high temperature under certain circumstances due to the fission of radionuclides, so thermal stability is one of the most

important physicochemical properties for evaluating adsorption performance.<sup>[315]</sup> Thus, the TG and DTG curves of BSG, IIP-BSG and IIP-Polymer were recorded in Fig. 6.5, and the DSC thermograms are given in Fig. 6.6. The extrapolated onset temperature (260 °C) of IIP-BSG is significantly higher than that of the IIP-Polymer (205 °C) and close to that of BSG (254 °C), which indicates that using BSG as the carrier has improved the thermal stability of imprinted polymer (Fig. 6.5, a). This is beneficial for its application to purify the uranium containing wastewater under certain circumstances.<sup>[315]</sup> The IIP-Polymer shows one sharp peak at 236 °C due to the ethylene cleavage of poly(DEVP) by elimination.<sup>[316]</sup> Another sharp peak at 345 °C is attributed to the depolymerisation of poly(HEMA) to HEMA monomer<sup>[317]</sup> and the breakdown of ester bonds in HEMA and EGDMA.<sup>[318]</sup> They are followed by a third DTG peak at 571 °C, which is attributed to the decomposition of polymer backbone.<sup>[316,318]</sup> Two sharp DTG peaks of the IIP-BSG curve occur after the onset temperature compared to the IIP-Polymer. The ethylene cleavage of poly(DEVP) (275 °C) and structural breakdown of HEMA and EGDMA (314 °C) indicate that grafting of HEMA and DEVP is successful. The new DTG peak at 370 °C is due to the cleavage of glycosidic linkages (C–O–C), causing depolymerisation of the BSG backbone.<sup>[217]</sup> Moreover, the fourth DTG peak at 589 °C results from the decomposition of support (BSG) and the polymer backbone. In addition, the DSC thermograms (Fig. 6.6) show that the decomposition of IIP-Polymer is exothermic over the whole temperature range. In contrast, the exothermic events between 40–300 °C for BSG and IIP-BSG are associated with several processes releasing decomposition products like CO<sub>2</sub> and CO as discussed for the first DTG peak.<sup>[319]</sup> The endothermic event at higher temperature (300–600 °C) is attributed to decomposition of the carbon backbone.



**Fig. 6.5.** (a) TG curves, and (b) DTG curves of BSG, IIP-BSG, and IIP-Polymer (10 °C/min, helium atmosphere).

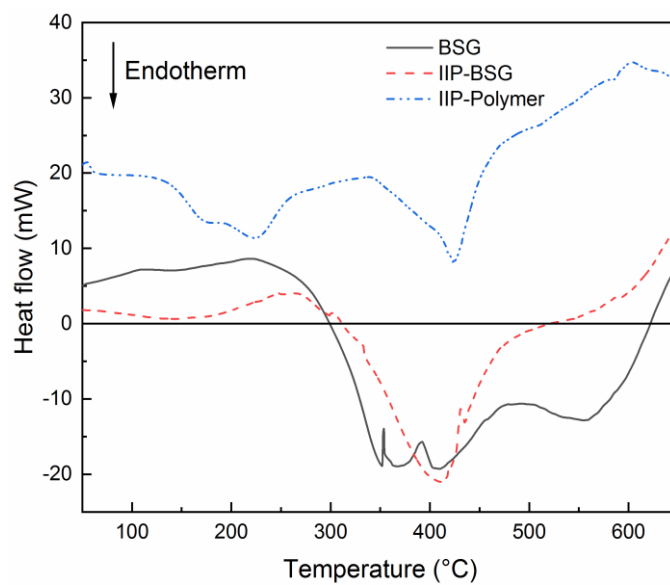


**Fig. 6.6.** DSC thermograms of BSG, IIP-BSG, and IIP-Polymer. For TG-DSC analysis: 10 °C/min, helium atmosphere.

## 6.3. Batch adsorption experiments

### 6.3.1 Adsorption kinetics and mass transfer mechanisms

For the removal uranium from wastewater, adsorption rates and mass transfer mechanisms are important for possible scaling up and implementation of future adsorption systems.<sup>[320]</sup> The influence of the contact time on the adsorption capacity of IIP-BSG at low ( $c_0(\text{U}) = 0.5 \text{ mM}$ ) and high ( $c_0(\text{U}) = 1.2 \text{ mM}$ ) initial concentrations of U(VI) is shown in Fig 6.7, a. For both initial concentrations, the amount of U(VI) adsorbed onto IIP-BSG increases as the contact time increases, and the adsorption equilibrium is reached at 90 min. Using the pseudo-first order (equation (22), see Section 10.5.1) and pseudo-second order (equation (24), see Section 10.5.1) kinetic models<sup>[194]</sup> to fit the kinetic data at  $c_0(\text{U}) = 0.5 \text{ mM}$  yields very close results regarding the statistical parameters ( $R^2 = 0.9980$  for both models, Table 6.4). In addition, the comparison of the kinetic models (Table 6.5) does not provide clear results regarding which kinetic model fits the experimental data better. Compared with the pseudo-second order kinetic model ( $q_{e,cal2} = 73.6 \text{ mg/g}$ ), the equilibrium adsorption capacity calculated by the pseudo-first order kinetic model ( $q_{e,cal1} = 63.0 \text{ mg/g}$ ) is closer to the experimental value ( $q_{e,exp} = 63.9 \text{ mg/g}$ ), indicating a better performance of the pseudo-first order kinetic model. When  $c_0(\text{U}) = 1.2 \text{ mM}$ , the pseudo-first order kinetic model shows better fitting results than the pseudo-second order kinetic model, as indicated by the statistical parameters ( $R^2$  (coefficient of determination), RSS (Residual Sum of Squares) and  $\chi^2$  (Reduce Chi-square), Table 6.4) and the comparison results (Table 6.5). Studies investigating cellulose adsorbents have reported and discussed the dependency of fitting results on the initial concentration and the close fitting results of both pseudo kinetic models.<sup>[320]</sup> Therefore, there is a further need for mechanistic models that provide accurate information on the mechanisms of mass transfer.

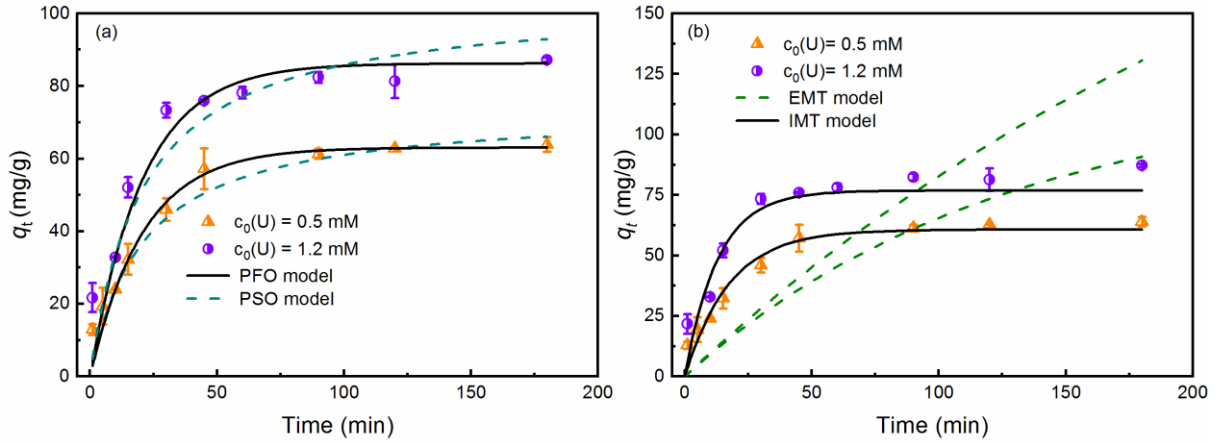


**Fig. 6.7.** Adsorption kinetics of U(VI) onto IIP-BSG and the fitting of (a) kinetic models and (b) mass transfer resistance models. For adsorption: 2 mg adsorbent/ 2mL solution,  $\text{pH}_0 = 4.7$ ,  $c_0(\text{U}) = 0.5$  and 1.2 mM.

**Table 6.4.** Fitting results of kinetic models for IIP-BSG. For adsorption: 2 mg adsorbent/ 2mL solution,  $\text{pH}_0 = 4.7$ ,  $c_0(\text{U}) = 0.5$  and 1.2 mM.

PFO model <sup>a</sup>	$k_1$ ( $\text{min}^{-1}$ )	$q_{e, \text{call}}$ (mg/g)	$q_{e, \text{exp}}$ (mg/g)	$R^2$	RSS	$\chi^2$
$c_0(\text{U}) = 0.5$ mM	0.0478	63.0	63.9	0.9980	48	6.9
$c_0(\text{U}) = 1.2$ mM	0.4805	86.2	87.2	0.9972	53	7.6
PSO model <sup>b</sup>	$k_2$ ( $\text{g} \cdot \text{mg}^{-1} \cdot \text{min}^{-1}$ )	$q_{e, \text{cal2}}$ (mg/g)	$q_{e, \text{exp}}$ (mg/g)	$R^2$	RSS	$\chi^2$
$c_0(\text{U}) = 0.5$ mM	$4.6 \times 10^{-4}$	73.6	63.9	0.9980	47	6.8
$c_0(\text{U}) = 1.2$ mM	$4.6 \times 10^{-4}$	103.6	87.2	0.9806	367	52

a) PFO model: pseudo-first order kinetic model; b) PSO model: pseudo-second order kinetic model.

**Table 6.5.** Comparison of the kinetic models for IIP-BSG.

	Model	RSS	AIC	Akaike's Weight	Preferred model	BIC	BIC difference	Preferred model
$c_0(\text{U}) = 0.5$ mM	PFO model	48	26.0	0.4732	No	21.8	0.2149	Inconclusive
	PSO model	53	25.8	0.5268	Yes	21.5	0	
$c_0(\text{U}) = 1.2$ mM	PFO model	47	26.7	0.9998	No	22.5	0	No
	PSO model	367	44.2	$1.6 \times 10^{-4}$	Yes	40.0	17.4516	Yes

a) PFO model: pseudo-first order kinetic model, b) PSO model: pseudo-second order kinetic model.

The above results indicate that the pseudo-first order kinetic model gives better results for IIP-BSG, suggesting that the diffusion process could be a rate-controlling step.<sup>[194]</sup> To further clarify the mechanisms of mass transfer, the external (EMT model, equation (28), see Section 10.5.2) and internal (IMT model, equation (29), see Section 10.5.2) mass transfer resistance models were employed.<sup>[321]</sup> Here, the Sips model was used to develop the mass transfer resistance models because it best describes the isotherm data (details discussed in Section 6.3.2). The internal mass transfer model shows a better fit ( $R^2 = 0.9261$  at  $c_0(\text{U}) = 0.5$  mM and  $R^2 = 0.8579$  at  $c_0(\text{U}) = 1.2$  mM), indicating that the internal mass transfer may be

the slowest step in the adsorption process (Fig. 6.7, b and Table 6.6). In addition, the SEM image of IIP-BSG (Fig. 6.8) shows a rough and irregular surface with some open pores, which is a possible cause of the internal mass transfer resistance when IIP-BSG swells in the metal solution as a cellulose-based material.<sup>[320]</sup>

**Table 6.6.** Fitting results of external (EMT) and internal (IMT) mass transfer resistance models for IIP-BSG. For adsorption: 2 mg adsorbent/ 2mL solution, pH<sub>0</sub> = 4.7, c<sub>0</sub>(U) = 0.5 and 1.2 mM.

	EMT model			IMT model		
	$k_{emt}$ (L·g <sup>-1</sup> ·min <sup>-1</sup> )	RSS	R <sup>2</sup>	$k_{imt}$ (min <sup>-1</sup> )	RSS	R <sup>2</sup>
c <sub>0</sub> (U) = 0.5 mM	0.0080	2784	0.1602	0.0487	245	0.9261
c <sub>0</sub> (U) = 1.2 mM	0.0036	8713	-0.9376	0.0727	639	0.8579

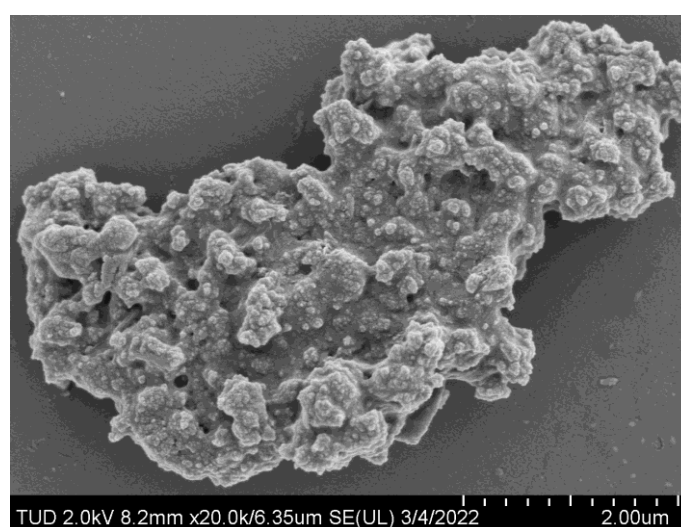


**Fig. 6.8.** SEM image of the IIP-BSG at 2.0 kV, magnification = 20,000 times.

In addition, the adsorption kinetic data of NIP-BSG were also collected at c<sub>0</sub>(U) = 1.2 mM as reference study. Fig. 6.9 shows that the adsorption equilibrium at c<sub>0</sub>(U) = 1.2 mM is reached at 2 h for NIP-BSG. The slower kinetics of NIP-BSG may be due to the higher equilibrium adsorption capacity of NIP-BSG (149 mg/g) than IIP-BSG (87.2 mg/g) and the high affinity of imprinted sites on IIP-BSG which facilitate fast adsorption.<sup>[291]</sup> The statistical parameters (Table 6.7) and the comparison results (Table 6.8) show that the pseudo-second order kinetic model has better fitting performance for NIP-BSG. However, the equilibrium adsorption capacity predicted by pseudo-first order kinetic model ( $q_{e,call} = 151$  mg/g) is closer to the experimental value ( $q_{e,exp} = 149$  mg/g) compared with the pseudo-second order kinetic model ( $q_{e,cal2} = 169$  mg/g). Thus, it is still possible that the diffusion step controls the adsorption on NIP-BSG, and the deceleration of adsorption indicated by the pseudo-second order kinetic

model may be due to depletion of the bulk concentration and the increased time to reach more remote binding sites.<sup>[320]</sup>

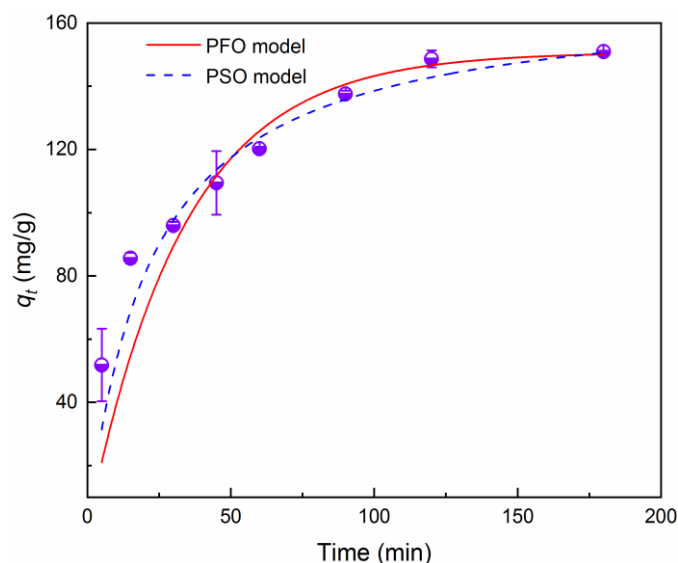


**Fig. 6.9.** Adsorption kinetics of U(VI) onto NIP-BSG and the fitting of kinetic models. For adsorption: 2 mg adsorbent/ 2mL solution,  $pH_0 = 4.7$ ,  $c_0(U) = 1.2$  mM.

**Table 6.7.** Fitting results of kinetic models for NIP-BSG. For adsorption: 2 mg adsorbent/ 2mL solution,  $pH_0 = 4.7$ ,  $c_0(U) = 1.2$  mM.

	$k$ ( $\text{min}^{-1}$ )	$q_{e,cal}$ (mg/g)	$q_{e,exp}$ (mg/g)	$R^2$	RSS	$\chi^2$
PFO model <sup>a</sup>	0.03	151	149	0.8992	465	77
PSO model <sup>b</sup>	$2.7 \times 10^{-4}$	169	149	0.9685	145	24

a) PFO model: pseudo-first order kinetic model; b) PSO model: pseudo-second order kinetic model.

**Table 6.8.** Comparison of the kinetic models for NIP-BSG.

Model	RSS	AIC	Akaike's Weight	Preferred model	BIC	BIC difference	Preferred model
PFO model <sup>a</sup>	465	45	0.0094	No	39	9.3	No
PSO model <sup>b</sup>	145	35	0.9906	Yes	29	0	Yes

a) PFO model: pseudo-first order kinetic model; b) PSO model: pseudo-second order kinetic model.

### 6.3.2 Adsorption isotherm

Fig. 6.10 displays the effect of equilibrium concentration on the adsorption capacity and selectivity of IIP-BSG in both U(VI) single and U(VI)/Eu(III) binary solution. An excellent selectivity of IIP-BSG is observed for U(VI) in the U(VI)/Eu(III) binary solution with equal molar concentrations ranging from 0.1 mM to 4.0 mM (Fig. 6.10, a). The recorded adsorption capacity of Eu(III) is less than 5 mg/g, which results in high selectivity coefficients of U(VI) ( $S_U$ ) of over 90%. The only exception is obtained at  $c_0 = 0.1$  mM ( $S_U = 84\%$ ) because of the low adsorption capacity of U(VI). In general, the adsorption capacity of IIP-BSG for U(VI) in the binary solution is lower than that in the single solution (Fig. 6.10, b). This is because Eu(III) ions in solution can act as additional cations, shielding the electrostatic attraction between U(VI) and the negatively charged IIP-BSG surface.<sup>[75]</sup> To investigate the adsorption mechanisms and the maximum adsorption capacities, three isotherm models, namely the Langmuir (equation (31)), Freundlich (equation (34)),<sup>[156]</sup> and Sips (equation (38))<sup>[322]</sup> models (see Section 10.5.3), were employed to fit the isotherm data (Fig. 6.10, b). The statistical parameters ( $R^2$ , RSS,  $\chi^2$ , Table 6.9) and the F-test results (Table 6.10) show that the Sips model is best at predicting the isotherm data, suggesting a monolayer adsorption of U(VI) on the heterogeneous adsorbent IIP-BSG.<sup>[199]</sup>

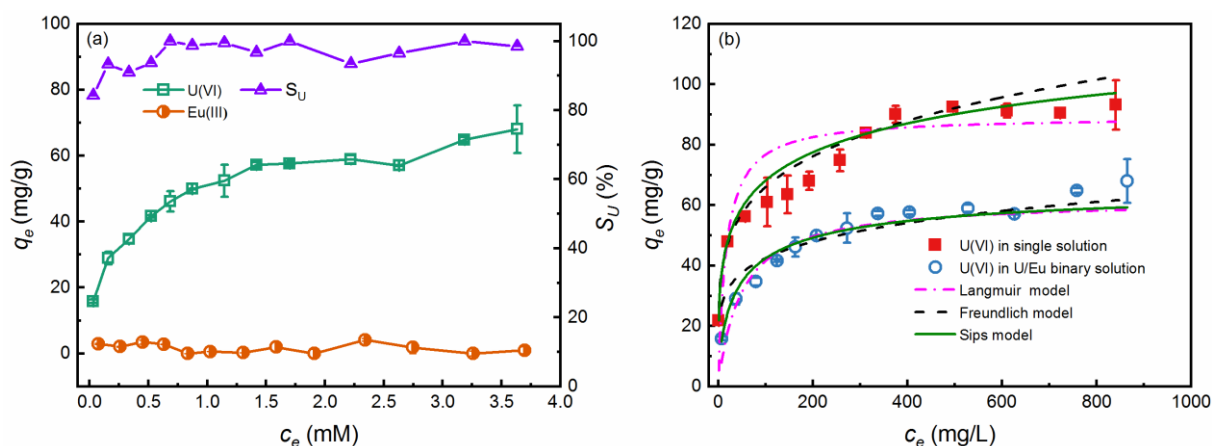


**Fig. 6.10.** (a) Effect of equilibrium concentration ( $c_e$ ) on the adsorption capacity ( $q_e$ ) and selectivity ( $S_U$ ) of IIP-BSG in the U(VI)/Eu(III) binary solution and (b) U(VI) adsorption isotherms and model fitting in U(VI) single and U(VI)/Eu(III) binary solutions. For adsorption, 2 mg adsorbent/ 2mL solution,  $\text{pH}_0 = 4.7$ ,  $t = 90$  min, for binary solution U/Eu molar ratio = 1.



**Table 6.9.** Fitting results of isotherm models for IIP-BSG. For adsorption, 2 mg adsorbent/ 2mL solution, pH<sub>0</sub> = 4.7, t = 90 min, for U(VI)/Eu(III) binary solution U/Eu molar ratio = 1.

Model	Solution	Parameters					
		$R^2$	$k_L$ (L/mg)		$q_{max,L}$ (mg/g)	RSS	$\chi^2$
Langmuir	U(VI)	0.7935	0.061		89.3	2925	266
	U(VI)/Eu(III)	0.9485	0.020		61.7	373	34
		$R^2$	$k_F$ ((mg/g) (L/mg) <sup>1/n</sup> )		$n$	RSS	$\chi^2$
Freundlich	U(VI)	0.9827	25.4		4.8	245	22
	U(VI)/Eu(III)	0.8843	19.0		5.7	837	76
		$R^2$	$k_s$ (L <sup>ms</sup> ·mg <sup>-ms</sup> )	$m_s$	$q_{max,s}$ (mg/g)	RSS	$\chi^2$
Sips	U(VI)	0.9958	0.151	0.33	165.7	60	6
	U(VI)/Eu(III)	0.9724	0.074	0.68	67.3	200	20

**Table 6.10.** Results of the F-test to compare the Sips model and Langmuir model for IIP-BSG.

		RSS	$N^a$	$p^b$	F	Prob>F
U(VI) single solution	Sips model	60	13	3	447.4	$9.02 \times 10^{-10} < 0.05^a$
	Langmuir model	2925	13	2		
U(VI)/Eu(III) binary solution	Sips model	200	13	3	8.6	$0.015 < 0.05^a$
	Langmuir model	373	13	2		

a). Number of data points, b) number of parameters, and c) at the 0.05 significance level, the Sips model is more likely to be correct.

Additionally, the adsorption isotherm of NIP-BSG in U(VI) single solution was also recorded as a reference study. Fig. 6.11 shows that the adsorption capacity of NIP-BSG for U(VI) increases with increasing equilibrium concentration and then reaches a plateau. The Langmuir and Freundlich models present poor results for the adsorption isotherm data of NIP-BSG with low  $R^2$  (<0.92) and large error functions, and the fitting of Sips model is reduced to the same as the Freundlich model (Table 6.11). On the contrary, the piecewise linear isotherm model (equation (39), see Section 10.5.3) could fit the data well,<sup>[323]</sup> showing a high  $R^2$  (0.9977) for the linear increase step ( $c_e \leq c_m = 267$  mg/L). Thus, the maximum adsorption capacity of NIP-BSG for U(VI) is estimated to be 202 mg/g. This indicates that the adsorption of U(VI) onto NIP-BSG is caused by electrostatic and Van-der-Waals interactions.<sup>[199]</sup>

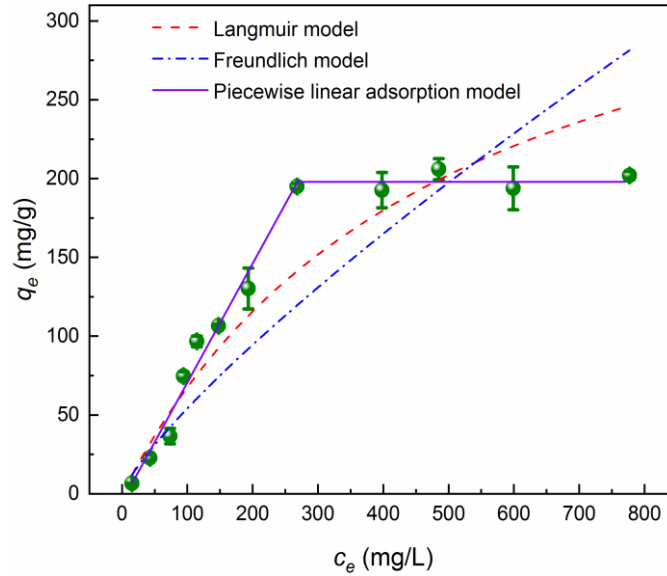


**Fig. 6.11.** Effect of equilibrium concentration ( $c_e$ ) on the adsorption capacity ( $q_e$ ) of NIP-BSG in U(VI) single solution and model fitting. For adsorption, 2 mg adsorbent/ 2mL solution,  $\text{pH}_0 = 4.7$ ,  $t = 2$  h.

**Table 6.11.** Fitting results of isotherm models for NIP-BSG. For adsorption, 2 mg adsorbent/ 2mL solution,  $\text{pH}_0 = 4.7$ ,  $t = 2$  h.

Model	Parameters					
Langmuir	$R^2$	$k_L$ (L/mg)	$q_{max,L}$ (mg/g)	RSS	$\chi^2$	
	0.9167	0.002	404.5	2152	215	
Freundlich	$R^2$	$k_F$ ((mg/g) (L/mg) $^{1/n}$ )	$n$	RSS	$\chi^2$	
	0.8282	1.3	1.2	4439	444	
Piecewise linear isotherm	$R^2$ ( $c_e \leq c_m$ )	$k_D$ (L/g)	$c_m$ (mg/L)	$q_{max}$ (mg/g)	RSS	$\chi^2$
	0.9977	0.7554	267	202	44	- <sup>a</sup>

a). Not calculated.

Estimated by the Sips model, the maximum U(VI) adsorption capacity of IIP-BSG in the single and binary solution is 165.7 mg/g and 67.3 mg/g, respectively. Table 6.12 shows that the maximum adsorption capacity of IIP-BSG is higher than or within the range of most of the adsorbents reported in the literature, including the uranyl ion-imprinted adsorbents (e.g. IIP-SALO-VP, 98.5 mg/g),<sup>[324]</sup> the surface ion-imprinted cellulose (U(VI)-IIP, 134 mg/g),<sup>[293]</sup> super-microporous phosphazene-based covalent organic framework (MPCOF, 124 mg/g),<sup>[325]</sup> and amidoximated cellulose fiber membrane (PAO-CFs membrane, 53 mg/g).<sup>[78]</sup> Two reasons account for this performance. One is the formation of a polymeric film over the BSG carrier increasing the availability of active sites. Another is the development of specific cavities matching with uranyl ions, which facilitates the adsorption of the U(VI) ions.<sup>[326]</sup> Currently, the market value of BSG is \$0.1–\$0.2/kg for dry mass,<sup>[97]</sup> which is well below the commonly used biosorbent material, chitosan (\$10/kg).<sup>[244]</sup> More importantly, the synthesis of IIP-BSG involves

only a small number of U(VI) templates (M:T ratio = 500:1) compared with the predominantly reported M:T ratios of 2:1 to 15:1.<sup>[294,297,299,324]</sup> Inexpensive starting materials, a simple synthetic procedure, and minimal use of toxic templates significantly reduce costs and minimize pollution, making the selective removal of uranyl ions by IIP-BSG even more attractive.

**Table 6.12.** Comparison of IIP-BSG with other adsorbents reported in literature.

Adsorbent	M:T ratio	$q_{max}$ (mg/g)	Reference
IIP-BSG	500:1	166	Present study
U(VI)-IIP	4:1	134	[293]
IIP-SALO-VP	4:1	98.5	[324]
UIMM3	15:1	122.7	[299]
IIP <sub>3</sub>	4:1	133	[297]
U-CMC-SAL	Not reported	180	[201]
Surface IIP	2:1	35.9	[294]
PAO-CFs membrane	- <sup>a</sup>	53	[78]
MPCOF	- <sup>a</sup>	124	[325]
V <sub>2</sub> CT <sub>x</sub> nanosheets	- <sup>a</sup>	174	[327]

a)The adsorbents are not ion-imprinted.

### 6.3.3 Site energy distribution of IIP-BSG in single and binary solution

The heterogeneity of binding sites on IIP-BSG as indicated by the study of the Sips model is common in non-covalently prepared imprinted polymers.<sup>[328]</sup> There are several reasons for the heterogeneity of adsorption sites, such as the grafting of functional groups,<sup>[329]</sup> dissociation of the template-functional monomer aggregates during synthesis, collapse of the binding sites during elution, heterogeneity of supports,<sup>[330]</sup> low number of imprinted sites, and clusters formation during the adsorption.<sup>[331]</sup> The site energy distribution function for the Sips isotherm by the condensation approximation method (equation (40), see Section 10.5.4) is employed to characterize the heterogeneity of the binding sites and compare their binding affinity for U(VI) in the presence or absence of competing ions.<sup>[332]</sup> The site energy ( $E^*$ ) is the minimum binding energy when adsorption occurs at equilibrium concentration  $c_e$  (equation (41), see Section 10.5.4). In both U(VI) single and U(VI)/Eu(III) binary solutions, the  $E^*$  values decrease with the increase in adsorption capacity of U(VI) (Fig. 6.12, a). This indicates that the U(VI) ions are more inclined to be adsorbed on the high-energy sites, followed by the low-energy sites.<sup>[329]</sup> According to the literature, the high-energy sites generally correspond to the high affinity and specific adsorption sites in imprinted polymers, whereas the low-energy sites are associated to the non-specific sites.<sup>[331]</sup> The approximate site energy distributions ( $f(E^*)$ ),

(mg/g)(J/mol)) versus  $E^*$  in the U(VI) single and U(VI)/Eu(III) binary solutions is depicted in Fig. 6.12, b, in which the solid lines represent the site energy distributions within the experimental data range (Table 10.9). First, within the isotherm range, the site energy distribution in the binary solution is lower than that in the single solution, and the peak value of the distribution ( $F(E_0^*)$ ) is reduced by 16% in the binary solution (Table 6.13). More specifically, the average site energy ( $E_m$ , calculated according to equation (42), see Section 10.5.4) describing the interaction forces between U(VI) and IIP-BSG decreases slightly from 17.1 kJ/mol to 16.1 kJ/mol in the presence of Eu(III) (Table 6.13).<sup>[333]</sup> These observations are consistent with the decreased U(VI) adsorption capacity of IIP-BSG in the presence of Eu(III) (see Fig. 6.10, b).<sup>[334]</sup> Secondly, the energy distribution heterogeneity ( $\sigma_e^*$ , calculated according to equation (43) and (44), see Section 10.5.4)<sup>[333]</sup> decreases from 4.6 kJ/mol to 2.9 kJ/mol. This indicates that the Eu(III) ions would make the U(VI) ions more likely to be adsorbed on the adsorption sites with similar energies. Furthermore, the peak position ( $E_0^*$ ) of the site energy distribution shifts from 12.1 kJ/mol for the single solution to 17.3 kJ/mol for the binary solution. This shows that due to the effect of Eu(III), the uranyl ions tend to be adsorbed onto the high-energy (specific) sites in the binary solution. Similar reports have been made on the competitive adsorption of Cd and Zn for natural sediments.<sup>[334]</sup> This results indicate that in the single solution, both the specific and non-specific sites contribute to the adsorption capacity, whereas in the binary solution, most of the adsorption capacity is attributed to the specific sites from the IIT.

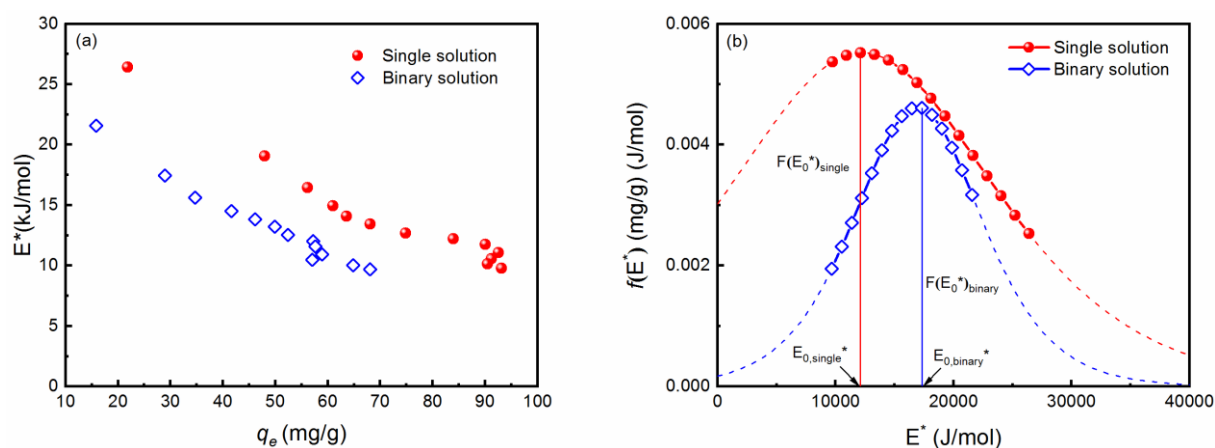


**Fig. 6.12.** (a) Site energy ( $E^*$ ) in dependent with the adsorption capacity ( $q_e$ ) of IIP-BSG in U(VI) single and U(VI)/Eu(III) binary solutions. For adsorption, 2 mg adsorbent/ 2mL solution,  $\text{pH}_0 = 4.7$ ,  $t = 90$  min, for binary solution U/Eu molar ratio = 1; and (b) the site energy distribution of IIP-BSG in the U(VI) single and U(VI)/Eu(III) binary solutions. The curves depicted in solid lines represent the site energy distributions in experimental data ranges: for single solution 9.8-26.4 kJ/mol and for binary solution 9.7-21.6 kJ/mol.

**Table 6.13.** Calculation results of the site energy distribution function.

	F(E <sub>0</sub> *) ((mg/g) (J/mol))	E <sub>m</sub> (kJ/mol)	σ <sub>e</sub> * (kJ/mol)	E <sub>0</sub> * (kJ/mol)
Single solution	0.0055	17.1	4.6	12.1
Binary solution	0.0046	16.1	2.9	17.3

### 6.3.4 Effect of pH on adsorption capacity and selectivity

The initial pH (pH<sub>0</sub>) of the metal solution determines both the species of metal ions and the surface charge of IIP-BSG, which shows great influence on the adsorption capacity (Fig. 6.13, a) and selectivity (Fig. 6.13, b) of the IIP-BSG. To avoid precipitation of the metal ions, the pH range in the present study is carefully chosen according to the calculation of Visual MINTEQ 3.1 software (Fig. 6.14, a).<sup>[14]</sup> Furthermore, the equilibrium pH values (pH<sub>e</sub>) of the metal solution are given in Table 6.14, and the point of zero charge (pH<sub>PZC</sub>) of IIP-BSG is determined in Fig. 6.14, b. The adsorption capacity of IIP-BSG for U(VI) rises with the increased pH<sub>0</sub>, reaching 57.8 mg/g in U(VI) single solution and 47.7 mg/g in U(VI)/Eu(III) binary solution at pH<sub>0</sub> = 4.7. The negatively charged surface of IIP-BSG when pH<sub>0</sub> > pH<sub>PZC</sub> (3.9) and the deprotonation of carboxyl groups, which increase the electrostatic interaction between the uranyl ions and IIP-BSG, may result in the enhanced adsorption capacity.<sup>[92]</sup> In addition, when pH rises to pH > 3.5, hydrolyzed species of U(VI) like (UO<sub>2</sub>)<sub>2</sub>(OH)<sub>2</sub><sup>2+</sup> and (UO<sub>2</sub>)<sub>3</sub>(OH)<sub>5</sub><sup>+</sup> appear together with UO<sub>2</sub><sup>2+</sup> (Fig. 6.14, a). As reported in the literature, the (UO<sub>2</sub>)<sub>2</sub>(OH)<sub>2</sub><sup>2+</sup> cation shows higher affinity toward the adsorbent surface compared with the unhydrolyzed UO<sub>2</sub><sup>2+</sup>, which also increases the adsorption capacity.<sup>[190]</sup> In the binary solution, the adsorption capacity of Eu(III) slightly increases from 0 to 4.6 mg/g, but the selectivity coefficient of U(VI) (*S<sub>U</sub>*%) remains above 90%. Therefore, IIP-BSG exhibits high selectivity under weakly acidic conditions, and considering the adsorption capacity, it is suitable for selective uranyl ion adsorption at pH<sub>0</sub> > 3.

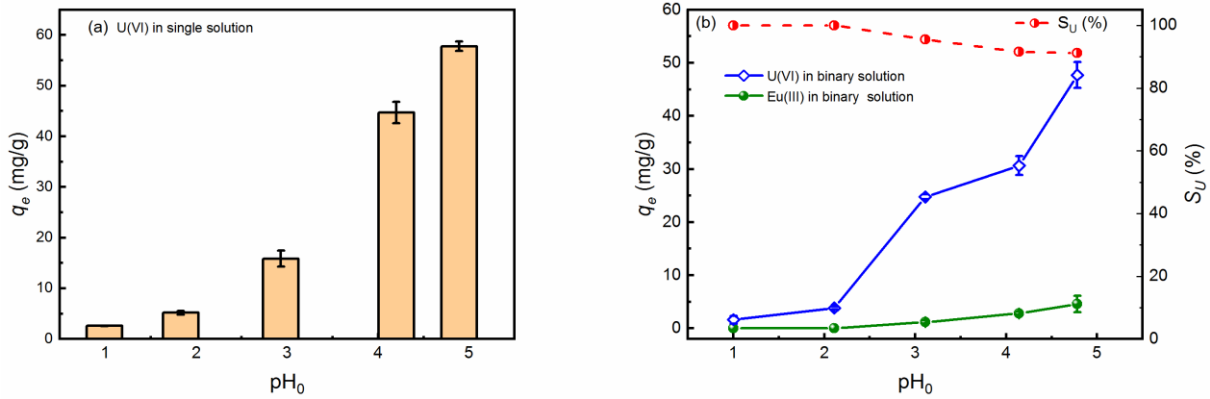


**Fig. 6.13.** Effect of  $pH_0$  on (a) the adsorption capacity of IIP-BSG in U(VI) single solution and (b) the selectivity of IIP-BSG in U(VI)/Eu(III) binary solution. For adsorption: 2 mg adsorbent/ 2mL solution,  $t = 90$  min, for single solution  $c_0(U) = 0.5$  mM, for binary solution  $c_0(U, Eu) = 0.5$  mM.

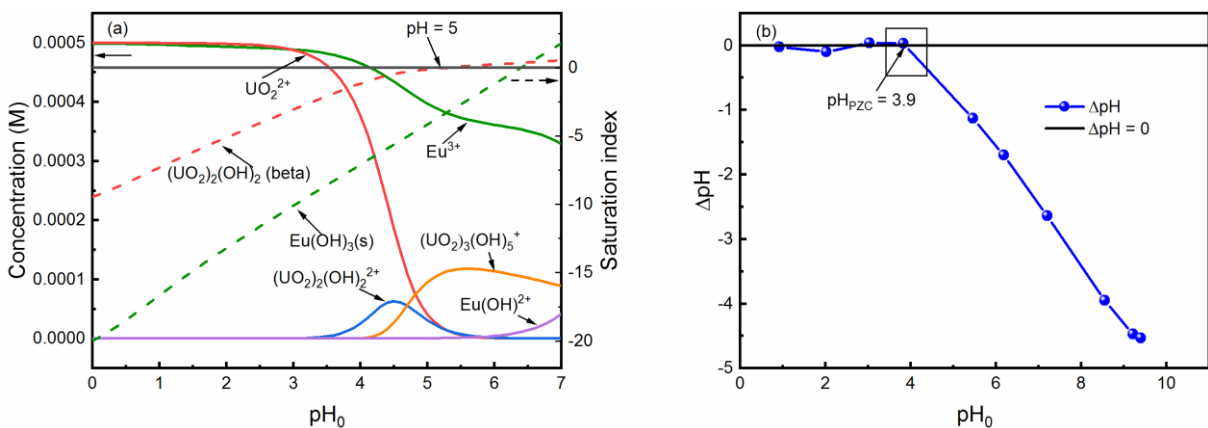


**Fig. 6.14.** (a) Species calculation of U(VI) and Eu(III) at 0.5 mM using Visual MINTEQ 3.1,<sup>[14]</sup> and (b) determination of point of zero charge ( $pHPZC$ ) of IIP-BSG.

**Table 6.14.** The initial ( $pH_0$ ) and equilibrium pH ( $pH_e$ ) values of the metal solution in the pH dependency studies.

U(VI) single solution		U(VI)/Eu(III) binary solution	
$pH_0$	$pH_e$	$pH_0$	$pH_e$
1.0	0.9	1.0	0.9
1.8	1.7	2.1	2.0
2.9	2.7	3.1	2.9
4.2	3.5	4.1	3.7
4.9	4.3	4.8	4.2

### 6.3.5 Effect of ionic strength and Eu(III)/U(VI) molar ratio

Because the uranium wastewater often contains high salinity, it is important to investigate the effect of ionic strength on the adsorption capacity of IIP-BSG for U(VI).<sup>[335]</sup> When the ionic strength increases from zero to 1.0 mol/L, the adsorption capacity decreases from 57.8 mg/g to 47.4 mg/g, keeping 82% of the adsorption capacity (Fig. 6.15, a). A high ionic strength may

shield the electrostatic effect between U(VI) and the IIP-BSG<sup>[173]</sup> and decreases the activity coefficient of the U(VI) ions, thereby limiting their transfer toward the adsorbent surface.<sup>[75]</sup> The correlation analysis shows that the adsorption capacity and the ionic strength are negatively correlated (Pearson's  $r = -0.9604$ ,  $p < 0.001$ ), indicating an outer-sphere complexation of U(VI) ions with the functional groups through electrostatic interaction.<sup>[336]</sup> Furthermore, the selectivity of IIP-BSG toward U(VI) was investigated with an excess amount of competing ions (Fig. 6.15, b). When the Eu/U molar ratio increases from 1 to 5, the adsorption capacity of U(VI) decreases from 47.7 mg/g to 34.2 mg/g. When the Eu/U molar ratio further increases up to 25, it only decreases slightly to 31 mg/g. Whereas, the adsorption capacity of Eu(III) is well below 6 mg/g within the experimental range, except at Eu/U molar ratio = 25 (12.1 mg/g). The results show that IIP-BSG exhibits a high selectivity for U(VI) ( $S_U > 80\%$ ) even when the molar concentration of Eu(III) is 20 times as high as U(VI). The good salinity tolerance and the high selectivity against an excess amount of competing ions of IIP-BSG may be due to the strong affinity of the imprinted adsorption sites from the multi-point interactions of HEMA and DEVP.<sup>[309]</sup> Therefore, it is proposed that the IIP-BSG could retain high adsorption capacity and selectivity in complex matrix, such as wastewater with high salinity and competing ions.

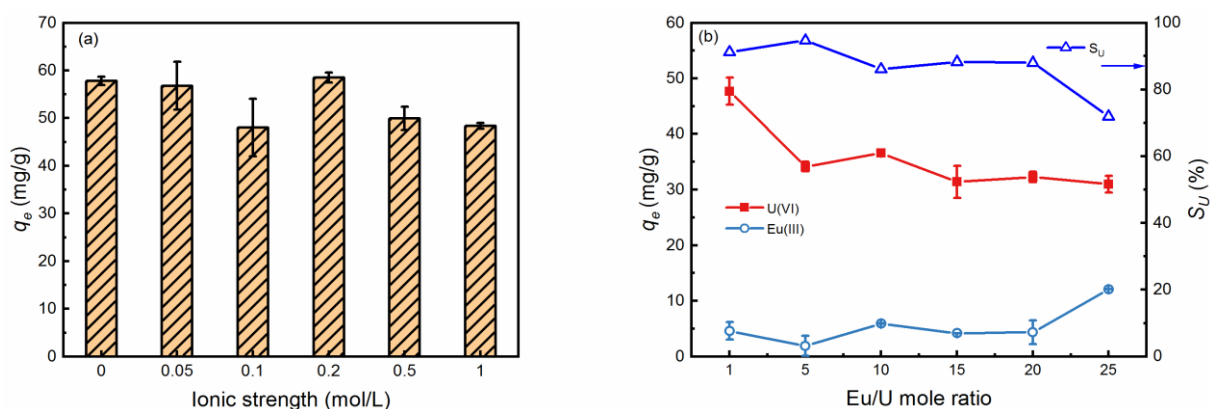


**Fig. 6.15.** (a) Effect of ionic strength on the adsorption capacity of IIP-BSG toward U(VI) and (b) effect of Eu/U molar ratio on the selectivity of IIP-BSG toward U(VI). For adsorption: 2 mg adsorbent/ 2mL solution,  $pH_0 = 4.7$ ,  $t = 2$  h. For (a)  $c_0(U) = 0.5$  mM,  $I = 0-1$  mol/L; for (b)  $c_0(U) = 0.5$  mM, Eu/U molar ratio = 1-25.

### 6.3.6 Desorption and reusability

The cost of practical uranium removal mainly depends on the reusability of adsorbents, including the adsorption capacity, selectivity and the desorption ratio of IIP-BSG during the adsorption-desorption cycles.<sup>[337]</sup> In the U(VI) single solution, no significant reduction in the adsorption capacity of IIP-BSG is observed after five cycles (Fig. 6.16, a). In the U(VI)/Eu(III) binary solution (Fig. 6.16, b), the adsorption capacity of U(VI) only decreases slightly at the fifth cycle (36.9 mg/g), keeping 90% of its capacity. Meanwhile, a high selectivity of  $S_U > 92\%$  is kept with the adsorption capacity of Eu(III)  $< 4$  mg/g throughout the experiments. Thus, no poisoning of the adsorbent is observed because few adsorption sites of IIP-BSG are occupied by the competing ions. The uranyl ions can be desorbed from the adsorbent surfaces using 0.5 M HCl via intense competition of  $H^+$  for the binding sites, indicating a surface complexation mechanism of U(VI).<sup>[338]</sup> In the single and binary solution, the desorption ratios are well above 80% during the five cycles (Fig. 6.16, b). Moreover, compared to the fresh prepared adsorbent ( $1.6 \pm 0.5$  mg/g), the P content in the IIP-BSG after five cycles (IIP-BSG-r,  $2.2 \pm 0.1$  mg/g) shows no significant change (Table 6.1), suggesting that IIP-BSG can be used for multi-cycles without losing functional groups. The excellent reusability of IIP-BSG may be attributed to the distribution of the adsorption sites within the thin polymer layer on the surface of BSG, which facilitates the regeneration and reuse of the adsorbent.<sup>[339]</sup> Since nearly 48% of the total cost for uranium removal and recovery is the cost of adsorbent,<sup>[80]</sup> an adsorbent such as IIP-BSG, which is stable enough to be used for five times and has no selectivity degradation and a degradation rate of no more than 2% adsorption capacity per cycle, would greatly improve cost-efficiency.

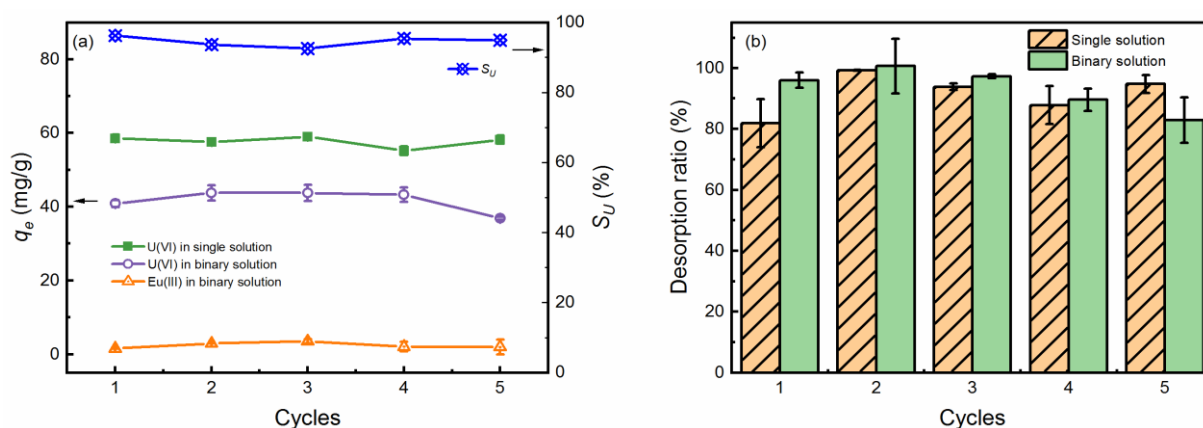


**Fig. 6.16.** (a) Adsorption capacity of IIP-BSG in U(VI) single solution and adsorption capacity and selectivity of IIP-BSG in U(VI)/Eu(III) binary solution, and (b) U(VI) desorption ratio of IIP-BSG in U(VI) single and U(VI)/Eu(III) binary solution for five cycles. For adsorption: 50 mg adsorbent/ 50 mL solution,  $pH_0 = 4.7$ ,  $t = 90$  min, for single solution  $c_0(U) = 0.5$  mM, for binary solution  $c_0(U, Eu) = 0.5$  mM. For desorption: 5 mg adsorbent/ mL HCl, 0.5M HCl,  $t = 2$  h.



## 6.4. Investigation of adsorption mechanisms

Adsorption of uranium on IIP-BSG surface is demonstrated by SEM/EDX analysis (Fig. 6.17). Even distributions of uranium (Fig. 6.17, b) together with oxygen (Fig. 6.17, c) and carbon (Fig. 6.17, d) originated from the adsorbents indicate strong interactions between the uranyl ions and functional groups. To further investigate the adsorption mechanisms, the FT-IR spectra of IIP-BSG and U(VI)-loaded IIP-BSG were recorded, and the detailed spectra between  $2000\text{ cm}^{-1}$  and  $400\text{ cm}^{-1}$  with a resolution of  $1\text{ cm}^{-1}$  are depicted in Fig. 6.18. Due to the interaction with U(VI) ions, the band intensity of  $\nu_{\text{as}}(\text{COO}^-)$  increases and the band assigned to  $\nu_{\text{s}}(\text{COO}^-)$  shifts from  $1454$  to  $1448\text{ cm}^{-1}$ . Due to the reduced symmetry of the functional groups, the difference between asymmetric and symmetric vibration of the carboxyl groups ( $\Delta\nu_{\text{as-s}}$ ) increases from  $180\text{ cm}^{-1}$  to  $188\text{ cm}^{-1}$  upon binding of U(VI),<sup>[170]</sup> indicating an electrostatic interaction with the metal center.<sup>[63]</sup> Furthermore, the band of  $\nu(\text{P}=\text{O})$  shifts slightly from  $1247\text{ cm}^{-1}$  to  $1245\text{ cm}^{-1}$ , and the intensity of the second band of  $\nu_{\text{as}}(\text{P}-\text{O}-\text{C})$  at  $960\text{ cm}^{-1}$  decreases significantly upon U(VI) loading. Both spectral changes indicate interactions between the phosphoryl groups and the uranyl ions. Moreover, the U=O stretching vibration ( $\nu_3(\text{U}=\text{O})$ ) is observed in the spectrum of U(VI)-IIP-BSG at  $916\text{ cm}^{-1}$ . When uranyl ions are bound by monocarboxylic ligands, the associated bands are typically observed at wavenumbers above  $920\text{ cm}^{-1}$ . Thus, the shift to  $916\text{ cm}^{-1}$  suggests a possible contribution from phosphoryl groups.<sup>[63]</sup> In conclusion, the electrostatic effect of carboxyl groups and the coordination by the phosphoryl groups provide multi-point interactions with uranyl ions, forming an outer-sphere coordination during the adsorption, as indicated by the ionic strength study (Section 6.3.5). Through the ion-imprinting technology, the selectivity is ensured by the tailor-made adsorption sites with size, shape, and geometry complementary to the uranyl ions.

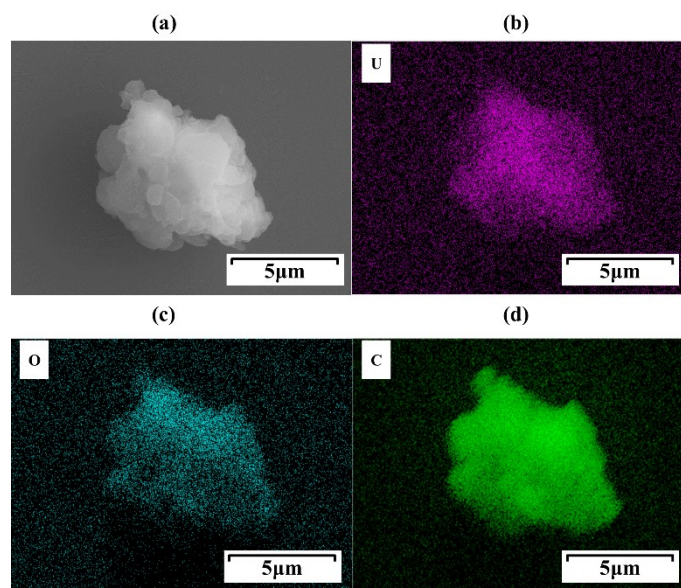


**Fig. 6.17.** (a) SEM image and the distributions of elemental (b) U, (c) O, and (d) C of U(VI)-IIP-BSG. SEM image was taken at 20 kV, magnification = 8,000 times, and EDX mappings were taken at 20 kV/15  $\mu$ A, magnification = 8,000 times, and 25 frames. For U(VI)-loading: 40 mg adsorbent/ 40 mL solution,  $c_0(\text{U}) = 500$  mg/L,  $\text{pH}_0 = 4.6$ ,  $t = 90$  min.

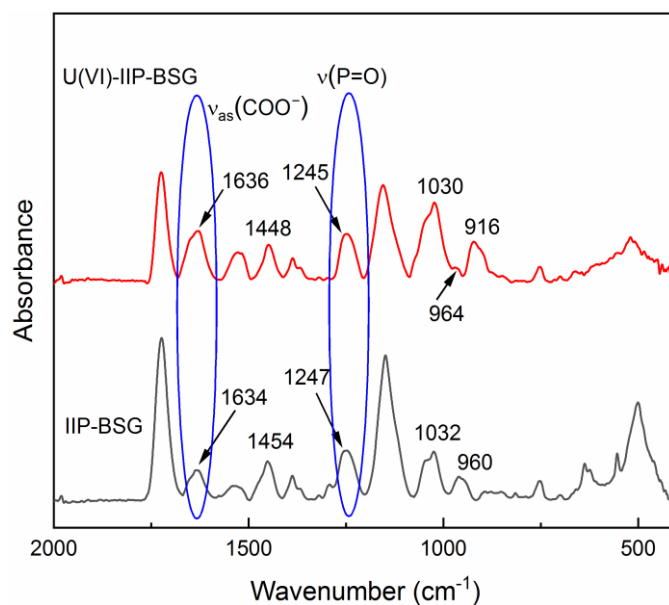


**Fig. 6.18.** FT-IR spectra of IIP-BSG and U(VI)-IIP-BSG. For U(VI)-loading: 40 mg adsorbent/ 40 mL solution,  $c_0(\text{U}) = 500$  mg/L,  $\text{pH}_0 = 4.6$ ,  $t = 90$  min.

## 7. Application of the BSG-derived adsorbents under real-world conditions

### 7.1. Adsorbent aging test

The aging of adsorbent in aqueous solution can affect its removal efficiency in practical application and is therefore significant to estimate the potential for multiple use. Herein, the effect of adsorbent aging on the adsorption capacity of BSG and its derived adsorbents in ultrapure water for 6 days was investigated, including hydrothermally treated BSG (ABSG), oxidized BSG (OBSG), highly cross-linked superabsorbent polymer supported BSG (BSG-SAP-H) and the imprinted BSG (IIP-BSG). The adsorption capacity of U(VI) was measured in duplicate and the data were subjected to an independent T-Test to determine whether there was a significant difference in the adsorption capacity before and after aging. As depicted in Fig. 7.1, after aging, BSG shows a decrease of 10% ( $p < 0.05$ ) in U(VI) adsorption capacity, which is probably due to loss of soluble components such as starch and amino acids.<sup>[98]</sup> ABSG has a higher affinity for U(VI), but aging results in a 60% decrease in adsorption capacity ( $p < 0.05$ ), indicating an unfavorable reusability. Presumably this is because of the solubilization of polysaccharides and associated phenolics after hydrothermal treatment, resulting in a loss of functional groups.<sup>[98]</sup> Nevertheless, due to their low-cost and availability, BSG and ABSG could be used as a one-time biosorbent for the removal of U(VI), which after adsorption could be either incinerated or disposed of in a landfill with low uranium loading<sup>[340]</sup> or used for uranium recovery with high loading.<sup>[341]</sup> In contrast, the adsorption capacity of OBSG shows no effect of the aging. The determined adsorption capacity increase slightly to  $157 \pm 3$  mg/g but is still within experimental error of  $153 \pm 8$  mg/g (before), indicating a great potential for multiple use. This is confirmed by the OBSG desorption and reusability study in the Section 4.5, where 60% of the original adsorption capacity is retained after five cycles. Despite a 6% decrease in adsorption capacity at a lower significant level ( $p < 0.1$ ), BSG-SAP-H was found to be reusable in the fixed bed column experiments in ultrapure water and simulated seawater, retaining 80–90% of its adsorption capacity (see Section 5.5.3) for four cycles. Moreover, aging has no influence on the adsorption capacity of IIP-BSG, which shows high adsorption capacity and selectivity after five cycles (see Section 6.3.6). Therefore, BSG and most of its derived adsorbents are expected to retain at least 90% of their adsorption capacity when subjected to an aquatic environment for 6 days. Hydrothermal treated BSG (ABSG) is the only exception that can be used only one time for a short period.

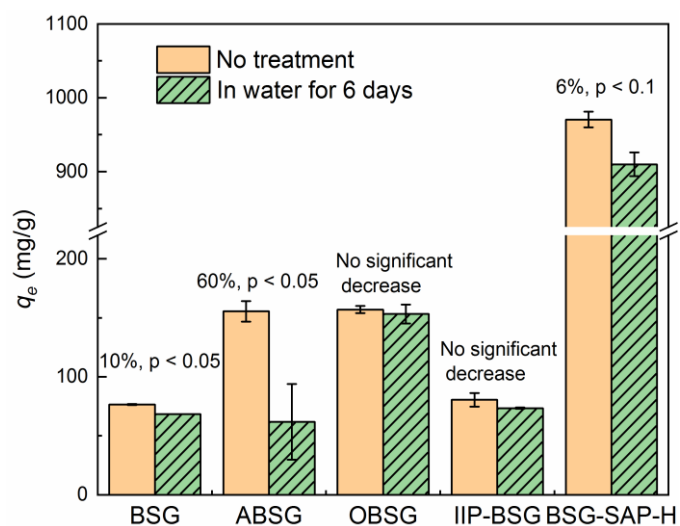


**Fig. 7.1.** Effect of adsorbent aging on the adsorption capacity of BSG and ABSG toward U(VI). For adsorption: 2 mg adsorbent/ 2 mL metal solution,  $c_0(\text{U}) = 300 \text{ mg/L}$  for BSG, ABSG, OBSG and IIP-BSG;  $c_0(\text{U}) = 1000 \text{ mg/L}$  for BSG-SAP-H;  $t_{\text{BSG}} = 2 \text{ h}$ ,  $t_{\text{ABSG}} = t_{\text{OBSG}} = 1 \text{ h}$ ,  $t_{\text{BSG-SAP-H}} = 45 \text{ min}$ ,  $t_{\text{IIP-BSG}} = 90 \text{ min}$ ,  $\text{pH}_0 = 4.6$ .

## 7.2. Adsorption test in simulated nuclear wastewater

Uranium containing wastewater is a complicated matrix with a number of competing ions whose concentrations are much higher than those of uranium and vary from case to case, which can negatively affect the efficiency of uranium removal and cause poisoning of the adsorbent.<sup>[299,309]</sup> To evaluate the performance and potential of the BSG and its derived adsorbents (ABSG, OBSG, BSG-SAP-H, IIP-BSG) in real-world conditions, the selectivity toward U(VI) in various simulated wastewater was tested in Section 7.2 and Section 7.3. In addition, the non-imprinted BSG (NIP-BSG) was tested as a reference to investigate the ion-imprinting effect. It should be noticed that the selectivity coefficient ( $S_U$  (%), equation (15), see Section 10.3.5) is less effective for describing the adsorption selectivity under these complex conditions because it cannot give a clear threshold value.<sup>[342]</sup> Therefore, the selective factor ( $k$ , equation (17), see Section 10.3.5) calculated from the distribution coefficient ( $K_d$  (mL/g), equation (16), see Section 10.3.5) was used in this section to describe the selectivity. It evaluates the adsorption affinity toward both the target and competing ions, and  $k > 1$  indicates that the adsorbent is selective.<sup>[342]</sup> The selectivity coefficients of U(VI) were also calculated in order to be consistent with results in the other sections of this study and to give additional information on the U(VI) selectivity.

With rapid development of the nuclear industry, toxic and low-level radioactive uranium-containing wastes from nuclear power plants have been released into the environment, accounting for most of the chemical toxicity in nuclear wastewater.<sup>[71,343]</sup> To mimic such a situation, a simulated nuclear wastewater containing 10 cations that found in nuclear power plant wastewater under weakly acidic conditions ( $\text{pH}_0 = 3.5$ , Table 10.5) is used for the selectivity test.<sup>[324]</sup> The adsorption capacity of OBSG for U(VI) (35 mg/g) is lower than that for Na(I) (40 mg/g), indicating poor selectivity (Fig. 7.2, a). Although BSG (18 mg/g), ABSG (76 mg/g), and BSG-SAP-H (227 mg/g) show a preference for U(VI) adsorption with the highest adsorption capacity among all the metal ions, their selectivity is hampered by co-adsorbing of competing ions, especially the rare earth and transitional metals show high distribution coefficients ( $K_d$ ). For example, the  $K_d$  value of BSG-SAP-H for Gd(III) is 2999 mL/g, while for U(VI) it is 3664 mL/g. The  $K_d$  value of ABSG for Ni(II) is 299 mL/g, while for U(VI) it is 500 mL/g (Fig. 7.2, b). Table 7.1 shows that BSG has poor U(VI)/Ni(II) selectivity and OBSG has a poor U(VI)/Na(I) selectivity. In contrast, ABSG has the best performance among the adsorbents without intentionally tailing the structure for improved selectivity during the synthesis. A determined adsorption capacity of ABSG for U(VI) of

76 mg/g, selective factors ( $k$ ) over 1 for all the competing ions, and a high selectivity coefficient ( $S_U = 61.7\%$ ) shows certain potential for uranium removal from nuclear wastewater. The adsorption capacity of IIP-BSG in simulated nuclear wastewater is 31 mg/g for U(VI) and lower than 2 mg/g for all the competing ions (Fig. 7.2, a). The  $K_d$  value of IIP-BSG for all other competing ions are lower than 35 mL/g, while for U(VI) is 200 mL/g. Moreover, IIP-BSG shows the best performance among all adsorbents with U(VI) selective factors higher than 6 for all elements and up to 53 against Co(II) and 32 against Sm(III), indicating a potential U(VI)/Ln(III) (e.g. La(III), and Nd(III), Sm(III)) separation from weak acidic nuclear wastewater (Table 7.1). Moreover, the calculated ion-imprinting factors ( $k'$ , equation (19), see Section 10.3.5) for most of the competing ions are greater than one, which indicates an efficient improvement in adsorption selectivity through the surface ion-imprinting technology (IIT) (Table 7.1). The only exception is Na, where no adsorption capacities were detected for both IIP-BSG and NIP-BSG in simulated nuclear wastewater. Hence, the values of  $k$  and  $k'$  cannot be calculated.

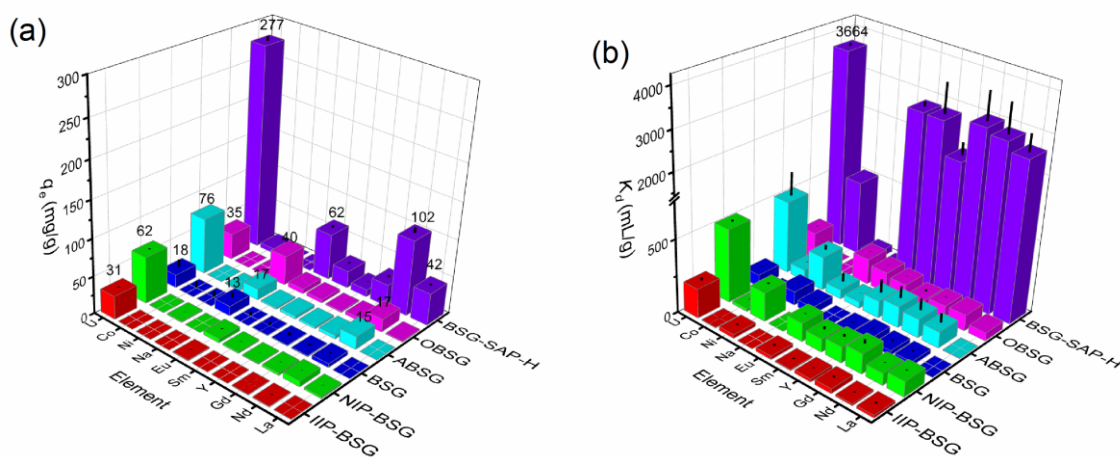


**Fig. 7.2.** (a) Adsorption capacity and (b) distribution coefficient of the BSG and BSG-derived adsorbents in simulated nuclear wastewater. For adsorption: 2 mg adsorbent/ 2 mL metal solution,  $t_{\text{BSG}} = 2$  h,  $t_{\text{ABSG}} = t_{\text{OBSG}} = 1$  h,  $t_{\text{BSG-SAP-H}} = 45$  min,  $t_{\text{IIP-BSG}} = 90$  min,  $t_{\text{NIP-BSG}} = 2$  h,  $\text{pH}_0 = 3.5$ .

**Table 7.1.** Selective factor ( $k$ ) and selectivity coefficient ( $S_U$ ) of the BSG and BSG-derived adsorbents in simulated nuclear wastewater. For adsorption: 2 mg adsorbent/ 2 mL metal solution,  $t_{\text{BSG}} = 2$  h,  $t_{\text{ABSG}} = t_{\text{OBSG}} = 1$  h,  $t_{\text{BSG-SAP-H}} = 45$  min,  $t_{\text{IIP-BSG}} = 90$  min,  $t_{\text{NIP-BSG}} = 2$  h,  $\text{pH}_0 = 3.5$ .

	k(BSG)	k(ABSG)	k(OBSG)	k(BSG-SAP)	k(IIP-BSG)	k(NIP-BSG)	$k'_{\text{IIP/NIP}}$
La(III)	- <sup>a</sup>	181.3	3.3	1.4	11.2	4.9	2.3
Nd(III)	2.8	4.6	1.7	1.3	17.7	6.3	2.8
Gd(III)	2.6	3.9	1.7	1.2	6.2	3.7	1.7
Y(III)	1.9	3.5	2.2	1.9	9.9	4.6	2.1
Sm(III)	4.7	4.3	1.5	1.3	31.7	5.6	5.6
Eu(III)	-	11.3	1.3	1.3	8.5	4.0	2.1
Na(I)	1.6	7.9	1.0	-	-	-	-
Ni(II)	0.9	2.2	-	78.1	7.9	2.6	3.1
Co(II)	-	6.5	-	7.2	53.4	24.8	2.2
$S_U$ (%)	45.3	61.7	32.0	50.4	87.9	72.4	1.2

a). The values of  $K_d$  become 0 and  $k$  become infinite as the adsorption capacity is zero.

### 7.3. Adsorption test in simulated mine and tailings water

The mining and processing of uranium ore is one of the main sources of uranium pollution of water bodies. Between 1945 and 1990, uranium mining in eastern Germany, especially in Saxony, created numerous mineshafts and mill tailings, from which the uranium is released and then transported with the water into the environment.<sup>[22]</sup> Bernhard et al. have reported on the detailed composition of mine and tailings water in Saxony, Germany, which was chosen as the reference for preparing simulated wastewater in the current study.<sup>[22]</sup> According to literature (Table 7.2),<sup>[22]</sup>  $\text{Ca}_2\text{UO}_2(\text{CO}_3)_3(\text{aq.})$  is the dominant species in carbonate- and calcium-containing mine water from Schlema at pH 7.1,  $\text{UO}_2(\text{CO}_3)_3^{4-}$  is the dominant species in carbonate-containing and calcium-poor tailings water from Helmsdorf at pH 9.8, and  $\text{UO}_2\text{SO}_4(\text{aq.})$  is the dominant species in sulfate-rich mine water from Königstein at pH 2.6. The detailed composition of the mine water from Schlema and Königstein, and the tailings water from Helmsdorf are summarized in Tables 10.6-10.8. Presumably, the pH, the predominant U(VI) species and the major competing cations and anions have a major influence on the selective adsorption of BSG and its derived adsorbents.

**Table 7.2.** Typical physiochemical properties and the dominant species of U(VI) of the mine and tailings water in Saxony, Germany.<sup>[22]</sup>

	Mine water	Mine water	Tailings water
Place	Schlema	Königstein	Helmsdorf
U(VI) (mmol/L)	0.021	0.073	0.025
pH	7.1	2.6	9.8
Characters	High content of $\text{Na}^+$ , $\text{SO}_4^{2-}$ , with $\text{CO}_3^{2-}$ and total organic carbon (TOC)	High content of $\text{SO}_4^{2-}$	High content of $\text{Na}^+$ , $\text{SO}_4^{2-}$ , $\text{Cl}^-$ , $\text{CO}_3^{2-}$ and TOC, contains $\text{AsO}_4^{3-}$ and $\text{PO}_4^{3-}$
Dominate species	$\text{Ca}_2\text{UO}_2(\text{CO}_3)_3(\text{aq.})$	$\text{UO}_2(\text{SO}_4)(\text{aq.})$	$\text{UO}_2(\text{CO}_3)_3^{4-}$

In the experiments with the simulated mine water from Schlema, an adsorption of Na(I), Ca(II) and Mg(II) is observed due to the high initial concentrations (200–600 mg/L) compared with U(VI) of 4.5 mg/L (see Fig. 7.3, a). Nevertheless, selectivity toward U(VI) is achieved for BSG and all derived adsorbents when the distribution coefficient of U(VI) is compared with the competing ions (Fig. 7.3, b), and the selective factors toward all competing ions are greater than 1 (Table 7.3). IIP-BSG shows the highest selectivity for U(VI) among all adsorbents with selective factors above 35 towards K(I), Na(I), Ca(II), and Mg(II). In addition, the calculated ion-imprinting factors ( $k'$ ) for all the competing ions are greater than 3, which indicates a



significant improvement in adsorption selectivity through the surface IIT in the Schlema mine water (Table 7.3). The U(VI) adsorption capacity of IIP-BSG (6.1 mg/g, Fig. 7.3, a) is limited due to the low initial concentration and the presence of the calcium uranyl carbonate complex  $\text{Ca}_2\text{UO}_2(\text{CO}_3)_{(\text{aq})}$  as the dominant species.<sup>[22]</sup> However, the high selectivity of IIP-BSG allows to concentrate U(VI) and reduce the concentrations of competing ions for further treatment. As shown in Table 7.4, a simple calculation employing the desorption condition and results of Section 6.3.6 (5 mg adsorbent/ mL HCl, desorption ratio = 80%) reveals that U(VI) could be enriched from 4.5 to 24.6 mg/L, while the concentrations of the competing ions are reduced to only  $\frac{1}{5}$  to  $\frac{1}{3}$  of their original concentrations. These results demonstrate a great potential of IIP-BSG for selective U(VI) removal from the wastewater.

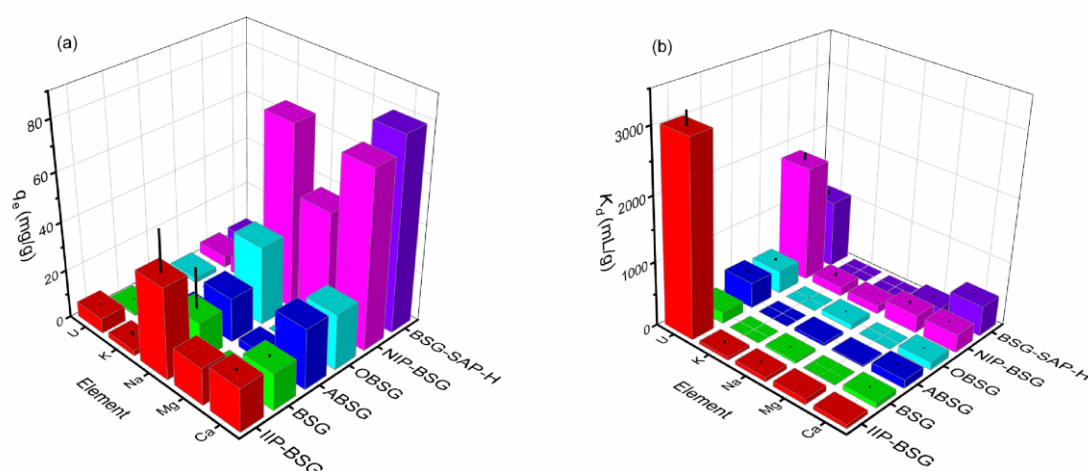


**Fig. 7.3.** (a) Adsorption capacity and (b) distribution coefficient of the BSG and BSG-derived adsorbents in Schlema mine water. For adsorption: 2 mg adsorbent/ 5 mL metal solution,  $t_{\text{BSG}} = 2$  h,  $t_{\text{ABSG}} = t_{\text{OBSG}} = 1$  h,  $t_{\text{BSG-SAP-H}} = 45$  min,  $t_{\text{IIP-BSG}} = 90$  min,  $t_{\text{NIP-BSG}} = 2$  h,  $\text{pH}_0 = 7.1$ .

**Table 7.3.** Selective factor ( $k$ ) and selectivity coefficient ( $S_U$ ) of the BSG and BSG-derived adsorbents in Schlema mine water. For adsorption: 2 mg adsorbent/ 5 mL metal solution,  $t_{\text{BSG}} = 2$  h,  $t_{\text{ABSG}} = t_{\text{OBSG}} = 1$  h,  $t_{\text{BSG-SAP-H}} = 45$  min,  $t_{\text{IIP-BSG}} = 90$  min,  $t_{\text{NIP-BSG}} = 2$  h,  $\text{pH}_0 = 7.1$ .

	$k(\text{BSG})$	$k(\text{ABSG})$	$k(\text{OBSG})$	$k(\text{BSG-SAP})$	$k(\text{IIP-BSG})$	$k(\text{NIP-BSG})$	$k'_{\text{IIP/NIP}}$
Ca(II)	2.2	3.0	3.0	2.3	47.5	6.5	7.4
Mg(II)	25.8	16.4	-	8.0	35.4	6.6	5.4
Na(I)	4.4	8.7	4.3	-	46.1	14.0	3.3
K(I)	- <sup>a</sup>	-	-	-	62.3	12.8	4.8
$S_U$ (%)	3.2	4.6	3.6	4.8	7.8	1.6	4.7

a). The values of  $K_d$  become 0 and  $k$  become infinite as the adsorption capacity is zero.

**Table 7.4.** Concentration effect of U(VI) and the reduction of competing ion concentrations by IIP-BSG in simulated Schlema mine water, and  $c_d$  (mg/L) is the metal ion concentration in the desorption solution, calculating using the conditions of 5 mg adsorbent/ mL HCl and desorption ratio = 80%.

Component	$c_0$ (mg/L)	$c_d$ (mg/L)
Ca(II)	289	72
Mg(II)	195	61
Na(I)	615	150
K(I)	51	9
U(VI)	4.5	24.6

The experiments with the simulated mine water from Königstein show that all BSG adsorbents exhibit selectivity for U(VI) over K(I), Na(I), Ca(II), and Mg(II) although there is significant adsorption of Na(I), Ca(II), and Mg(II) (Fig. 7.4). Surprisingly, due to its high selective factors ( $k > 5$ , Table 7.5) and adsorption capacity (28 mg/g), BSG could be used as a low-cost and readily available adsorbent to remove uranyl ions from the Königstein mine water without any modification. This is likely due to the ability to adsorb a sufficient amount of U(VI) at a low pH (2.6) using amide groups, as indicated by the study in Section 3.3.1 (Fig. 3.11). Moreover, although IIP-BSG presents good selectivity of U(VI) in the presence of competing ions, the ion-imprinting effect is not observed under the current condition except for K(I) ( $k' = 1.4 > 1$ ) due to a better performance of the non-imprinted BSG (NIP-BSG) (Table 7.5). The stronger electrostatic effect of the NIP-BSG compared to IIP-BSG originates from the physically bonded (non-specific) functional groups of NIP-BSG, which results in a higher adsorption capacity of U(VI) and accounts for the better selectivity of NIP-BSG. In addition, the competing ions in Königstein mine water have lower charge and smaller ionic radius compared with the rare earth metals in the acidic ( $\text{pH}_0 = 3.5$ ) simulated nuclear wastewater, which reduces their competing effect toward the non-specific sites on NIP-BSG.<sup>[190,258]</sup> This could probably explain the better selectivity of NIP-BSG in the Königstein mine water despite the lower pH.

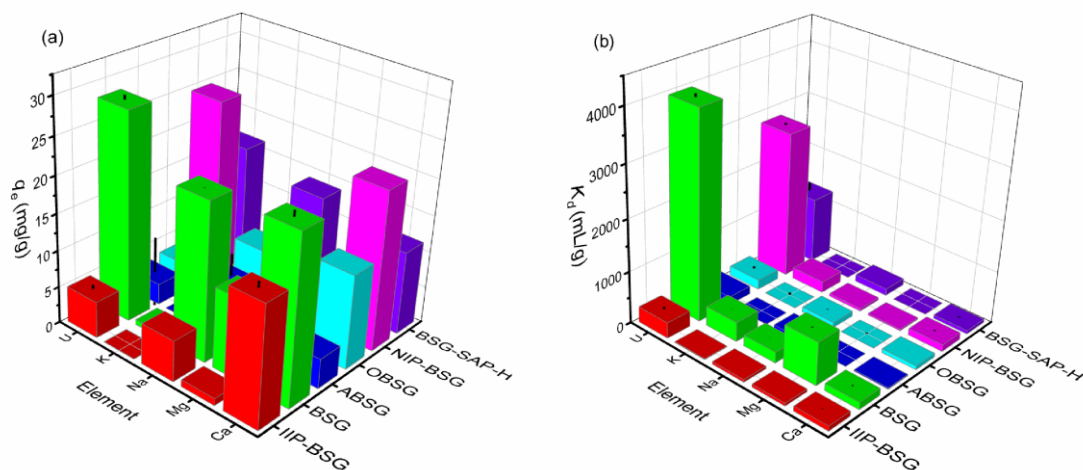


**Fig. 7.4.** (a) Adsorption capacity and (b) distribution coefficient of the BSG and BSG-derived adsorbents in Königstein mine water. For adsorption: 2 mg adsorbent/ 5 mL metal solution,  $t_{\text{BSG}} = 2$  h,  $t_{\text{ABSG}} = t_{\text{OBSG}} = 1$  h,  $t_{\text{BSG-SAP-H}} = 45$  min,  $t_{\text{IIP-BSG}} = 90$  min,  $t_{\text{NIP-BSG}} = 2$  h,  $\text{pH}_0 = 2.6$ .

**Table 7.5.** Selective factor ( $k$ ) and selectivity coefficient ( $S_U$ ) of the BSG and BSG-derived adsorbents in Königstein mine water. For adsorption: 2 mg adsorbent/ 5 mL metal solution,  $t_{\text{BSG}} = 2$  h,  $t_{\text{ABSG}} = t_{\text{OBSG}} = 1$  h,  $t_{\text{BSG-SAP-H}} = 45$  min,  $t_{\text{IIP-BSG}} = 90$  min,  $t_{\text{NIP-BSG}} = 2$  h,  $\text{pH}_0 = 2.6$ .

	$k(\text{BSG})$	$k(\text{ABSG})$	$k(\text{OBSG})$	$k(\text{BSG-SAP})$	$k(\text{IIP-BSG})$	$k(\text{NIP-BSG})$	$k'_{\text{IIP/NIP}}$
Ca	29.4	6.8	2.1	19.1	3.2	21.9	0.1
Mg	4.8	- <sup>a</sup>	-	-	5.5	100.7	0.05
Na	18.9	2.2	1.6	9.7	5.9	55.7	0.1
K	10.6	-	-	-	18.4	13.2	1.4
$S_U$ (%)	33.6	19.5	12.5	39.3	17.8	46.6	0.4

a). The values of  $K_d$  become 0 and  $k$  become infinite as the adsorption capacity is zero.

In addition, studies were carried out with simulated tailings water from Helmsdorf. The results depicted in Fig. 7.5 show that only IIP-BSG and NIP-BSG exhibit adsorption capacity for U(VI), which is probably due to the strong alkaline condition ( $\text{pH} = 9.8$ ), high salinity (2950 mg/L of Na(I)), and the highly negatively charged  $\text{UO}_2(\text{CO}_3)_3^{4-}$  species. Since all adsorbents have a point of zero charge ( $\text{pH}_{\text{PZC}}$ ) of less than 9.8, their surface is negatively charged and electrostatic repulsion hinders the adsorption of U(VI). Whereas, the adsorption capacity of IIP-BSG and NIP-BSG may originate from the coordination effect of the phosphoryl groups. As shown in Table 7.6, IIP-BSG shows excellent selectivity of U(VI) with the highest selective factor of 18.7 compared to Na(I) and a significant ion-imprinting effect is observed with  $k'$  up to 83 toward K(I). Both results indicate that the ion-imprinting technology could dramatically improve the selectivity of the adsorbents in Helmsdorf tailings water. Although

the adsorption capacity of IIP-BSG toward U(VI) is low (2.3 mg/g), it exceeds the sludge concentration (50 mg/kg) suggested by the U.S. EPA for uranium recovery.<sup>[340]</sup> The high selectivity of IIP-BSG allows to concentrate U(VI) and reduce the concentrations of competing ions for further recovery. As shown in Table 7.7, a simple calculation employing the desorption condition and results of Section 6.3.6 (5 mg adsorbent/ mL HCl, desorption ratio = 80%) reveals that U(VI) could be enriched from 4.5 to 9.2 mg/L, while the concentration of the Na(I) is reduced to only  $1/7$  of its original concentration.

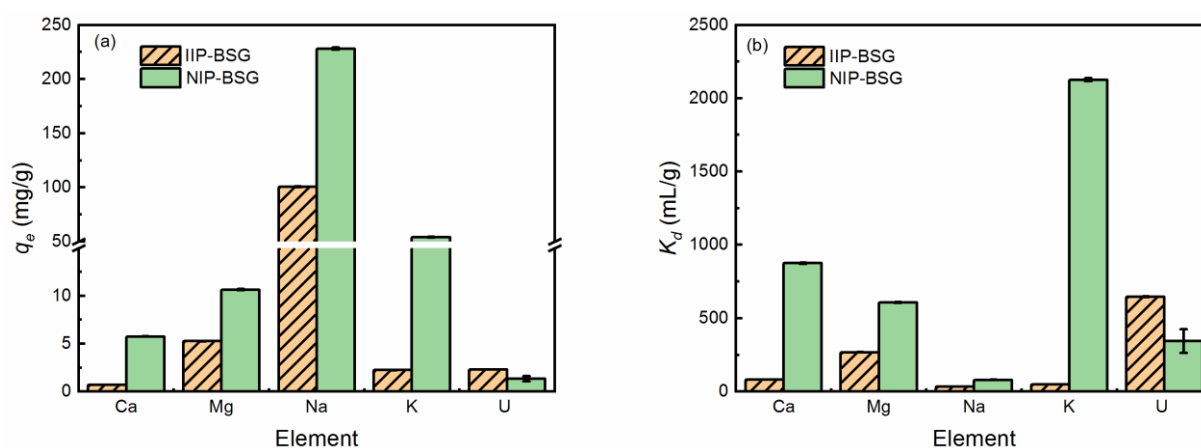


**Fig. 7.5.** Adsorption capacity and distribution coefficient of the IIP-BSG in Helmsdorf tailings water. For adsorption: 2 mg adsorbent/ 5 mL metal solution,  $t_{\text{IIP-BSG}} = 90$  min,  $t_{\text{NIP-BSG}} = 2$  h,  $\text{pH}_0 = 9.8$ .

**Table 7.6.** Selective factor ( $k$ ) and selectivity coefficient ( $S_U$ ) of the IIP-BSG and NIP-BSG in Helmsdorf tailings water. For adsorption: 2 mg adsorbent/ 5 mL metal solution,  $t_{\text{IIP-BSG}} = 90$  min,  $t_{\text{NIP-BSG}} = 2$  h,  $\text{pH}_0 = 9.8$ .

	$k(\text{IIP-BSG})$	$k(\text{NIP-BSG})$	$k'_{\text{IIP/NIP}}$
Ca	7.9	0.4	20
Mg	2.4	0.6	4
Na	18.7	3.0	6
K	13.3	0.16	83
$S_U$ (%)	2.1	0.35	6

**Table 7.7.** Concentration effect of U(VI) and the reduction of competing ion concentrations by IIP-BSG in simulated Helmsdorf tailings water, and  $c_d$  (mg/L) is the metal ion concentration in the desorption solution, calculating using the conditions of 5 mg adsorbent/ mL HCl and desorption ratio = 80%.

Component	$c_0$ (mg/L)	$c_d$ (mg/L)
Ca(II)	9	2.8
Mg(II)	23	21.1
Na(I)	2950	402.7
K(I)	37.6	9.0
U(VI)	4.5	9.2



## 8. Summary

In the present work, BSG was successfully converted into effective uranium adsorbents using various approaches, including hydrothermal treatment (ABSG), nitro-oxidation (OBSG), graft polymerization (BSG-SAP-H) and surface ion-imprinting technology (IIP-BSG). In this chapter, the results are summarized and important conclusions are drawn out from four perspectives, namely the modification methods, the adsorbent properties, the adsorption mechanisms, and the performance under real-world conditions.

**(1). Modification methods:** In the first part of the study, BSG is successfully converted into an effective biosorbent ABSG by mild hydrothermal treatment (150 °C, 16 h). This is done at a significantly lower temperature than conventional hydrothermal treatment without an additional activation process, minimizing energy consumption and environmental impact during treatment. Maillard reaction with the formation of melanoidins plays an important role in increasing the adsorption capacity, along with other pathways such as dehydration, decarboxylation, aromatization and oxidation. Thus, ABSG has an increase in carboxyl groups content from 0.15 mmol/g (BSG) to 1.46 mmol/g with increasing adsorption capacity. The second part of the study shows for the first time the successful oxidization of BSG with 85 wt% H<sub>3</sub>PO<sub>4</sub> and NaNO<sub>2</sub>, resulting in an increase in carboxyl groups content from 0.15 mmol/g in BSG to 1.3 mmol/g in OBSG and an increase in adsorption capacity. In the third part of this study, a biomass-supported superabsorbent polymer (BSG-SAP) is prepared by a one-pot swelling and grafting polymerization. A 7 wt% NaOH solution was used as the swelling agent for BSG and the neutralization agent for AA without producing alkaline wastewater. Biomass utilization and grafting polymerization allow a large increase in available hydroxyl, carboxyl and amide groups, leading to a highly cross-linked and strongly hydrophilic 3D polymer network of BSG-SAP. This enables BSG-SAP with higher adsorption capacity and better reusability compared to the pure polymer reference, especially the BSG-SAP prepared with high cross-linking density (BSG-SAP-H). The fourth part of the work describes a new strategy to prepare a surface ion-imprinted natural polymeric material (IIP-BSG) for the removal of uranyl ions from wastewater with higher selectivity compared with the non-imprinted BSG. The difficulties of template removal, template bleeding, and poor accessibility of the imprinted sites of the conventional ion-imprinted polymers are overcome by the IIP-BSG, which is prepared with a much higher monomer-to-template ratio (M:T ratio, 500:1) compared to the literature (common M:T ratio = 4:1). The prepared IIP-BSG shows excellent selectivity towards U(VI).

**(2). Adsorbent properties:** The basic properties of the prepared adsorbents derived from BSG such as adsorption kinetics, adsorption capacity, selectivity, salinity tolerance, aging of adsorbent, and reusability, etc. are listed in Table 8.1. All adsorbents prepared from BSG show higher adsorption capacity and faster mass transfer than the unmodified BSG, indicating efficient improvement of adsorbents properties. In terms of adsorption capacity, the graft polymerization method leads to a significant improvement in adsorption capacity from 96 mg/g of BSG up to 1465 mg/g for BSG-SAP-H, which is due to a large amount of carboxyl groups and a 3D polymer network. The surface ion-imprinting technology with a high monomer: template ratio of 500:1 generates the IIP-BSG with the best selectivity under various conditions. OBSG (10.8 mg/g for  $c_0(\text{U}) = 10 \text{ mg/L}$ ,  $\text{pH}_0 = 7.7$ ) and BSG-SAP-H (17.6 mg/g for  $c_0(\text{U}) = 8 \text{ mg/L}$ ,  $\text{pH}_0 = 8$ ) both show good salinity tolerance in the simulated seawater (193 mg/L  $\text{NaHCO}_3$  and 25.6 g/L  $\text{NaCl}$ ). IIP-BSG was able to retain 82% of its initial adsorption capacity for U(VI) (57.8 mg/g) up to an ionic strength of 1 mol/L. Moreover, at least 90% of the adsorption capacity for BSG (77 mg/g), OBSG (157 mg/g), BSG-SAP-H (970 mg/g) and IIP-BSG (80 mg/g) was retained when exposed to the water bodies for 6 days. ABSG, on the other hand, loses 60% of its adsorption capacity (155 mg/g) after aging, indicating a low potential for reuse. Moreover, 0.1M HCl was chosen as the desorption condition. OBSG retained 60% of its adsorption capacity (167 mg/g) after five reuse cycles, and the IIP-BSG retained over 90% of its adsorption capacity (41 mg/g) with high selectivity ( $S_U > 92\%$ ). The BSG-SAP-H could be used in both water spiked with U(VI) and simulated seawater for four cycles with high stability. The uranyl ions could be concentrated by the BSG-SAP-H up to 14.6 folds in the water spiked with U(VI) and 13 folds in simulated seawater in the fixed bed column experiments, which is favorable for further recovery of uranium.



**Table 8.1.** Summary of the basic information of the BSG-derived adsorbents in the current study.

Adsorbents	BSG	ABSG	OBSG	BSG-SAP-H	IIP-BSG
Modification method	None	Hydrothermal treatment	Nitro-oxidation	Graft polymerization	Surface ion-imprinting
Equilibrium time (min)	120	60	60	45	90
$q_{max}(U)$ (mg/g)	96 <sup>a</sup>	220.6 <sup>a</sup>	297.3 <sup>b</sup>	1465 <sup>c</sup>	165.7 in single solution and 67.3 in U(VI)/Eu(III) binary solution <sup>d</sup>
Point of zero charge (pH <sub>PZC</sub> )	5.7	4.1	2.1	6.2	3.9
Salinity tolerance	Not studied	Not studied	10.8 mg/g in simulated seawater (c <sub>0</sub> (U) = 10 mg/L)	17.6 mg/g in simulated seawater (c <sub>0</sub> (U) = 8 mg/L)	82% up to 1 mol/L
Adsorbent aging	10%, p < 0.05 <sup>e</sup>	60%, p < 0.05 <sup>e</sup>	No decrease	6%, p < 0.1 <sup>g</sup>	No decrease
Reusability	Not studied	Not studied	Five cycles <sup>f</sup>	Four cycles <sup>g</sup>	Five cycles <sup>f</sup>

a). Estimated from the Langmuir model; b). Obtained from the isotherm study; c). Estimated from the Toth model; d). Estimated from the Sips model; e) T-test, f). In bath experiments, and g). In fixed bed column experiments.

**(3). Adsorption mechanism:** Mechanistically, the adsorption of U(VI) on BSG and ABSG is a monolayer adsorption whose adsorption rate is controlled by the adsorption on active sites. Although no spectral information was obtained for BSG, the results of ABSG indicate the involvement of O-containing and N-containing functional groups (e.g. carboxyl, hydroxyl and amide groups). The adsorption of U(VI) on OBSG is a multilayer adsorption on the heterogeneous surface of OBSG via the proton exchange effect and a bidentate coordination of  $UO_2^{2+}$  by the carboxyl groups, whose adsorption rate is controlled by the diffusion step. Moreover, a monolayer adsorption occurs on the heterogeneous surface of BSG-SAP, which is dominated by the electrostatic interactions between  $UO_2^{2+}$  and the carboxyl groups, the coordination of amide groups, and the cation exchange between  $Na^+$  and  $UO_2^{2+}$ , the adsorption rate of which is controlled by the adsorption on active sites. In addition, studies of the mechanism of IIP-BSG have revealed the electrostatic interaction and a coordination of uranyl ions by carboxyl and phosphoryl groups, the predominant contribution of high-energy (specific) sites during selective adsorption, and internal mass transfer as the rate-controlling step of U(VI) adsorption (Table 8.2).

**Table 8.2.** Summary of the results that related to the adsorption mechanisms.

	BSG	ABSG	OBSG	BSG-SAP-H	IIP-BSG
Kinetic model	PSO <sup>a</sup>	PSO	PFO <sup>b</sup>	Ritchie's equation	PFO and IMT <sup>c</sup>
Rate controlling step	Adsorption on active sites	Adsorption on active sites	Diffusion	Adsorption on active sites	Internal mass transfer
Isotherm model	Langmuir	Langmuir	Freundlich	Toth	Sips
Type of adsorption	Monolayer	Monolayer	Multilayer; Heterogeneous	Monolayer; Heterogeneous	Monolayer; Heterogeneous
Complexation type				Outer sphere	Outer sphere
Functional groups		O- and N-containing	Carboxyl-	Carboxyl-, amide groups	Carboxyl-, phosphoryl-
Type of interaction			H <sup>+</sup> exchange, Bidentate binding of -COOH	Electrostatic; Coordination; Cation exchange	Electrostatic; Coordination

a). Pseudo-second order kinetic model; b). Pseudo-first order kinetic model; c). Internal mass transfer resistance model.

**(4). Real-world application.** In the last part of this study, BSG and its derived adsorbents are tested in simulated wastewater to evaluate their potential for better practical application. The IIP-BSG shows efficient U(VI)/Ln(III) separation in weak acidic nuclear wastewater and U(VI) concentration in carbonate rich-mine and tailings water, demonstrating high potential for practical use. There is also selectivity for acid mine water. In addition, unmodified BSG and BSG-SAP-H could effectively remove uranyl ions from the acidic mine water with high selectivity. In particular, the cost-effectiveness and availability of the unmodified BSG make it very interesting for the remediation of uranium containing acidic mine water (Table 8.3).

**Table 8.3.** Summary of the adsorbent performance in simulated wastewaters.

	BSG	ABSG	OBSG	BSG-SAP-H	IIP-BSG
Nuclear wastewater (pH <sub>0</sub> = 3.5)	U(VI)/Ni(II) not selective	Applicable selectivity ( $k > 2$ )	U(VI)/Na(I) not selective	Low selectivity ( $k(\text{U}/\text{REEs}) < 2$ )	High selectivity ( $k > 6$ )
Schlema mine water (pH <sub>0</sub> = 7.1)	Applicable selectivity ( $k > 2$ )	Applicable selectivity ( $k > 2$ )	Applicable selectivity ( $k > 2$ )	Applicable selectivity ( $k > 2$ )	High selectivity ( $k > 35$ )
Königstein mine water (pH <sub>0</sub> = 2.6)	High selectivity ( $k > 4$ )	Applicable selectivity ( $k > 2$ )	Low selectivity ( $k(\text{U}/\text{Na}) < 2$ )	High selectivity ( $k > 9$ )	Applicable selectivity ( $k > 2$ )
Helmsdorf tailings water (pH <sub>0</sub> = 9.8)	No U(VI) adsorption	No U(VI) adsorption	No U(VI) adsorption	No U(VI) adsorption	Applicable selectivity ( $k > 2$ )



## 9. Perspectives

The interactions between the uranyl ions and the various functional groups of the adsorbents prepared from BSG deserve further investigations to clarify the adsorption mechanisms. Advanced characterization technologies such as X-ray photoelectron spectroscopy (XPS), time-resolved laser fluorescence spectroscopy (TRLFS), and isothermal titration calorimetry (ITC) should be used to gain a deeper understanding of adsorption mechanisms. XPS can quantitatively measure the elemental composition, bonding relationships, and chemical or electronic state of the elements present on the surface of adsorbents (except H, He),<sup>[7]</sup> and is reported in the literature to be widely used to study the mechanism of uranium adsorption.<sup>[344–346]</sup> By comparing the binding energy of the functional groups before and after adsorption, the contribution of different functional groups could be evaluated.<sup>[344,345]</sup> In addition, finding the uranium 4f peak obviously supports the adsorption of U(VI) and provides information about the nature of binding sites.<sup>[346]</sup> TRLFS is a highly sensitive and selective method that can determine the speciation and local atomic structures of radionuclides on the water/solid interface, which is important to understand the coordination chemistry of U(VI).<sup>[347]</sup> However, it is currently applied only for the study of uranium adsorption on soil, minerals and metal oxides, and, to best of my knowledge, there are no reports in the literature of its application to U(VI) adsorption on biomass.<sup>[7,347]</sup> Therefore, using the TRLFS to study the speciation of surface adsorbed U(VI) on biomass adsorbents would be a promising method to improve our understanding of adsorption mechanisms. In addition, detailed thermodynamic information on molecular binding events, the stoichiometry and equilibrium constants could be obtained from ITC analysis<sup>[348]</sup> instead of traditional thermodynamic calculation from the isotherm data at different temperatures. Although the latter is much simpler and more popular, the estimation of thermodynamic parameters largely depends on the choice of standard state and equilibrium conditions, which may lead to inaccurate and misleading results.<sup>[349]</sup> Therefore, ITC is useful to study the behavioral enthalpy of U(VI) adsorption and to understanding the adsorption mechanisms.<sup>[167]</sup>

The successful application of surface ion-imprinting technology onto BSG opens a new way for producing selective adsorbents for other *f*-elements such as rare earth elements (REEs) and thorium (Th) with low cost and high availability. REEs are widely used as catalysts (Ce, La), magnets (Sm, Nd, Dy), alloys, powder production and phosphors.<sup>[350]</sup> However, they can be bioaccumulated in a tissue-specific manner, causing damage to lungs, liver, and brain.<sup>[351]</sup> Thorium (Th) is considered a next-generation nuclear fuel and is much more abundant than

uranium,<sup>[352]</sup> and poses the greatest radiation risk in rare earth production.<sup>[305]</sup> Both the toxicity and the importance of Th and REEs for application necessitate selective adsorption for pollution remediation and resources recovery. It is expected that the established synthesis strategy of surface uranyl-ion imprinted BSG can be easily converted into selective adsorbents for Th and REEs using the corresponding template in small amount. Moreover, more economic and effective functional monomers could be explored and synthesized, and the synthetic formula could be further optimized for a higher grafting ratio of the functional monomers. In addition to the selective adsorption of Th and REEs, two more applications of the ion-imprinted adsorbents are of particular interests. The first one is to prepare ion-imprinted adsorbents for selective extraction of heavy and transactinides using their chemical homologues as the imprinting ions, e.g. using Ce(IV) as the chemical homologue of Bk(IV).<sup>[353]</sup> This would be important for the separation of heavy and transactinides from fission products and the study of their nuclear and chemical properties. However, the radiation stability of the adsorbents prepared from BSG needs to be tested in advance. The second option is to use the metal ion-loaded adsorbents as environmentally friendly and cheap catalysts.<sup>[354]</sup> As reported in the literature, Ce<sup>3+</sup> could be firstly adsorbed by the amidoximated polyacrylonitrile nanofibrous membranes, and then the complex is used as a heterogeneous Fenton photocatalyst in dye degradation under visible irradiation.<sup>[355]</sup> Therefore, the surface-imprinted BSG is expected to selectively recovery Ce<sup>3+</sup> from wastewaters and then be converted into useful catalysts *in situ*. Further functionalization of BSG by using the terminal amino groups of proteins with salicylaldehyde or its derivatives to form Schiff bases would be of great interest. Schiff bases are particularly promising for the separation of actinides and lanthanides due to their chemical structure, which could provide metal-binding pockets with a controllable number of binding sites and electronic properties suitable for selective adsorption.<sup>[356]</sup> In addition, metal Schiff-base complexes derived from amino acids are already known and have been studied.<sup>[357]</sup> As shown in the present study, the content of amino acids in BSG is slightly increased by a short thermal treatment (150 °C, 1 h, Fig. 3.5). Therefore, the pretreated BSG is expected to form Schiff bases with component such as salicylaldehyde and carboxybenzaldehyde to introduce more functionality into the adsorbents, which is favorable for the selective adsorption of uranyl ions.

Since nuclear fuel reprocessing uses a large amount of HNO<sub>3</sub> for uranium leaching and spent fuel dissolution,<sup>[358]</sup> the adsorption efficiency of uranium in strongly acidic media should be considered in the application of the adsorbents prepared from BSG. Although the adsorbents prepared from BSG show good performance under weak acidic conditions, it is important to

further increase their efficiency in high HNO<sub>3</sub> concentrations. To date, there are a few studies in which biosorbents have been used to remove uranyl ions at high HNO<sub>3</sub> concentrations. One possible solution to this is to use the solvothermal polymerization method to graft P-containing monomers (e.g. DEVP and ethylene glycol methacrylate phosphate (EGMP))<sup>[359]</sup> onto the BSG backbone with improved grafting efficiency (Fig. 9.1).<sup>[358]</sup> The introduction of phosphoryl groups is expected to improve the adsorption capacity under acidic conditions. In addition, solvothermal polymerization may achieve a controllable porous structure and high specific surface area of the adsorbents,<sup>[315]</sup> which will benefit the adsorption capacity and kinetics.

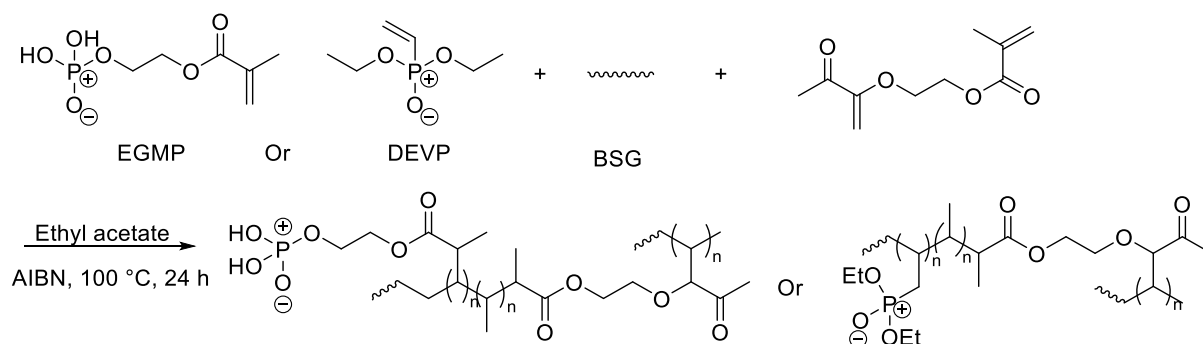


**Fig. 9.1.** Grafting of DEVP onto BSG using solvothermal polymerization.<sup>[358]</sup>





## 10. Experimental section

### 10.1. General information

#### 10.1.1 Materials

Acrylic acid (AA, 99 wt%, stabilized with ca. 200 ppm 4-Methoxyphenol, ABCR GmbH), acrylamide (AM, 98 wt%, Fluka Analytical), N,N-methylenebisacrylamide (MBA, 97 wt%, ABCR GmbH), diethyl vinylphosphonate (DEVP, 97 wt%, Acros Organics), 2,2'-azobis(2-methylpropionitrile) (AIBN, 98 wt%, Acros Organics), 2-hydroxyethyl methacrylate (HEMA, 98 wt%, Evonik GmbH), ethylene glycol dimethacrylate (EGDMA, Evonik GmbH), sorbitan monostearate (Span 60, Serva Feinbiochemica), and toluene (technical grade) were used as purchased.

$\text{Eu}(\text{NO}_3)_3 \cdot 5\text{H}_2\text{O}$  (99.9 wt%),  $\text{Yb}(\text{NO}_3)_3 \cdot 5\text{H}_2\text{O}$  (99.9 wt%),  $\text{Cu}(\text{NO}_3)_2 \cdot 3\text{H}_2\text{O}$  (97 wt%),  $\text{Ni}(\text{NO}_3)_2 \cdot 6\text{H}_2\text{O}$  (98 wt%),  $\text{Sm}(\text{NO}_3)_3 \cdot 6\text{H}_2\text{O}$  (99 wt%),  $\text{Gd}(\text{NO}_3)_3 \cdot 6\text{H}_2\text{O}$  (99 wt%), and  $\text{Y}(\text{NO}_3)_3 \cdot 6\text{H}_2\text{O}$  (99 wt%) are purchased from Sigma-Aldrich.  $\text{UO}_2(\text{CH}_3\text{COO})_2 \cdot 2\text{H}_2\text{O}$  (analytical pure), HF (40 wt%),  $\text{K}_2\text{S}_2\text{O}_8$  (99 wt%), NaCl (99.5 wt%),  $\text{Mg}(\text{NO}_3)_2 \cdot 6\text{H}_2\text{O}$  (99 wt%),  $\text{KNO}_3$  (99 wt%),  $\text{Zn}(\text{NO}_3)_2 \cdot 4\text{H}_2\text{O}$  (98.5 wt%),  $\text{Co}(\text{NO}_3)_2 \cdot 6\text{H}_2\text{O}$  (99 wt%), and  $\text{Fe}(\text{NO}_3)_3 \cdot 9\text{H}_2\text{O}$  (99 wt%) are obtained from Merck KGaA.  $\text{Na}_2\text{CO}_3$  (99.5 wt%),  $\text{NaHCO}_3$  (99 wt%),  $\text{NaNO}_3$  (99.5 wt%),  $\text{CaCl}_2 \cdot 2\text{H}_2\text{O}$  (99.5 wt%),  $\text{MgSO}_4$  (99 wt%), and  $\text{K}_2\text{SO}_4$  (99 wt%) are purchased from Grüssing GmbH.  $\text{HNO}_3$  (supra pure, 69 wt%),  $\text{H}_2\text{O}_2$  (35 wt%), and D(+)-Glucose ( $\text{C}_6\text{H}_{12}\text{O}_6$ , ACS reagent) are obtained from Carl Roth GmbH, and  $\text{H}_3\text{PO}_4$  (85 wt%),  $\text{NaNO}_2$  (>99 wt%), and  $\text{KMnO}_4$  (>99 wt%) are obtained from Fisher Scientific.

$\text{NaClO}_4 \cdot \text{H}_2\text{O}$  ( $\geq 98$  wt%, Fluka Analytical),  $\text{CaSO}_4$  (analytical pure, Fluka AG),  $\text{Na}_2\text{SO}_4$  ( $\geq 99$  wt%, Fisher Chemical),  $\text{Pb}(\text{NO}_3)_2$  ( $\geq 99$  wt%, Fisher Chemical),  $\text{Na}_3\text{VO}_4$  (99.9 wt%, Alfa Aesar),  $\text{H}_3\text{BO}_3$  (99.9 wt%, Alfa Aesar), NaOH (97 wt%, VWR chemicals), HCl (37 wt%, VWR chemicals),  $\text{La}(\text{NO}_3)_3 \cdot 6\text{H}_2\text{O}$  (99.9 wt%, Thermo Fisher GmbH),  $\text{Nd}(\text{NO}_3)_3 \cdot 5\text{H}_2\text{O}$  (99 wt%, Honeywell),  $\text{Na}_2\text{SO}_3$  (95 wt%, Roanal), and potassium hydrogen phthalate (analytical pure, Laborchemie Apolda GmbH) were used as purchased.

Ultrapure water (18.2 M $\Omega$ ·cm, arium pro, Sartorius) was used in all experiments.

### 10.1.2 Preparation of standardized BSG

Brewer's spent grain (BSG, water content 78 wt%) was obtained from our laboratory-scale brewery plant (Technical University Dresden, Germany) during the production of a Pilsner beer directly after the mashing process. Pilsner malt (14.6 kg, Weyermann) was used in this brewing. During the mashing process, 53 L of water was poured initially, with a replenishment volume of 58 L. The temperature and time of different mashing procedures are summarized in Table 10.1. The fresh BSG was then stored at  $-16\text{ }^{\circ}\text{C}$  until further processing. For the preparation of standardized BSG, the material was defrosted at room temperature and dried at  $60\text{ }^{\circ}\text{C}$  under reduced pressure ( $<70\text{ mbar}$ ) for 72 h to reduce the water content to less than 5 wt%. Afterward, BSG was milled using a coffee grinder (MayOcean) for 30 s, left to rest for 10 s and milled again for 20 s. The milled BSG was sieved into three different fractions ( $>710\text{ }\mu\text{m}$ ,  $315\text{--}710\text{ }\mu\text{m}$ ,  $<315\text{ }\mu\text{m}$ ). For general synthesis, adsorption studies and characterization, the fraction smaller than  $315\text{ }\mu\text{m}$  (designated as BSG) with water content of 3.0 wt%, N content of 5.1 wt% and an estimated protein content of  $\sim 29.5\text{ wt}\%$  was used.

**Table 10.1.** Parameters of the mashing process to produce BSG.

Procedure	Initial temperature ( $^{\circ}\text{C}$ )	End temperature ( $^{\circ}\text{C}$ )	Time (min)
Mash-in	55	54.8	10
Protein rest	62	61.8	30
Maltose rest	68	67.8	10
Sugar rest	72	71.8	25
Mash-out	78	77.8	10

### 10.1.3 Chemical composition of BSG

The water content and ash content ( $20\text{ }^{\circ}\text{C}/\text{min}$ , Air,  $40\text{--}850\text{ }^{\circ}\text{C}$ ) of BSG was obtained from TG analysis. The protein content was estimated according to the N content by multiplying by a factor of 5.83.

The cellulose content was measured using the method proposed by Updegraff<sup>[360,361]</sup> according to literature with minor modification. Generally, four replicates of 20 to 40 mg BSG were weighed in 6 mL glass tubes with screw caps. After adding 3 mL of a mixture of acetic acid/water/nitric acid (8/2/1, v/v/v), the suspension was heated in a boiling water bath for 30 min with occasional mixing. After cooling in an ice bath, the tubes were centrifuged for 10 min at 1000 g and the supernatant was discarded. The pellet was thoroughly resuspended in 5 mL bidistilled water and centrifuged again. The washing process was repeated once more,

and the supernatant was discarded. The remaining pellet was then incubated with 2.5 mL of 72 wt% sulphuric acid for 1 h with vortex every 5–10 min. The clear solution was transferred into a 10 mL volumetric flask and filled to the marking with water (after sufficient cooling time). For the photometric determination of cellulose, 20  $\mu$ L aliquots were diluted to 400  $\mu$ L with water and 1 mL of ice-cold 100 mg anthrone in 50 mL sulphuric acid (95 wt%) was added. The mixture was heated for 15 min in a boiling water bath, cooled in an ice bath for 2 min and let stand at room temperature for 10 min prior to photometric measurement at 620 nm against reagent blank. A cellulose stock solution for calibration was prepared by dissolving 57.4 mg of microcrystalline cellulose in 10 mL of 72 wt% sulphuric acid and diluting to 500 mL with water. Dilutions in the range of 2.87  $\mu$ g to 28.7  $\mu$ g in 400  $\mu$ L water were prepared in duplicate and processed by anthrone assay as mentioned above.

The content of lignin was determined according to ASTM E1758–01 and method reported by Balogun et.al.<sup>[138]</sup> More specifically, 300  $\pm$  10 mg BSG was incubated in 3 mL 72 wt% H<sub>2</sub>SO<sub>4</sub> for 1 h at 30 °C, then diluted into 4 wt % H<sub>2</sub>SO<sub>4</sub>, and subjected to a secondary hydrolysis in an autoclave reactor (DAB-3, Berghof Products+Instruments GmbH) at 121 °C for 1 h. The hydrolyzed mixture was filtrated, and the obtained solid was weighted. The content of acid-insoluble lignin was obtained by subtracting the ash content from the solid content. Meanwhile, the filtrate was collected for the measurement using a UV-vis spectrometer (Lambda 25, PerkinElmer) with a quartz cuvette (10 mm) in the range of 200–250 nm with a resolution of 0.1 nm. The acid-soluble lignin content was calculated according to the absorbance at 205 nm using an absorption coefficient of 110 L g<sup>-1</sup> cm<sup>-1</sup>. The chemical composition of BSG is shown in Table 10.2.

**Table 10.2.** Chemical composition of the standardized BSG.

Water (wt%)	Ash (wt%)	Acid insoluble lignin (wt%)	Acid soluble lignin (wt%)	Lignin (wt%)	Protein (wt%)	Cellulose (wt%)	Other (wt%)
3.0	3.6	32.5 $\pm$ 3.8	0.34 $\pm$ 0.01	32.8 $\pm$ 3.8	29 $\pm$ 0.6	8.75 $\pm$ 0.8	22.8 $\pm$ 5.2

#### 10.1.4 General characterization methods

**Infrared (FT-IR) and Raman spectra.** Fourier transform infrared (FT-IR) and Raman spectra were obtained with a single-beam Fourier transform infrared VERTEX 70 spectrometer (Bruker) equipped with a RAM II module (Nd-YAG laser, 1064 nm). An ATR (attenuated total reflectance) unit (diamond) with a single reflection optics at an interaction angle of 45° was used. The spectra were recorded over the range of 4500 to 400 cm<sup>-1</sup> with a resolution of 4 cm<sup>-1</sup>,

and averaged over 32 scans. In special cases, a higher resolution of  $1\text{ cm}^{-1}$  was used and the number of scan increases to 64. In order to investigate the detailed changes of chemical structures, the obtained spectra were processed using the OPUS software package as provided by Bruker to compare the intensity of certain bands. Baseline corrections were applied at selected wave numbers and the spectra were normalized respecting to  $-\text{CH}_2-$  antisymmetric stretching vibration bands. For normalization, the absorbance value of this band was set to 1.0 and the complete spectrum was multiplied by a ratio factor. The Raman spectra were recorded using a laser power of 100 mW between 800 to  $1000\text{ cm}^{-1}$  with a resolution of  $4\text{ cm}^{-1}$  and averaged over 100 scans.

**$^{13}\text{C}$  solid-state NMR spectra.**  $^{13}\text{C}$  solid-state NMR spectra were recorded on a Bruker Ascend 800 MHz spectrometer using a commercial 3.2 mm MAS NMR probe and operating at a resonance frequency of 201.2 MHz. The MAS frequency was 15 kHz. Adamantane was used as external standard. Ramped  $^1\text{H}$ - $^{13}\text{C}$  cross-polarization (CP, contact time: 4 ms) and SPINAL  $^1\text{H}$ -decoupling during the signal acquisition was applied. The recycle delay was 3 s and 26,000 scans were accumulated for signal-to-noise improvement. Especially, 28,000 scans was used for ABSG.

**Specific surface area.** The specific surface area of BSG and ABSG was determined by the Brunauer-Emmett-Teller (BET) method (SA 9600, Horiba Scientific). The sample was subjected to a pre-treatment at  $110\text{ }^\circ\text{C}$  for 90 min. The analysis was performed using 8%  $\text{N}_2$  in He. The adsorption took place at  $-196\text{ }^\circ\text{C}$  and the desorption was at room temperature.

**SEM-EDX.** Scanning electron microscopy (SEM) and energy-dispersive X-ray spectroscopy (EDX) analysis were performed on a scanning electron microscope (SU8020, HITACHI) equipped with an energy-dispersive X-ray spectrometer X-MaxN (OXFORD Instrument) at an electron beam voltage of 20 kV. The samples were dried at  $60\text{ }^\circ\text{C}$  under reduced pressure ( $<70\text{ mbar}$ ) for 48 h and coated with an Au layer by a rotary pumped coater (Q150R ES, Quorum) at 5 mA. The surface morphology images were taken at an electron beam voltage of 2.0 kV and the EDX elemental mappings were taken at 20 kV/10 mA for 25 frames.

### 10.1.5 General analytical methods

**Mineral element contents.** The content of Ca, Fe, Mn, Mg, Zn, K, Na, and P were determined by inductively coupled plasma–optical emission spectrometry (ICP-OES, OPTIMA 2000DV, PerkinElmer) after microwave-assisted digestion. In general, 10 mL  $\text{HNO}_3$  (supra pure, 69 wt%) were added to 0.1 g adsorbent and reacted for 15 min at room temperature before heating for 15 min at  $210\text{ }^\circ\text{C}$  (MARS 6, CEM GmbH).

**Mineral element contents including Si.** The mineral element contents including Si were determined by ICP-OES after microwave-assisted digestion. Generally, 3 mL HNO<sub>3</sub> (supra pure, 69 wt%) and 2 mL HCl (37 wt%) were added into ca. 0.05 g biosorbents. After 1 h at room temperature, 1 mL HF (40 wt%) was added, and the mixture was vortexed. After standing for another 1 h, 10 mL saturated H<sub>3</sub>BO<sub>3</sub> was added into the mixture to complex the HF before heating for 10 min at 170°C (MARS 6, CEM GmbH).

**Elemental analysis.** Elemental analysis were performed on a Vario MICRO cube (Elementar Analysatorsysteme GmbH) in CHNS mode to determine the content of carbon, nitrogen, hydrogen and sulfur. The oxygen content was calculated by mass balance considering the content of carbon, nitrogen, hydrogen, sulfur and the mineral elements determined by ICP-OES.

**Content of oxygen functional groups (OFGs).** The content of oxygen functional groups (OFGs) were quantified using Boehm titration.<sup>[362]</sup> In general, a mixture of 0.9 g adsorbents and 50.00 mL of one of the three reaction bases, NaHCO<sub>3</sub>, Na<sub>2</sub>CO<sub>3</sub> and NaOH, in a concentration of 0.05 M was shaken for 24 h. The mixtures were filtered and three 10.00 mL aliquots were taken for titration. The NaHCO<sub>3</sub> and NaOH samples were acidified with 20.00 mL 0.05 M HCl, whereas for Na<sub>2</sub>CO<sub>3</sub> samples 30.00 mL of 0.05 M HCl was added. The acidified solutions were then put into ultrasonic bath (Sonorex RK 52H, Bandelin electronic GmbH & Co. KG) for 20 min to expel dissolved CO<sub>2</sub> and titrated with 0.05 M NaOH using phenolphthalein indicator.

**Content of amine groups.** The amount of amine groups (–NH<sub>2</sub>) was determined using a volumetric method according to literature.<sup>[363]</sup> 0.1 g adsorbent was suspended in 50 mL 0.05 M HCl for 16 h, and the remaining amount of HCl was titrated with 0.05 M NaOH using phenolphthalein indicator.

**Point of zero charge.** The point of zero charge (pH<sub>pzc</sub>) of adsorbents was determined by solid addition method,<sup>[364]</sup> using 0.2 g adsorbent suspended in 10 mL 0.1 M NaNO<sub>3</sub> solution. The initial pH value (pH<sub>0</sub>) of the solution was adjusted to 1–10 using 0.1 M HNO<sub>3</sub> or 0.1 M NaOH. The equilibrium pH (pH<sub>e</sub>) was recorded after mixing for 16 h and the change of pH (ΔpH) was calculated. The pH<sub>pzc</sub> was determined by plotting ΔpH versus pH<sub>0</sub>, and the pH<sub>pzc</sub> is equal to the pH<sub>0</sub> value when ΔpH = 0.

#### 10.1.6 Thermal stability and differential scanning calorimetry analysis

**STA-GC-MS analysis of BSG and ABSG.** The thermal stability of adsorbents and volatile products produced during decomposition were analyzed by simultaneous thermal analyzer (STA 8000, PerkinElmer) coupled with a GC-MS (GC Clarus 680, MS Clarus SQ 8S, PerkinElmer). The samples were heated from 40 °C to 600 °C with a heating rate of 20 °C/min

under helium atmosphere. The volatile products generated at 375–385 °C (BSG, ABSG) and at 340–360 °C (Yb-ABSG) were detected using GC-MS. The GC temperature was initially set to 35 °C with a hold time of 3 min, and then increased with a heat rate of 5 °C/min until 220 °C, and hold at 220 °C for 3 min. The obtained MS spectra were interpreted using NIST mass spectral search program provided by PerkinElmer.

**Thermal stability test of OBSG.** The thermogravimetric (TG) analysis of the biosorbents was performed by a simultaneous thermal analyzer (STA 8000, PerkinElmer). The samples were heated from 40 to 600 °C with a heating rate of 20 °C /min under a helium atmosphere.

**TG-DSC analysis of BSG-SAP and IIP-BSG.** The thermogravimetric (TG) and differential scanning calorimetry (DSC) analysis of BSG-SAP was performed by a simultaneous thermal analyzer (STA 8000, PerkinElmer). The samples were dried at 60 °C under reduced pressure (<70 mbar) for 48 h to remove the adsorbed water before measurement and heated from 40 °C to 700 °C with a heating rate of 20 °C/min under a helium atmosphere. For IIP-BSG, a slower heating rate of 10 °C/min was used to obtain more detailed information about the thermal decomposition.

#### 10.1.7 Adsorbent aging test in ultrapure water

The adsorbent aging in ultrapure water was tested by immersing ca. 20 mg of the adsorbents into 20 mL ultrapure water at room temperature for 6 days. After 6 days, the adsorbents were dried at 60 °C under reduced pressure (<70 mbar) for 12 h before used for adsorption experiments. The adsorption capacity of U(VI) was measured before and after aging in water.

#### 10.1.8 Analysis of Maillard reaction products of BSG and ABSG

Maillard reaction products (MRPs) were analyzed according to literature with slight modifications.<sup>[365]</sup> Typically, the samples were enzymatically hydrolyzed, cleaned up through a solid phase extraction cartridge, and analyzed via HPLC-MS/MS (Agilent Technologies). For separation, a HPLC-column (Kinetex-C-18 column, 1.7 μm, 100 Å, 50 x 2.1 mm) was used. Amino acid analysis (ion-exchange chromatography with ninhydrin detection) was performed by the method proposed by Hellwig et al.<sup>[366]</sup>

#### 10.1.9 Cross-linking and swelling test for BSG-SAP

**Swelling ratio.** The swelling ratio (*S*) of the adsorbents was measured by swelling ca. 0.1 g of 315–800 μm BSG-SAP into 100 mL of the ultrapure water or simulated water with high salinity

and alkaline condition (25.6 g/L NaCl, 193 mg/L NaHCO<sub>3</sub>, pH = 7.0) for 24 h. The swollen polymer was weighed after removing surface water of the polymer by filter paper. The swelling ratio ( $S$ ) was calculated as equation (1):

$$S = m_0/m_s \quad (1)$$

where  $m_0$  (g) is the mass of the dry polymer, and  $m_s$  (g) is the mass of swollen BSG-SAP.

**Reswelling ratio.** A primary reswelling test was performed to investigate the chemical stability of the synthesized polymer during the regeneration process. Briefly, 50 mg of the adsorbent was mixed with 50 mL of 1000 mg/L U(VI) solution for 45 min using an overhead shaker at room temperature. Afterward, the adsorbed U(VI) was desorbed from the adsorbent using 50 mL 0.5 M HCl for 30 min and the adsorbent was regenerated by 20 mL 0.1 M NaOH for 10 min. The regenerated polymer was washed three times and reswollen in 100 mL of ultrapure water for 2 h. The reswollen polymer was weighed after removing surface water using filter paper, and the reswelling ratio (%) was calculated as equation (2):

$$\text{reswelling ratio (\%)} = \frac{m_d \times S}{m_{rs}} \times 100\% \quad (2)$$

where  $m_d$  (g) is the dry mass of the polymer,  $S$  is the swelling ratio, and  $m_{rs}$  (g) is the reswelling mass of the polymer.

**Average molecular weight between cross-links.** The average molecular weight between cross-links ( $\bar{M}_C$ ) of BSG-SAP, which is inversely proportional with the cross-linking density, was calculated according to Flory-Rehner theory as described in equation (3).<sup>[238]</sup>

$$\bar{M}_C = -V_1 \rho \frac{v_s^{1/3} - v_s/2}{\ln(1 - v_s) + v_s + \chi v_s^2} \quad (3)$$

where  $V_1$  is the molar volume of the solvent (water, 18 cm<sup>3</sup>/mol),  $\rho$  (g/cm<sup>3</sup>) is the density of the BSG-SAP (g/cm<sup>3</sup>),  $v_s$  (cm<sup>3</sup>) is the volume fraction of the polymer in the swollen polymer, and  $\chi$  is the Flory-Huggins interaction parameter between the solvent and the polymer. Particularly,  $v_s$  is calculated by equation (4):

$$v_s = \frac{m_0/\rho}{(m_s - m_0)/\rho_s} \quad (4)$$

where  $m_0$  (g) is the mass of the dry BSG-SAP,  $m_s$  (g) is the mass of swollen BSG-SAP,  $\rho_s$  (g/cm<sup>3</sup>) is the density of solvent (water, 1 g/cm<sup>3</sup>), and the value of  $\chi$  is taken from literature as equation (5):<sup>[367]</sup>

$$\chi = 0.431 - 0.311v_s - 0.036 v_s^2 \quad (5)$$

The density of synthesized polymer was obtained employing Archimedes principle with slight modification using *n*-octane (95%, VWR Chemicals) as a non-swelling solvent.<sup>[368]</sup> Generally, ca. 0.1 g of the sample was weighted into a volumetric flask of 5.00 mL, and a certain amount

of *n*-octane was added afterwards until the total volume of the liquid and solid inside the flask reached to 5.00 mL. The polymer density  $\rho$  (g/cm<sup>3</sup>) is calculated by equation (6):

$$\rho = m_p / \left( 5 - \frac{m_{octane}}{\rho_{octane}} \right) \quad (6)$$

where  $m_p$  (g) is the mass of the polymer,  $m_{octane}$  (g) is the mass of *n*-octane added into the volumetric flask, and  $\rho_{octane}$  (0.73 g/cm<sup>3</sup>) is the density of *n*-octane.



## 10.2. Synthetic methods

### 10.2.1 Hydrothermal treatment of brewer's spent grain

Hydrothermal treatment of BSG was conducted in an autoclave reactor (DAB-3, Berghof Products+Instruments GmbH) with 250 mL volume. Typically, 15 g fresh, defrosted BSG was mixed manually inside the reactor with 10 mL ultrapure water and the pH was adjusted to 10 using 0.01 M NaOH. The reactor was heated in an oven (Dry-line 115, VWR International) at different temperatures (100 °C, 125 °C, 150 °C, 175 °C) for various time periods (1 h, 4 h, 8 h, 16 h, 24 h). After reaction, the solid product was collected and dried at 60 °C under reduced pressure (<70 mbar) overnight to reduce the water content to less than 5 wt%, crushed and passed through 315 µm sieve to obtain a homogeneous fraction. The hydrothermal treated BSG was designated with ABSG- $\theta$ ,  $t$ , where  $\theta$  is the reaction temperature and  $t$  is the reaction time, in order to investigate the influence of the hydrothermal treatment parameters. For general characterization (<sup>13</sup>C solid state NMR, oxygen functional groups and STA-GC-MS analysis) and adsorption study, ABSG (ABSG-150 °C, 16 h) was used with a water content of 4.3 wt%, N content of 5.0 wt% and an estimate protein content of 29.2 wt%.

### 10.2.2 Oxidation of brewer's spent grain

The oxidation of BSG was performed at room temperature by stirring 1 g standardized BSG with 16 mL of 85 wt% H<sub>3</sub>PO<sub>4</sub> and 0.8 g NaNO<sub>2</sub> in a 100 mL Erlenmeyer flask using magnetic stirrer (IKA, RCT basic) at a stirrer speed of 140 rpm for 10 min, followed by reacting for another 16 h without stirring. After that, 50 mL of cold ultrapure water was added to quench the reaction. The oxidized BSG was washed with ultrapure water and filtrated repeatedly until the pH of the filtrate reached 5. Effects of NaNO<sub>2</sub> amount, the concentration and volume of H<sub>3</sub>PO<sub>4</sub>, and the reaction time on the adsorption capacity of oxidized BSG toward La(III) were investigated to determine the optimal conditions and is shown in Fig. 10.1.

In order to explore other possible oxidation methods for BSG, H<sub>2</sub>O<sub>2</sub> and KMnO<sub>4</sub> have also been tested as oxidants according to literature with modification. For H<sub>2</sub>O<sub>2</sub> method,<sup>[176,177]</sup> 2 g BSG was mixed with 20 mL ultrapure water and 0.4 mL 1 M HCl at 100°C. Afterwards 10 mL 35 wt% H<sub>2</sub>O<sub>2</sub> was added into the mixture dropwise and the mixture was reflux at 100°C for 2 h. For oxidation using KMnO<sub>4</sub>,<sup>[178]</sup> 1 g BSG was stirred with 0.18 g KMnO<sub>4</sub> and 20 mL 0.15 M H<sub>2</sub>SO<sub>4</sub> at 60°C for 2 h. Then the oxidation products were filtrated and washed with ultrapure water repeatedly. All the materials obtained from three different oxidation methods were dried

at 60°C under reduced pressure (<70 mbar) to reduce the water content to less than 5 wt%. For general adsorption studies and characterization, nitro-oxidized BSG obtained from the fraction smaller than 315  $\mu\text{m}$  (designated as OBSG) with water content of 3.6 wt%, N content of 1.1 wt% and an estimated protein content of 6.4 wt% was used.

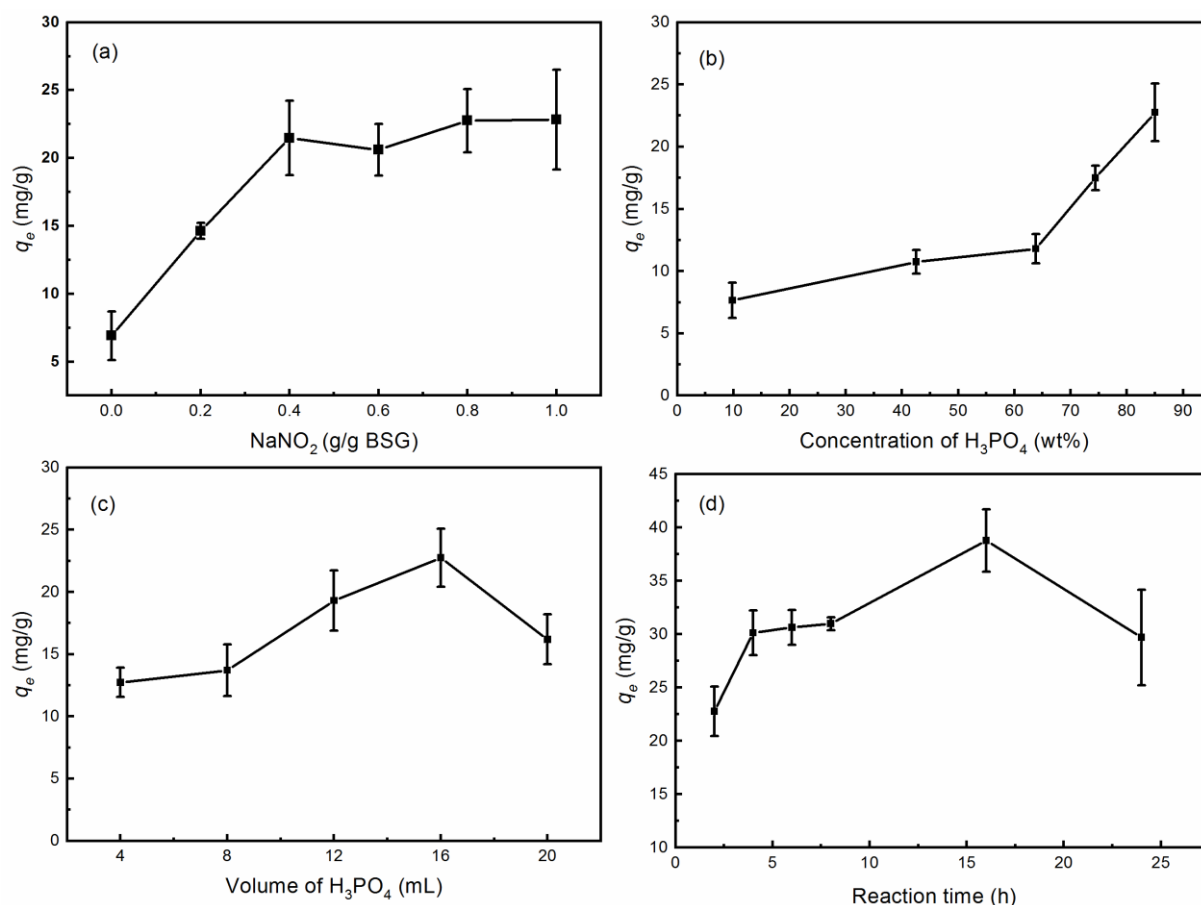


**Fig. 10.1.** Adsorption capacity of La(III) of the oxidized BSG in dependence of (a) the amount of  $\text{NaNO}_2$ , (b) the concentration of  $\text{H}_3\text{PO}_4$ , (c) the volume of  $\text{H}_3\text{PO}_4$ , and (d) the reaction time. For adsorption: 2 mg adsorbent/ 2 mL solution,  $c_0(\text{La}) = 100 \text{ mg/L}$ ,  $\text{pH} = 5.5$ , 2 h, room temperature.

### 10.2.3 Synthesis of brewer's spent grain-supported superabsorbent polymer

In general, 0.2 g of dry BSG was swollen in 18.7 mL of 7 wt% NaOH solution using a magnetic stirrer (IKA, RCT basic, stirrer speed = 140 rpm) at 40 °C for 1 h. After swelling, 7 mL of 40 g/L  $\text{K}_2\text{S}_2\text{O}_8$  solution and 4.3 mL of 20 g/L  $\text{Na}_2\text{SO}_3$  solution were added into the mixture as initiators. Then 3 mL of AA and 0.155 g of AM were added, and the amount of NaOH in the mixture resulted in a neutralization degree of AA equal to 75 mol%. Either 2 mL (0.5 mol% of the total monomers) or 9 mL (2.0 mol% of the total monomers) of 15 g/L MBA solution was added as the cross-linker to produce the BSG-SAP with low or high cross-linking density,

respectively. The reaction was kept at 40 °C for 3 h. The obtained BSG-SAP was washed with ethanol and ultrapure water for three times to remove unreacted impurities and then dried at 105 °C under reduced pressure (<70 mbar) for 12 h. The synthesized polymer with 0.5 mol% and 2.0 mol% of MBA was designated as BSG-SAP-L and BSG-SAP-H, respectively. The dry BSG-SAP was crushed and sieved through 800 µm and 315 µm sieves to obtain two fractions (<315 µm and 315–800 µm). Cross-linked block polymers without grafting onto the BSG backbone were also prepared with 0.5 mol% and 2.0 mol% of MBA and designated as reference polymers RP-L and RP-H, respectively.

#### 10.2.4 Synthesis of surface ion-imprinted brewer's spent grain

The surface ion-imprinted brewer's spent grain (IIP-BSG) was prepared referring to several literatures with modification.<sup>[293,295,300,308,369]</sup> Firstly, 0.57 g of BSG was swollen in 16.4 mL 0.2 M NaOH at 40 °C for 1 h using an overhead stirrer (Heidolph) and strongly stirred at 500 rpm. Then, 0.5 mL HEMA (4.1 mmol), 0.8 mL DEVP (5.2 mmol), and 0.9 mL U(VI) solution (5000 mg/L, 0.019 mmol) were added into the mixture and stirred for 10 min to form stable complexes. The M:T ratio was designated in the current study as 500:1. AIBN (193 mg, 40 mmol/L) and EGDMA (0.9 mL, 50 mol% of the monomer) were dissolved in 10.6 mL toluene and added dropwise to the mixture as the initiator and cross-linker, respectively. Span 60 (0.4g) was added as a dispersant and the mixture was stirred for 20 min to form a stable suspension. Then the suspension was allowed to react for 3 h at 65 °C and stirred slowly at 80 rpm. After reaction, the suspension was centrifuged (3500 rpm, 5 min) and the supernatant was discarded. The solid was redispersed in 10 mL ethanol and centrifuged again. The washing process was performed twice with ethanol and once with ultrapure water, and the solid was dried at 60 °C under reduced pressure (<70 mbar) for 16 h to obtain the unleached IIP-BSG. To remove the template, 0.1 g of unleached IIP-BSG was mixed with 50 mL 0.5 M HCl for 2 h. After acid leaching, the mixture was centrifuged (3500 rpm, 5 min) and the supernatant was collected to determine the concentration of U(VI) by ICP-OES. The elution efficiency (%) of the template was determined by the following equation (7):

$$Elution\ efficiency\ (\%) = \frac{c_l(U) \times V_l}{c_s(U) \times m} \times 100 \quad (7)$$

where  $c_s(U)$  (mg/g) is the content of the U(VI) template in the unleached IIP-BSG determined by microwave digestion (Table 6.1),  $m$  (g) is the mass of the unleached IIP-BSG,  $c_l(U)$  (mg/L) is the concentration of U(VI) in the leached supernatant, and  $V_l$  (L) the volume of HCl. The leached IIP-BSG was washed with ultrapure water for three times and the pH of the supernatant

was monitored to reach a pH above 6. Then the adsorbent was dried at 60 °C under reduced pressure (<70 mbar) for 16 h. A non-ion-imprinted BSG (NIP-BSG) and ion-imprinted polymer without BSG (IIP-Polymer) were prepared accordingly without U(VI) template and BSG, respectively. To investigate the effect of M:T ratio, a reference adsorbent was synthesized using a common choice of M:T ratio of 4:1 reported in the literature<sup>[293,300]</sup> and designated as IIP-BSG(4:1).

To verify the grafting of DEVP monomer onto the BSG surface and investigate the change of functional groups during acid leaching and reusability test, the P content of the unleached IIP-BSG, IIP-BSG (leached), and IIP-BSG after five cycles of reuse (designated as IIP-BSG-r) was determined by ICP-OES after complete digestion using a microwave (Table 6.1). Since it is possible that not all DEVP monomers were grafted during the synthesis, the real M:T ratio was calculated according to the mass balance of P content and the synthetic formula (Table 6.2).

In order to find the best combination of functional monomers and cross-linkers, HEMA, AA and DEVP were chosen as the potential functional monomers, and EGDMA and MBA were chosen as the potential cross-linkers. The synthesis followed the protocol mentioned above and the detailed formula are summarized in Table 10.3. The as prepared U(VI)-imprinted BSG was tested in the U(VI) single and U(VI)/Eu(III) binary solutions and the results are shown in Fig. 10.2. The selective factor ( $k$ ) and selectivity coefficient ( $S_U$ ) of the U(VI)-imprinted BSG are summarized in Table 10.4. The binary monomer compositions DEVP-AA or DEVP-HEMA show higher adsorption capacity than using the single monomer DEVP (Fig. 10.2, a). Using single monomer HEMA also results in a high adsorption capacity that is comparable to the DEVP-HEMA combination, indicating a potential benefit of HEMA monomer for the adsorption capacity. In addition, using MBA as the cross-linker results in an increased adsorption capacity compared with the adsorbent using EGDMA. As for the selectivity, the binary monomer compositions DEVP-AA or DEVP-HEMA also present great advantages compared to the adsorbents using single monomer DEVP or HEMA (Table 10.4). On the contrary, using MBA as the cross-linker results in a decreased selectivity compared with the adsorbent using EGDMA. On the basis of adsorption capacity and selectivity, binary monomer composition DEVP-HEMA and the cross-linker EGDMA were chosen to synthesize the IIP-BSG for further studies.

**Table 10.3.** Synthetic formula using different monomers and cross-linkers. For synthesis, BSG/monomer mass ratio = 0.4, 0.2 M NaOH = 16.4 mL, AIBN = 40 mM, M:T ratio = 500:1, Span 60 = 0.4 g, toluene = 10.6 mL, T = 65 °C and time = 3 h.

Sample	Monomer			Cross-linker (50 mol% of monomer)	
	DEVP (mmol)	HEMA (mmol)	AA (mmol)	EGDMA (mmol)	MBA (mmol)
DEVP+AA	5.2	0	4.1	4.65	0
DEVP	5.2	0	0	2.60	0
DEVP+HEMA (IIP-BSG)	5.2	4.1	0	4.65	0
HEMA	0	4.1	0	2.05	0
MBA-HEMA+DEVP	5.2	4.1	0	0	4.65

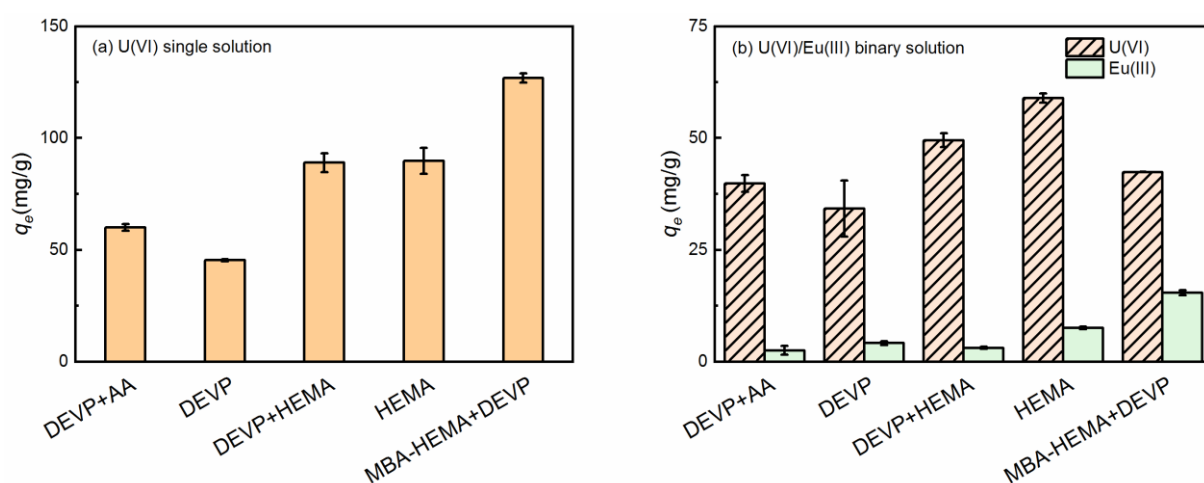


**Fig. 10.2.** Adsorption capacity of the U(VI)-imprinted BSG in (a) U(VI) single solution and (b) U(VI)/Eu(III) binary solution. For adsorption: 2 mg/ 2mL solution,  $pH_0 = 4.7$ ,  $t = 2$  h, for single solution  $c_0(U) = 1.2$  mM, and for binary solution  $c_0(U, Eu) = 0.5$  mM.

**Table 10.4.** Selective factor ( $k$ ) and selectivity coefficient ( $S_U$ ) of the U(VI)-imprinted BSG. For adsorption: 2 mg/ 2mL solution,  $pH_0 = 4.7$ ,  $t = 2$  h, for single solution  $c_0(U) = 1.2$  mM, and for binary solution  $c_0(U, Eu) = 0.5$  mM.

Sample	$k(U/Eu)$	$S_U$ (%)
DEVP+AA	13.8	94.0
DEVP	6.8	89.2
DEVP+HEMA	16.1	94.1
HEMA	7.4	88.6
MBA-HEMA+DEVP	2.1	73.3

## 10.3. Batch adsorption experiments

### 10.3.1 General batch adsorption experiments

Generally, batch adsorption experiments were performed by suspending 2 mg dry adsorbent in 2 mL solution containing the metal ions of the required concentration in micro centrifuge tubes (2 cm<sup>3</sup>, Safe-Lock, Eppendorf) with an overhead shaker (Reax 2, Heidolph) with a rotation speed of 60 rpm at room temperature. After adsorption the solution was filtrated through a 13 mm syringe filter with a 0.22 μm PTFE film (Fisher Scientific), and the mass concentration (mg/L), which refers to the elemental content before and after adsorption, was determined using ICP-OES (OPTIMA 2000DV, PerkinElmer, USA). The adsorption capacity ( $q_e$ , mg/g) was calculated using the following equation (8):

$$q_e = \frac{c_0 - c_e}{m} \times V \quad (8)$$

where  $c_0$  (mg/L) and  $c_e$  (mg/L) are the metal concentrations before and after adsorption,  $m$  (g) is the mass of adsorbent and  $V$  (L) is the volume of metal solution. The adsorption experiments were performed in duplicate and both the average value and standard deviation are reported.

**Effect of initial pH value.** In order to determine the optimum pH for adsorption, 1.0 mol/L or 0.1 mol/L HNO<sub>3</sub> was used to adjust the initial pH to certain range, which was carefully chosen in order to prevent precipitation according to the calculated speciation distribution using Visual MINTEQ 3.1 software.<sup>[14]</sup> The equilibrium pH was measured with an InLab micro pH electrode (Mettler Toledo).

**Adsorption kinetics.** For kinetic study, a series of adsorption experiments were performed at different time intervals at the optimum initial pH with a constant initial concentration of metal ions.

**Adsorption isotherms.** Adsorption isotherms were obtained with different initial metal concentrations at the optimum pH using equilibrium time from the kinetic studies.

**Effects of anion species and ionic strength.** The influence of different anions on the adsorption was investigated at a constant ionic strength ( $I = 0.1$  mol/L) using different supporting electrolytes (NaClO<sub>4</sub>, NaCl, NaNO<sub>3</sub>, and Na<sub>2</sub>SO<sub>4</sub>). The effect of ionic strength on the adsorption was examined by adding different concentrations of NaClO<sub>4</sub> (0, 0.05 M, 0.1 M, 0.2 M, 0.5 M, and 1 M).

**Adsorption in the high salinity and alkaline condition.** The adsorption experiments under high salinity and alkaline condition are performed referring to literature that employ the simulated seawater, which consists of 25.6 g/L NaCl, 193 mg/L NaHCO<sub>3</sub>, and various U(VI)

concentrations of 8 mg/L (pH<sub>0</sub> = 8), 10 mg/L (pH<sub>0</sub> = 7.7), or 30 mg/L (pH<sub>0</sub> = 7.0).<sup>[250,251]</sup> The removal efficiency of uranium was calculated as equation (9):

$$\text{removal efficiency(\%)} = \frac{c_0 - c_e}{c_e} \times 100\% \quad (9)$$

### 10.3.2 Adsorption experiments using <sup>169</sup>Yb radiotracer

For the experiments using <sup>169</sup>YbCl<sub>3</sub> radiotracer, 1 mg of adsorbent and 1 mL of metal solution were used. In these experiments, the metal ions distribution between the solution and adsorbent was determined radiometrically employing radiation from <sup>169</sup>Yb with a NaI (TI) scintillation counter (Hidex AMG, Hidex GmbH). The count rate (*CPM*, counts per minute) of 0.5 mL of the supernatant liquid and the remaining 0.5 mL supernatant liquid with the adsorbent were determined. The adsorption capacity (*q<sub>e</sub>*, mg/g) is calculated as equation (10):

$$q_e = \frac{CPM_{LS} - CPM_L}{CPM_{LS} + CPM_L} \times \frac{c_0 V}{m} \quad (10)$$

where *CPM<sub>LS</sub>*, *CPM<sub>L</sub>* are the determined count rate for the adsorption sample with and without solid adsorbent, *c<sub>0</sub>* (mg/L) is the metal concentration before adsorption determined by ICP-OES, *m* (g) is the mass of adsorbent and *V* (L) is the volume of metal solution. All the adsorption experiments were performed in duplicate and the average value and standard deviation are reported.

### 10.3.3 Effect of temperature on the adsorption capacity

Effects of temperature on the adsorption capacity of the biosorbents were examined by performing adsorption isotherms at three different temperatures. Generally, 2 mg adsorbent was mixed with 2 mL metal ions solution with different initial concentrations in 10 mL test tube using magnetic stirrer (IKA, RCT basic) at a stirrer speed of 180 rpm. The temperature was controlled by a circulation thermostat (UH 4, MLW-Medingen). Thermodynamic parameters were calculated according to the following equations (11) and (12) when the adsorption isotherms follow the Langmuir isotherm model:

$$\Delta G = \Delta H^0 - T\Delta S^0 \quad (11)$$

$$\ln K_e^0 = \frac{-\Delta H^0}{R} \times \frac{1}{T} + \frac{\Delta S^0}{R} \quad (12)$$

where  $\Delta G^0$  (J/mol) is the change in Gibb's energy,  $\Delta H^0$  (J/mol) is the change in enthalpy,  $\Delta S^0$  (J/(mol·K)) is the change in entropy, *T* (K) is the adsorption temperature, *R* (8.3143 J/(mol·K))

is the gas constant, and  $K_e^0$  ( $l$ ) is the dimensionless thermodynamic equilibrium constant.  $K_e^0$  is calculated according to literature (equation (13)):<sup>[370]</sup>

$$K_e^0 = \frac{1000 \times K_d \times M_{ads} \times c_{ads}^0}{\gamma} \quad (13)$$

where  $M_{ads}$  (g/mol) is the molar mass of the adsorbate,  $c_{ads}^0$  (mol/L) is the standard concentration of adsorbate (1mol/L),  $\gamma$  ( $l$ ) indicates the dimensionless coefficient of activity (activity coefficient is assumed to be 1 since the adsorbate solution is very diluted), and  $K_d$  is the isotherm equilibrium constant from the best isotherm model fitted, which in the cases of BSG and ABSG is Langmuir isotherm model ( $K_L$ , L/mg).

#### 10.3.4 Desorption and reusability test

The desorption and reusability were examined through five adsorption-desorption cycles. Therefore, 50 mg adsorbent was added into 50 mL metal ions solution and shaken with an overhead shaker to reach adsorption equilibrium. After adsorption, the mixture was centrifuged, and the supernatant was analyzed for remaining metal ion concentration. The metal ion-loaded adsorbent was washed once with ultrapure water and dried at 60 °C under reduced pressure (<70 mbar) for 12 h. Afterwards the adsorbent was weighted again, suspended with 0.5 M HCl as desorption agent with an adsorbent/acid ratio of 5 mg/mL for 2 h. The regenerated adsorbent was centrifuged, and the supernatant was collected for ICP-OES analysis. The adsorbent was washed 3 times (ultrapure water) and then dried at 60 °C for 12 h before the next cycle. The desorption ratio  $D_e$  (%) was calculated as equation (14):

$$D_e = \frac{c_d V_d}{m_d q_e} \times 100 \quad (14)$$

where  $c_d$  (mg/L) is the metal ion concentration after desorption,  $V_d$  (L) is the volume of HCl,  $m_d$  (g) is the mass of metal ion-loaded adsorbent for desorption and  $q_e$  (mg/g) is the adsorption capacity of adsorbent determined every cycle. All adsorption and desorption experiments were performed in triplicate and both the average value and standard deviation are reported.

#### 10.3.5 Adsorption selectivity and ion-imprinting factor

The selectivity coefficient ( $S_M$ , %) was calculated according to equation (15) to describe the selectivity of prepared adsorbents toward the target metal ions ( $M^{n+}$ ) in the presence of competing ions:<sup>[190]</sup>



$$S_M = \frac{q_{e,M}}{q_{e,total}} \times 100\% \quad (15)$$

where  $q_{e,M}$  (mg/g) is the adsorption capacity of  $M^{n+}$  in the mixed cations solution, and  $q_{e,total}$  (mg/g) is the adsorption capacity of all the metal ions adsorbed onto the prepared adsorbents. It should be noticed that the selectivity coefficient ( $S_M$ ) was generally used in the model solution that the concentration (mass or molar) of the target metal ions and the competing ions were close.

In simulate wastewater that the concentration (mass or molar) of the target metal ions and the competing ions were largely different from each other, the distribution coefficient ( $K_d$ , mL/g) and selective factor ( $k$ ) were also calculated to better describe the selectivity of the adsorbents.<sup>[342]</sup> Distribution coefficient ( $K_d$ , mL/g) demonstrates the distribution of adsorbates between liquid and solid phase and is calculated according to equation (16):

$$K_d = q_e/c_e \times 1000 \quad (16)$$

where  $c_e$  (mg/L) is the adsorbate concentration after adsorption and  $q_e$  (mg/g) is the adsorption capacity

Selective factor ( $k$ ) is designated as the ratio of  $K_d$  between the target ions and competing ions, which is illustrated in equation (17):

$$k = K_{dA}/K_{dB} \quad (17)$$

where  $K_{dA}$ ,  $K_{dB}$  (mL/g) are the distribution coefficient of target ions (A) and competing ions (B) The ion-imprinting factor was calculated to indicate the improvement of selectivity by the IIT using the selectivity coefficient  $S_U$  ( $\beta$ , equation (18)) or the selective factor  $k$  ( $k'$ , equation (19)):

$$\beta = S_{U,IIP}/S_{U,NIP} \quad (18)$$

$$k' = k_{IIP}/k_{NIP} \quad (19)$$

### 10.3.6 Adsorption performance in simulated wastewater

For practical application, the adsorbents were tested in simulated nuclear wastewater<sup>[324]</sup> and uranium containing mine and tailings water.<sup>[22]</sup> The experiments were performed by suspending 2 mg of the adsorbents with 2 mL of the wastewater using an overhead shaker (rotation speed = 60 rpm) at room temperature with  $t_{IIP} = 90$  min and  $t_{NIP} = 2$  h. When testing the simulated mine and tailings water, the adsorbent dosage was increased from 2 mg adsorbent/ 2 mL simulated wastewater to 2 mg adsorbent/ 5 mL simulated wastewater due to the low initial concentration of U(VI) to have an obvious adsorption and more accurate results. The composition of the simulated nuclear wastewater is given in Table 10.5, and the compositions

of the mine water from Schlema and Königstein, and the tailings water from Helmsdorf are summarized in Tables 10.6-10.8.

**Table 10.5.** The composition of simulated nuclear wastewater according to literature with slight modification (approx. 10 times diluted).<sup>[324]</sup>

Component	Concentration (mg/L)
La(III)	26 ± 5.3
Nd(III)	100 ± 1
Gd(III)	26 ± 0.9
Y(III)	13 ± 0.4
Sm(III)	25 ± 0.6
Eu(III)	49 ± 1.5
Na(I)	174 ± 3.1
Ni(II)	10 ± 0.5
Co(II)	19 ± 1.7
U(VI) <sup>a</sup>	187 ± 12
pH <sub>0</sub> <sup>b</sup>	3.5

a). The anion for all cations was NO<sub>3</sub><sup>-</sup> except for U(VI), which is CH<sub>3</sub>COO<sup>-</sup>; and b). pH was adjusted using 1 M HNO<sub>3</sub>.

**Table 10.6.** The composition of simulated mine water at Schlema (Saxony, Germany).<sup>[22]</sup>

Component	Concentration	Chemicals	Concentration (tested)	
	mmol/L		mg/L	mmol/L
Ca(II)	6.9	CaCl <sub>2</sub> ·2H <sub>2</sub> O, CaSO <sub>4</sub> ,	289 ± 18	7.2 ± 0.5
Mg(II)	11.6	MgSO <sub>4</sub>	195 ± 9	8.0 ± 0.4
Na(I)	20.6	Na <sub>2</sub> SO <sub>4</sub> , Na <sub>2</sub> CO <sub>3</sub> , NaClO <sub>4</sub> <sup>c</sup>	614 ± 38	26.7 ± 1.7
K(I)	1.0	K <sub>2</sub> SO <sub>4</sub>	51 ± 3	1.3 ± 0.1
U(VI)	0.021	UO <sub>2</sub> (CH <sub>3</sub> COO) <sub>2</sub> ·2H <sub>2</sub> O	4.5 ± 0.001	0.019 ± 0.001
SO <sub>4</sub> <sup>2-</sup>	20.7	CaSO <sub>4</sub> , MgSO <sub>4</sub> , Na <sub>2</sub> SO <sub>4</sub> , K <sub>2</sub> SO <sub>4</sub>		
HCO <sub>3</sub> <sup>-</sup> /CO <sub>3</sub> <sup>2-</sup> /CO <sub>2</sub>	3.9	Na <sub>2</sub> CO <sub>3</sub>		
Cl <sup>-</sup>	3.3	CaCl <sub>2</sub> ·2H <sub>2</sub> O		
PO <sub>4</sub> <sup>3-a</sup>	<0.02			
AsO <sub>4</sub> <sup>3-a</sup>	0.03			
TOC (mg/L) <sup>b</sup>	62	Glucose (C <sub>6</sub> H <sub>12</sub> O <sub>6</sub> ) (mg/L)	155	
pH <sup>d</sup>	7.1		7.1	

a). Not considered due to the low concentration;

b). Simulated by glucose;

c). ClO<sub>4</sub><sup>-</sup> was used to balance the cation charge;

d). pH was adjusted using 37 wt% HCl.

**Table 10.7.** The composition of simulated mine water at Königstein (Saxony, Germany).<sup>[22]</sup>

Component	Concentration	Chemicals	Concentration (tested)	
	mmol/L		mg/L	mmol/L
Ca(II)	5.9	CaCl <sub>2</sub> ·2H <sub>2</sub> O, CaSO <sub>4</sub>	188.3 ± 0.6	4.7 ± 0.1
Mg(II)	0.7	MgSO <sub>4</sub>	16.5 ± 0.3	0.7 ± 0.1
Na(I)	6.1	Na <sub>2</sub> SO <sub>4</sub>	165.0 ± 2	7.2 ± 0.1
K(I)	0.04	K <sub>2</sub> SO <sub>4</sub>	2.0 ± 0.1	0.1 ± 0.01
U(VI)	0.073	UO <sub>2</sub> (CH <sub>3</sub> COO) <sub>2</sub> ·2H <sub>2</sub> O	14.8 ± 0.4	0.0621 ± 0.001
SO <sub>4</sub> <sup>2-</sup>	23.9	CaSO <sub>4</sub> , MgSO <sub>4</sub> , Na <sub>2</sub> SO <sub>4</sub> , K <sub>2</sub> SO <sub>4</sub>		
HCO <sub>3</sub> <sup>-</sup> /CO <sub>3</sub> <sup>2-</sup> /CO <sub>2</sub>	<0.02			
Cl <sup>-</sup>	3.8	CaCl <sub>2</sub> ·2H <sub>2</sub> O		
PO <sub>4</sub> <sup>3-a</sup>	<0.02			
AsO <sub>4</sub> <sup>3-a</sup>	0.01			
TOC (mg/L) <sup>a</sup>	3.5			
pH <sup>b</sup>	2.6		2.6	

a). Not considered due to the low concentration;

b). pH was adjusted using 2M H<sub>2</sub>SO<sub>4</sub>.

**Table 10.8.** The composition of simulated tailings water at Helmsdorf (Saxony, Germany).<sup>[22]</sup>

Component	Concentration	Chemicals	Concentration (tested)	
	mmol/L		mg/L	mmol/L
Ca(II)	0.3	CaCl <sub>2</sub> ·2H <sub>2</sub> O	9 ± 2	0.2 ± 0.04
Mg(II)	0.9	MgCl <sub>2</sub> ·6H <sub>2</sub> O	23 ± 2	0.9 ± 0.1
Na(I)	166.3	Na <sub>2</sub> SO <sub>4</sub> , NaCl, Na <sub>2</sub> CO <sub>3</sub> , NaClO <sub>4</sub> <sup>b</sup> , Na <sub>3</sub> PO <sub>4</sub> , Na <sub>2</sub> HAsO <sub>4</sub> ·7H <sub>2</sub> O	2950 ± 143	128.4 ± 6
K(I)	0.9	KCl	37.6 ± 9	1.0 ± 0.2
U(VI)	0.025	UO <sub>2</sub> (CH <sub>3</sub> COO) <sub>2</sub> ·2H <sub>2</sub> O	4.5 ± 0.2	0.019 ± 0.001
SO <sub>4</sub> <sup>2-</sup>	35.6	Na <sub>2</sub> SO <sub>4</sub>		
HCO <sub>3</sub> <sup>-</sup> /CO <sub>3</sub> <sup>2-</sup> /CO <sub>2</sub>	10.3	Na <sub>2</sub> CO <sub>3</sub>		
Cl <sup>-</sup>	25.8	CaCl <sub>2</sub> ·2H <sub>2</sub> O, MgCl <sub>2</sub> ·6H <sub>2</sub> O, KCl		
PO <sub>4</sub> <sup>3-</sup>	0.29	Na <sub>3</sub> PO <sub>4</sub>		
AsO <sub>4</sub> <sup>3-</sup>	0.52	Na <sub>2</sub> HAsO <sub>4</sub> ·7H <sub>2</sub> O		
TOC (mg/L) <sup>a</sup>	132	Glucose (C <sub>6</sub> H <sub>12</sub> O <sub>6</sub> ) (mg/L)	330	
pH <sup>c</sup>	9.8		9.8	

a). Simulated by glucose;

b). ClO<sub>4</sub><sup>-</sup> was used to balance the cation charge;

c). pH was adjusted using 37 wt% HCl.

#### 10.4. Fixed bed column adsorption experiments of BSG-SAP

The adsorption behaviors and regeneration properties of BSG-SAP were examined in the fixed bed column adsorption experiments in both the U(VI) spiked water and simulated seawater ( $c_0(\text{U}) = 30 \text{ mg/L}$ ,  $25.6 \text{ g/L NaCl}$ ,  $193 \text{ mg/L NaHCO}_3$ ,  $\text{pH}_0 = 7.0$ ). A chromatography column (internal diameter = 15 mm, height = 20 cm) with a PTFE stopcock (bore 2.5 mm) and a fused glass filter plate (Por. 0, Rettberg) was used for the experiments at room temperature. Dry BSG-SAP (315–800  $\mu\text{m}$ ) was swollen in ultrapure water for 12 h before the experiment. When the influent was simulated seawater, BSG-SAP was preswollen in similar conditions with  $25.6 \text{ g/L NaCl}$  and  $193 \text{ mg/L NaHCO}_3$  at  $\text{pH} = 7.0$  instead of ultrapure water to avoid the large change of bed volume due to the change of swelling ratio in different solutions. Then, the surface water of the swollen BSG-SAP was carefully removed using filter paper, packed inside the column to reach a certain bed depth, keeping the packing density of the BSG-SAP-L and BSG-SAP-H in the column same. On top of the swollen BSG-SAP, 1 cm height of glass filler was packed to provide a uniform distribution of the influent. The influent was pumped through the column using a peristaltic pump (PLP 33, Labor-Technik Düsseldorf). The U(VI) concentration of the influent and effluent was determined by ICP-OES. The fixed bed column adsorption capacity ( $q_{\text{FB}}$ , mg/g) of the polymer was calculated as the following equation (20):

$$q_{\text{FB}} = \frac{Q \int_0^t (c_0 - c_t) dt}{m} \times 10^{-3} = \frac{Q \times 10^{-3}}{m} \left( c_0 t - \int_0^t c_t dt \right) \quad (20)$$

where  $Q$  (mL/min) is the average flow rate of the pump,  $t$  (min) is the working duration,  $c_0$  (mg/L) is the initial concentration of U(VI), and  $c_t$  (mg/L) is the effluent concentration. The value of  $\int_0^t c_t dt$  was obtained by integrating the breakthrough curves using Origin 2019b software.

After adsorption, 50 mL of the 0.5 M HCl was passed through the column at 2.0 mL/min to desorb the U(VI) from the BSG-SAP. The U(VI) concentration in the desorption effluent was detected by ICP-OES, and the desorption ratio ( $D_{e,\text{FB}}$ ) was calculated as follows (equation (21)):

$$D_{e,\text{FB}} = \frac{q_{e,\text{FB}} m}{c_d V_d} \times 100 \quad (21)$$

where  $c_d$  (mg/L) is the U(VI) concentration of the desorption effluent, and  $V_d$  (L) is the volume of the effluent. To regenerate the BSG-SAP, 25 mL of the 0.1 M NaOH was passed through the column with a flow rate of 2.0 mL/min, followed by approximate 500 mL of the ultrapure water until the pH of the outlet solution reached 7. After the first cycle, the reswelling ratio of the adsorbent was also calculated. The adsorption-desorption-regeneration cycles were performed four times to investigate the reusability of BSG-SAP.

## 10.5. Models and data processing

In general, model fit and model performance comparison were calculated using Origin 2019b software. For the formulas of mass transfer resistance models, the equations were solved using the 4 or 5 order Runge-Kutta method, and then the experimental kinetic data was fitted by employing a nonlinear least square method. The Matlab R2019b software was used for this process.

### 10.5.1 Batch adsorption kinetic models

Adsorption kinetic models employed in this work including pseudo-first order kinetic model (equation (22), nonlinear form; and equation (23), linear form), pseudo-second order kinetic model (equation (24), nonlinear form; and equation (25), linear form),<sup>[192]</sup> intraparticle diffusion model (equation (26)), and the Ritchie's equation (equation (27)).<sup>[242]</sup>

$$q_t = q_{cal,1}(1 - e^{-k_1 t}) \quad (22)$$

$$\ln(q_{e,exp} - q_t) = -k_1 t + \ln q_{cal,1} \quad (23)$$

$$q_t = \frac{q_{cal,2}^2 k_2 t}{1 + q_{cal,2} k_2 t} \quad (24)$$

$$\frac{t}{q_t} = \frac{1}{k_2 q_{cal,2}^2} + \frac{t}{q_{cal,2}} \quad (25)$$

where  $q_t$  (mg/g) is the adsorption capacity at time  $t$  (min),  $q_{e,exp}$  (mg/g) is the adsorption capacity at equilibrium time,  $q_{cal,1}$  (mg/g) and  $q_{cal,2}$  (mg/g) are the equilibrium adsorption capacities estimated by the pseudo-first order and pseudo-second order kinetic models, respectively, and  $k_1$  ( $\text{min}^{-1}$ ) and  $k_2$  ( $\text{g} \cdot \text{mg}^{-1} \cdot \text{min}^{-1}$ ) are the rate constants of pseudo-first order and pseudo-second order kinetic models

$$q_t = k_i t^{0.5} \quad (26)$$

where  $k_i$  ( $\text{mg/g} \cdot \text{min}^{0.5}$ ) is the intraparticle diffusion parameter

$$q_t = q_\infty - q_\infty (1 + (n - 1)\alpha t)^{1/(1-n)} \quad (27)$$

where  $n$  is the number of active sites occupied by an adsorbate ion or molecule,  $\alpha$  ( $\text{min}^{-1}$ ) is the rate constant of Ritchie's equation, and  $q_\infty$  (mg/g) is the equilibrium adsorption capacity at infinite time, which could be obtained from the best fitted isotherm model ( $q_\infty = f(c_e)$ ) when  $c_0(\text{U}) = c_0(\text{U})_{\text{kinetics}}$ .

### 10.5.2 Mass transfer resistance models

Mass transfer resistance models adopted from the Sips model (best isotherm model fitted), namely the external mass transfer model (EMT model, equation (28)) and internal mass transfer model (IMT model, equation (29)), are applied for further investigation of the kinetic data:<sup>[321]</sup>

$$\frac{dq_t}{dt} = k_{ext} \left\{ c_0 - \frac{mq_t}{V} - \left[ \frac{q_t}{(q_{max,s} - q_t)k_s} \right]^{1/m_s} \right\} \quad (28)$$

$$\frac{dq_t}{dt} = -k_{int} \left[ q_t - \frac{q_{max,s}k_s(c_0 - \frac{mq_t}{V})^{m_s}}{1 + k_s(c_0 - \frac{mq_t}{V})^{m_s}} \right] \quad (29)$$

where  $m$  (0.002 g) is the mass of the adsorbent,  $V$  (0.002 L) is the volume of the metal solution,  $c_0$  (mg/L) is the initial concentration of metal ions,  $k_s$  ( $L^{m_s} \cdot mg^{-m_s}$ ) and  $m_s$  are the Sips constants obtained from the isotherm data, and  $k_{emt}$  ( $L \cdot g^{-1} \cdot min^{-1}$ ) and  $k_{imt}$  ( $min^{-1}$ ) are the rate constants for EMT and IMT model, respectively.

The equation (28) and (29) were solved using the 4 or 5 order Runge-Kutta method with the initial condition  $q_0 = 0$ , and then the experimental kinetic data were fitted by employing nonlinear least square method. The Matlab R2019b software was used in this process.

The coefficient of determination ( $R^2$ ) is calculated as follows (equation (30)):

$$R^2 = 1 - \frac{RSS}{\sum_t (q_t - \bar{q}_t)^2} \quad (30)$$

where  $RSS$  is the residual sum of squares calculated by the Matlab R2019b software,  $q_t$  (mg/g) is the adsorption capacity at time  $t$  (min), and  $\bar{q}_t$  is the average value of  $q_t$ .

### 10.5.3 Batch adsorption isotherm models

Adsorption isotherm models employed in this work including Langmuir (nonlinear form, equation (31) and linear form, equation (32)), Freundlich (nonlinear form, equation (34) and linear form, equation (35)),<sup>[156]</sup> Redlich-Peterson (R-P, equation (36)), Toth (equation (37)),<sup>[247]</sup> Sips (equation (38)),<sup>[322]</sup> and piecewise linear adsorption isotherm (equation (39))<sup>[323]</sup> models:

$$q_e = \frac{q_{max}k_Lc_e}{1+k_Lc_e} \quad (31)$$

$$\frac{c_e}{q_e} = \frac{1}{q_{max}k_L} + \frac{c_e}{q_{max}} \quad (32)$$

$$R_L = \frac{1}{1+k_Lc_0} \quad (33)$$

where  $c_0$  (mg/L) and  $c_e$  (mg/L) are the initial and equilibrium concentration of metal ions, respectively;  $q_e$  (mg/g) is the adsorption capacity,  $q_{max,L}$  (mg/g) is the maximum adsorption

capacity estimated by Langmuir model,  $k_L$  (L/mg) is the Langmuir isotherm constant,  $R_L$  is the separation factor

$$q_e = k_F c_e^{1/n} \quad (34)$$

$$\ln q_e = \ln k_F + \frac{1}{n} c_e \quad (35)$$

where  $k_F$  ((mg/g) (L/mg)<sup>1/n</sup>) is the Freundlich isotherm constant related to adsorption capacity, and  $n$  is the Freundlich isotherm constant related to adsorption intensity

$$q_e = \frac{k_R c_e}{1 + a_R c_e^\beta} \quad (36)$$

where  $k_R$  (L/g) and  $a_R$  (L<sup>β</sup>/mg<sup>β</sup>) are the Redlich–Peterson isotherm constants, and  $\beta$  is the Redlich–Peterson isotherm exponent.

$$q_e = \frac{q_{max,T} c_e}{(a_T + c_e^z)^{1/z}} \quad (37)$$

where  $q_{max,T}$  (mg/g) is the maximum adsorption capacity estimated by Toth model,  $a_T$  (mg<sup>z</sup>·L<sup>-z</sup>) is the Toth constant, and  $z$  is a component that describes the degree of heterogeneity of the adsorption systems.

$$q_e = \frac{q_{max,s} k_S c_e^{m_s}}{1 + k_S c_e^{m_s}} \quad (38)$$

where  $q_{max,s}$  (mg/g) is the maximum adsorption capacity estimated by the Sips model and  $k_S$  (L<sup>m<sub>s</sub></sup>·mg<sup>-m<sub>s</sub></sup>) and  $m_s$  are the Sips constants,

$$q_e = \begin{cases} k_D c_e & c_e \leq c_m \\ q_{max} & c_e > c_m \end{cases} \quad (39)$$

where  $q_{max}$  (mg/g) is the maximum adsorption capacity obtained by the adsorption isotherm,  $k_D$  (L/g) is the partition coefficient, and  $c_m$  (mg/L) is the critical liquid-phase concentration calculated by  $c_m = q_{max}/k_D$ .

### 10.5.4 Site energy distribution function

The site energy distribution derived from the Sips model for the current study was calculated according to the following equation (equation (40)):<sup>[332]</sup>

$$f(E^*) = \frac{\exp\left(-\frac{m_s E^*}{RT}\right) k_s m_s q_{max} c_s^{m_s}}{\left(\exp\left(-\frac{m_s E^*}{RT}\right) k_s c_s^{m_s} + 1\right)^2 RT} \quad (40)$$

where  $f(E^*)$  ((mg/g) (J/mol)) is the approximate site energy distribution,  $E^*$  (J/mol) is the minimum binding energy when adsorption occurs at equilibrium concentration  $c_e$ ,  $c_s$  (mg/L) is the maximum solubility of the solute (43,212.9 mg/L for  $UO_2^{2+}$ ),  $T$  (298 K) is the temperature,  $R$  (8.314 J K<sup>-1</sup> mol<sup>-1</sup>) is the gas constant,  $q_{max,s}$  (mg/g) is the maximum adsorption capacity estimated by the Sips model, and  $k_s$  (L<sup>ms</sup>·mg<sup>-ms</sup>) and  $m_s$  are the Sips constants.

The upper ( $E_{max}^*$ ) and lower ( $E_{min}^*$ ) limits of the site energy distribution were calculated by the following equation (equation (41)) according to the lowest and highest  $c_e$  in isotherm data, and the results are given in Table 10.9.

$$E^* = -RT \ln\left(\frac{c_e}{c_s}\right) \quad (41)$$

**Table 10.9.** Calculation of the upper ( $E_{max}^*$ ) and lower ( $E_{min}^*$ ) limits of the site energy distribution.

	$c_{e,min}$ (mg/L)	$E_{max}^*$ (J/mol)	$c_{e,max}$ (mg/L)	$E_{min}^*$ (J/mol)
Single solution	1.0	26405	840.4	9762
Binary solution	7.2	21568	864.6	9691

The average site energy ( $E_m$ ) (equation (42)) and the energy distribution heterogeneity ( $\sigma_e^*$ ) (equation (43) and (44)) were calculated as follows:<sup>[333]</sup>

$$E_m = \frac{\int_{E_{min}}^{E_{max}} E^* \times f(E^*) dE^*}{\int_{E_{min}}^{E_{max}} f(E^*) dE^*} \quad (42)$$

$$E_p(E^{*2}) = \frac{\int_{E_{min}}^{E_{max}} E^{*2} \times f(E^*) dE^*}{\int_{E_{min}}^{E_{max}} f(E^*) dE^*} \quad (43)$$

$$\sigma_e^* = \sqrt{E_p(E^{*2}) - E_m^2} \quad (44)$$



### 10.5.5 Dynamic model for fixed bed column experiments

The Bohart-Adams model (equation (45)) is employed in the fixed bed column experiments to predict the behavior of the breakthrough curves and the maximum adsorption capacity:<sup>[269,270]</sup>

$$\frac{c_t}{c_0} = \frac{\exp(k_{BA}c_0t)}{\exp\left(\frac{k_{BA}N_0L}{u}\right) - 1 + \exp(k_{BA}c_0t)} \quad (45)$$

where  $c_0$  and  $c_t$  (mg/L) are the concentrations of U(VI) in the inlet and outlet at time  $t$  (min),  $k_{BA}$  (L min<sup>-1</sup>·mg<sup>-1</sup>) is the Bohart-Adams rate constant,  $N_0$  (mg/L) is the adsorption capacity per unit volume of fixed bed,  $u$  (cm/min) is the superficial velocity, and  $L$  (cm) is the bed depth. The maximum adsorption capacity  $q_M$  (mg/g) of the adsorbent is calculated accordingly (equation (46)):

$$q_M = \frac{N_0LA_c \times 10^{-3}}{m} \quad (46)$$

where  $A_c$  (cm<sup>2</sup>) is the cross-sectional area of the fixed bed column, and  $m$  (g) is the dry mass of the adsorbent.

### 10.5.6 Comparison of the performance of different models

**Akaike Information Criterion (AIC).**<sup>[195]</sup> AIC method could be used to compare two models with the same number of parameters. The comparison is performed by calculating *AIC* (equation (47)) and Akaike's weight (equation (48)), which is the probability that the model having the lower AIC is better than the alternative model. The model that has lower *AIC* value is  $e^{(-1/0.5\Delta AIC)}$  times more likely to be correct.

$$AIC = N \ln\left(\frac{RSS}{N}\right) + 2p + \frac{2p(p+1)}{N-p-1} \quad (47)$$

$$Akaike's\ weight = \frac{e^{-0.5\Delta AIC}}{1 + e^{-0.5\Delta AIC}} \quad (48)$$

where  $N$  is the number of data points,  $p$  is the number of free parameters to be estimated, and  $\Delta AIC$  is the difference between two *AIC* values

**Bayesian Information Criteria (BIC) test.**<sup>[371]</sup> The BIC test could also be used to compare two models with the same number of parameters. The comparison is performed by calculating *BIC* (equation (49)) and the difference between two BIC values ( $\Delta BIC$ ). The model that has lower *BIC* value is more likely to be correct. BIC difference ( $\Delta BIC$ ) more than 10 gives decisive conclusion.

$$BIC = N \ln \left( \frac{RSS}{N} \right) + p \ln(N) \quad (49)$$

**F-test.**<sup>[248]</sup> When two models have the same number of parameters, the F value is calculated according to equation (50). Afterwards P value is obtained from the F distribution. If the P value is large (greater than  $\alpha$ , usually 0.05) then the first model is statistically better than the second one. When they have different number of parameters, the F value is calculated by equation (51). Afterwards P value is obtained from the F distribution. If the calculated P values is less than the chosen level of significance (usually 0.05) then it can be concluded that the complex model fits the data significantly better than the simpler model.

$$F = RSS_1 / RSS_2 \quad (50)$$

$$F = \frac{(RSS_1 - RSS_2) / (df_1 - df_2)}{RSS_2 / df_2} \quad (51)$$

where  $RSS_1$  and  $df_1$  are the residual sum of squares and degrees of freedom of the simple model, respectively; and  $RSS_2$  and  $df_2$  are the residual sum of squares and degrees of freedom of the complex model, respectively.

## 10.6. Degradability test of BSG-SAP

Biodegradability test of the BSG-SAP was investigated using soil burial method.<sup>[282]</sup> Generally, the dry polymer (ca. 0.2 g, 315–800  $\mu\text{m}$ ) was weighed in a nylon filter bag (Graveda, 5 cm  $\times$  10 cm) with a mesh size of 160  $\mu\text{m}$  and sealed properly. Then the samples were buried in commercial garden soil (Compo GmbH) in a pot at a depth of 4 cm with equal distance between each other. The soil was filled up to 8 cm height in total. The pot was put in indoors at room temperature and fed with water every 3 days to keep the surface moisture. The samples were dug out every 7 days, cleaned with water to remove soil particles, dried at 60  $^{\circ}\text{C}$  for 12 h, and weighed again before buried back into the soil. The BSG-SAP-H sample obtained after 49 days was subjected to the FT-IR measurement.



## 11. References

- [1] B.-M. Jun, H.-K. Lee, S. Park, T.-J. Kim, *Sep. Purif. Technol.* **2022**, 278, 119675.
- [2] *World Nuclear Performance Report 2021, Report No. 2021/003*, **2021**.
- [3] International Atomic Energy Agency, “Uranium 2020: Resources, Production and Demand,” can be found under [https://www.oecd-nea.org/jcms/pl\\_52718/uranium-2020-resources-production-and-demand](https://www.oecd-nea.org/jcms/pl_52718/uranium-2020-resources-production-and-demand), **2021**.
- [4] M. Ma, R. Wang, L. Xu, M. Xu, S. Liu, *Environ. Int.* **2020**, 145, 106107.
- [5] R. W. Herschy, in *Encycl. Lakes Reserv.* (Eds.: L. Bengtsson, R.W. Herschy, R.W. Fairbridge), Springer Netherlands, Dordrecht, **2012**, pp. 876–883.
- [6] S. H. Frisbie, E. J. Mitchell, B. Sarkar, *Environ. Sci. Process. Impacts* **2013**, 15, 1817–1823.
- [7] Y. Xie, C. Chen, X. Ren, X. Wang, H. Wang, X. Wang, *Prog. Mater. Sci.* **2019**, 103, 180–234.
- [8] G. M. Gadd, *J. Chem. Technol. Biotechnol.* **2009**, 84, 13–28.
- [9] S. I. Mussatto, G. Dragone, I. C. Roberto, *J. Cereal Sci.* **2006**, 43, 1–14.
- [10] S. I. Mussatto, *J. Sci. Food Agric.* **2014**, 94, 1264–1275.
- [11] A. Waseem, H. Ullah, M. K. Rauf, I. Ahmad, *Crit. Rev. Environ. Sci. Technol.* **2015**, 45, 2391–2423.
- [12] P. Byrne, C. C. Fuller, D. L. Naftz, R. L. Runkel, N. J. Lehto, W. L. Dam, *Sci. Total Environ.* **2021**, 761, 143314.
- [13] K. Müller, V. Brendler, H. Foerstendorf, *Inorg. Chem.* **2008**, 47, 10127–10134.
- [14] J. P. Gustafsson, “Visual MINTEQ ver. 3.1,” can be found under <https://vminteq.lwr.kth.se/download/>, **2021**.
- [15] Y. Sun, Z. Y. Wu, X. Wang, C. Ding, W. Cheng, S. H. Yu, X. Wang, *Environ. Sci. Technol.* **2016**, 50, 4459–4467.
- [16] D. Brugge, V. Buchner, *Rev. Environ. Health* **2011**, 26, 231–249.
- [17] G. Björklund, Y. Semenova, L. Pivina, M. Dadar, M. M. Rahman, J. Aaseth, S. Chirumbolo, *Arch. Toxicol.* **2020**, 94, 1551–1560.
- [18] P. Kurttio, A. Auvinen, L. Salonen, H. Saha, J. Pekkanen, I. Mäkeläinen, S. B. Väisänen, I. M. Penttilä, H. Komulainen, *Environ. Health Perspect.* **2002**, 110, 337–342.
- [19] N. Gao, Z. Huang, H. Liu, J. Hou, X. Liu, *Chemosphere* **2019**, 237, 124548.
- [20] WHO, *Depleted Uranium: Sources, Exposure and Health Effects*. World Health Organization, **2001**.
- [21] A. Navarro, X. Font, M. Viladevall, *Toxics* **2016**, 4, 1–20.
- [22] G. Bernhard, G. Geipel, V. Brendler, H. Nitsche, *J. Alloys Compd.* **1998**, 271–273, 201–205.
- [23] J. Veliscek-Carolan, *J. Hazard. Mater.* **2016**, 318, 266–281.
- [24] R. G. Riley, J. M. Zachara, F. J. Wobber, *US DOE Off. Energy Res. Subsurf. Res. Program, Washingt. DC* **1992**, 27–29.
- [25] J. Nolan, K. A. Weber, *Environ. Sci. Technol. Lett.* **2015**, 2, 215–220.
- [26] R. M. Coyte, R. C. Jain, S. K. Srivastava, K. C. Sharma, A. Khalil, L. Ma, A. Vengosh, *Environ. Sci. Technol. Lett.* **2018**, 5, 341–347.
- [27] L. Salonen, in *IAHS Publ. Proc. Reports-Intern Assoc Hydrol. Sci.*, **1994**, pp. 71–84.
- [28] A. C. Q. Ladeira, C. A. Morais, *Miner. Eng.* **2005**, 18, 1337–1340.
- [29] M. Zuykov, S. W. Fowler, P. Archambault, G. Spiers, M. Schindler, *Mar. Pollut. Bull.* **2020**, 151, 110860.
- [30] Y. Wu, Y. Wang, X. Xie, *Sci. Total Environ.* **2014**, 472, 809–817.
- [31] H. S. Magdo, J. Forman, N. Graber, B. Newman, K. Klein, L. Satlin, R. W. Amler, J. A. Winston, P. J. Landrigan, *Environ. Health Perspect.* **2007**, 115, 1237–1241.
- [32] J. Steffanowski, A. Banning, *Environ. Earth Sci.* **2017**, 76, 1–11.
- [33] J. Nriagu, D. H. Nam, T. A. Ayanwola, H. Dinh, E. Erdenechimeg, C. Ochir, T. A. Bolormaa, *Sci. Total Environ.* **2012**, 414, 722–726.
- [34] V. E. A. Post, S. I. Vassolo, C. Tiberghien, D. Baranyikwa, D. Miburo, *Sci. Total Environ.* **2017**, 607–608, 281–293.
- [35] S. A. Ansari, P. K. Mohapatra, *J. Chromatogr. A* **2017**, 1499, 1–20.
- [36] E. J. Werner, S. M. Biros, *Inorg. Chem. Front.* **2019**, 6, 2067–2094.
- [37] J. Wang, S. Zhuang, *Rev. Environ. Sci. Biotechnol.* **2019**, 18, 437–452.
- [38] T. Liu, J. Yuan, B. Zhang, W. Liu, L. Lin, Y. Meng, S. Yin, C. Liu, F. Luan, *Environ. Sci. Technol.* **2019**, 53, 14612–14619.
- [39] A. M. Lakaniemi, G. B. Douglas, A. H. Kaksonen, *J. Hazard. Mater.* **2019**, 371, 198–212.
- [40] S. Banerjee, A. Kundu, P. Dhak, *J. Radioanal. Nucl. Chem.* **2022**, 331, 2409–2435.
- [41] Y. Ge, Z. Li, *ACS Sustain. Chem. Eng.* **2018**, 6, 7181–7192.
- [42] I. Anastopoulos, A. Bhatnagar, E. C. Lima, *J. Mol. Liq.* **2016**, 221, 954–962.
- [43] F. Ma, Y. Gui, P. Liu, Y. Xue, W. Song, *Chem. Eng. J.* **2020**, 390, 124597.
- [44] E. A. Gendy, D. T. Oyekunle, J. Ali, J. Ifthikar, A. El-Motaleb Mosad Ramadan, Z. Chen, *J. Environ. Radioact.* **2021**, 238–239, 106710.

- [45] M. Gao, G. Zhu, C. Gao, *Energy Environ. Focus* **2014**, 3, 219–226.
- [46] W. Yang, Q. Pan, S. Song, H. Zhang, *Inorg. Chem. Front.* **2019**, 6, 1924–1937.
- [47] P. Rajasulochana, V. Preethy, *Resource-Efficient Technologies*. **2016**, 2, 175–184.
- [48] N. R. Nicomel, L. Otero-Gonzalez, L. Arashiro, M. Garfi, I. Ferrer, P. Van Der Voort, K. Verbeken, T. Hennebel, G. Du Laing, *Green Chem.* **2020**, 22, 1985–1995.
- [49] M. Fan, X. Wang, Q. Song, L. Zhang, B. Ren, X. Yang, *J. Radioanal. Nucl. Chem.* **2021**, 330, 589–602.
- [50] N. K. Gupta, A. Sengupta, A. Gupta, J. R. Sonawane, H. Sahoo, *J. Environ. Chem. Eng.* **2018**, 6, 2159–2175.
- [51] T. Tatarchuk, A. Shyichuk, I. Mironyuk, M. Naushad, *J. Mol. Liq.* **2019**, 293, 111563.
- [52] Y. Hua, D. Li, T. Gu, W. Wang, R. Li, J. Yang, W. X. Zhang, *Acta Chim. Sin.* **2021**, 79, 1008–1022.
- [53] E. C. Giese, *World J. Microbiol. Biotechnol.* **2020**, 36, 52.
- [54] A. Demirbas, *J. Hazard. Mater.* **2008**, 157, 220–229.
- [55] M. Bader, K. Müller, H. Foerstendorf, M. Schmidt, K. Simmons, J. S. Swanson, D. T. Reed, T. Stumpf, A. Cherkouk, *PLoS One* **2018**, 13, 1–17.
- [56] H. A. Mansour, K. F. Mahmoud, H. M. Kamal, H. M. A. Mahdy, *Egypt. J. Chem.* **2020**, 63, 4039–4054.
- [57] K. Akhtar, M. Waheed Akhtar, A. M. Khalid, *Water Res.* **2007**, 41, 1366–1378.
- [58] U. K. Banala, N. P. I. Das, S. R. Toleti, *Environ. Technol. Innov.* **2021**, 21, 101254.
- [59] D. Schleuter, A. Günther, S. Paasch, H. Ehrlich, Z. Kljajić, T. Hanke, G. Bernhard, E. Brunner, *Carbohydr. Polym.* **2013**, 92, 712–718.
- [60] R. A. A. Muzzarelli, *Carbohydr. Polym.* **2011**, 84, 54–63.
- [61] H. Yang, H. Ding, X. Zhang, X. Luo, Y. Zhang, *Colloids Surfaces A Physicochem. Eng. Asp.* **2019**, 583, 123914.
- [62] Z. Wang, Z. Liu, T. Ye, Y. Wang, L. Zhou, *J. Radioanal. Nucl. Chem.* **2020**, 326, 1843–1852.
- [63] B. Li, J. Raff, A. Barkleit, G. Bernhard, H. Foerstendorf, *J. Inorg. Biochem.* **2010**, 104, 718–725.
- [64] H. Zänker, K. Heine, S. Weiss, V. Brendler, R. Husar, G. Bernhard, K. Gloe, T. Henle, A. Barkleit, *Inorg. Chem.* **2019**, 58, 4173–4189.
- [65] L. Zhou, M. Bosscher, C. Zhang, S. Özçubukçu, L. Zhang, W. Zhang, C. J. Li, J. Liu, M. P. Jensen, L. Lai, C. He, *Nat. Chem.* **2014**, 6, 236–241.
- [66] H. Ye, C. Liu, M. B. Wu, L. L. Ma, S. C. Liu, Y. Zhong, J. Yao, *J. Mater. Chem. A* **2022**, 10, 2987–2994.
- [67] Y. Yuan, Q. Yu, J. Wen, C. Li, Z. Guo, X. Wang, N. Wang, *Angew. Chemie - Int. Ed.* **2019**, 58, 11785–11790.
- [68] B. Koul, M. Yakoob, M. P. Shah, *Environ. Res.* **2021**, 112285.
- [69] M. Zhu, F. Li, W. Chen, X. Yin, Z. Yi, S. Zhang, *Environ. Sci. Pollut. Res.* **2021**, 28, 47354–47366.
- [70] M. M. Nezhad, A. Semnani, N. Tavakkoli, M. Shirani, *J. Environ. Manage.* **2021**, 299, 113587.
- [71] X. Lu, D. Zhang, A. Tesfay Reda, C. Liu, Z. Yang, S. Guo, S. Xiao, Y. Ouyang, *Ind. Eng. Chem. Res.* **2017**, 56, 11936–11947.
- [72] S. A. Nicolae, H. Au, P. Modugno, H. Luo, A. E. Szego, M. Qiao, L. Li, W. Yin, H. J. Heeres, N. Berge, M.-M. Titirici, *Green Chem.* **2020**, 22, 4747–4800.
- [73] M. Heidari, A. Dutta, B. Acharya, S. Mahmud, *J. Energy Inst.* **2019**, 92, 1779–1799.
- [74] Z. Zhang, Z. Zhu, B. Shen, L. Liu, *Energy* **2019**, 171, 581–598.
- [75] Z. B. Zhang, X. H. Cao, P. Liang, Y. H. Liu, *J. Radioanal. Nucl. Chem.* **2013**, 295, 1201–1208.
- [76] H. Cai, X. Lin, L. Tian, X. Luo, *Ind. Eng. Chem. Res.* **2016**, 55, 9648–9656.
- [77] S. Hokkanen, A. Bhatnagar, M. Sillanpää, *Water Res.* **2016**, 91, 156–173.
- [78] Y. Wang, Y. Zhang, Q. Li, Y. Li, L. Cao, W. Li, *Carbohydr. Polym.* **2020**, 245, 116627.
- [79] S. Ş. Başarir, N. P. Bayramgil, *Cellulose* **2013**, 20, 827–839.
- [80] N. Tang, J. Liang, C. Niu, H. Wang, Y. Luo, W. Xing, S. Ye, C. Liang, H. Guo, J. Guo, Y. Zhang, G. Zeng, *J. Mater. Chem. A* **2020**, 8, 7588–7625.
- [81] R. E. Abou-Zeid, S. Dacrory, K. A. Ali, S. Kamel, *Int. J. Biol. Macromol.* **2018**, 119, 207–214.
- [82] S. Coseri, G. Biliuta, B. C. Simionescu, K. Stana-Kleinschek, V. Ribitsch, V. Harabagiu, *Carbohydr. Polym.* **2013**, 93, 207–215.
- [83] H. Ma, B. S. Hsiao, B. Chu, *ACS Macro Lett.* **2012**, 1, 213–216.
- [84] V. Kumar, T. Yang, *Carbohydr. Polym.* **2002**, 48, 403–412.
- [85] P. R. Sharma, A. Chattopadhyay, S. K. Sharma, B. S. Hsiao, *Ind. Eng. Chem. Res.* **2017**, 56, 13885–13893.
- [86] D. Roy, M. Semsarilar, J. T. Guthrie, S. Perrier, *Chem. Soc. Rev.* **2009**, 38, 2046–2064.
- [87] F. Rol, M. N. Belgacem, A. Gandini, J. Bras, *Prog. Polym. Sci.* **2019**, 88, 241–264.
- [88] Z. Bai, Q. Liu, H. Zhang, J. Liu, R. Chen, J. Yu, R. Li, P. Liu, J. Wang, *J. Hazard. Mater.* **2020**, 381, 120984.
- [89] X. Song, J. An, C. He, J. Zhou, Y. Xu, H. Ji, L. Yang, J. Yin, W. Zhao, C. Zhao, *J. Mater. Chem. A* **2019**, 7, 21386–21403.
- [90] C. Wei, M. Yang, Y. Guo, W. Xu, J. Gu, M. Ou, X. Xu, *J. Radioanal. Nucl. Chem.* **2018**, 315, 211–221.
- [91] E. S. A. Haggag, *Int. J. Environ. Anal. Chem.* **2021**, 00, 1–25.
- [92] R. H. Moghaddam, S. Dadfarnia, A. M. H. Shabani, M. Tavakol, *Carbohydr. Polym.* **2019**, 206, 352–361.

- [93] A. Marcus, G. Fox, *Foods* **2021**, *10*, 2159.
- [94] Barth Haas, *Barth Haas Report (Hops 2020/2021)*, **2021**.
- [95] D. Assandri, N. Pampuro, G. Zara, E. Cavallo, M. Budroni, *Agric.* **2021**, *11*, 1–12.
- [96] W. G. Sganzerla, L. C. Ampese, S. I. Mussatto, T. Forster-Carneiro, *Biofuels, Bioprod. Biorefining* **2021**, *15*, 1965–1988.
- [97] K. M. Lynch, E. J. Steffen, E. K. Arendt, *J. Inst. Brew.* **2016**, *122*, 553–568.
- [98] A. Chettrariu, A. Dabija, *Appl. Sci.* **2020**, *10*, 5619.
- [99] P. Arauzo, M. Olszewski, A. Kruse, *Energies* **2018**, *11*, 3226.
- [100] S. F. Reis, E. Coelho, M. A. Coimbra, N. Abu-Ghannam, *Ultrason. Sonochem.* **2015**, *24*, 155–164.
- [101] H. Liu, H. Chung, *J. Polym. Sci. Part A Polym. Chem.* **2017**, *55*, 3515–3528.
- [102] E. Coelho, M. A. M. Rocha, A. S. P. Moreira, M. R. M. Domingues, M. A. Coimbra, *Carbohydr. Polym.* **2016**, *139*, 167–176.
- [103] T. Bonifácio-Lopes, J. A. Teixeira, M. Pintado, *Crit. Rev. Food Sci. Nutr.* **2020**, *60*, 2730–2741.
- [104] M. Jackowski, Ł. Niedźwiecki, K. Jagiełło, O. Uchańska, A. Trusek, *Biomolecules* **2020**, *10*, 1–18.
- [105] S. Aliyu, M. Bala, *African J. Biotechnol.* **2011**, *10*, 324–331.
- [106] A. Kezerle, N. Velic, D. Hasenay, D. Kovačević, *Croat. Chem. Acta* **2018**, *91*, 53–64.
- [107] J. P. Silva, S. Sousa, J. Rodrigues, H. Antunes, J. J. Porter, I. Gonçalves, S. Ferreira-Dias, *Sep. Purif. Technol.* **2004**, *40*, 309–315.
- [108] H. A. Chanzu, J. M. Onyari, P. M. Shiundu, *J. Hazard. Mater.* **2019**, *380*, 120897.
- [109] T. P. de Araújo, H. B. Quesada, R. Bergamasco, D. T. Vareschini, M. A. S. D. de Barros, *Bioresour. Technol.* **2020**, *310*, 123399.
- [110] A. F. C. Sousa, M. V. Gil, V. Calisto, *Environ. Sci. Pollut. Res.* **2020**, *27*, 36463–36475.
- [111] M. Stjepanović, N. Velić, A. Lončarić, D. Gašo-Sokač, V. Bušić, M. Habuda-Stanić, *J. Mol. Liq.* **2019**, *285*, 535–544.
- [112] K. H. Carrasco, E. G. Höfgen, D. Brunner, K. B. L. Borchert, B. Reis, C. Steinbach, M. Mayer, S. Schwarz, K. Glas, D. Schwarz, *Polysaccharides* **2022**, *3*, 356–379.
- [113] S. Wierzba, A. Kłos, *J. Clean. Prod.* **2019**, *225*, 112–120.
- [114] A. I. Osman, E. O'Connor, G. McSpadden, J. K. Abu-Dahrieh, C. Farrell, A. H. Al-Muhtaseb, J. Harrison, D. W. Rooney, *J. Chem. Technol. Biotechnol.* **2020**, *95*, 183–195.
- [115] Q. Li, L. Chai, W. Qin, *Chem. Eng. J.* **2012**, *197*, 173–180.
- [116] L. Chai, Q. Li, Y. Zhu, Z. Zhang, Q. Wang, Y. Wang, Z. Yang, *Bioresour. Technol.* **2010**, *101*, 6269–6272.
- [117] E. Kordialik-Bogacka, *Int. Biodeterior. Biodegrad.* **2014**, *96*, 191–197.
- [118] A. E. Samuel, I. C. Nwankwo, F. Ezebor, A. A. Ojuolape, *African J. Pure Appl. Chem.* **2019**, *13*, 64–71.
- [119] C. Yunnen, C. Liyuan, N. Jinxia, L. Xianping, W. Dongshuang, *Desalin. Water Treat.* **2015**, *53*, 1371–1376.
- [120] T. P. de Araújo, F. de O. Tavares, D. T. Vareschini, M. A. S. D. Barros, *Environ. Technol.* **2021**, *42*, 2925–2940.
- [121] A. I. Ferraz, M. T. Tavares, J. A. Teixeira, in *CHEMPOR 2005 - 9th Int. Chem. Eng. Conf.*, Coimbra, **2005**.
- [122] A. I. Ferraz, C. Amorim, T. Tavares, J. A. Teixeira, *Int. J. Environ. Sci. Technol.* **2015**, *12*, 1591–1602.
- [123] S. Lu, S. W. Gibb, *Bioresour. Technol.* **2008**, *99*, 1509–1517.
- [124] O. Izinyon, O. Nwosu, L. Akhigbe, I. Ilaboya, *Niger. J. Technol.* **2016**, *35*, 970.
- [125] Q. Li, L. Chai, Z. Yang, Q. Wang, Y. Wang, *Water Environ. Res.* **2010**, *82*, 2290–2296.
- [126] Q. Li, L. Chai, Q. Wang, Z. Yang, H. Yan, Y. Wang, *Bioresour. Technol.* **2010**, *101*, 3796–3799.
- [127] K. S. Low, C. K. Lee, S. C. Liew, *Process Biochem.* **2000**, *36*, 59–64.
- [128] Q. Li, L. Chai, Z. Yang, Q. Wang, *Appl. Surf. Sci.* **2009**, *255*, 4298–4303.
- [129] K. S. Low, C. K. Lee, C. H. Low, *J. Appl. Polym. Sci.* **2001**, *82*, 2128–2134.
- [130] L. Chai, Y. Chen, Z. Yang, *Water Environ. Res.* **2009**, *81*, 843–848.
- [131] L. Chai, Q. Wang, Q. Li, Z. Yang, Y. Wang, *Water Sci. Technol.* **2010**, *62*, 2157–2166.
- [132] H. S. Kambo, A. Dutta, *Renew. Sustain. Energy Rev.* **2015**, *45*, 359–378.
- [133] M. Hellwig, T. Henle, *Angew. Chemie - Int. Ed.* **2014**, *53*, 10316–10329.
- [134] A. Funke, F. Ziegler, *Biofuels, Bioprod. Biorefining* **2010**, *4*, 160–177.
- [135] P. J. Arauzo, L. Du, M. P. Olszewski, M. F. Meza Zavala, M. J. Alhndi, A. Kruse, *Bioresour. Technol.* **2019**, *293*, 122117.
- [136] X. Xu, R. Tu, Y. Sun, Y. Wu, E. Jiang, J. Zhen, *Bioresour. Technol.* **2019**, *271*, 427–438.
- [137] H. Simsir, N. Eltugral, S. Karagoz, *Bioresour. Technol.* **2017**, *246*, 82–87.
- [138] A. O. Balogun, F. Sotoudehniakarani, A. G. McDonald, *J. Anal. Appl. Pyrolysis* **2017**, *127*, 8–16.
- [139] M. N. Lund, C. A. Ray, *J. Agric. Food Chem.* **2017**, *65*, 4537–4552.
- [140] M. Hellwig, J. Rückriemen, D. Sandner, T. Henle, *J. Agric. Food Chem.* **2017**, *65*, 3532–3540.
- [141] J. A. Rufián-Henares, S. P. De La Cueva, *J. Agric. Food Chem.* **2009**, *57*, 432–438.

- [142] Y. Li, D. Cui, Y. Tong, L. Xu, *Int. J. Biol. Macromol.* **2013**, *62*, 663–669.
- [143] B. Weber, E. A. Stadlbauer, S. Eichenauer, C. Koch, K. Albert, M. Kramer, D. Steffens, *J. Biobased Mater. Bioenergy* **2013**, *7*, 367–375.
- [144] X. Qi, L. Li, T. Tan, W. Chen, R. L. Smith, *Environ. Sci. Technol.* **2013**, *47*, 2792–2798.
- [145] A. Yousefifar, S. Baroutian, M. M. Farid, D. J. Gapes, B. R. Young, *Bioresour. Technol.* **2017**, *226*, 229–237.
- [146] D. M. Dos Santos, A. De Lacerda Bukzem, D. P. R. Ascheri, R. Signini, G. L. B. De Aquino, *Carbohydr. Polym.* **2015**, *131*, 125–133.
- [147] A. Hardy, G. Vanhoyland, E. Geuzens, M. K. Van Bael, J. Mullens, L. C. Van Poucke, J. D’Haen, *J. Sol-Gel Sci. Technol.* **2005**, *33*, 283–298.
- [148] A. Kruse, T. Zevaco, *Energies* **2018**, *11*, 674.
- [149] M. P. Olszewski, P. J. Arauzo, P. A. Maziarka, F. Ronsse, A. Kruse, *Catalysts* **2019**, *9*, 625.
- [150] G. Özsin, A. E. Pütün, *Energy Convers. Manag.* **2017**, *149*, 675–685.
- [151] J. Qu, X. Meng, Y. Zhang, Q. Meng, Y. Tao, Q. Hu, X. Jiang, H. You, C. A. Shoemaker, *J. Hazard. Mater.* **2019**, *379*, 120804.
- [152] X. Guo, R. Chen, Q. Liu, J. Liu, H. Zhang, J. Yu, R. Li, M. Zhang, J. Wang, *Environ. Sci. Nano* **2018**, *5*, 2346–2356.
- [153] P. Misaelides, A. Godelitsas, A. Filippidis, D. Charistos, I. Anousis, *Sci. Total Environ.* **1995**, *173–174*, 237–246.
- [154] W. Zhao, X. Lin, H. Cai, T. Mu, X. Luo, *Ind. Eng. Chem. Res.* **2017**, *56*, 12745–12754.
- [155] Y. Zhang, X. Yue, W. Xu, H. Zhang, F. Li, *J. Hazard. Mater.* **2019**, *379*, 120783.
- [156] K. Y. Foo, B. H. Hameed, *Chem. Eng. J.* **2010**, *156*, 2–10.
- [157] S. J. Allen, G. Mckay, J. F. Porter, *J. Colloid Interface Sci.* **2004**, *280*, 322–333.
- [158] T. W. Weber, R. K. Chakravorti, *AIChE J.* **1974**, *20*, 228–238.
- [159] A. C. Texier, Y. Andrès, C. Faur-Brasquet, P. Le Cloirec, *Chemosphere* **2002**, *47*, 333–342.
- [160] E. Kusriani, W. Wicaksono, C. Gunawan, N. Z. A. Daud, A. Usman, *J. Environ. Chem. Eng.* **2018**, *6*, 6580–6588.
- [161] B. Arunraj, T. Sathvika, V. Rajesh, N. Rajesh, *ACS Omega* **2019**, *4*, 940–952.
- [162] X. R. Zhao, X. Xu, X. Y. Jiang, J. Teng, J. G. Yu, *Desalin. Water Treat.* **2019**, *148*, 188–194.
- [163] X. Zhao, X. Jiang, D. Peng, J. Teng, J. Yu, *J. Rare Earths* **2021**, *39*, 90–97.
- [164] R. Bai, F. Yang, Y. Zhang, Z. Zhao, Q. Liao, P. Chen, P. Zhao, W. Guo, C. Cai, *Carbohydr. Polym.* **2018**, *190*, 255–261.
- [165] S. Chen, J. Hong, H. Yang, J. Yang, *J. Environ. Radioact.* **2013**, *126*, 253–258.
- [166] L. Tan, Q. Liu, D. Song, X. Jing, J. Liu, R. Li, S. Hu, L. Liu, J. Wang, *New J. Chem.* **2015**, *39*, 2832–2838.
- [167] M. S. Alam, D. Gorman-Lewis, N. Chen, S. Safari, K. Baek, K. O. Konhauser, D. S. Alessi, *Environ. Sci. Technol.* **2018**, *52*, 13057–13067.
- [168] S. Iftekhhar, D. L. Ramasamy, V. Srivastava, M. B. Asif, M. Sillanpää, *Chemosphere* **2018**, *204*, 413–430.
- [169] J. Zhang, Q. Wang, *J. Clean. Prod.* **2016**, *112*, 3927–3934.
- [170] O. W. Duckworth, S. T. Martin, *Geochim. Cosmochim. Acta* **2001**, *65*, 4289–4301.
- [171] F. Quilès, A. Burneau, *Vib. Spectrosc.* **2000**, *23*, 231–241.
- [172] H. F. G. Barbosa, É. T. G. Cavalheiro, *Int. J. Biol. Macromol.* **2019**, *121*, 1179–1185.
- [173] G. Tian, J. Geng, Y. Jin, C. Wang, S. Li, Z. Chen, H. Wang, Y. Zhao, S. Li, *J. Hazard. Mater.* **2011**, *190*, 442–450.
- [174] J. Pan, Y. Gao, B. Gao, K. Guo, X. Xu, Q. Yue, *J. Clean. Prod.* **2019**, *240*, 118264.
- [175] T. J. Painter, A. Cesàro, F. Delben, S. Paoletti, *Carbohydr. Res.* **1985**, *140*, 61–68.
- [176] G. C. Quintana, G. J. M. Rocha, A. R. Gonçalves, J. A. Velásquez, *BioResources* **2008**, *3*, 1092–1102.
- [177] R. Koshani, T. G. M. Van De Ven, A. Madadlou, *J. Agric. Food Chem.* **2018**, *66*, 7692–7700.
- [178] L. Zhou, N. Li, J. Shu, Y. Liu, K. Wang, X. Cui, Y. Yuan, B. Ding, Y. Geng, Z. Wang, Y. Duan, J. Zhang, *ACS Sustain. Chem. Eng.* **2018**, *6*, 12403–12410.
- [179] A. J. Jay, M. L. Parker, R. Faulks, F. Husband, P. Wilde, A. C. Smith, C. B. Faulds, K. W. Waldron, *J. Cereal Sci.* **2008**, *47*, 357–364.
- [180] R. C. Oliveira, P. Hammer, E. Guibal, J. M. Taulemesse, O. Garcia, *Chem. Eng. J.* **2014**, *239*, 381–391.
- [181] F. Lin, Y. You, X. Yang, X. Jiang, Q. Lu, T. Wang, B. Huang, B. Lu, *Cellulose* **2017**, *24*, 5025–5040.
- [182] S. Kushwaha, H. Soni, B. Sreedhar, P. Padmaja, *J. Environ. Chem. Eng.* **2017**, *5*, 2480–2487.
- [183] X. Sun, J. Zhu, Q. Gu, Y. You, *Colloids Surfaces A Physicochem. Eng. Asp.* **2018**, *555*, 103–110.
- [184] E. Ferraz, J. Coroado, J. Gamelas, J. Silva, F. Rocha, A. Velosa, *J. Mater. Civ. Eng.* **2013**, *25*, 1638–1646.
- [185] M. Becidan, Ø. Skreiberg, J. E. Hustad, *J. Anal. Appl. Pyrolysis* **2007**, *78*, 207–213.
- [186] L. D. M. S. Borel, T. S. Lira, J. A. Ribeiro, C. H. Ataíde, M. A. S. Barrozo, *Ind. Crops Prod.* **2018**, *121*, 388–395.
- [187] I. Jankowska, R. Pankiewicz, K. Pogorzelec-Glaser, P. Ławniczak, A. Łapiński, J. Tritt-Goc, *Carbohydr. Polym.* **2018**, *200*, 536–542.
- [188] J. Wu, W. Zhu, X. Shi, Q. Li, C. Huang, Y. Tian, S. Wang, *Carbohydr. Polym.* **2020**, *236*, 115999.



- [189] J. Zhang, X. Chen, J. Zhou, X. Luo, *J. Hazard. Mater.* **2020**, *385*, 121588.
- [190] Y. Cai, L. Chen, S. Yang, L. Xu, H. Qin, Z. Liu, L. Chen, X. Wang, S. Wang, *ACS Sustain. Chem. Eng.* **2019**, *7*, 5393–5403.
- [191] U. K. Saha, S. Taniguchi, K. Sakurai, *Soil Sci. Soc. Am. J.* **2002**, *66*, 117–128.
- [192] H. Qiu, L. Lv, B. Pan, Q. Zhang, W. Zhang, Q. Zhang, *J. Zhejiang Univ. A* **2009**, *10*, 716–724.
- [193] C. Zheng, H. Zheng, Y. Sun, B. Xu, Y. Y. Wang, X. Zheng, Y. Y. Wang, *Bioresour. Technol.* **2019**, *293*, 122038.
- [194] J. Wang, X. Guo, *J. Hazard. Mater.* **2020**, *390*, 122156.
- [195] G. F. Malash, M. I. El-Khaiary, *Chem. Eng. J.* **2010**, *163*, 256–263.
- [196] X. Wei, Q. Liu, H. Zhang, Z. Lu, J. Liu, R. Chen, R. Li, Z. Li, P. Liu, J. Wang, *Dalton Trans.* **2017**, *46*, 15746–15756.
- [197] S. Mallakpour, F. Tabesh, *Int. J. Biol. Macromol.* **2019**, *133*, 754–766.
- [198] T. Chen, T. Da, Y. Ma, *J. Mol. Liq.* **2021**, *322*, 114980.
- [199] J. Wang, X. Guo, *Chemosphere* **2020**, *258*, 127279.
- [200] Y. Su, W. Böhm, M. Wenzel, S. Paasch, M. Acker, T. Doert, E. Brunner, T. Henle, J. J. Weigand, *RSC Adv.* **2020**, *10*, 45116–45129.
- [201] M. Monier, D. A. Abdel-Latif, *Carbohydr. Polym.* **2013**, *97*, 743–752.
- [202] M. K. Sureshkumar, D. Das, M. B. Mallia, P. C. Gupta, *J. Hazard. Mater.* **2010**, *184*, 65–72.
- [203] T. Shahnaz, M. M. F. S., P. V. C., S. Narayanasamy, *Int. J. Biol. Macromol.* **2020**, *151*, 322–332.
- [204] S. Fält, L. Wågberg, *Nord. Pulp Pap. Res. J.* **2003**, *18*, 69–73.
- [205] T. Hemraj-Benny, S. Banerjee, S. S. Wong, *Chem. Mater.* **2004**, *16*, 1855–1863.
- [206] K. Müller, H. Foerstendorf, R. Steudtner, S. Tsushima, M. U. Kumke, G. Lefèvre, J. Rothe, H. Mason, Z. Szabó, P. Yang, C. K. R. Adam, R. André, K. Brennenstuhl, I. Chiorescu, H. M. Cho, G. Creff, F. Coppin, K. Dardenne, C. Den Auwer, B. Drobot, S. Eidner, N. J. Hess, P. Kaden, A. Kremleva, J. Kretzschmar, S. Krüger, J. A. Platts, P. J. Panak, R. Polly, B. A. Powell, T. Rabung, R. Redon, P. E. Reiller, N. Rösch, A. Rossberg, A. C. Scheinost, B. Schimmelpennig, G. Schreckenbach, A. Skerencak-Frech, V. Sladkov, P. L. Solari, Z. Wang, N. M. Washton, X. Zhang, *ACS Omega* **2019**, *4*, 8167–8177.
- [207] S. Kumar, T. Shahnaz, N. Selvaraju, P. V. Rajaraman, *Environ. Monit. Assess.* **2020**, *192*, 248.
- [208] Y. Oyola, C. J. Janke, S. Dai, *Ind. Eng. Chem. Res.* **2016**, *55*, 4149–4160.
- [209] W. Yantasee, G. E. Fryxell, K. Pattamakomsan, T. Sangvanich, R. J. Wiacek, B. Busche, R. S. Addleman, C. Timchalk, W. Ngamcherdtrakul, N. Siriwon, *J. Hazard. Mater.* **2019**, *366*, 677–683.
- [210] R. Sellin, S. D. Alexandratos, *Ind. Eng. Chem. Res.* **2013**, *52*, 11792–11797.
- [211] H. Zhang, H. Liang, Q. Chen, X. Shen, *J. Radioanal. Nucl. Chem.* **2013**, *298*, 1705–1712.
- [212] A. Tellería-Narvaez, W. Talavera-Ramos, L. Dos Santos, J. Arias, A. Kinbaum, V. Luca, *RSC Adv.* **2020**, *10*, 6654–6657.
- [213] C. W. Abney, R. T. Mayes, T. Saito, S. Dai, *Chem. Rev.* **2017**, *117*, 13935–14013.
- [214] C. Ling, X. Liu, X. Yang, J. Hu, R. Li, L. Pang, H. Ma, J. Li, G. Wu, S. Lu, D. Wang, *Ind. Eng. Chem. Res.* **2017**, *56*, 1103–1111.
- [215] L. Zhang, S. Yang, J. Qian, D. Hua, *Ind. Eng. Chem. Res.* **2017**, *56*, 1860–1867.
- [216] X. Li, Q. Li, Y. Su, Q. Yue, B. Gao, Y. Su, *J. Taiwan Inst. Chem. Eng.* **2015**, *55*, 170–179.
- [217] R. K. Sharma, R. Kumar, *Int. J. Biol. Macromol.* **2019**, *134*, 704–721.
- [218] Y. Chen, Q. Li, Y. Li, Q. Zhang, J. Huang, Q. Wu, S. Wang, *Polymers (Basel)*. **2020**, *12*, 333.
- [219] M. Martínez-Sanz, A. A. Vicente, N. Gontard, A. Lopez-Rubio, J. M. Lagaron, *Cellulose* **2015**, *22*, 535–551.
- [220] H. Dai, H. Huang, *J. Agric. Food Chem.* **2017**, *65*, 565–574.
- [221] S. Ariaeenejad, E. Hosseini, E. Motamedi, A. A. Moosavi-Movahedi, G. H. Salekdeh, *Chem. Eng. J.* **2019**, *375*, 122022.
- [222] J. P. Zhang, F. S. Zhang, *Chem. Eng. J.* **2018**, *331*, 169–176.
- [223] S. Liu, G. Sun, *Carbohydr. Polym.* **2008**, *71*, 614–625.
- [224] D. Ciolacu, A. M. Oprea, N. Anghel, G. Cazacu, M. Cazacu, *Mater. Sci. Eng. C* **2012**, *32*, 452–463.
- [225] H. Dai, Y. Zhang, L. Ma, H. Zhang, H. Huang, *Carbohydr. Polym.* **2019**, *215*, 366–376.
- [226] F. Wu, Y. Zhang, L. Liu, J. Yao, *Carbohydr. Polym.* **2012**, *87*, 2519–2525.
- [227] S. Huang, L. Wu, T. Li, D. Xu, X. Lin, C. Wu, *Int. J. Biol. Macromol.* **2019**, *137*, 939–947.
- [228] W. Maatar, S. Boufi, *Carbohydr. Polym.* **2015**, *126*, 199–207.
- [229] V. K. Gupta, S. Sood, S. Agarwal, A. K. Saini, D. Pathania, *Int. J. Biol. Macromol.* **2018**, *107*, 2534–2543.
- [230] E. N. ISO, *Int. Organ. Stand. Geneva, Switz.* **2014**.
- [231] J. Liu, Q. Wang, A. Wang, *Carbohydr. Polym.* **2007**, *70*, 166–173.
- [232] M. Haroon, H. Yu, L. Wang, R. S. Ullah, F. Haq, L. Teng, *Int. J. Biol. Macromol.* **2019**, *138*, 349–358.
- [233] Q. Liu, Y. Li, H. Chen, J. Lu, G. Yu, M. Möslang, Y. Zhou, *J. Hazard. Mater.* **2020**, *382*, 121040.
- [234] E. ASTM, *Stand. test method Assign. Glas. Transit. Temp. by Differ. scanning calorimetry, B. Stand.* **n.d.**, *14*.

- [235] C. O. M'Bareck, Q. T. Nguyen, M. Metayer, J. M. Saiter, M. R. Garda, *Polymer (Guildf)*. **2004**, *45*, 4181–4187.
- [236] M. T. Am Ende, N. A. Peppas, *J. Control. Release* **1997**, *48*, 47–56.
- [237] M. Li, L. Zhang, J. C. Yang, X. M. Xie, *J. Appl. Polym. Sci.* **2002**, *86*, 2272–2278.
- [238] Z. Y. Ding, J. J. Aklonis, R. Salovey, *J. Polym. Sci. Part B Polym. Phys.* **1991**, *29*, 1035–1038.
- [239] F. Ganji, S. Vasheghani-Farahani, E. Vasheghani-Farahani, *Iran. Polym. J.* **2010**, *19*, 375–398.
- [240] S. Sharma, A. Dua, A. Malik, *Eur. Polym. J.* **2014**, *59*, 363–376.
- [241] X.-F. Sun, Y. Hao, Y. Cao, Q. Zeng, *Int. J. Biol. Macromol.* **2019**, *127*, 511–519.
- [242] A. G. Ritchie, *J. Chem. Soc. Faraday Trans. 1 Phys. Chem. Condens. Phases* **1977**, *73*, 1650.
- [243] S.-C. Liu, M.-B. Wu, H. Ye, L. Liu, L.-L. Ma, J. Yao, *Chem. Eng. J.* **2021**, *426*, 131378.
- [244] M. Szlachta, R. Neitola, S. Peräniemi, J. Vepsäläinen, *Sep. Purif. Technol.* **2020**, *253*, 117493.
- [245] O. A. Oyewo, M. S. Onyango, C. Wolkersdorfer, *J. Environ. Radioact.* **2016**, *164*, 369–376.
- [246] L. Li, R. Ma, T. Wen, P. Gu, S. Zhang, M. Zheng, X. Wu, X. Zhang, T. Hayat, X. Wang, *Sci. Total Environ.* **2019**, *694*, 133697.
- [247] L. Jossens, J. M. Prausnitz, W. Fritz, E. U. Schlünder, A. L. Myers, *Chem. Eng. Sci.* **1978**, *33*, 1097–1106.
- [248] H. J. Motulsky, L. A. Ransnas, *FASEB J.* **1987**, *1*, 365–374.
- [249] W. Yao, X. Wang, Y. Liang, S. Yu, P. Gu, Y. Sun, C. Xu, J. Chen, T. Hayat, A. Alsaedi, X. Wang, *Chem. Eng. J.* **2018**, *332*, 775–786.
- [250] T. Saito, S. Brown, S. Chatterjee, J. Kim, C. Tsouris, R. T. Mayes, L. J. Kuo, G. Gill, Y. Oyola, C. J. Janke, S. Dai, *J. Mater. Chem. A* **2014**, *2*, 14674–14681.
- [251] F. F. Li, W. R. Cui, W. Jiang, C. R. Zhang, R. P. Liang, J. D. Qiu, *J. Hazard. Mater.* **2020**, *392*, 122333.
- [252] J. Yu, C. Yu, W. Zhu, G. He, Y. Wei, J. Zhou, *Chemosphere* **2022**, *286*, 131626.
- [253] Y. Oyola, S. Dai, *Dalton Trans.* **2016**, *45*, 8824–8834.
- [254] L.-J. Kuo, C. J. Janke, J. R. Wood, J. E. Strivens, S. Das, Y. Oyola, R. T. Mayes, G. A. Gill, *Ind. Eng. Chem. Res.* **2016**, *55*, 4285–4293.
- [255] M. Xu, X. Han, D. Hua, *J. Mater. Chem. A* **2017**, *5*, 12278–12284.
- [256] Z. Huang, H. Dong, N. Yang, H. Li, N. He, X. Lu, J. Wen, X. Wang, *ACS Appl. Mater. Interfaces* **2020**, *12*, 16959–16968.
- [257] R. D. Hancock, A. E. Martell, *J. Chem. Educ.* **1996**, *73*, 654–661.
- [258] H. Chen, W. Li, J. Wang, H. Xu, Y. Liu, Z. Zhang, Y. Li, Y. Zhang, *Bioresour. Technol.* **2019**, *292*, 121948.
- [259] A. L. Allred, *J. Inorg. Nucl. Chem.* **1961**, *17*, 215–221.
- [260] R. H. Byrne, Y. R. Luo, R. W. Young, *Mar. Chem.* **2000**, *70*, 23–35.
- [261] P. L. Zanonato, P. Di Bernardo, A. Bismondo, G. Liu, X. Chen, L. Rao, *J. Am. Chem. Soc.* **2004**, *126*, 5515–5522.
- [262] J. Wu, T. Wang, Y. Zhang, W.-P. Pan, *Bioresour. Technol.* **2019**, *291*, 121859.
- [263] N. Mohammed, N. Grishkewich, H. A. Waeijen, R. M. Berry, K. C. Tam, *Carbohydr. Polym.* **2016**, *136*, 1194–1202.
- [264] Y. Li, S. Liu, C. Wang, Z. Ying, M. Huo, W. Yang, *J. Hazard. Mater.* **2020**, *386*, 121942.
- [265] A. B. Dichiaro, S. J. Weinstein, R. E. Rogers, *Ind. Eng. Chem. Res.* **2015**, *54*, 8579–8586.
- [266] D. Zhou, L. Zhang, J. Zhou, S. Guo, *J. Appl. Polym. Sci.* **2004**, *94*, 684–691.
- [267] X. Luo, J. Yuan, Y. Liu, C. Liu, X. Zhu, X. Dai, Z. Ma, F. Wang, *ACS Sustain. Chem. Eng.* **2017**, *5*, 5108–5117.
- [268] W. Zhang, Q. Deng, Q. He, J. Song, S. Zhang, H. Wang, J. Zhou, H. Zhang, *Chem. Eng. J.* **2018**, *351*, 462–472.
- [269] H. Patel, *Appl. Water Sci.* **2019**, *9*, 1–17.
- [270] K. H. Chu, *J. Hazard. Mater.* **2010**, *177*, 1006–1012.
- [271] K. H. Chu, *Chem. Eng. J.* **2020**, *380*, 122513.
- [272] A. M. Atta, A. A. H. Abdel-Rahman, I. E. El Aassy, F. Y. Ahmed, M. F. Hamza, *J. Dispers. Sci. Technol.* **2011**, *32*, 84–94.
- [273] M. Vakili, S. Deng, T. Li, W. Wang, W. Wang, G. Yu, *Chem. Eng. J.* **2018**, *347*, 782–790.
- [274] R. Gupta, V. M. Pandey, S. R. Pranesh, A. B. Chakravarty, *Hydrometallurgy* **2004**, *71*, 429–434.
- [275] M. Oh, K. Lee, R. I. Foster, K. Kim, C. Lee, in *Proc. Korean Radioact. Waste Soc. Conf.*, Korean Radioactive Waste Society, **2018**, pp. 229–230.
- [276] G. Lefèvre, J. Kneppers, M. Fédoroff, *J. Colloid Interface Sci.* **2008**, *327*, 15–20.
- [277] A. Barkleit, H. Foerstendorf, B. Li, A. Rossberg, H. Moll, G. Bernhard, *Dalton Trans.* **2011**, *40*, 9868.
- [278] D. Y. Leshok, V. N. Alekseenko, P. M. Gavrilov, S. N. Alekseenko, A. S. Dyachenko, A. A. Samoilo, A. A. Kondrasenko, S. D. Kirik, *Radiochim. Acta* **2015**, *103*, 477–486.
- [279] C. Nguyen-Trung, G. M. Begun, D. A. Palmer, *Inorg. Chem.* **1992**, *31*, 5280–5287.
- [280] M. Jansson-Charrier, I. Saucedo, E. Guibal, P. Le Cloirec, *React. Funct. Polym.* **1995**, *27*, 209–221.
- [281] S.-J. Lin, T.-N. Hong, J.-Y. Tung, J.-H. Chen, *Inorg. Chem.* **1997**, *36*, 3886–3891.
- [282] P. Wadhera, R. Jindal, R. Dogra, *Polym. Eng. Sci.* **2020**, *60*, 1231–1243.

- [283] C. Bastioli, F. Bettarini, in *Handb. Biodegrad. Polym.*, De Gruyter, **2020**, pp. 147–182.
- [284] B. Wilske, M. Bai, B. Lindenstruth, M. Bach, Z. Rezaie, H. G. Frede, L. Breuer, *Environ. Sci. Pollut. Res.* **2014**, *21*, 9453–9460.
- [285] J. D. Stahl, M. D. Cameron, J. Haselbach, S. D. Aust, *Environ. Sci. Pollut. Res.* **2000**, *7*, 83–88.
- [286] Z. Zhou, C. Du, T. Li, Y. Shen, Y. Zeng, J. Du, J. Zhou, *Environ. Sci. Pollut. Res.* **2015**, *22*, 8672–8682.
- [287] H. Gu, H. Geng, D. Wang, W. Li, *Waste Manag.* **2021**, *126*, 527–535.
- [288] B. Wang, J. Xuan, X. Yang, Z. Bai, *Colloids Surfaces A Physicochem. Eng. Asp.* **2021**, *626*, 127030.
- [289] V. V. Kusumkar, M. Galamboš, E. Viglašová, M. Daňo, J. Šmelková, *Materials* **2021**, *14*, 1083.
- [290] Q. Gan, M. Xu, Q. Li, S. Yang, J. Yin, D. Hua, *ACS Sustain. Chem. Eng.* **2021**, *9*, 7973–7981.
- [291] M. Liu, C. Chen, T. Wen, X. Wang, *Dalton Trans.* **2014**, *43*, 7050–7056.
- [292] L. Hou, C. Yang, X. Rao, L. Hu, Y. Bao, Y. Gao, X. Zhu, *Colloids Surfaces A Physicochem. Eng. Asp.* **2021**, *625*, 126949.
- [293] T. S. Anirudhan, J. Nima, P. L. Divya, *J. Environ. Chem. Eng.* **2015**, *3*, 1267–1276.
- [294] H. Meng, Z. Li, F. Ma, L. Jia, X. Wang, W. Zhou, L. Zhang, *J. Radioanal. Nucl. Chem.* **2015**, *306*, 139–146.
- [295] J. Wackerlig, P. A. Lieberzeit, in *Ullmann's Encycl. Ind. Chem.*, Wiley-VCH Verlag GmbH & Co. KGaA, Weinheim, Germany, **2016**, pp. 1–20.
- [296] L. Wang, J. Li, J. Wang, X. Guo, X. Wang, J. Choo, L. Chen, *J. Colloid Interface Sci.* **2019**, *541*, 376–386.
- [297] D. K. Singh, S. Mishra, *Anal. Chim. Acta* **2009**, *644*, 42–47.
- [298] D. Yuan, S. Zhang, J. Tan, Y. Dai, Y. Wang, Y. He, Y. Liu, X. Zhao, M. Zhang, Q. Zhang, *Sep. Purif. Technol.* **2020**, *237*, 116379.
- [299] S. Yang, M. Xu, J. Yin, T. Zhao, C. Li, D. Hua, *Sep. Purif. Technol.* **2020**, *246*, 116917.
- [300] D. James, G. Venkateswaran, T. Prasada Rao, T. P. Rao, *Microporous Mesoporous Mater.* **2009**, *119*, 165–170.
- [301] O. Brüggemann, K. Haupt, L. Ye, E. Yilmaz, K. Mosbach, *J. Chromatogr. A* **2000**, *889*, 15–24.
- [302] N. Li, H. Yang, *J. Hazard. Mater.* **2021**, *403*, 123643.
- [303] X. Hao, R. Chen, Q. Liu, J. Liu, H. Zhang, J. Yu, Z. Li, J. Wang, *Inorg. Chem. Front.* **2018**, *5*, 2218–2226.
- [304] Y. Yuan, Y. Yang, X. Ma, Q. Meng, L. Wang, S. Zhao, G. Zhu, *Adv. Mater.* **2018**, *30*, 1–7.
- [305] Z. Zhu, Y. Pranolo, C. Y. Cheng, *Miner. Eng.* **2015**, *77*, 185–196.
- [306] D. A. Giannakoudakis, I. Anastopoulos, M. Barczak, E. Antoniou, K. Terpiłowski, E. Mohammadi, M. Shams, E. Coy, A. Bakandritsos, I. A. Katsoyiannis, J. C. Colmenares, I. Pashalidis, *J. Hazard. Mater.* **2021**, *413*, 125279.
- [307] A. Leoncini, J. Huskens, W. Verboom, *Chem. Soc. Rev.* **2017**, *46*, 7229–7273.
- [308] T. E. Milja, K. P. Prathish, T. Prasada Rao, *J. Hazard. Mater.* **2011**, *188*, 384–390.
- [309] L. Zhou, M. Xu, J. Yin, R. Shui, S. Yang, D. Hua, *ACS Appl. Mater. Interfaces* **2021**, *13*, 6322–6330.
- [310] X. Liu, Y. Xie, M. Hao, Z. Chen, H. Yang, G. I. N. Waterhouse, S. Ma, X. Wang, *Adv. Sci.* **2022**, 2201735.
- [311] H. Hu, Z. Ren, Y. Xi, L. Fang, D. Fang, L. Yang, P. Shao, H. Shi, K. Yu, X. Luo, *Chem. Eng. J.* **2021**, *420*, 129611.
- [312] O. A. Kazantsev, K. V. Shirshin, A. P. Sivokhin, S. V. Tel'nov, I. V. Zhiganov, A. E. Kuznetsov, Y. L. Mironycheva, *Russ. J. Appl. Chem.* **2003**, *76*, 1296–1298.
- [313] J. Zakzeski, P. C. A. Bruijninx, B. M. Weckhuysen, *Green Chem.* **2011**, *13*, 671–680.
- [314] X. S. Li, L. D. Xu, Y. B. Shan, B. F. Yuan, Y. Q. Feng, *J. Chromatogr. A* **2012**, *1265*, 24–30.
- [315] Z. Huo, S. Zhao, J. Yi, H. Zhang, J. Li, *Appl. Sci.* **2020**, *10*, 5455.
- [316] S. Salzinger, U. B. Seemann, A. Plikhta, B. Rieger, *Macromolecules* **2011**, *44*, 5920–5927.
- [317] K. Demirelli, M. Coşkun, E. Kaya, *Polym. Degrad. Stab.* **2001**, *72*, 75–80.
- [318] B. Podkościelna, A. Bartnicki, B. Gawdzik, *Express Polym. Lett.* **2012**, *6*, 759–771.
- [319] S. S. Hassan, R. Ravindran, S. Jaiswal, B. K. Tiwari, G. A. Williams, A. K. Jaiswal, *Waste Manag.* **2020**, *105*, 240–247.
- [320] M. Hubbe, S. Azizian, S. Douven, *BioResources* **2019**, *14*, 7582–7626.
- [321] S. Zhuang, Y. Liu, J. Wang, *Environ. Pollut.* **2019**, *253*, 616–624.
- [322] R. Sips, *J. Chem. Phys.* **1948**, *16*, 490–495.
- [323] H. Xie, Y. Chen, Z. Lou, L. Zhan, H. Ke, X. Tang, A. Jin, *Chemosphere* **2011**, *85*, 1248–1255.
- [324] C. R. Preetha, J. M. Gladis, T. P. Rao, G. Venkateswaran, *Environ. Sci. Technol.* **2006**, *40*, 3070–3074.
- [325] S. Zhang, X. Zhao, B. Li, C. Bai, Y. Li, L. Wang, R. Wen, M. Zhang, L. Ma, S. Li, *J. Hazard. Mater.* **2016**, *314*, 95–104.
- [326] L. Zhou, C. Shang, Z. Liu, G. Huang, A. A. Adesina, *J. Colloid Interface Sci.* **2012**, *366*, 165–172.
- [327] L. Wang, L. Yuan, K. Chen, Y. Zhang, Q. Deng, S. Du, Q. Huang, L. Zheng, J. Zhang, Z. Chai, M. W. Barsoum, X. Wang, W. Shi, *ACS Appl. Mater. Interfaces* **2016**, *8*, 16396–16403.
- [328] J. Fasihi, S. A. Alahyari, M. Shamsipur, H. Sharghi, A. Charkhi, *React. Funct. Polym.* **2011**, *71*, 803–808.
- [329] Y. Zhou, Y. He, Y. He, X. Liu, B. Xu, J. Yu, C. Dai, A. Huang, Y. Pang, L. Luo, *Sci. Total Environ.* **2019**,

- 650, 2260–2266.
- [330] K. V. Kumar, S. Gadipelli, B. Wood, K. A. Ramisetty, A. A. Stewart, C. A. Howard, D. J. L. Brett, F. Rodriguez-Reinoso, *J. Mater. Chem. A* **2019**, *7*, 10104–10137.
- [331] J. A. García-Calzón, M. E. Díaz-García, *Sensors Actuators, B Chem.* **2007**, *123*, 1180–1194.
- [332] K. V. Kumar, J. C. Serrano-Ruiz, H. K. S. Souza, A. M. Silvestre-Albero, V. K. Gupta, *J. Chem. Eng. Data* **2011**, *56*, 2218–2224.
- [333] X. Shen, X. Guo, M. Zhang, S. Tao, X. Wang, *Environ. Sci. Technol.* **2015**, *49*, 4894–4902.
- [334] L. Huang, Q. Jin, P. Tandon, A. Li, A. Shan, J. Du, *Chemosphere* **2018**, *197*, 411–419.
- [335] J. Yin, S. Yang, W. He, T. Zhao, C. Li, D. Hua, *Sep. Purif. Technol.* **2021**, *271*, 118849.
- [336] M. B. McBride, *Clays Clay Miner.* **1997**, *45*, 598–608.
- [337] H. Lindner, E. Schneider, *Energy Econ.* **2015**, *49*, 9–22.
- [338] W. Ahmed, A. Núñez-Delgado, S. Mehmood, S. Ali, M. Qaswar, A. Shakoor, D.-Y. Chen, *Environ. Res.* **2021**, *201*, 111518.
- [339] J. Wang, J. Wei, J. Li, *Chem. Eng. J.* **2016**, *293*, 24–33.
- [340] T. P. Gandhi, P. V. Sampath, S. M. Maliyekkal, *Sci. Total Environ.* **2022**, *825*, 153947.
- [341] C. Zhan, P. R. Sharma, H. He, S. K. Sharma, A. McCauley-Pearl, R. Wang, B. S. Hsiao, *Environ. Sci. Water Res. Technol.* **2020**, 3080–3090.
- [342] L. N. Pincus, H. E. Rudel, P. V. Petrović, S. Gupta, P. Westerhoff, C. L. Muhich, J. B. Zimmerman, *Environ. Sci. Technol.* **2020**, *54*, 9769–9790.
- [343] B. Zhao, L. Yuan, Y. Wang, T. Duan, W. Shi, *ACS Appl. Mater. Interfaces* **2021**, *13*, 16300–16308.
- [344] P. Mei, R. Wu, S. Shi, B. Li, C. Ma, B. Hu, Y. Yuan, H. Wang, T. Liu, N. Wang, *Chem. Eng. J.* **2021**, *420*, 130382.
- [345] J. Yu, X. Luo, B. Liu, J. Zhou, J. Feng, W. Zhu, S. Wang, Y. Zhang, X. Lin, P. Chen, *J. Mater. Chem. A* **2018**, *6*, 15359–15370.
- [346] Y. Tian, L. Liu, F. Ma, X. Zhu, H. Dong, C. Zhang, F. Zhao, *J. Hazard. Mater.* **2021**, *419*, 126538.
- [347] X. Tan, M. Fang, X. Wang, *Molecules* **2010**, *15*, 8431–8468.
- [348] M. Li, S. A. Messele, Y. Boluk, M. Gamal El-Din, *Carbohydr. Polym.* **2019**, *221*, 231–241.
- [349] S. Salvestrini, V. Leone, P. Iovino, S. Canzano, S. Capasso, *J. Chem. Thermodyn.* **2014**, *68*, 310–316.
- [350] N. Swain, S. Mishra, *J. Clean. Prod.* **2019**, *220*, 884–898.
- [351] G. Pagano, M. Guida, F. Tommasi, R. Oral, *Ecotoxicol. Environ. Saf.* **2015**, *115*, 40–48.
- [352] Z. Wang, A. T. Brown, K. Tan, Y. J. Chabal, K. J. Balkus, *J. Am. Chem. Soc.* **2018**, *140*, 14735–14739.
- [353] A. Mhatre, C. Agarwal, T. N. Nag, A. Bhattacharyya, R. Tripathi, *ACS Appl. Polym. Mater.* **2021**, *3*, 1465–1478.
- [354] X. Zhang, X. Ou, J. Zhang, Z. Chen, C. Liu, H. Li, X. Li, Y. Sun, Z. Chen, J. Zhu, S. Lu, P. Zhang, *J. Hazard. Mater.* **2021**, *417*, 126072.
- [355] F. Li, Y. Dong, W. Kang, B. Cheng, X. Qu, G. Cui, *Bull. Korean Chem. Soc.* **2016**, *37*, 1934–1941.
- [356] L. Whitty-Léveillé, N. Reynier, D. Larivière, *Ind. Eng. Chem. Res.* **2019**, *58*, 306–315.
- [357] A. A. El-Sherif, M. S. Aljahdali, *J. Coord. Chem.* **2013**, *66*, 3423–3468.
- [358] D. Yuan, Y. Wang, Y. Qian, Y. Liu, G. Feng, B. Huang, X. Zhao, *J. Mater. Chem. A* **2017**, *5*, 22735–22742.
- [359] S. Nishihama, S. Takayama, K. Yoshizuka, T. Fujigaya, N. Nakashima, *Sep. Sci. Technol.* **2016**, *51*, 2492–2500.
- [360] D. M. Updegraff, *Anal. Biochem.* **1969**, *32*, 420–424.
- [361] S. Bauer, A. B. Ibáñez, *Biotechnol. Bioeng.* **2014**, *111*, 2355–2357.
- [362] A. M. Oickle, S. L. Goertzen, K. R. Hopper, Y. O. Abdalla, H. A. Andreas, *Carbon* **2010**, *48*, 3313–3322.
- [363] A. A. Galhoum, M. G. Mahfouz, A. A. Atia, S. T. Abdel-Rehem, N. A. Gomaa, T. Vincent, E. Guibal, *Ind. Eng. Chem. Res.* **2015**, *54*, 12374–12385.
- [364] L. S. Balistrieri, J. W. Murray, *Am. J. Sci.* **1981**, *281*, 788–806.
- [365] U. Schwarzenbolz, T. Hofmann, N. Sparmann, T. Henle, *J. Agric. Food Chem.* **2016**, *64*, 5071–5078.
- [366] M. Hellwig, S. Witte, T. Henle, *J. Agric. Food Chem.* **2016**, *64*, 7234–7243.
- [367] D. Yiamsawas, W. Kangwansupamonkon, O. Chailapakul, S. Kiatkamjornwong, *React. Funct. Polym.* **2007**, *67*, 865–882.
- [368] C. Arvieu, C. Galy, E. Le Guen, E. Lacoste, *J. Manuf. Mater. Process.* **2020**, *4*, 83.
- [369] J. M. Gladis, T. P. Rao, *Microchim. Acta* **2004**, *146*, 251–258.
- [370] T. Kegl, I. Ban, A. Lobnik, A. Košak, *J. Hazard. Mater.* **2019**, *378*, 120764.
- [371] G. Schwarz, *Ann. Stat.* **1978**, *6*, 461–464.

## 12. Acknowledgement

I own my deepest gratitude to my supervisor Prof. Jan J. Weigand for his comprehensive support and advice. I thank him for providing me a great research topic, first-level laboratory research conditions, and excellent scientific cooperation and communication opportunities, which are extremely rare and difficult to achieve during the pandemic.

I would like to emphasize my special thanks to Dr. Marco Wenzel for his support, encouragement, practical advices on my research plan, and corrections and suggestions on the publications. I am deeply inspired by his rigorous and responsible research attitude.

I would like to thank Dr. Markus Seifert for the SEM-EDX measurements, Phillip Lange for the elemental analysis, Nicole Herold for the STA and GC-MS analysis, and Mathias Marschall for the HF digestion. I am grateful to Dr. Margret Acker for her guidance and advice regarding the adsorption experiments using radiotracers. I would like to thank Dr. Silvia Paasch and Prof. Eike Brunner for the  $^{13}\text{C}$  CP/MAS solid-state NMR measurement. I would like to thank Wendelin Böhm for measuring the Maillard reaction products and the chemical composition of BSG, and Prof. Thomas Henle who supports the cooperation between Wendelin and me. I also thank Prof. Thomas Doert for the support of SEM-EDX measurements.

Many thanks to my former and current colleagues: Dr. Oliver Busse, Katja Elsner, Dr. Linda Götzke, Mathias Hauk, Ali Ameri, Andres Carrasco, Gerrit Schaper, Clemens Taube, Manuel Sauer, Julia Frötschel, Jannis Fidelius, Johannes Steup, Michael Müller, Philipp Royla, Tobis Schneider, Liane Haufe, Nils Kretzschmar, Vladislav Timoshev, Stephen Schulz, Jan Haberstroh, Mario Süß, and Quan Tuan Bui for your friendly support and help. Further thanks to my Chinese colleagues: Chun-Xiang Guo, Jun-Jie Wang, Yu-Jian Zhou, Jian-Feng Zhang, Sai Li, Jian-Zhang Wang, Lin-Wei Huang, and Chuan-Lei Li for a warm community overseas. I would like to express my gratitude to the Chinese Scholarship Council (CSC No. 201804910464) for financial support during the four years of doctoral studies.

My final and sincere appreciation goes to my parents, my boyfriend Dr. Jun-ping Zhang, and my friends who support me and care about me thousands miles away from Dresden. It is my great pleasure and honor to finish my doctoral study here in TU Dresden.



## 13. Publications and conference contributions

### Peer-reviewed publications

1. Y. Su, M. Wenzel, M. Seifert, J. J. Weigand “Surface ion-imprinted brewer’s spent grain with low template loading for selective uranyl ion adsorption from simulated wastewater”, *Journal of Hazardous Materials*, **2022**, 440, 129682.
2. Y. Su, M. Wenzel, S. Paasch, M. Seifert, T. Doert, E. Brunner, J. J. Weigand “One-pot synthesis of brewer’s spent grain-supported superabsorbent polymer for highly efficient uranium adsorption from wastewater”, *Environmental Research*, **2022**, 212, 113333.
3. Y. Su, M. Wenzel, S. Paasch, M. Seifert, W. Böhm, T. Doert, J. J. Weigand “Recycling of Brewer’s Spent Grain as a Biosorbent by Nitro-Oxidation for Uranyl Ion Removal from Wastewater”, *ACS Omega*, **2021**, 6, 19364-19377.  
(**Inside Cover** available at: <https://pubs.acs.org/toc/acsodf/6/30>)
4. Y. Su, W. Böhm, M. Wenzel, S. Paasch, M. Acker, T. Doert, E. Brunner, T. Henle, J. J. Weigand “Mild hydrothermal treated brewer’s spent grain for efficient removal of uranyl and rare earth metal ions”, *RSC Advances*, **2020**, 10, 45116-45129.

### Poster presentation

1. Y. Su, M. Wenzel, S. Paasch, E. Brunner, J. J. Weigand “Oxidation of brewer’s spent grain for *f*-elements adsorption”, *Jahrestreffen der ProcessNet-Fachgruppen Fluidverfahrenstechnik, Adsorption und Extraktion 2020*, Berchtesgaden, **2020**.
2. Y. Su, M. Wenzel, W. Böhm, S. Paasch, M. Seifert, M. Acker, T. Doert, E. Brunner, T. Henle, J. J. Weigand “Brewer’s spent grain: A promising starting material for efficient uranyl ion adsorbents?”, *Actinides Revisited 2022*, Dresden, **2022**, Abstract accepted.





## **Versicherung**

Hiermit versichere ich, dass ich die vorliegende Arbeit ohne unzulässige Hilfe Dritter und ohne Benutzung anderer als der angegebenen Hilfsmittel angefertigt habe; die aus fremden Quellen direkt oder indirekt übernommenen Gedanken sind als solche kenntlich gemacht. Die Arbeit wurde bisher weder in Inland noch im Ausland in gleicher oder ähnlicher Form einer anderen Prüfungsbehörde vorgelegt.

## **Erklärung**

Die vorliegende Dissertation wurde in der Zeit von 09/2018 bis 09/2022 in der Professur für Anorganische Molekülchemie der Technischen Universität Dresden unter der wissenschaftlichen Betreuung von Herrn Prof. Dr. rer. nat. habil. Jan. J. Weigand angefertigt.

Frühere Promotionsverfahren haben nicht stattgefunden.

Ich erkenne die Promotionsordnung vom 23.02.2011 der Fakultät Mathematik und Naturwissenschaften der Technischen Universität Dresden und Ihre Änderung durch die Beschlüsse des Fakultätsrates vom 15.06.2011 und 18.06.2014 sowie des Bereichsrates vom 23.05.2018 in vollem Umfang an.

---

Yi Su